

# Multiscale Cohort Modeling of Atrial Electrophysiology

Risk Stratification for Atrial Fibrillation through Machine  
Learning on Electrocardiograms

Zur Erlangung des akademischen Grades einer

DOKTORIN DER INGENIEURWISSENSCHAFTEN (Dr.-Ing.)

von der KIT-Fakultät für

Elektrotechnik und Informationstechnik

des Karlsruher Instituts für Technologie (KIT)

genehmigte

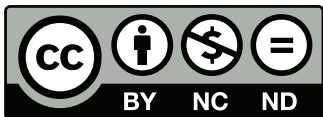
DISSERTATION

von

Claudia Nagel, M.Sc.

geb. in Heidelberg

|                             |                                 |
|-----------------------------|---------------------------------|
| Tag der mündlichen Prüfung: | 17. November 2022               |
| Referent:                   | PD Dr.-Ing. Axel Loewe          |
| 1. Korreferentin:           | Prof. Dr. Blanca Rodriguez      |
| 2. Korreferent:             | Prof. Dr. rer. nat. Olaf Dössel |



*This document - excluding the cover, pictures, tables and graphs - is licensed under the Creative Commons Attribution-NonCommercial-NoDerivs 4.0 International License (CC BY-NC-ND 4.0): <https://creativecommons.org/licenses/by-nc-nd/4.0/>*

# Abstract

Patients affected by atrial fibrillation are exposed to a fivefold increased risk of ischemic stroke. An early detection and diagnosis of the arrhythmia would therefore set the course for timely intervention to prevent potentially occurring comorbidities. A dilation of the left atrium as well as the presence of fibrotically infiltrated atrial tissue are risk factors for atrial fibrillation as they provide the necessary substrate for the maintenance of electrical reentrant activity. Identifying fibrotic atrial cardiomyopathy and left atrial enlargement based on machine learning techniques applied to P waves representing the atrial activity in the 12-lead electrocardiogram in sinus rhythm could thus be an important means for a non-invasive and remote risk stratification of new-onset atrial fibrillation episodes and the selection of appropriate subjects for in-depth screening.

For this purpose, it was investigated if simulated atrial electrocardiogram data added to a clinical training dataset of a machine learning model could contribute to an improved classification of the above mentioned diseases. Two virtual cohorts characterized by both anatomical and functional variability were compiled and served as a basis for generating large-scale and unbiased datasets of P waves with exactly known ground truth labels of the underlying pathology. In this way, the simulated data fulfilled the essential requirements for the development of a machine learning algorithm what sets them apart from clinical data usually not available in large numbers in evenly distributed classes and labels possibly affected by inadequate expert annotations.

A shallow feature-based feedforward neural network was set up to perform the regression task of predicting the tissue volume fraction of left atrial fibrosis. Compared to training the model only on clinical data, training on a hybrid dataset led to a reduction of the absolute estimation error from 17.5 % fibrotic volume on average to 16.5 % evaluated on a clinical test set. A long short-term memory network tailored at performing the binary classification task between P waves of healthy subjects and left atrial enlargement patients yielded an accuracy on a clinical test set of 0.95 when trained on a hybrid dataset, of 0.91 when trained on clinical data only comprising samples with 100 % label certainties and of 0.83 when trained on clinical data including all samples independent on their label certainties.

The results of the studies presented in this thesis demonstrate that electrocardiogram data resulting from electrophysiological modeling and simulations on virtual patient cohorts, covering relevant variability aspects complying with real-world observations, can be a valuable data resource for improving automated atrial fibrillation risk stratification. In this regard, the drawbacks of clinical datasets for developing machine learning models can be

compensated for. This ultimately leads to an enhanced early detection of the arrhythmia, which allows for choosing appropriate treatment strategies in due time and thus, reduces the risk of stroke in affected patients.

# Zusammenfassung

Patienten mit Vorhofflimmern sind einem fünffach erhöhten Risiko für einen ischämischen Schlaganfall ausgesetzt. Eine frühzeitige Erkennung und Diagnose der Arrhythmie würde ein rechtzeitiges Eingreifen ermöglichen, um möglicherweise auftretende Begleiterkrankungen zu verhindern. Eine Vergrößerung des linken Vorhofs sowie fibrotisches Vorhofgewebe sind Risikomarker für Vorhofflimmern, da sie die notwendigen Voraussetzungen für die Aufrechterhaltung der chaotischen elektrischen Depolarisation im Vorhof erfüllen. Mithilfe von Techniken des maschinellen Lernens könnten Fibrose und eine Vergrößerung des linken Vorhofs basierend auf P Wellen des 12-Kanal Elektrokardiogramms im Sinusrhythmus automatisiert identifiziert werden. Dies könnte die Basis für eine nicht-invasive Risikostratifizierung neu auftretender Vorhofflimmerepisoden bilden, um anfällige Patienten für ein präventives Screening auszuwählen.

Zu diesem Zweck wurde untersucht, ob simulierte Vorhof-Elektrokardiogrammdaten, die dem klinischen Trainingssatz eines maschinellen Lernmodells hinzugefügt wurden, zu einer verbesserten Klassifizierung der oben genannten Krankheiten bei klinischen Daten beitragen könnten. Zwei virtuelle Kohorten, die durch anatomische und funktionelle Variabilität gekennzeichnet sind, wurden generiert und dienten als Grundlage für die Simulation großer P Wellen-Datensätze mit genau bestimmbarer Annotationen der zugrunde liegenden Pathologie. Auf diese Weise erfüllen die simulierten Daten die notwendigen Voraussetzungen für die Entwicklung eines Algorithmus für maschinelles Lernen, was sie von klinischen Daten unterscheidet, die normalerweise nicht in großer Zahl und in gleichmäßig verteilten Klassen vorliegen und deren Annotationen möglicherweise durch unzureichende Expertenannotation beeinträchtigt sind.

Für die Schätzung des Volumenanteils von linksatrialem fibrotischen Gewebe wurde ein merkmalsbasiertes neuronales Netz entwickelt. Im Vergleich zum Training des Modells mit nur klinischen Daten, führte das Training mit einem hybriden Datensatz zu einer Reduzierung des Fehlers von durchschnittlich 17,5 % fibrotischem Volumen auf 16,5 %, ausgewertet auf einem rein klinischen Testsatz. Ein Long Short-Term Memory Netzwerk, das für die Unterscheidung zwischen gesunden und P Wellen von vergrößerten linken Vorhöfen entwickelt wurde, lieferte eine Genauigkeit von 0,95 wenn es auf einem hybriden Datensatz trainiert wurde, von 0,91 wenn es nur auf klinischen Daten trainiert wurde, die alle mit 100 % Sicherheit annotiert wurden, und von 0,83 wenn es auf einem klinischen Datensatz trainiert wurde, der alle Signale unabhängig von der Sicherheit der Expertenannotation enthielt.

In Anbetracht der Ergebnisse dieser Arbeit können Elektrokardiogrammdaten, die aus elektrophysiologischer Modellierung und Simulationen an virtuellen Patientenkohorten resultieren und relevante Variabilitätsaspekte abdecken, die mit realen Beobachtungen übereinstimmen, eine wertvolle Datenquelle zur Verbesserung der automatisierten Risikostratifizierung von Vorhofflimmern sein. Auf diese Weise kann den Nachteilen klinischer Datensätze für die Entwicklung von Modellen des maschinellen Lernens entgegengewirkt werden. Dies trägt letztendlich zu einer frühzeitigen Erkennung der Arrhythmie bei, was eine rechtzeitige Auswahl geeigneter Behandlungsstrategien ermöglicht und somit das Schlaganfallrisiko der betroffenen Patienten verringert.

# Acknowledgments

First and foremost, I would like to express my deepest gratitude to Prof. Dr. Olaf Dössel for inspiring and fascinating me with continuous enthusiasm for the field of biomedical engineering and for giving me the opportunity to conduct research leading to this thesis at the Institute of Biomedical Engineering at KIT. By no means less important was the guidance and mentoring of Dr.-Ing. Axel Loewe. Your valuable feedback and insightful comments did not only help me to gain a deeper understanding of cardiac modeling but were also decisive for staying focused and keeping track of my work.

Additionally, I would like to thank Prof. Dr. Blanca Rodriguez for hosting me during my research stay at University of Oxford, showing interest in my work and for co-refereeing my thesis. In this regard, I would also like to express my deepest gratitude to Karlsruhe House of Young Scientists (KHYS) for funding the entire stay, which made all of it possible in the first place.

Furthermore, I would like to thank all members of the institute for making everyday life in the office very enjoyable and diversified, also in times when we worked remotely. I especially like to thank all members of the CaMo group for scientific discussions, the group culture of helping each other, keeping up the team spirit, as well as sharing my passion for tennis and spending various lunch breaks with me at the tennis courts. I would also like to thank the group in Oxford for warmly and open-mindedly welcoming me, and including me not only scientifically but also socially in their group.

Large parts of this research were funded by the EMPIR program under grant MedalCare 18HLT07. In this regard, I would not only like to thank the funding organization but also all partners in this EU-funded project whom I had the opportunity to collaborate with in the last three years. I appreciate the fruitful collaboration, stimulating discussions and being provided valuable feedback regarding both modeling and metrology aspects during monthly online meetings. In particular, I would like to thank Karli, Matthias, Jenny and Benjamin for not only being reliable and dedicated colleagues but also for sharing a lot of memories outside of work.

Furthermore, thank you to all the Bachelor and Master students I supervised. I especially would like to highlight the outstanding work of Hannes Welle, Jule Bender and Fabian Anzlinger contributing to parts of my thesis.

Finally, I would like to thank my friends and family for your invaluable support in every situation. My most profound gratitude goes to my brother and my parents, for all your unconditional love and uncompromised support throughout my entire life without which I

would have never made it anywhere close to where and, most importantly, who I am today. Lastly, thank you, Daniel, for being by my side and having my back whenever I need it and beyond. I will be forever thankful for your calming, unwavering and wholehearted encouragement and for your unexceptional support every step of the way.

# Contents

|                                                                                   |            |
|-----------------------------------------------------------------------------------|------------|
| <b>Abstract</b> . . . . .                                                         | <b>i</b>   |
| <b>Zusammenfassung</b> . . . . .                                                  | <b>iii</b> |
| <b>Acknowledgments</b> . . . . .                                                  | <b>v</b>   |
| <b>Abbreviations</b> . . . . .                                                    | <b>xi</b>  |
| <b>1 Introduction</b> . . . . .                                                   | <b>1</b>   |
| 1.1 Motivation . . . . .                                                          | 1          |
| 1.2 State of the Art . . . . .                                                    | 2          |
| 1.3 Research Question and Hypothesis . . . . .                                    | 4          |
| 1.4 Structure of the Thesis . . . . .                                             | 5          |
| <hr/>                                                                             |            |
| <b>I Fundamentals</b>                                                             | <b>7</b>   |
| <hr/>                                                                             |            |
| <b>2 Medical Fundamentals</b> . . . . .                                           | <b>9</b>   |
| 2.1 Cardiac Anatomy and Physiology . . . . .                                      | 9          |
| 2.2 Electrical Excitation System . . . . .                                        | 10         |
| 2.3 Atrial Fibrillation . . . . .                                                 | 13         |
| <b>3 Mathematical Fundamentals</b> . . . . .                                      | <b>17</b>  |
| 3.1 Multi-scale Electrophysiological Modeling . . . . .                           | 17         |
| 3.2 Statistical Shape Modeling . . . . .                                          | 23         |
| 3.3 Principal Component Analysis . . . . .                                        | 27         |
| 3.4 Machine Learning . . . . .                                                    | 29         |
| <hr/>                                                                             |            |
| <b>II Validation of Simplified Modeling Approaches</b>                            | <b>33</b>  |
| <hr/>                                                                             |            |
| <b>4 Comparison of Propagation Models and Forward Calculation Methods</b> . . . . | <b>35</b>  |
| 4.1 Introduction . . . . .                                                        | 35         |
| 4.2 Methods . . . . .                                                             | 36         |
| 4.3 Results . . . . .                                                             | 43         |
| 4.4 Discussion . . . . .                                                          | 48         |

|            |                                                                                                                                     |            |
|------------|-------------------------------------------------------------------------------------------------------------------------------------|------------|
| 4.5        | Conclusion . . . . .                                                                                                                | 57         |
| <hr/>      |                                                                                                                                     |            |
| <b>III</b> | <b>Multi-scale Generation of Virtual Cohorts of Computational Models</b>                                                            | <b>59</b>  |
| <hr/>      |                                                                                                                                     |            |
| <b>5</b>   | <b>Development and Evaluation of a Bi-atrial Statistical Shape Model . . . . .</b>                                                  | <b>61</b>  |
| 5.1        | Introduction . . . . .                                                                                                              | 61         |
| 5.2        | Methods . . . . .                                                                                                                   | 64         |
| 5.3        | Results . . . . .                                                                                                                   | 72         |
| 5.4        | Discussion . . . . .                                                                                                                | 77         |
| <b>6</b>   | <b>Population of Multiscale Models . . . . .</b>                                                                                    | <b>83</b>  |
| 6.1        | Introduction . . . . .                                                                                                              | 83         |
| 6.2        | Methods . . . . .                                                                                                                   | 84         |
| 6.3        | Results . . . . .                                                                                                                   | 90         |
| 6.4        | Discussion . . . . .                                                                                                                | 97         |
| <b>7</b>   | <b>Large-scale Dataset of Healthy and Pathological ECGs . . . . .</b>                                                               | <b>105</b> |
| 7.1        | Introduction . . . . .                                                                                                              | 105        |
| 7.2        | Methods . . . . .                                                                                                                   | 106        |
| 7.3        | Results . . . . .                                                                                                                   | 109        |
| 7.4        | Discussion . . . . .                                                                                                                | 110        |
| <hr/>      |                                                                                                                                     |            |
| <b>IV</b>  | <b>Improving Non-invasive Risk Stratification of Atrial Fibrillation<br/>through Machine Learning and <i>in silico</i> ECG Data</b> | <b>115</b> |
| <hr/>      |                                                                                                                                     |            |
| <b>8</b>   | <b>Estimation of Left Atrial Fibrosis . . . . .</b>                                                                                 | <b>117</b> |
| 8.1        | Introduction . . . . .                                                                                                              | 117        |
| 8.2        | Methods . . . . .                                                                                                                   | 119        |
| 8.3        | Results . . . . .                                                                                                                   | 132        |
| 8.4        | Discussion . . . . .                                                                                                                | 143        |
| 8.5        | Conclusion . . . . .                                                                                                                | 148        |
| <b>9</b>   | <b>Detection of Left Atrial Enlargement . . . . .</b>                                                                               | <b>149</b> |
| 9.1        | Introduction . . . . .                                                                                                              | 149        |
| 9.2        | Methods . . . . .                                                                                                                   | 150        |
| 9.3        | Results . . . . .                                                                                                                   | 154        |
| 9.4        | Discussion . . . . .                                                                                                                | 155        |
| 9.5        | Conclusion . . . . .                                                                                                                | 159        |
| <hr/>      |                                                                                                                                     |            |
| <b>V</b>   | <b>Final Remarks</b>                                                                                                                | <b>161</b> |
| <hr/>      |                                                                                                                                     |            |
| <b>10</b>  | <b>Outlook . . . . .</b>                                                                                                            | <b>163</b> |

---

|                                                                                    |            |
|------------------------------------------------------------------------------------|------------|
| 10.1 Application and Validation of Multiscale Populations of Atrial Models . . .   | 163        |
| 10.2 ECG-based Differential Diagnosis of Atrial Fibrillation Related Pathologies   | 165        |
| <b>11 Conclusion . . . . .</b>                                                     | <b>167</b> |
| <b>A P waves and Amplitude Features in Fibrosis Remodeling Scenarios . . . . .</b> | <b>171</b> |
| <b>B Ventricular Pathologies in Large-scale ECG Dataset . . . . .</b>              | <b>177</b> |
| <b>References . . . . .</b>                                                        | <b>181</b> |
| <b>List of Publications and Supervised Theses . . . . .</b>                        | <b>205</b> |



# Abbreviations

cv[CVs]conduction velocities

|                 |                                                                   |     |
|-----------------|-------------------------------------------------------------------|-----|
| <b>AFs</b>      | atrial fibrillations . . . . .                                    | 1   |
| <b>APs</b>      | action potentials . . . . .                                       | 5   |
| <b>APDs</b>     | action potential durations . . . . .                              | 12  |
| <b>AUCs</b>     | area under the curves . . . . .                                   | 146 |
| <b>AVBs</b>     | atrioventricular blocks . . . . .                                 | 106 |
| <b>BEMs</b>     | boundary element methods . . . . .                                | 22  |
| <b>BSAs</b>     | body surface areas . . . . .                                      | 98  |
| <b>CTs</b>      | computed tomographys . . . . .                                    | 25  |
| <b>CVs</b>      | conduction velocitys . . . . .                                    | 13  |
| <b>ECGs</b>     | electrocardiograms . . . . .                                      | 1   |
| <b>FAMs</b>     | arrhythmogenic fibrotic atrial cardiomyopathys . . . . .          | 14  |
| <b>FEMs</b>     | finite element methods . . . . .                                  | 46  |
| <b>GPs</b>      | Gaussian processs . . . . .                                       | 68  |
| <b>GPMMs</b>    | Gaussian process morphable models . . . . .                       | 26  |
| <b>IABs</b>     | interatrial conduction blocks . . . . .                           | 106 |
| <b>ICPs</b>     | iterative closest points . . . . .                                | 66  |
| <b>IVCs</b>     | infinite volume conductors . . . . .                              | 46  |
| <b>L-BFGSs</b>  | limited-memory Broyden–Fletcher–Goldfarb–Shannos . . . . .        | 69  |
| <b>LAs</b>      | left atriums . . . . .                                            | 64  |
| <b>LAAs</b>     | left atrial appendages . . . . .                                  | 64  |
| <b>LAEs</b>     | left atrial enlargements . . . . .                                | 14  |
| <b>LATs</b>     | local activation times . . . . .                                  | 5   |
| <b>LAVs</b>     | left atrial volumes . . . . .                                     | 150 |
| <b>LBBBs</b>    | left bundle branch blocks . . . . .                               | 106 |
| <b>LGE-MRIs</b> | late Gadolinium enhancement magnetic resonance imagings . . . . . | 14  |
| <b>LSTMs</b>    | long short-term memorys . . . . .                                 | 32  |
| <b>MIIs</b>     | myocardial infarctions . . . . .                                  | 106 |
| <b>MRs</b>      | magnetic resonances . . . . .                                     | 25  |
| <b>mSES</b>     | mean squared errors . . . . .                                     | 29  |
| <b>MVDs</b>     | multivariate normal distributions . . . . .                       | 107 |
| <b>PCAs</b>     | principal component analysis . . . . .                            | 23  |
| <b>PVs</b>      | pulmonary veins . . . . .                                         | 61  |

---

|              |                                               |     |
|--------------|-----------------------------------------------|-----|
| <b>PVIs</b>  | pulmonary vein isolations . . . . .           | 146 |
| <b>PWds</b>  | P wave durations . . . . .                    | 118 |
| <b>RAs</b>   | right atriums . . . . .                       | 64  |
| <b>RAAs</b>  | right atrial appendages . . . . .             | 69  |
| <b>RBBBs</b> | right bundle branch blocks . . . . .          | 106 |
| <b>REs</b>   | reaction-Eikonals . . . . .                   | 36  |
| <b>rmss</b>  | root mean squareds . . . . .                  | 118 |
| <b>rmse</b>  | root mean squared errors . . . . .            | 29  |
| <b>ROCs</b>  | receiver operating characteristicss . . . . . | 29  |
| <b>SSMs</b>  | statistical shape models . . . . .            | 4   |
| <b>TGFs</b>  | transforming growth factors . . . . .         | 41  |

---

# Introduction

## 1.1 Motivation

In addition to numerous technical advances and public debates in the last decade, the global COVID-19 pandemic has most recently again brought the need for and benefits of digitalization in healthcare and the rollout of telemedicine services into focus. These technologies call for artificial intelligence and machine learning solutions [1] supporting clinical decision making and remote patient monitoring, guiding therapy and predicting clinical outcome. High throughput as well as the ability to discern patterns by examining multivariate feature combinations and detecting signal or image characteristics not conceivable for a human observer are among the advantages of machine learning-based analysis tools in medicine.

As a non-invasively acquirable, easily accessible, inexpensive and widely available system in hospitals worldwide, the 12-lead electrocardiogram (ECG) is a powerful diagnostic tool in clinical practice to monitor and evaluate the cardiac function. As such, it can be an alternative to intracardiac signals recorded during invasive procedures or to expensive imaging techniques requiring trained personnel and entailing potential exposure to radiation. Thus, the automated analysis of ECG data has great potential as a preventive screening tool for cardiovascular diseases [2, 3], which are the leading cause of death in most developed countries [4]. In particular, patients affected by atrial fibrillation (AF), the most common sustained cardiac arrhythmia [5–9], would benefit from remote ECG monitoring and automated analysis software [10–12] as a considerable percentage of AF patients remain asymptomatic [13]. If left untreated, silent and sub-clinical AF can lead to unexpected and life-threatening thromboembolic events and ischemic stroke [14, 15].

However, progress in developing ECG-based computer assisted diagnostic tools is hampered due to limited supply of appropriate patient datasets. High-quality data curation, collection and preparation is time-consuming and involves considerable effort and expenses preventing open data sharing across centers and research groups. Furthermore, patient data is highly sensitive explaining the strict regulations in sharing and reuse of medical datasets. In the few open [16] or gated access [17] ECG databases available online, data samples usually stem from only a limited number of sources. Thus, patient enrollment in

single center studies may not only cause an imbalance among the classes to be distinguished by the machine learning model, but may also introduce a bias in both demographic, as for example gender [18–20], age or ethnicity [21], and technical aspects, such as device manufacturer or acquisition site [22]. To avoid a distorted prediction adversely discriminating under-represented groups and to prevent overfitting of the model to the given input samples, datasets employed for machine learning models must not only be as large, but also as diverse as possible [23]. Moreover, inter- and intra-observer variability clearly impairs expert signal annotation certainty and quality [24] impeding the training of a supervised learning algorithm from the outset.

Computational models of the heart have contributed to elucidating fundamental cardiac disease mechanisms in various previous studies. In contrast to data-driven synthetic ECG generators based on generative adversarial networks [25, 26], mechanistic electrophysiological models underlying the simulation do not only allow for composing large-scale, unbiased, noise-free and reliably labeled cardiac signals, but also provide a well-controlled framework to identify the mechanisms driving and terminating cardiac arrhythmias. Recently, personalized multiscale modeling of cardiac electrophysiology demonstrated added clinical value for example in the fields of ventricular tachycardia [27–29] and AF [30–32]. To generate mechanistic insight that is not only applicable to a single patient but to entire subgroups of the population as a complementary source of evidence and data for automated signal analysis and disease classification, cohort based modeling capturing relevant anatomical, disease-specific and functional variability occurring in clinical practice is warranted.

In contrast to cardiac digital twins [33, 34], where a personalized model of a patient’s heart is replicated *in silico* to allow for patient-specific therapy guidance, cohort modeling aims at predicting risk and investigating the efficacy of different therapy options on a population basis and derive specific treatment criteria applicable to entire subgroups of the population. Covering variability in a virtual population is key for generating large-scale synthetic ECG datasets encompassing a wide range of signal variation prevailing also in clinical cohorts [35, 36]. These cohorts of computational models can form the basis for large-scale mechanistic simulations of cardiac signals in a well-controlled environment enriching and extending clinically recorded datasets for machine learning applications to investigate the potential of the 12-lead ECG for non-invasive, automated and remote AF risk stratification.

## 1.2 State of the Art

Since AF is the most frequently clinically diagnosed supraventricular tachycardia worldwide and is associated with an increased risk of stroke, various clinical studies have focused on individual risk stratification to allow for timely and appropriate intervention or prevent new-onset AF episodes altogether [37–40]. Among them is the Apple Heart Study, where a smartwatch worn by >400,000 participants was meant to release a notification in case of irregular pulse occurrence [41] detected using photoplethysmography. Upon receiving

the notification, eligible patients were mailed an ECG patch to be worn for up to 7 days so that trained physicians could inspect the long-term recordings and possibly confirm the AF diagnosis. During a period of about 4 months, 0.52 % of the participants received an irregular pulse notification. Among the patients returning the ECG patch, the positive predictive value of AF actually being detectable in the ECG was 0.84. Attia *et al.* [42] applied a convolutional neural network to 10 second 12-lead ECG traces in normal sinus rhythm and succeeded in identifying AF patients with an accuracy of 79.4%. Kurshid *et al.* [43] showed that fitting a hazard model not only with the clinical CHARGE-AF risk score [44, 45] but additionally with the 5-year AF probability predicted by a convolutional neural network trained with clinical 12-lead ECGs yielded superior results than using clinical risk scores alone. Eichenlaub *et al.* [46] showed that patients in whom AF recurs after ablation therapy can be identified based on non-invasively recorded body surface potential maps with 91.3% sensitivity and 93.7% specificity. Thus, different previous studies have confirmed that machine learning enabled algorithms are suitable for an early identification of AF patients based on sinus rhythm ECGs of different clinical cohorts. To address and overcome the shortcomings of clinical ECG data as elaborated on in section 1.1, numerous simulation studies have been carried out predominantly for optimizing AF therapy planning.

Regarding AF treatment by ablation, Luongo *et al.* [47] showed that a prediction of acute pulmonary vein isolation success based on the ECG is possible with a specificity of 82% and a sensitivity of 73% on a clinical test set of 46 AF patients. Importantly, this classifier was trained exclusively on synthetic data (1,128 ECGs) and tested on clinical data [47]. By drawing on simulations, the vulnerability of the atria for developing new-onset AF episodes can be evaluated [48]. Thereafter, the suitability of pharmaceutical agents [49, 50] or virtual ablation lines [30, 31, 51] regarding termination of rotational activity can be assessed using computational models. However, a major challenge in previous simulation studies focusing on therapy planning for entire subpopulations of patients usually lies in the generation of large populations of atrial models.

To create a patient-specific computational atrial model, a geometrical representation of the atria obtained from tomographic imaging or electroanatomical mapping studies serves as a basis to replicate a patient's heart *in silico* [52]. The process of segmenting tomographic images and building a simulation-ready atrial geometrical model from the resulting endocardial wall, requires time and rule-based augmentation tools [53]. Thus, most of the simulation studies mentioned before were conducted by employing only a limited number of patient-specific geometries. This is acknowledged as a limitation in these publications, as observing only few patients might not be sufficient to thoroughly represent anatomical variability of the atria across a population. However, large populations of ionic models have been compiled in previous studies by varying conductances of several ion channels in the cell model to represent the biological variability observed in experimental studies [54]. These populations of models have been used to study drug-induced effects on different action potential and ionic current biomarkers to predict either the risk of cardiotoxicity in the field of safety pharmacology [55–58] or to determine the efficacy of different channel blockers and their doses on anti-arrhythmic properties in the field of precision medicine [50, 59–63].

It has been shown that these *in silico* drug testing methods can predict cardiotoxicity more accurately than animal trials [55].

These populations of cell models aim at capturing the cellular electrophysiological variability. To cover the aspect of cardiac shape and anatomical variability in cohorts of computational models, statistical shape models (SSMs) provide the basis to generate a large variety of geometrical models representing atrial anatomy and its clinically observed statistical variability [64]. SSMs of the human heart have previously been constructed for the purpose of active shape modeling segmentation approaches or to investigate the suitability of left atrial shape scores as a predictor for AF [65, 66].

In consequence, addressing the disadvantages of clinically recorded ECG data for AF risk prediction by drawing on simulations is a promising approach. However, the lack of comprehensive and calibrated datasets of atrial multiscale computational models bars the way to progress for extensive atrial ECG simulations. Based on these aspects, the aim of this thesis is defined as outlined in section 1.3.

### 1.3 Research Question and Hypothesis

The aim of this thesis is to simulate and validate large-scale synthetic ECG datasets covering various types of underlying model variability applicable as an extension to clinical input data for machine learning algorithms and in this way counteract the shortcomings of clinically recorded patient data. Thereby, a particular focus is set on the application of machine learning techniques for detecting risk markers for AF from 12-lead ECGs in normal sinus rhythm. Specifically, the following research question and hypothesis are aimed to be answered and put to test:

#### Research Question

**Can modeling and simulation applied to populations of multiscale atrial models covering various types of variability contribute to overcome the lack of high quality, unbiased, well-controlled and large-scale clinical ECG datasets to identify AF susceptible patients?**

#### Hypothesis

It is hypothesized that the performance of machine learning algorithms trained to identify patients with fibrotic atrial substrate and enlarged left atrial volumes improves when adding simulated atrial ECGs to the input dataset compared to using clinical data only during training.

The following methodological milestones relevant to answer the research questions presented above are addressed and implemented in this thesis:

- Assessing fidelity of simplified simulation models by evaluating the accuracy of resulting action potential (AP) and ECG signals as well as local activation times (LATs) compared to the simulation results obtained from the gold standard methods to speed up the generation of large, yet physiologically accurate, simulated ECG datasets.
- Development and evaluation of a bi-atrial SSM as a basis to compile a wide range of anatomical models applicable to electrophysiological simulations.
- Calibration of a large population of multiscale atrial computational models comprising anatomical and functional variability to ensure realistic and representative phenotypic variability of simulated ECGs comparable to clinical data variability.
- Generation of a simulated ECG dataset comprising 10,000 signals of 10 seconds length representing a healthy cohort and selected pathologies.
- Application of simulated atrial ECGs as an additional input source to machine learning algorithms to identify patients with fibrotic atrial substrate and enlarged left atrial volumes at a higher accuracy than by using clinical data only for training the classifier.

Summarizing, the research presented in this thesis is meant to serve as groundwork to support and contribute to the vision of an early and non-invasive identification of asymptomatic AF patients via remote monitoring, selecting susceptible patients for in-depth AF screening and in this way reduce their risk of stroke through timely intervention.

## 1.4 Structure of the Thesis

The thesis is structured as described below.

**Part I** outlines selected fundamentals relevant to the analysis in this work and the resulting findings.

- In **Chapter 2**, the underlying physiological principles of the cardiac electrical excitation system and the arrhythmogenesis of atrial fibrillation are described.
- **Chapter 3** summarizes the mathematical underpinnings of electrophysiological cardiac modeling and simulation, statistical shape modeling and machine learning.

In **Part II**, the drawback of biophysically detailed simulation approaches being demanding in terms of computational resources to solve the model equations is addressed. Especially for large-scale simulations of atrial electrophysiology, as they should be conducted for the studies presented in this thesis, a fast and accurate simulation framework is indispensable.

- In **Chapter 4**, the applicability of computationally less complex though also biophysically less detailed simulation models is investigated by comparing the simulation results between simplified and gold standard methods.

**Part III** describes the generation of computational atrial model cohorts.

- **Chapter 5** details the construction and evaluation of an SSM of the human atria. In this way, the limitation of small sample sizes of atrial geometries in previous simulation studies is addressed which led to an insufficient capture of anatomical variability and of resulting ECG morphology in these virtual multiscale model cohorts.
- In **Chapter 6**, the generation and calibration of a population of multiscale atrial models built based on geometrical instances of the SSM combined with electrophysiological variability on tissue and cellular scale are described.
- In **Chapter 7**, the generation of 10,000 12-lead ECGs is shown. These signals comprise not only the atrial activity of a single heartbeat but represent instead a complete 10 second time series of simulated cardiac signals for a healthy control group and selected pathologies. In this way, the synthetic signals are of a comparable format to actual clinical recordings without the need for preceding waveform delineation or feature extraction and thus provide the necessary input for a potential application of deep learning methods based on multi-dimensional time series signals.

**Part IV** refers to the aim of this thesis to identify patients at high risk for developing new-onset AF episodes supported by simulated ECG signals. Thus, the generated model populations were applied for large-scale simulations of atrial activity in sinus rhythm, optionally considering anatomical, electrical and structural remodeling typically occurring in AF patients. Machine learning techniques are applied to distinguish between healthy individuals and patients with fibrotic atrial cardiomyopathy or left atrial enlargement, both of which are reported to promote and contribute to the arrhythmogenesis of AF.

- In **Chapter 8**, P wave features were extracted from simulated and clinical ECG datasets comprising healthy subjects and patients with fibrotic substrate patches in the atria. These were subsequently used as input to a shallow neural network tailored at detecting fibrotic atrial cardiomyopathy.
- In **Chapter 9**, the signals representing a healthy and a left atrial enlargement population were fed into a long short-term memory network to distinguish between the two cohorts. The study design was again translational to identify the added value that simulated data can carry when extending clinically recorded ECGs as input for machine learning techniques.

An outlook for future projects and a general conclusion drawn from the findings of the research leading to this thesis are outlined in **Chapter 10** and **11**, respectively.

---

PART I

---

# FUNDAMENTALS



---

# Medical Fundamentals

## 2.1 Cardiac Anatomy and Physiology

The human heart is located behind the sternum in the chest and consists of four chambers: The left and the right atria are connected through the mitral and tricuspid valve to the left and right ventricles below. The atrial and ventricular septal wall separate the left from the right cardiac chambers (see Figure 2.1). [67–69]

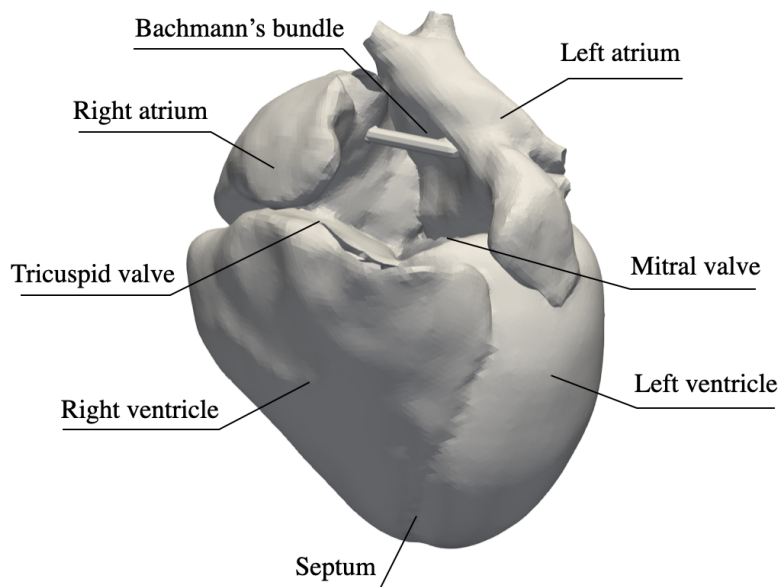


Figure 2.1: Anatomy of the human heart.

The cardiac cycle starts with ventricular diastole. The left and the right atrium receive blood through the pulmonary veins from the lungs and mostly through the venae cavae from

the body periphery, respectively. The atria contract and pump blood through the valves into the ventricles. During ventricular systole, the ventricles contract. Oxygenated blood from the left ventricle is ejected through the aorta branching into different arteries connecting the heart to other organs and systems in the human body. Right ventricular contraction initiates the flow of oxygen-depleted blood through the pulmonary valve to the lungs where it is reoxygenated. Thereafter, the ventricles relax again and the next cardiac cycle starts. [67–69]

## 2.2 Electrical Excitation System

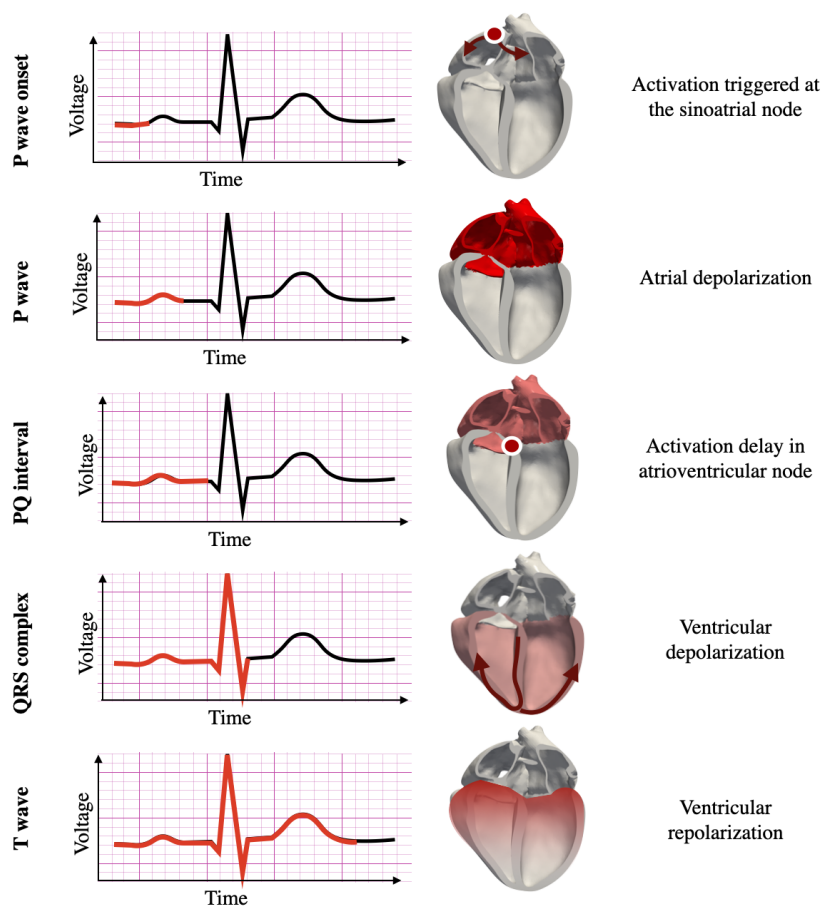


Figure 2.2: Genesis of the electrocardiogram.

The contraction of the heart is caused and preceded by its electrical activation, which can be measured non-invasively on the body surface via electrocardiography (see Figure 2.2). For the acquisition of a 12-lead electrocardiogram (ECG), 9 electrodes are placed on the left and right arm (LA, RA), the left leg (LL) and along the rib cage (v1-v6). In this way, the ECG in 12 channels representing different axes of excitation propagation can be calculated

as the difference in potential recorded at the electrode positions as:

$$I = LA - RA$$

$$II = LL - RA$$

$$III = LL - LA$$

$$aVR = RA - (LA + LL)/2$$

$$aVL = LA - (RA + LL)/2$$

$$aVF = LL - (LA + RA)/2$$

$$V1 = v1 - (LL + LA + RA)/3$$

$$V2 = v2 - (LL + LA + RA)/3$$

$$V3 = v3 - (LL + LA + RA)/3$$

$$V4 = v4 - (LL + LA + RA)/3$$

$$V5 = v5 - (LL + LA + RA)/3$$

$$V6 = v6 - (LL + LA + RA)/3$$

The excitation origin of the electrical activation in the heart is triggered by the sinoatrial node located in the right atrium. It automatically releases electrical stimuli at a pace determining the heart rate in physiological sinus rhythm scenarios [70]. The preferred direction of activation in the right atrium is defined by rapid and anisotropic conduction via crista terminalis and the pectinate muscles on the posterior wall and Bachmann's bundle on the anterior wall. As both atria are electrically isolated from one another at the septal wall, the activation of the left atrium in the healthy sinus rhythm case takes place via interatrial connections, such as Bachmann's bundle on the anterior wall or posterior bridges and the coronary sinus bridge. The activation of both atria is represented by the P wave in the ECG. Following the atrial activation, the depolarization wavefront is delayed at the atrioventricular node, which reflects in the PQ segment in the ECG. Subsequently, the ventricles are activated through the bundle of His conducting electrical impulses to the terminal branches of the Purkinje fibers from where the excitation transfers to the ventricular myocardial tissue causing the QRS complex in the ECG. Atrial repolarization takes place simultaneously to ventricular activation and thus, a supposedly occurring  $T_a$  wave does not show in the ECG as it is buried within the QRS complex. Finally, the repolarization of the ventricles cause an upright and concordant T wave in the ECG as tissue regions in close proximity to the ventricular apex start to repolarize first before the repolarization wavefront traverses the ventricular tissue mainly in apicobasal direction towards the valves. [71, 72]

The electrophysiological principles underlying the activation initiation and propagation as well as the formation of cardiac electrical sources measurable on the body surface can be explained on a cellular level. If a cell in the myocardial tissue is activated, an action potential is triggered. The latter describes the time course of the difference in potential across the cell membrane between the intra- and extracellular space of a single cell arising due to

differences in ionic concentrations in both domains [71, 72]. The typical signal course of an atrial action potential is depicted in Figure 2.3.

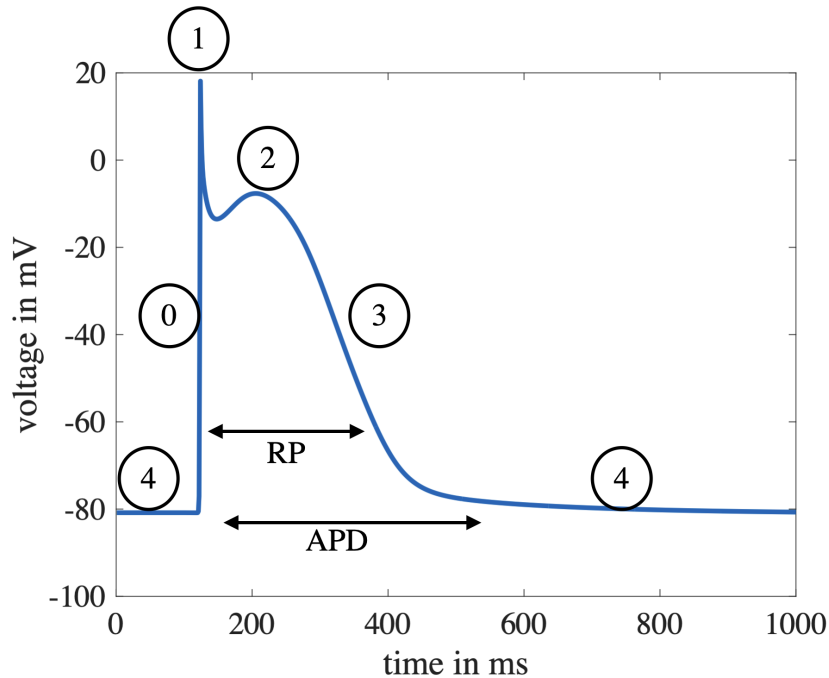


**Figure 2.3: Time course of an atrial action potential.** Phase 0-4 upstroke, peak, plateau phase, repolarization, and resting membrane potential, respectively. APD = action potential duration, RP = refractory period

In phase 4, the cell is not yet depolarized and a resting membrane potential of approximately -80 mV prevails [73]. When triggered, e.g., by an action potential of a neighboring cell, fast  $\text{Na}^+$  channels open causing an inflow of sodium to the intracellular space and consequently, an increase in transmembrane voltage in phase 0. The peak conductance of the  $\text{Na}^+$  channels coincides with the time step of the steepest action potential upstroke denoting the activation time of the cardiomyocyte. The peak of the action potential in phase 1 is marked by a transmembrane voltage of approximately +20 mV and  $\text{Na}^+$  channels are inhibited. In response to the change in transmembrane voltage,  $\text{K}^+$  and  $\text{Ca}^{2+}$  channels open. Potassium outward and calcium inward currents electrically balance each other which reflects in the plateau phase of constant voltage in phase 2. As the potassium outward current starts to dominate in phase 3, the transmembrane voltage declines again during the repolarization phase. During the refractory period (see Figure 2.3),  $\text{Na}^+$  channels remain closed, sodium cannot leak in the intracellular space and thus, the cell would not respond with the initiation of a new action potential when triggered in this interval. The refractory period of a cardiomyocyte is a protective mechanisms to prevent rapid and recurring depolarization of the the same cardiac tissue regions. The decline in voltage in the repolarization phase lasts until the

resting membrane potential of approximately  $-80$  mV is reached again marking the offset of the action potential duration (APD). Sodium-calcium exchangers and sodium-potassium pumps ensure a restoration of the initial ion distribution between the intra- and extracellular space so that a new action potential can be triggered in the subsequent cardiac cycle. [71]

Moving from single cell to the excitation of an entire tissue patch, the action potential is propagated via gap junctions connecting adjacent cells and thus cause the electrical depolarization wave to advance across the myocardial tissue. The speed the activation wavefront traverses the tissue with is commonly referred to as conduction velocity (CV). [71]

## 2.3 Atrial Fibrillation

Atrial fibrillation (AF) is the most frequently encountered cardiac arrhythmia and affects 2-3% of the population in Europe and North America [5]. Advanced age is one of the risk factors for developing new-onset AF episodes. Therefore, even higher AF prevalence rates are expected for the years to come due to the ongoing aging of the society in industrialized countries. In contrast to normal sinus rhythm, AF episodes are characterized by disorganized reentrant waves traversing the atrial tissue. The maintenance of the arrhythmia requires either rapid foci firing or a remodeled substrate supporting the reentry, for example due to fibrotic infiltrations that alter conduction and cellular electrophysiology facilitating the formation of reentry circuits. Due to hemodynamic impairment and blood stasis induced by the electrical disorganization, AF favors the formation of blood clots and therefore increases the risk of ischemic stroke for individual patients as well as morbidity and mortality rates on a population level. Consequently, the development of optimal treatment strategies is crucial to not only reduce the enormous financial burden for the public health system of 45 billion € per year in the European Union [74] but also to improve the quality of life for affected patients by achieving long-term freedom from arrhythmia recurrence. Anti-arrhythmic drug therapy is one of the treatment options for AF to either control the heart rate in rate control strategies or to restore and maintain sinus rhythm in rhythm control strategies [75]. However, a patient-specific selection of the drug as well as a personalized adjustment of the optimal drug dose is likely necessary to maximize therapeutic yield. An alternative first-line therapy or follow-up treatment option for drug-resistant AF patients is catheter ablation [75]. During the minimally invasive procedure, scars are created at selected locations on the myocardial tissue, which aim at blocking pathological excitation pathways. To treat substrate-based arrhythmia in persistent AF patients, a mapping procedure precedes the intervention to localize the origin of the pathological excitation [76, 77]. However, neither therapeutic option can provide permanent cure for AF as recurrence rates of 30-60% prevail [78]. Recent work showed that a patient-specific ablation approach by targeting atrial areas of high spatiotemporal dispersion in the electrograms arising due to locally reduced conduction velocities can reduce arrhythmia recurrence rates to 14% whereas the patient group undergoing pulmonary vein isolation alone was characterized by 41% recurrence [79].

Moreover, Jadidi *et al.* [80] found that low voltage guided ablation procedures can help to identify additional ablation targets for arrhythmia termination in persistent AF patients.

Structural and anatomical remodeling of the atria, as for example fibrotic substrate or enlargement of the atrial chambers, frequently occurs together with AF and is commonly referred to as atrial cardiomyopathy. Although it is still under debate whether remodeling is a cause or a consequence of AF, the presence of atrial fibrosis and dilation of the left atrium are known to set the stage for the development of reentrant activity as will be explained in section 2.3.1 and 2.3.2.

### 2.3.1 Fibrotic Atrial Cardiomyopathy

Arrhythmogenic fibrotic atrial cardiomyopathy (FAM) manifests in the presence of fibrotic substrate replacing and interfering with healthy myocardial tissue in the atria. The proliferation and activation of fibroblasts leads to an accumulation of collagen and other extracellular matrix proteins in the interstitial space and cause neighboring cells to be electrically isolated from one another impeding transverse wave propagation [81]. Furthermore, down-regulation of gap junctions entails conduction slowing in fiber direction. Generally, the resulting reduced conduction velocity facilitates the formation of reentry circuits in AF patients. This is because the time for a wavefront reaching excitable tissue regions after traversing an anatomical or functional obstacle is increased. This comes along with an increased likelihood that firstly, the effective refractory period of the cells in the vulnerable region has already passed, secondly, a new action potential in these cells can be triggered and finally, a reentry on a macroscopic level can occur. Ionic remodeling in fibrotic regions also contributes to promoting AF as a reduction of  $G_{K_1}$  and  $G_{CaL}$  conductances in fibrotically infiltrated regions cause a shortened refractory period [82]. The inhomogeneities in refractory period as well as fibroblast-myocyte coupling can also lead to uni-directional conduction block increasing reentry vulnerability.

State-of-the-art methods for identifying fibrosis in the atria comprise electroanatomical voltage mapping and late Gadolinium enhancement magnetic resonance imaging (LGE-MRI). The former is acquired during a minimally invasive procedure preceding catheter ablation. Applying a threshold of 0.5 mV for bipolar electrograms recorded in sinus rhythm allows for the identification of fibrotic areas [83, 84] serving as potential additional ablation targets in recurrent AF after pulmonary vein isolation. LGE-MRI is an imaging technique with Gadolinium-based contrast agents requiring expensive equipment and trained personnel for segmenting areas of high intensity image ratios to be identified as fibrosis. However, the spatial location of fibrosis found based on LGE-MRI and electroanatomical mapping is reported to differ from one another. Furthermore, there is no clear consensus in the community on the efficacy of choosing areas of anchoring rotors as additional targets for catheter ablation up to date [31, 80, 85].

### 2.3.2 Left Atrial Enlargement

Structural remodeling in AF patients comprise among others an enlargement of the left atrium occurring as a consequence of chronic pressure overload. An enlargement of the left atrial chamber leads to an increased path length of the reentrant wave in the atria resulting in an increased likelihood that a reentrant wavefront hits excited and non-refractory tissue in the critical temporal window of AF vulnerability [86, 87]. Thus, left atrial enlargement (LAE) can be an independent predictor for AF [65] which is why an early detection of LAE could contribute to effectively select asymptomatic individuals for in-depth screening and thus mitigate or prevent severe disease progression. Trans-thoracic echocardiography is a common diagnostic tool to identify LAE patients. Chamber quantification guidelines recommend a threshold value of  $34 \text{ ml/m}^2$  for the atrial volume indexed to the body surface area of the patient for a standardized diagnosis of LAE [88].



# Mathematical Fundamentals

## 3.1 Multi-scale Electrophysiological Modeling

Computational cardiac modeling and simulation carry the potential of providing profound mechanistic insights into the properties underlying cardiac excitation initiation and propagation [89, 90]. As such, they can contribute to overcome the lack of experimental and clinical signals of human cardiac action potentials, electrograms and electrocardiograms (ECGs) as clinical data collection requires trained personnel, ideally extensive patient enrollment and entails cumbersome and time-consuming laboratory work.

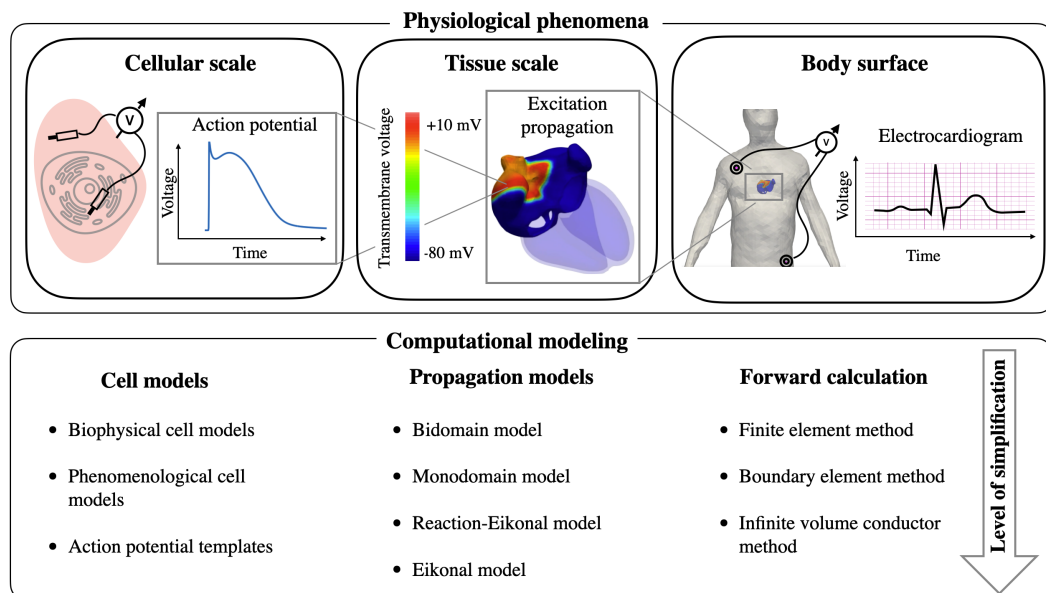


Figure 3.1: Bottom-up design of multi-scale cardiac electrophysiological modeling.

Applying computational models under healthy and diseased conditions to electrophysiological simulations has been shown to reveal insights into the underlying principles of cardiac (dys-)function and provide a framework for developing new therapy options on multiple levels (see Figure 3.1): On cellular scale, cell models are built to replicate ionic current flow *in silico* leading to the action potential of a cardiomyocyte and thus, can improve the understanding of mechanisms underlying cellular pathophysiology and the impact of pharmacological agents on them. The mathematical underpinnings in these cell models are described in section 3.1.1.

On tissue scale, the spread of the electrical depolarization wave on the cardiac tissue as well as the genesis of electrograms can be studied by employing propagation models (see section 3.1.2). In this way, various disease phenomena, such as arrhythmia vulnerability or rotor dynamics, could potentially be traced back to electrophysiological properties of the heart in the computational model. Moreover, the impact of ablation lines or pharmacological treatment on arrhythmia termination and recurrence can be investigated on tissue level.

By solving the forward problem of electrocardiography (see section 3.1.3), the electrical source distribution in the heart can be projected onto the body surface. In this way, body surface potential maps are obtained and from them, ECGs can be extracted. These provide the basis for systematically and reliably investigating the impact of possible underlying cardiac abnormalities on the ECG and in turn, stratifying arrhythmia risk by only employing non-invasively measurable signals on the body surface.

### 3.1.1 Cell Models

In 1952, Hodgkin and Huxley developed the first mathematical model describing the electrical behaviour of a cell. Since then, various different cellular models of atrial, ventricular, or human-induced pluripotent stem cell-derived cardiomyocytes have been developed. An established model for atrial electrophysiology is the Courtemanche *et al.* cell model [91]. With nonlinear-coupled ordinary differential equations, ionic currents and the transmembrane voltage can be calculated by considering different ion channels, transporters and pumps. The time dependent course of the transmembrane voltage  $V_m$  is calculated as

$$\frac{dV_m}{dt} = \frac{-(I_{ion} + I_{stim})}{C_m} \quad (3.1)$$

where  $C_m$  denotes the membrane capacity and  $I_{stim}$  a stimulus current applied externally. The ionic current across the membrane  $I_{ion}$  is calculated as the sum of twelve single ionic currents considered in the model. Each of them can be described by Ohm's law and can thus be calculated as the product of the ion channel conductivity and an ion specific voltage multiplied by gating variables. The latter are introduced to describe the open probability of an ionic channel in the cell membrane defining whether a specific ion can move from the extra- to the intracellular space or vice versa.

By solving the ordinary differential equations, the time course of an action potential in response to an externally applied stimulus can be calculated.

**Table 3.1: Inaccuracies and simplifications of different propagation drivers.**

|                                                                       | Monodomain                                                                                       | Reaction-Eikonal                                                                     | Eikonal                                                                                                      |
|-----------------------------------------------------------------------|--------------------------------------------------------------------------------------------------|--------------------------------------------------------------------------------------|--------------------------------------------------------------------------------------------------------------|
| Assumptions and resulting inaccuracies compared to the bidomain model | bath loading effects are ignored                                                                 | bath loading effects are ignored                                                     | bath loading effects are ignored                                                                             |
|                                                                       | assumption of equal anisotropy ratio in intra- and extracellular domain does not hold in reality | no accurate representation of high wavefront curvatures, reentry and wave collisions | no accurate representation of high wavefront curvatures, reentry and wave collisions                         |
|                                                                       |                                                                                                  |                                                                                      | computation of activation sequence only and hence, no interaction of neighboring cells during repolarization |
|                                                                       |                                                                                                  |                                                                                      | diffusion term is ignored                                                                                    |
| Simplifications leading to reduced computational costs                | elliptical differential equation omitted or only solved at a coarser time scale                  | less complex model equations if not coupled with bidomain model                      | less complex model equations                                                                                 |
|                                                                       |                                                                                                  | relaxed mesh resolution requirements                                                 | relaxed mesh resolution requirements                                                                         |

### 3.1.2 Propagation Models

Propagation models can be employed to calculate the spatio-temporal spread of the electrical depolarization wavefront on the cardiac tissue either in form of transmembrane voltages  $V_m$  and extracellular potential fields  $\Phi_e$  (see section 3.1.2.1 and section 3.1.2.2) or local activation times (see section 3.1.2.3). The optimal choice of which propagation model to apply depends on the problem to be solved. In Table 3.1, simplifications and inaccuracies of different methods are listed. Even though the bidomain model is biophysically the most accurate description, is it computationally notably more expensive to solve compared to simplified model solutions. Various assumptions summarized in Table 3.1 are necessary for the latter to reduce computational cost and speed up simulations. Independent on the choice of the propagation model, the domain has to be discretized in space to numerically solve the model equations, for which different schemes, like for example finite differences, finite elements or finite volumes [92], are applicable.

### 3.1.2.1 Bidomain Model

The bidomain model presents the biophysically most detailed and accurate description of cardiac excitation propagation on tissue level to date [93–95]. By solving the system of partial differential equations 3.2 and 3.3, the potentials in the coupled intra- and extracellular space  $\Phi_i$  and  $\Phi_e$  can be calculated:

$$-\nabla \cdot ((\sigma_i + \sigma_e) \nabla \Phi_e) = \nabla \cdot (\sigma_i \nabla V_m) \quad (3.2)$$

$$\nabla \cdot (\sigma_i \nabla V_m) + \nabla \cdot (\sigma_i \nabla \Phi_e) = \beta \left( C_m \frac{\partial V_m}{\partial t} + I_{ion} - I_s \right) \quad (3.3)$$

In the equation system above,  $\sigma_i$  and  $\sigma_e$  denote the conductivity tensors in the intra- and extracellular domain,  $\beta$  the surface-to-volume ratio of the cell,  $C_m$  the membrane capacitance.  $I_{ion}$  and  $I_s$  describe the sum of all ionic and externally applied stimulus current densities across the membrane, respectively.  $V_m$  is the difference in potential between the intra- and extracellular space (equation 3.4), and is thus defined as the transmembrane voltage:

$$V_m = \Phi_i - \Phi_e \quad (3.4)$$

Solving the partial differential equation system requires a specification of boundary and initial conditions [96]. Homogeneous Neumann boundary conditions can be imposed for the tissue-bath interface in the intra- and extracellular domain. No flux is assumed for the normal current at the tissue-bath interface in the intracellular domain:

$$\vec{n} \cdot \sigma_i \cdot \nabla \Phi_i = 0 \quad (3.5)$$

In the extracellular domain, no flux is also enforced for  $\Phi_e$  at the boundary of the torso not in contact with myocardial tissue:

$$\vec{n} \cdot \sigma_b \cdot \nabla \Phi_e = 0 \quad (3.6)$$

whereby  $\sigma_b$  denotes the conductivity of the specific tissue type considered in a simulation setup of a heterogeneous torso volume conductor. Furthermore, continuity of the potential in the interstitial space (equation 3.7) as well as of the normal component of the extracellular current at the myocardial tissue-bath interface (equation 3.8) are enforced:

$$\Phi_e|_e = \Phi_e|_b \quad (3.7)$$

$$\vec{n} \cdot \sigma_e \cdot \nabla \Phi_e = \vec{n} \cdot \sigma_b \cdot \nabla \Phi_e \quad (3.8)$$

State variables of the cell model described in section 3.1.1 paced to a limit cycle at 1 Hz account for the initial conditions of the model.

### 3.1.2.2 Monodomain Model

The monodomain model constitutes a simplification of the bidomain formulation [94, 95, 97, 98]. Under the assumption of equal anisotropy ratios in the intra- and extracellular domain, the bidomain model can be reduced to the following non-linear partial differential equation:

$$\nabla \cdot (\sigma_m \nabla V_m) = \beta \left( I_{ion} + C_m \cdot \frac{\partial V_m}{\partial t} \right) \quad (3.9)$$

$\sigma_m$  denotes the monodomain conductivity, which can be calculated as half of the harmonic mean between intra- and extracellular conductivity:

$$\sigma_m = \frac{\sigma_i \cdot \sigma_e}{\sigma_i + \sigma_e} \quad (3.10)$$

In the monodomain model, only the currents in the intracellular space and through gap junctions are considered. Thus, the torso volume conductor does not have an impact on the transmembrane voltage, which leads to bath loading effects being ignored. However, an approximation of the extracellular potential  $\Phi_e$  can still be obtained by a temporally infrequent solve of the computationally expensive elliptical bidomain equation 3.2 [99].

When applying either of the mono- or bidomain model, strict requirements on the mesh resolution need to be fulfilled to avoid the effect of a coarse mesh slowing down conduction velocity or even breaking down wave propagation [100].

### 3.1.2.3 Eikonal Model

By solving the Eikonal equation, the activation time  $T$  for each node  $x$  in the spatial domain of the cardiac model can be computed as

$$\sqrt{\nabla T(x)^\top \cdot M \cdot \nabla T(x)} = 1 \quad (3.11)$$

where  $M$  is the squared conduction velocity (CV) tensor. Defining a set of trigger points  $x \in \Gamma$  where excitation is initiated is required to set up the initial conditions to solve equation 3.11:

$$T(x) = T_0 \text{ for } x \in \Gamma \quad (3.12)$$

Methods for solving the Eikonal equation comprise for example the fast marching [101] or the fast iterative method [102].

Unlike in biophysically detailed excitation propagation models (see section 3.1.2.1 and 3.1.2.2), solving the Eikonal equation only yields local activation times (LATs) on each node belonging to the cardiac tissue. However, a complete representation of the transmembrane voltage distribution would be required to further compute cardiac signals, such as for example electrograms [103] or ECGs. Thus, the transmembrane voltage  $V_m(x, t)$  at each node  $x$  and for each timestep  $t$  can be inferred in a postprocessing step based on the calculated LATs as follows:

$$V_m(x, t) = U(x, t - T(x)) \quad (3.13)$$

whereby  $U(x, t)$  is an action potential time course. It can be obtained for example based on a mono- or bidomain simulation of a planar wave propagation in a tissue strand experiment from which the time course of  $V_m$  was extracted at a node located in the center of the strand mesh.

#### 3.1.2.4 Reaction-Eikonal Model

In the reaction-Eikonal model, activation times are in the first place obtained by solving the Eikonal equation and are used subsequently to allow for the application of biophysical models, such as the bi- or monodomain formulation, to coarse meshes [104]. An  $I_{foot}$  current is introduced to mimic the effect of the diffusion term and is applied at the activation time obtained as the solution to the Eikonal equation 3.11. In the  $RE^+$  variant coupled to the monodomain model, the respective equation (compare equation 3.9) is modified as follows:

$$\nabla \cdot (\sigma_m \nabla V_m) + I_{foot} = \beta \left( I_{ion} + C_m \cdot \frac{\partial V_m}{\partial t} \right) \quad (3.14)$$

In this way, a node can either be activated by the diffusion term or the  $I_{foot}$  current. Furthermore, adjacent nodes also interact during the repolarization phase.

### 3.1.3 Forward Calculation Methods

By solving the forward problem of electrocardiography, the dipole sources of  $V_m$  in the heart obtained from simulations of excitation propagation as explained in section 3.1.2 can be mapped onto the body surface [105]. In this way, body surface potential maps can be generated or ECGs can be calculated by extracting the potentials at common electrode positions on the upper body. Different methods to approach this problem are published and are summarized in the following sections.

#### 3.1.3.1 Finite Element Method

The term finite element method usually refers to solving the Poisson equation from the parabolic bidomain equation 3.2 using a finite element discretization scheme [106]. Thus, the entire torso domain must be discretized volumetrically with finite elements. The torso together with all organs inside except for the heart are then modeled as a passive volume conductor and the respective elements assigned conductivities  $\sigma_e$ . In this way, equation 3.2 can be solved numerically and the extracellular potential field  $\Phi_e$  on the body surface can be obtained.

### 3.1.3.2 Boundary Element Method

The basic principle underlying the boundary element method (BEM) is that only equivalent dipole sources on the cardiac surface are considered when calculating body surface potentials and ECGs to reduce computational cost. To transfer a reduced set of dipole sources onto the surfaces bounding organs of heterogeneous conductivity properties, isotropic myocardial conduction properties in the extracellular space are assumed [106]. Applying Green's theorem and boundary conditions as well as assuming equal anisotropy ratios in the intra- and extracellular space, equation 3.2 can be reformulated as follows for calculating the extracellular potential field  $\Phi_e$  at any point  $\vec{r}$  on the surface  $S^l$  [107]:

$$\Phi_e(\vec{r}) = \frac{2\sigma_s}{\sigma_-^l + \sigma_+^l} \Phi_e^\infty(\vec{r}) - \frac{1}{2\pi} \sum_{k=1}^K \frac{\sigma_-^k - \sigma_+^k}{\sigma_-^k + \sigma_+^k} \int_{S^k} \Phi(\vec{r}') \frac{(\vec{r} - \vec{r}')}{|\vec{r} - \vec{r}'|} \cdot d\vec{S}', \quad \vec{r} \notin S^k \quad (3.15)$$

where  $\sigma_-^k$  and  $\sigma_+^k$  denote the conductivities inside and outside of surface  $k$ .  $\Phi^\infty$  is the potential that would be generated if the heart was immersed in an infinite, homogeneous medium characterized by a conductivity of  $\sigma_s$ . The dipole sources can either be expressed as transmembrane voltages on the cardiac surface [108] or volumetrically as primary impressed currents  $\vec{J}_p$  in the volume conductor  $V_h$ :

$$\Phi_e^\infty(\vec{r}) = \frac{1}{4\pi\sigma_s} \int_{V_h} \frac{\vec{J}_p \cdot (\vec{r} - \vec{r}')}{|\vec{r} - \vec{r}'|} dV_h \quad (3.16)$$

### 3.1.3.3 Infinite Volume Conductor Method

The infinite volume conductor forward calculation method relies on the assumption that the heart and thus all cardiac dipole sources are immersed in an unbounded, homogeneous medium. Hence, the surface integral of the secondary sources introduced by the bounded volume conductor in equation 3.15 are neglected and the extracellular potentials  $\Phi_e$  are calculated as follows:

$$\Phi_e(\vec{r}) \approx \Phi_e^\infty(\vec{r}) = \frac{1}{4\pi\sigma_s} \int_{V_h} \frac{\vec{J}_p \cdot (\vec{r} - \vec{r}')}{|\vec{r} - \vec{r}'|} dV_h \quad (3.17)$$

## 3.2 Statistical Shape Modeling

A statistical shape model (SSM) describes the variability in shape of a geometrical object in a cohort of individual instances. Point distribution models constitute the most common subclass of SSMs and aim at parameterizing shape deformations by describing the spatial movement of a set of unique landmarks annotated on the surface of each individual instance [109]. The processing steps preceding the acquisition of the coordinate vectors of these landmarks as an input applicable to principal component analysis (PCA) to eventually evaluate the shape statistics are shown along with the mathematical notation in Figure 3.2.

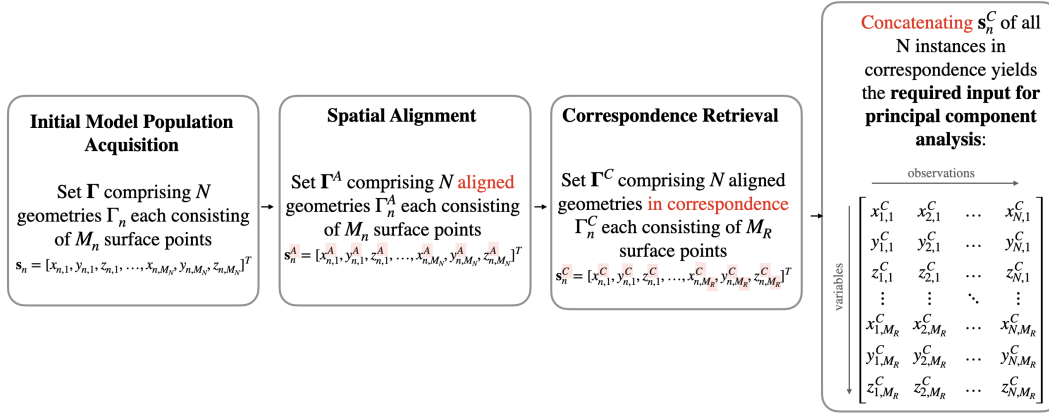


**Figure 3.2: Processing steps and mathematical notation for building a statistical shape model (SSM).** The red text and boxes indicate the changes applied to the shapes  $\Gamma$  and their vectorized surface point representations  $\mathbf{s}$  in each step. The acquisition of the initial model population forms the basis for building the SSM and is explained in section 3.2.1. After aligning these instances in space (see section 3.2.2) and establishing correspondence (see section 3.2.3), the shape vectors can be rearranged in a matrix notation and are applicable as an input for principal component analysis to evaluate the shape statistics.

First, a set of  $N$  individual instances  $\Gamma$ , the SSM will be built on, needs to be obtained. In the field of medical engineering, it can either consist of anatomical maps of the organ of interest recorded during minimally invasive catheter procedures or of tomographic image segmentations (see section 3.2.1). Subsequently, all individual instances  $\Gamma_n, n \in [1, \dots, N]$  need to be aligned in space yielding a set of aligned geometries  $\Gamma^A$  (see section 3.2.2). Thereafter, correspondence among them has to be established to obtain a vectorized representation  $\mathbf{x}^C$  for each instance  $n$  comprising  $M_R$  homogeneously sampled surface points  $\mathbf{s}_n^C = [x_{n,1}^C, y_{n,1}^C, z_{n,1}^C, \dots, x_{n,M_R}^C, y_{n,M_R}^C, z_{n,M_R}^C]^T$  with  $x, y$  and  $z$  denoting the Cartesian coordinates of the surface nodes in instance  $n$ . Correspondence can be retrieved either manually by relying on expert annotations or automatically through a generic and iterative deformation process considered as an optimization problem (see section 3.2.3).

### 3.2.1 Acquisition of Individual Instances

A population of individual instances  $\Gamma$  serves as a basis for statistically evaluating possible real-world object deformations among them. If a human organ is the object the statistical shape model should be built for, this initial cohort of individual instances can either be obtained by segmenting tomographic images or as anatomical maps recorded in the course of catheter interventions.

(Electro-)Anatomical maps of the cardiac chambers are for example recorded during electrophysiological studies usually preceding ablation procedures to identify pathological electrical excitation pathways, specify ablation targets and thus, guide the procedure. Commercial mapping systems, such as CARTO (Biosense Webster, Irvine, CA, USA) or RHYTHMIA HDx (Boston Scientific, Boston, MA, USA), are equipped with three orthogo-

nal sensors at a catheter's tip that is inserted by a clinician through a vein into the heart. When moving the catheter along the endocardial wall of the cardiac chamber, the position of the catheter can be tracked in real-time by evaluating the strength of a magnetic field generated by magnetic coils in a locator pad placed beneath the patient. In this way, the catheter position traced over time can be used to reconstruct the endocardial surface of the cardiac chamber of interest. However, the intention when recording electro-anatomical maps is not to obtain a detailed and exact representation of the cardiac anatomy, but rather to visualize and analyze spatio-temporal information of the electrical depolarization wave. Thus, not all anatomical structures are mapped accurately and dense enough, let alone examined during the mapping process at all, and thus impede evaluating highly variable and localized shape deformations in a cohort.

Thus, segmentation of tomographic images, such as magnetic resonance (MR) or computed tomography (CT) recordings, are sometimes inevitable to obtain anatomically detailed and high resolution geometries of the organ to be analyzed. The segmentation process can be time-intensive and cumbersome when manually performed by trained personnel from scratch. Algorithms based on edge detection or clustering techniques are capable of finding possible contours of the organs in single image planes or across different planes automatically. These can be applied to obtain a suggested segmentation subject to subsequent manual corrections if necessary.

Independent on the modality for acquiring the initial model population, all instances can be exported as triangular surface meshes comprising a point cloud bounding the surface of the organ and a connectivity list containing information on the spatial arrangement and linking of these surface vertices.

### 3.2.2 Spatial Alignment

The triangular meshes of the individual instances in the initial patient-specific model population need to be spatially aligned to avoid a representation of translation and rotation of the object in the shape statistics and ensure that only shape-related deformations are captured in the eigenmodes of the SSM.

The set of spatially aligned geometries  $\Gamma^A$  can be obtained either manually by annotating landmarks on characteristic anatomical structures in each individual instance or automatically using algorithms such as the iterative closest point algorithm [110] for example. In either case, one geometry in the set of individual instances has to be chosen as a reference defining the target orientation and position of all other instances in the cohort and thus of the SSM to be constructed.

Whereas an alignment using a set of landmarks can be performed with a standard linear least squares estimation, the iterative closest point algorithm iteratively translates and rotates a target instance to minimize the vertex-to-nearest neighbor distance to the reference instance. The former option comes along with the drawback of manual and expert input being required whereas a robust performance of the iterative closest point algorithm hinges on the quality of the initial estimate of the rigid transformation between each pair of instances to be aligned.

### 3.2.3 Correspondence Retrieval

Having aligned all individual instances, correspondence between them needs to be established, i.e., a set of points needs to be found located at the same anatomical position in all geometries. Based on these, the point distribution model is constructed which will provide statistical information on how each of these vertices moves in space in the cohort of individual instances.

These points can again be annotated manually by experts. However, in contrast to the set of landmarks that are needed for the alignment described in section 3.2.2, a much larger amount of surface nodes needs to be annotated for defining correspondence. This is because only the spatial movement of these points are represented in the SSM entailing a low spatial resolution and presumably an inaccurate representation of the final model as well as the need to interpolate between sparsely sampled surface points to retrospectively increase the mesh resolution of any SSM instance.

Thus, establishing dense point-by-point correspondence in the cohort of aligned individual instances  $\Gamma^A$  is usually preferable and can be performed using Gaussian process morphable models (GPMMs) to not only automate the process but also to reduce the impact of inter-observer variability on manually selected landmarks. An overview outlining the automated correspondence retrieval process is depicted in Figure 3.3. Thereby, one geometry in the set of aligned individual instances is chosen as a reference template  $\Gamma_R^A$  (yellow surface in Figure 3.3) and is subjected to a generic deformation defined by GPMMs. The latter are defined by Gaussian kernels  $k$  which describe the spatial relationship between two surface vertices  $\mathbf{v}_1$  and  $\mathbf{v}_2$  as:

$$k(\mathbf{v}_1, \mathbf{v}_2) = s \cdot \exp\left(-\frac{(\mathbf{v}_1 - \mathbf{v}_2)^2}{l^2}\right) \quad (3.18)$$

In equation 3.18,  $s$  denotes a linear scaling factor determining the height of the Gaussian bell and  $l$  represents the width of the kernel. These Gaussian kernels with a predefined variance modulated by the parameter  $l$  are applied to a subset of uniformly sampled vertices on the reference shape  $\Gamma_R^A$ . Approximating them with the leading eigenvectors of their Karhunen-Loève transform yields a compact and low-rank description of the morphable reference template (grey surface in Figure 3.3). Thereby, the weighting factors  $s$  in equation 3.18 introduce the free parameters affecting the generic deformation [111].

Each remaining individual instance other than the geometry selected as a reference template is chosen as a target mesh  $\Gamma_T^A$  at a time (green surface in Figure 3.3) and the weights of the generically deformable reference template  $\tilde{\Gamma}_R^A$  are iteratively optimized to minimize the mean distance between each vertex in the deformed reference mesh and its nearest neighbor in the current target mesh. The generic deformation manifests only in a universal movement of the surface points but neither in a change in the amount of nodes  $M_R$  in the deformed mesh nor in any rearrangement or reindexing of vertices. Therefore, replacing each target mesh with the deformed reference mesh leads to a set of homogeneously and densely sampled surface meshes  $\Gamma^C$ .

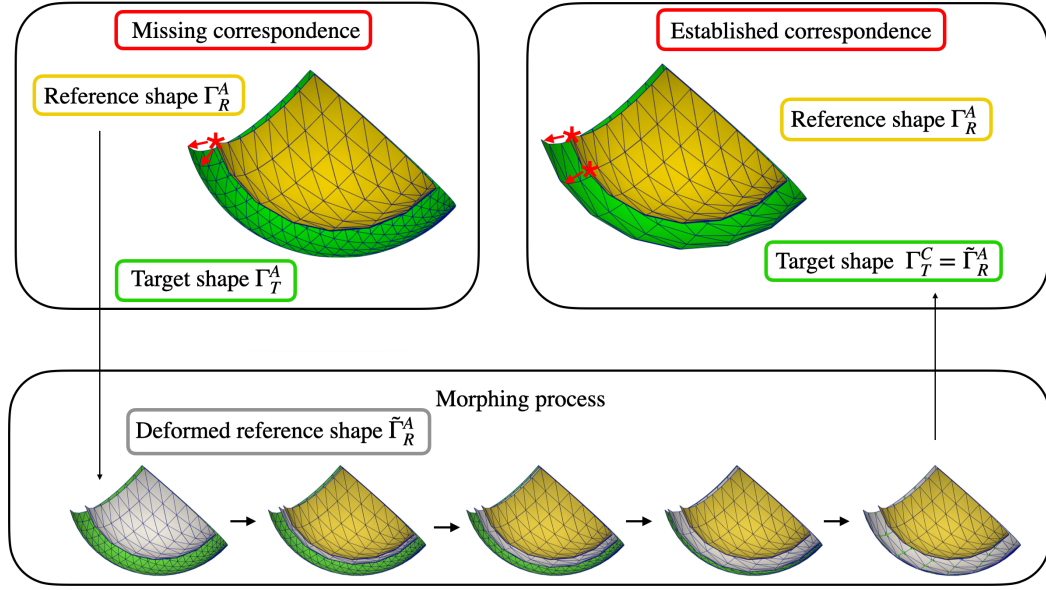


**Figure 3.3: Correspondence retrieval process** One geometry in the set of aligned instances  $\Gamma^A$  is chosen once as a reference  $\Gamma_R^A$  (yellow surface) to generate the morphable model  $\tilde{\Gamma}_R^A$  (grey surface) defined by Gaussian processes. The morphing process can be regarded as an optimization during which the free parameters in the morphable model are adjusted so that the surface-to-surface distance between the deformed reference shape  $\tilde{\Gamma}_R^A$  and the current target shape  $\Gamma_T^A$  (green surface) is minimized. Replacing the target shape  $\Gamma_T^A$  with the deformed reference shape found during the optimization procedure yields a representation of the target shape in correspondence with the reference geometry ( $\Gamma_T^C$ ). Repeating this procedure  $N - 1$  times while choosing another target shape  $\Gamma_n^A, \{n \in [1, N] | n \neq R\}$  in each iteration, results in a set of  $N$  geometries in correspondence  $\Gamma^C$ .

Introducing the notation of a shape vector by stacking x-, y- and z-coordinates of the  $M_R$  surface node in one instance on top of each other yields a vectorized representation of the  $M_R$  surface points' coordinates for each geometry  $\Gamma_n^C$  as  $\mathbf{s}_n^C = [x_{n,1}^C, y_{n,1}^C, z_{n,1}^C, \dots, x_{n,M}^C, y_{n,M}^C, z_{n,M}^C]^T$ . Horizontally concatenating all of these column vectors for all instances yields a matrix of shape vectors. Rows in this matrix can be considered as different variables and columns as different observations delivering the required input for applying PCA as described in section 3.3. Thus, the final SSM consists of a set of eigenvectors and -values ordered by the variance in the data they explain.

### 3.3 Principal Component Analysis

PCA is a technique to reduce dimensionality of datasets represented by many variables or features. The aim is to find the directions of the maximum variance in the high-dimensional feature space and project the original data onto this new subspace. By restricting the new data representation to a reduced number of leading orthogonal basis vectors, the amount of features or variables used to represent the single data samples can be decreased while still preserving the maximum possible data variation [112]. This new orthogonal coordinate

system can be obtained by eigendecomposition of the covariance matrix  $\mathbf{C} \in \mathbb{R}^{D \times D}$  computed from the data matrix  $\mathbf{X} \in \mathbb{R}^{N \times D}$  as

$$\mathbf{C} = \frac{1}{N-1} \sum_{i=1}^N (\mathbf{X}_i - \bar{\mathbf{X}})(\mathbf{X}_i - \bar{\mathbf{X}})^T \quad (3.19)$$

where  $\bar{\mathbf{X}}$  denotes the mean of the datamatrix  $\mathbf{X}$ . In case dimensionality reduction should be performed for  $N$  shape vectors in correspondence  $\mathbf{s}_n^C, n \in [1, \dots, N]$  represented by  $M_R$  three-dimensional coordinate pairs as described in section 3.2.3, the data matrix is of the following form:

$$\mathbf{X}_{SSM} = \begin{bmatrix} x_{1,1}^C & x_{2,1}^C & \dots & x_{N,1}^C \\ y_{1,1}^C & y_{2,1}^C & \dots & y_{N,1}^C \\ z_{1,1}^C & z_{2,1}^C & \dots & z_{N,1}^C \\ \vdots & \vdots & \ddots & \vdots \\ z_{1,M_R}^C & z_{2,M_R}^C & \dots & z_{N,M_R}^C \end{bmatrix} \quad (3.20)$$

where  $3 \cdot M_R = D$  for the calculation of the covariance matrix with equation 3.19. In case, PCA should be performed on time series of  $D$  12-lead ECGs, the samples can be arranged in a data matrix as follows:

$$\mathbf{X}_{ECG} = \begin{bmatrix} \text{I}_1(t_1, \dots, t_P) & \text{II}_1(t_1, \dots, t_P) & \dots & \text{V6}_1(t_1, \dots, t_P) \\ \text{I}_2(t_1, \dots, t_P) & \text{II}_2(t_1, \dots, t_P) & \dots & \text{V6}_2(t_1, \dots, t_P) \\ \vdots & \vdots & \ddots & \vdots \\ \text{I}_D(t_1, \dots, t_P) & \text{II}_D(t_1, \dots, t_P) & \dots & \text{V6}_D(t_1, \dots, t_P) \end{bmatrix} \quad (3.21)$$

whereby the ECG time trace comprising  $t_P$  sampled time steps are concatenated horizontally for each of the 12 leads in the order I, II, III, aVR, aVL, aVF, V1-V6. Thus,  $12 \cdot P = N$  holds for the calculation of the covariance matrix with equation 3.19.

Regardless of the entries in the data matrix  $\mathbf{X}$ , diagonalizing the covariance matrix  $\mathbf{C}$  leads to a set of eigenvalues and eigenvectors

$$\mathbf{C} = \mathbf{V}\mathbf{L}\mathbf{V}^T \quad (3.22)$$

where each column in  $\mathbf{V}$  represents an eigenvector  $\mathbf{v}_i, i \in [1, \dots, N-1]$  and each entry in the diagonal matrix  $\mathbf{L}$  denotes an eigenvalue  $\lambda_i$  in decreasing order of the total variance. Thus, the projection of each data sample  $x_j, j \in [1, \dots, D]$  onto the new feature subspace can be expressed as:

$$x_j = \bar{\mathbf{X}} + \sum_{i=1}^{N-1} r_{ij} \cdot \lambda_i \cdot \mathbf{v}_i \quad (3.23)$$

By reducing the number of eigenmodes  $N-1$  in equation 3.23, the data sample  $x_j$  can be represented by the respective amount of the newly created, transformed variables  $\mathbf{r}$ , which are also referred to as principal component scores in the following.

## 3.4 Machine Learning

A machine learning model aims at analysing data and identifying patterns among them. During the development process, a statistical model is first trained on an explicit training set and subsequently evaluated on an independent test set. This serves the purpose of ensuring that the model learns to derive patterns from the training samples transferable to previously unseen data instead of overfitting to the provided training data. Leaving only one fixed subset of data out for the testing procedure is commonly referred to as *hold out-validation*. Alternatively, *k-fold cross-validation* can be performed describing the process of subdividing the total data available into  $k$  subsets, saving one subset at a time for testing while combining the remaining ones for training. The network is repeatedly trained  $k$  times from scratch while rotating the specific fold left out for testing, so that after all, each subset was used for testing once. Most times, cross-validation is preferred over hold out-validation as the source of evidence that the model is capable to generalize well to unseen data is increased by a factor of  $k$ . [113]

In supervised learning, the network is fed with a set of input data and associated ground truth annotations. Between these two entities, the network has to make connections and learn relationships to perform the annotation task for the unseen data during testing itself. In case the ground truth annotations are defined as discrete labels and can be summarized in a dictionary, the network is meant to perform a *classification* task [114]. If the annotations are continuous numbers instead, the network is denoted as a *regression* model. In unsupervised learning, no ground truth annotations are provided. Instead, the model should find similarities among the training data and derive rules to cluster them into appropriate groups itself.

The metrics to assess the performance of the network depend on the specific task it should perform. For classification problems, confusion matrices can be specified visualizing the relation between correctly labeled and misclassified data samples in the test set (see Figure 3.4).

From the confusion matrix, accuracy ( $ACC$ ), sensitivity (or true positive rate,  $TPR$ ) and specificity (or true negative rate,  $TNR$ ) can be calculated class-wise as follows:

$$ACC = \frac{TP + TN}{TP + TN + FP + FN} \quad (3.24)$$

$$TPR = \frac{TP}{TP + FN} \quad (3.25)$$

$$TNR = \frac{TN}{TN + FP} \quad (3.26)$$

with  $TP$ ,  $TN$ ,  $FP$ ,  $FN$  being the rate of samples correctly classified as positive, correctly classified as negative, wrongly classified as positive and wrongly classified as negative, respectively, when considering the class of interest as positive. Especially for binary classification problems, oftentimes a receiver operating characteristics (ROC) curve is constructed by visualizing sensitivity over 1-specificity when varying the discrimination threshold of the model. The area under the ROC curve (AUC) thus provides another metric to assess the

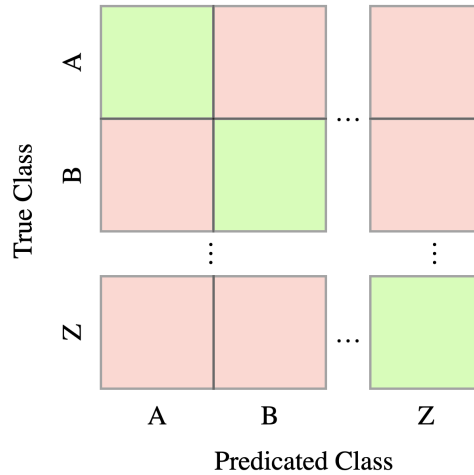


**Figure 3.4:** Schematic representation of a confusion matrix to visualize (mis-)classification results.

network performance. Moreover, an optimal discrimination threshold as the best possible trade-off between sensitivity and specificity performance can be chosen by selecting the point on the ROC curve closest to the top left corner. For regression models, the mean squared error (mse) or root mean squared error (rmse) can be calculated between the predicted ( $\hat{y}$ ) output and the target ( $y$ ) annotation for all test samples  $N$  as:

$$mse = \frac{1}{N} \sum_{i=1}^N (\hat{y} - y)^2 \quad (3.27)$$

$$rmse = \sqrt{\frac{1}{N} \sum_{i=1}^N (\hat{y} - y)^2} \quad (3.28)$$

The set of input data provided to the network can be of different shapes and sizes. Deep learning models are capable of directly extracting high-level features [115] from either images in case of convolutional neural networks or multi-dimensional time series in case of long short-term memory networks (see section 3.4.2) themselves. Shallow networks (see section 3.4.1) instead require a distinct feature extraction step from the raw data prior to providing them as input to the network tailored at performing the intended regression or classification task.

Numerous types of machine learning models exist, two of which employed for studies presented in this thesis are described in section 3.4.1 and 3.4.2.

### 3.4.1 Neural Networks

The topology of a neural network typically involves an input layer, one or more hidden layers and an output layer. Each layer comprises multiple neurons that are linked to the neurons in subsequent layers [116, 117] (see Figure 3.5). In a *feedforward* neural network, these

connections exclusively point in the direction of the output layer and contain no feedback loops as is the case in *recurrent* neural networks instead.

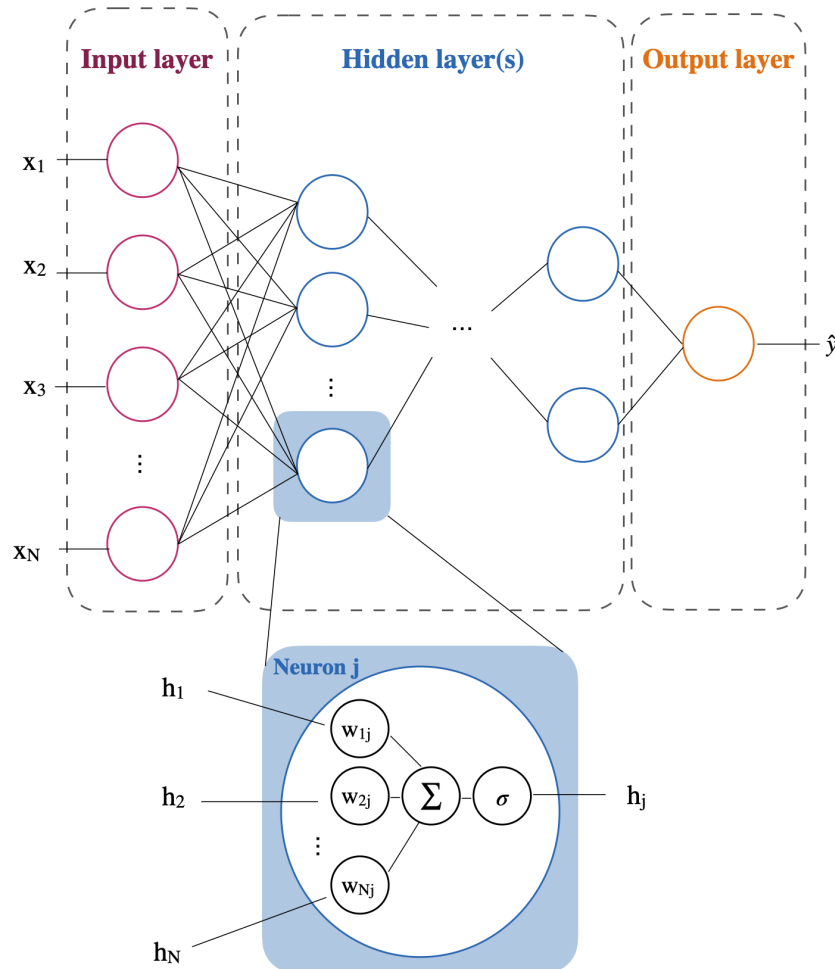


**Figure 3.5: Schematic representation of the structure of a feedforward neural network (top panel) and a neuron (bottom panel).** An input, one or multiple hidden and an output layer comprise the basic framework of the model. Each layer consists of multiple neurons, multiplying the input values  $h$  with weighting factors  $w_{ij}$ , combining them with the input function ( $\Sigma$ ) and passing them through an activation function ( $\sigma$ ) to the next layer.

Feature values extracted from the available dataset are propagated from the input to the output layer. In each neuron  $j$ , the input values  $h_i$  are multiplied with the weights  $w_{ij}$  and their sum is then passed on to an activation function to account for non-linearities between data samples [118]. The resulting value is then propagated to a neuron in the successive layer that processes it accordingly. Once the entity in the output layer is reached, an error function determines the deviation between the ground truth annotation and the prediction of the network. To minimize this error, the weights in each neuron are adjusted iteratively through *backpropagation*. Thereby, the gradients of the error function with respect to the

weights of the neurons are calculated in each layer and combined by the chain rule for partial derivatives. Approaches like gradient descent or the ADAM procedure allow for updating the weights until the error function converges to a minimum. Besides the weighting factors that are implicitly optimized during the learning process, a neural network typically comprises numerous other tunable hyperparameters. Among them are the number of layers or neurons themselves or the learning rate, which governs the pace for optimizing the weights during backpropagation.

### 3.4.2 Long Short-term Memory Networks

Whereas shallow feedforward neural networks rely on extracted features obtained from an indispensable pre-processing step, deep neural networks, are capable of omitting this step and process the data in a format of images or time series [115, 119, 120]. The latter constitute the typical input format for long short-term memory (LSTM) networks, which evolved from recurrent neural networks explained in section 3.4.1. By building on the concept of recurrent neural networks, the LSTM network has memory capacity, i.e., the output from previous time steps is taken into consideration for the computation of the current output. This property makes it particularly suitable for time series input data where sequential data samples are naturally related to one another. In contrast to vanilla recurrent neural networks, the design of an LSTM avoids the problem of long-term gradients vanishing to zero during backpropagation. Thus, the specific LSTM structure allows for considering both long and short term memory during the learning process. Equivalent to neurons in feedforward neural networks, the essential unit in an LSTM is called LSTM cell. It consists of an input, an output and a forget gate. The input gate decides whether a specific input value is important for learning the intended task by allocating weights and thus decides if the cell's memory is affected by that value. In contrast, the forget gate controls which details that are to be discarded for the ongoing learning process. The output gate finally combines the information from the input gate and the memory of the cell to determine the output value  $h_t$  that is not only propagated to the LSTM cell in the next layer but instead also to the cell of the subsequent input data sample. A fully connected layer can be employed for pooling the output values of the LSTM cells in the last layer and calculating the final classification result.

The training of an LSTM network can be performed by optimizing weights based on error backpropagation as explained in 3.4.1.

---

PART II

---

# VALIDATION OF SIMPLIFIED MODELING APPROACHES



---

# Comparison of Propagation Models and Forward Calculation Methods

In this chapter, simulated atrial signals computed with different propagation models and forward calculation methods are compared with respect to action potential duration (APD), local activation time (LAT) and electrocardiogram (ECG) biomarkers. This serves the purpose to assess whether computational cost for large-scale simulations can be reduced by resorting to simplified electrophysiological models without compromising the accuracy of resulting signals.

*The content of this chapter is taken and adapted from a paper that has been published open access under licence CC-BY 4.0 in IEEE Transactions on Biomedical Engineering [121]. Most passages have been quoted verbatim from the publication.*

## 4.1 Introduction

In computational cardiac modeling, the bidomain model (see section 3.1.2.1) is the biophysically most detailed formulation to compute the spread of the de- and repolarization wavefront and the electrical source distribution throughout the cardiac tissue to date. Furthermore, the finite element method (see section 3.1.3.1) is considered the gold standard for computing the body surface potentials from a given distribution of the electrical sources in the heart to extract ECGs at standardized electrode positions. However, both methods are computationally expensive and are thus suboptimal for generating large *in silico* datasets of cardiac signals for machine learning applications [122, 123], or for efficiently simulating excitation propagation in cardiac digital twins for certain clinical applications with real time requirements, such as guiding ablation therapy [48] or parameter inference [124]. Hence, simplified models with fast solution times are needed to speed up the generation of *in silico* datasets of cardiac

signals, such as LATs, electrograms or ECGs by several orders of magnitude [103, 104, 125]. Yet, the signals obtained with these simplified methods need to be physiologically accurate and have to highly resemble the results obtained with the gold standard methods for a meaningful application of the former. It is therefore essential to quantify the inaccuracies arising in simulated atrial signals when resorting to simplified computational methods to demonstrate their possibilities and limitations for particular use cases. While comparisons of this type have already been performed for the ventricles [99, 104, 126] and partly also for four chamber heart models [127], a study focusing on atrial electrophysiology has not yet been carried out to a sufficient extent. However, this is substantial since the atria stand out by a highly complex myocardial fiber structure, locally heterogeneous properties regarding ion channel and tissue conductivities and higher anisotropy ratios as compared to the ventricles.

The monodomain (see section 3.1.2.2), the reaction-Eikonal (RE) (see section 3.1.2.4), and the Eikonal model (see section 3.1.2.3) solved by the fast iterative method constitute the simplified propagation models investigated in the study presented in this chapter. Forward calculation techniques applied in this study comprise the boundary element (see section 3.1.3.2) and the infinite volume conductor (see section 3.1.3.3) methods. Simulations were carried out in sinus rhythm with and without the inclusion of fibrotic tissue modeled as passive conduction barriers [128], slow conducting tissue patches and rescaled ion channel conductances representing cytokine effects [82, 129]. Errors were assessed between simplified propagation models and forward calculation methods to the gold standard bidomain (see section 3.1.2.1) and finite element formulations (see section 3.1.3.1) with metrics extracted from the simulation results on cellular, tissue and organ scale comprising APDs, LATs, and ECGs, respectively.

## 4.2 Methods

### 4.2.1 Atrial Model and Simulation Setups

An anatomically detailed model of the torso was obtained by multi-label magnetic resonance image segmentation as described by Krueger *et al.* [130]. The contours of atria, ventricles, lungs, liver and torso were exported as triangular surface meshes. These were smoothed and resampled with an average edge length of 0.5 mm, 5 mm, 5 mm, 7 mm and 15 mm, respectively, using *Meshmixer* (Autodesk, San Rafael, CA, USA) and *InstantMeshes* [131] whereby details were corrected manually in *Blender* (Blender Foundation, Amsterdam, The Netherlands) to avoid intersecting segments and ensure a sufficient mesh quality and topology. The segmented atrial endocardial surfaces were fed into the pipeline described by Azzolin *et al.* [52, 129, 132] to obtain a volumetric tetrahedral bi-atrial geometry with a homogeneous wall thickness of 3 mm and an average edge length of 523  $\mu\text{m}$  augmented with inter-atrial connections, labels for anatomical structures and myocardial fiber orientation. In contrast to fully personalized approaches where fiber orientation can be defined based on information extracted from diffusion tensor imaging data [133, 134], myocardial fiber architecture was

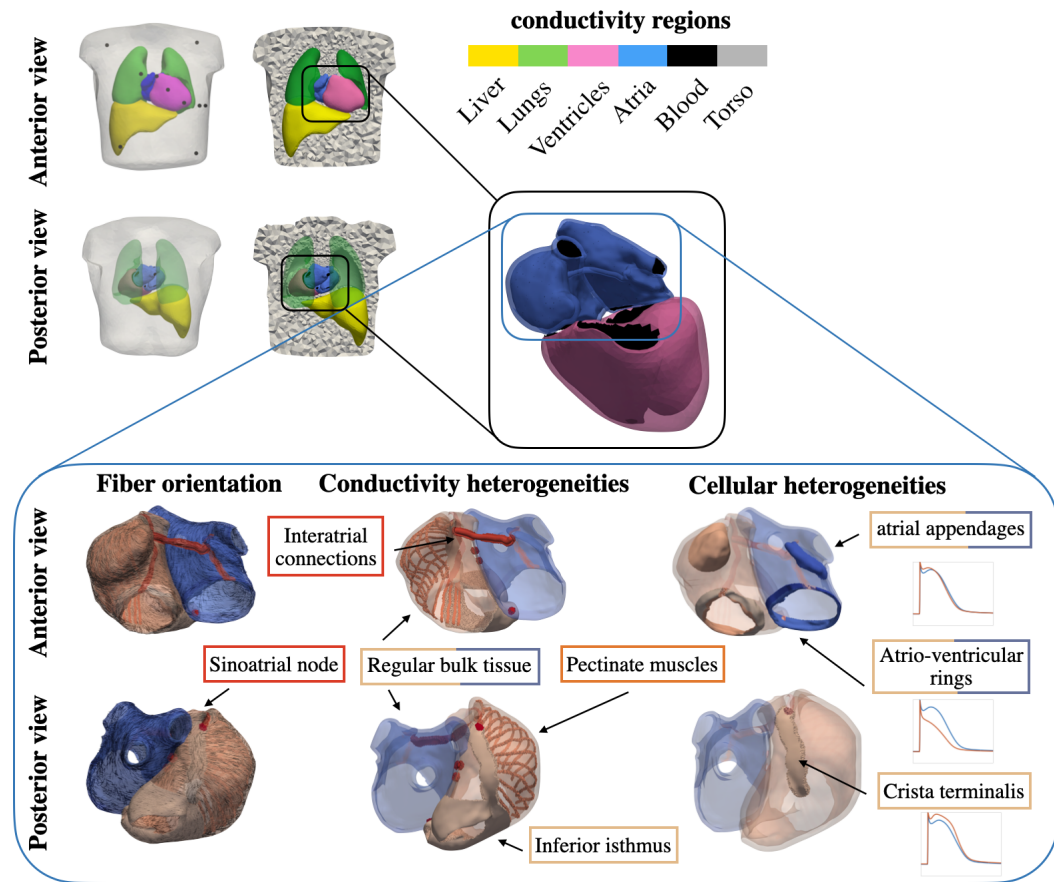


**Figure 4.1: Torso model with the segmented organs and electrode positions.** Transparent and clipped views are shown from the anterior and posterior side in the top and bottom row, respectively. The bottom panel shows the anatomically detailed atrial model that was augmented with fiber orientation and labels for anatomical structures. Heterogeneous conductivity and ionic properties were assigned to spatially distinct regions in the mesh. Resulting APs featuring ionic heterogeneity are depicted on the right side in red together with the baseline Courtemanche *et al.* cellular model solution in blue.

defined in a rule-based way [52] building on the solution of Laplace’s equation [135, 136]. *Meshtool* [137] was used to generate a tetrahedral model of the full torso while preserving the surfaces of the considered organs. Tags for the atrial and ventricular blood pools were allocated to all elements in the volumetric torso model located inside the surfaces bounded by the atrial and ventricular endocardial walls with closed valve and vein orifices. A detailed view of the torso and the atrial model is depicted in Figure 4.1.

Isotropic conductivity of 0.0389 S/m, 0.028 S/m, 0.06 S/m, 0.7 S/m and 0.22 S/m was assigned to lungs, liver, ventricles, atrial and ventricular blood pools and the remaining torso tissue, respectively, as reported in previous work [34, 138, 139].

In order to conduct comparable experiments with the mono- or bidomain model that require conductivities, and the Eikonal-based models that resort instead to conduction velocities (CVs), it is crucial to consistently associate conductivities and CVs for all heterogeneous tissue regions in the atria (see Figure 4.2). Anisotropic and locally heterogeneous conduc-

tivities were assigned to five different regions in the atria comprising regular bulk tissue, crista terminalis, pectinate muscles, inferior isthmus, and inter-atrial connections. CVs corresponding to the monodomain conductivities reported in [140] for 0.33 mm resolution voxel models were therefore first calculated as described by Krueger *et al.* [141]. Using *tuneCV* [98, 100], intra- ( $\sigma_i$ ) and extracellular ( $\sigma_e$ ) conductivities as well as the monodomain conductivities ( $\sigma_m$ ) were iteratively optimized for the tetrahedral mesh setup described above while keeping the  $\sigma_i/\sigma_e$  ratio fixed. For this purpose, five strand geometries with a length of 10 cm were generated each characterized by a resolution corresponding to the average edge length of one of the heterogeneous conductivity regions in the atria (see Figure 4.1, bottom panel). Intra- and extracellular conductivities in longitudinal and transversal fiber direction as reported by Clerc *et al.* [142] as well as by Roberts *et al.* [143] were initially assigned to the elements in the slab meshes. In an iterative optimization procedure, the conductivities were adjusted until the CVs converged to the target value derived from Loewe *et al.* [140]. In this way, the originally reported intra- and extracellular conductivity values were scaled while the ratios between them were kept constant along the eigenaxes [100]. In the following, the tuned conductivities obtained by iteratively scaling the values reported by Clerc [142] and Roberts *et al.* [143] in the *tuneCV* setup are referred to as "Clerc" and "Roberts" conductivities, respectively. The resulting heterogeneous and anisotropic conductivity setup for each atrial region is summarized in Table 4.1. For the monodomain simulations, two different cases were considered which are referred to as "monodomain with and without explicit conductivity tuning". For the first one, the *tuneCV* optimization was repeated using the monodomain propagation model and obtained the monodomain conductivities listed in Table 4.1. In the second case, the monodomain conductivities were directly computed from the tuned intra- and extracellular bidomain conductivities as half of their harmonic mean. The final conduction velocities and conductivities are summarized in Table 4.1 and Table 4.2.

The Courtemanche *et al.* cell model [91] described in section 3.1.1 was used for the simulations in this study. To reflect regionally heterogeneous electrophysiology, maximum ion channel conductances were rescaled compared to the baseline model as reported in previous work [140, 144] and are summarized in Table 4.2. The final CVs values in longitudinal and transversal fiber direction as used for the Eikonal and RE simulations were subsequently calculated with *tuneCV* [98] based on the tissue and ion channel conductivity settings in each atrial region.

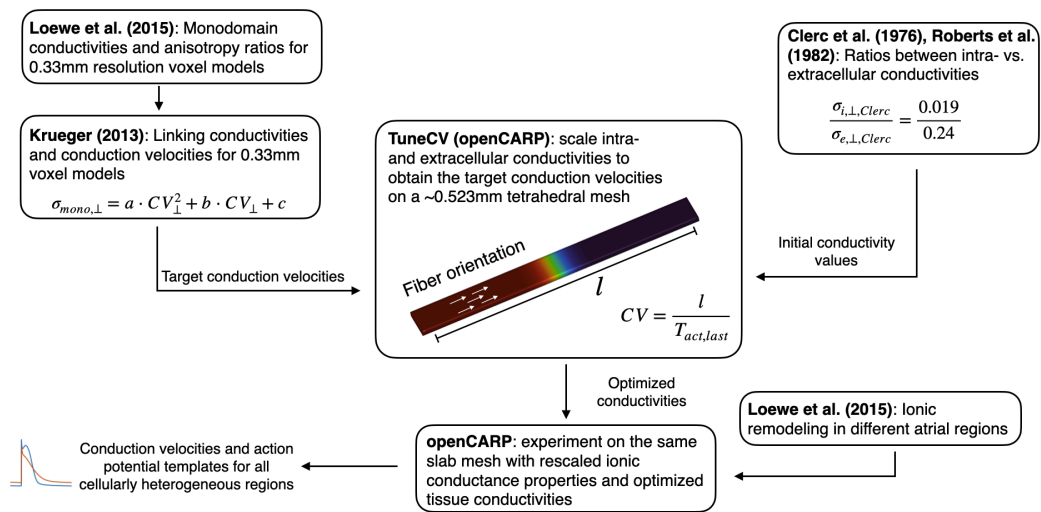


**Figure 4.2: Workflow for tuning conductivities and conduction velocities with *tuneCV*.** The monodomain conductivities reported in Loewe *et al.* (2015) were transferred in conduction velocities using the formulas reported by Krueger (2013). On a slab mesh with a resolution corresponding to the average edge length of the regions in the bi-atrial geometry, the initial intra- and extracellular conductivities as reported by Clerc *et al.* as well as by Roberts *et al.* were assigned. In an iterative optimization process, these conductivities were linearly scaled until the target conduction velocity was reached. In an openCARP experiment, action potential templates were computed using the ionic remodeling settings reported by Loewe *et al.* (2015) and the optimized conductivity settings on the same slab mesh.

**Table 4.1:** Conductivities calculated with the intra- and extracellular conductivity ratios reported by Clerc *et al.* [142] and Roberts *et al.* [143] as well as monodomain conductivities.

| Atrial region               | res ( $\mu m$ ) | Roberts conductivities |                  |                      |                      | Clerc conductivities |                  |                      |                      | Monodomain conductivities |                      |
|-----------------------------|-----------------|------------------------|------------------|----------------------|----------------------|----------------------|------------------|----------------------|----------------------|---------------------------|----------------------|
|                             |                 | $\sigma_i^\perp$       | $\sigma_e^\perp$ | $\sigma_i^\parallel$ | $\sigma_e^\parallel$ | $\sigma_i^\perp$     | $\sigma_e^\perp$ | $\sigma_i^\parallel$ | $\sigma_e^\parallel$ | $\sigma_m^\perp$          | $\sigma_m^\parallel$ |
| Regular atrial myocardium   | 523             | 2.9135                 | 1.0283           | 0.3526               | 0.4702               | 1.0189               | 3.7160           | 0.2197               | 2.7749               | 0.2037                    | 0.8036               |
| Atrial appendages           | 507             | 2.9135                 | 1.0283           | 0.3526               | 0.4702               | 1.0189               | 3.7160           | 0.2197               | 2.7749               | 0.2037                    | 0.8036               |
| Atrio-ventricular rings     | 501             | 2.9135                 | 1.0283           | 0.3526               | 0.4702               | 1.0189               | 3.7160           | 0.2197               | 2.7749               | 0.2037                    | 0.8036               |
| Crista terminalis           | 534             | 5.3727                 | 1.8962           | 0.3557               | 0.4743               | 1.8784               | 6.8507           | 0.2216               | 2.7990               | 0.2055                    | 1.4815               |
| Pectinate muscles           | 510             | 5.7922                 | 2.0443           | 0.2383               | 0.3177               | 2.0239               | 7.3814           | 0.1481               | 1.8702               | 0.1373                    | 1.5964               |
| Bachmann's bundle           | 530             | 8.8775                 | 3.1332           | 0.4090               | 0.5454               | 3.0979               | 11.2980          | 0.2550               | 3.2214               | 0.2365                    | 2.4430               |
| Inferior isthmus            | 525             | 0.6573                 | 0.2320           | 0.3070               | 0.4093               | 0.2250               | 0.8207           | 0.1911               | 2.4142               | 0.1773                    | 0.1772               |
| Fibrosis (non conductive)   | 523             | 0                      | 0                | 0                    | 0                    | 0                    | 0                | 0                    | 0                    | 0                         | 0                    |
| Fibrosis (slow conducting)  | 523             | 0.8208                 | 0.2897           | 0.0466               | 0.0621               | 0.2823               | 1.0296           | 0.0288               | 0.3644               | 0.0267                    | 0.2223               |
| Fibrosis (ionic remodeling) | 523             | 2.9135                 | 1.0283           | 0.3526               | 0.4702               | 1.0189               | 3.7160           | 0.2197               | 2.7749               | 0.2037                    | 0.8036               |

**Table 4.2:** Scaling factors for ion channel conductances with respect to the baseline Courtemanche *et al.* cell model and resulting CVs in different atrial regions.

| Atrial region               | Ionic heterogeneity |           |          |          | CV (m/s)     |                  |
|-----------------------------|---------------------|-----------|----------|----------|--------------|------------------|
|                             | $g_{to}$            | $g_{CaL}$ | $g_{Na}$ | $g_{K1}$ | $CV^{\perp}$ | $CV^{\parallel}$ |
| Regular atrial myocardium   |                     |           |          |          | 0.5905       | 1.2465           |
| Atrial appendages           | 0.68                | 1.06      |          |          | 0.5950       | 1.2467           |
| Atrio-ventricular rings     | 1.53                | 0.67      |          |          | 0.5965       | 1.2456           |
| Crista terminalis           |                     | 1.67      |          |          | 0.5911       | 1.6839           |
| Pectinate muscles           |                     |           |          |          | 0.4612       | 1.7435           |
| Bachmann's bundle           |                     |           |          |          | 0.6450       | 2.1511           |
| Inferior isthmus            |                     |           |          |          | 0.5402       | 0.5402           |
| Fibrosis (non conductive)   |                     |           |          |          | 0            | 0                |
| Fibrosis (slow conducting)  |                     |           |          |          | 0.1181       | 0.6232           |
| Fibrosis (ionic remodeling) |                     | 0.5       | 0.6      | 0.5      | 0.4812       | 1.0063           |

## 4.2.2 Simulation Scenarios

Simulations were carried out on the bi-atrial volumetric model described in section 4.2.1 in sinus rhythm with and without the inclusion of fibrotic tissue patches. For the former case, several elliptically shaped patches with their principal axis aligned to the macroscopic atrial fiber orientation were manually defined predominantly on the posterior wall of the left atrium and the left pulmonary vein antrum as reported by Highuchi *et al.* [145]. These regions extended transmurally and are shown in Figure 4.3. To not only account for the patchiness of atrial fibrosis but also for its diffuse deposition, 80 % of the cells within the elliptical candidate regions were defined as fibrotic. In this way, the volume fraction of left atrial fibrosis quantified to 22 % of the total left atrial tissue volume. Remodeled conduction properties were assigned to fibrotic regions in three different ways as shown in Figure 4.3 and described in the following.

In the first case, fibrotic elements were removed from the atrial mesh and instead assigned to the extracellular domain following the concept of percolation [128, 146]. In this way, passive conduction barriers were introduced that do not exhibit any transmembrane voltage and thus do not contribute to the electrical source distribution on the myocardial tissue surface. In the second case, fibrotic regions were characterized as slow conducting patches with CVs reduced by 80 % in transversal and 50 % in longitudinal fiber direction compared to the healthy baseline case [48, 141]. Conductivities in these regions were subsequently obtained as described in section 4.2.1. In this way, anisotropy ratios were inherently increased by a

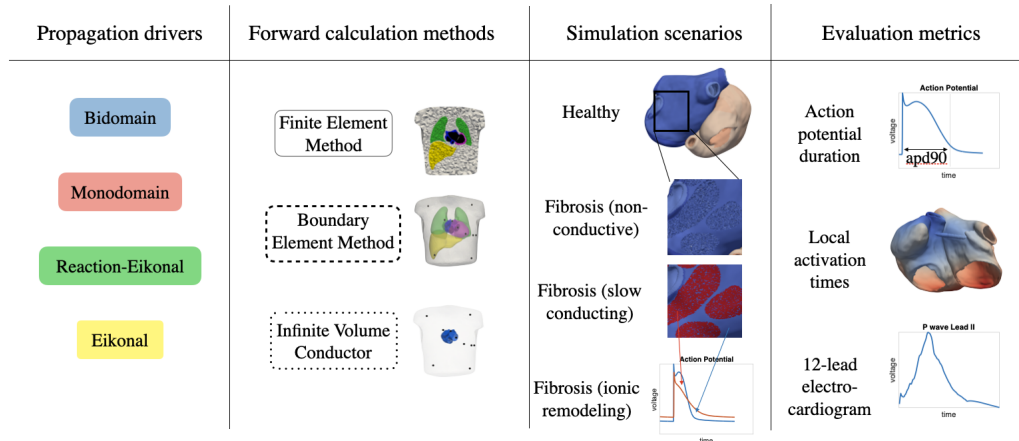


**Figure 4.3:** Overview of the different propagation models, forward calculation methods, simulation scenarios and evaluation metrics used in this work.

factor of 2.5 in fibrotic areas promoting wave propagation along myocardial fiber orientation and thus forming the basis for functional reentry circuits [81]. In the third case, ionic properties of the fibrotic cells were remodeled by rescaling the conductances of the sodium ( $g_{Na}$ ), the L-type calcium ( $g_{CaL}$ ) and the inward rectifier potassium current ( $g_{K1}$ ) by a factor of 0.6, 0.5 and 0.5, respectively, compared to the baseline conductances of the Courtemanche *et al.* cell model to account for cytokine induced effects mediated by transforming growth factor (TGF)- $\beta$ 1 [82, 147, 148].

Sinus rhythm simulations were initiated by triggering the activation propagation at a sinoatrial node exit site located at the junction of crista terminalis and the superior vena cava [149, 150]. The transmembrane voltage distribution for the LATs computed with the Eikonal model was obtained as described in equation 3.13, whereby the respective ionic model parameters in each region as listed in Table 4.2 were taken into account for calculating the action potential (AP) templates.

The Cardiac Arrhythmia Research Package (*CARP*) [151] and *openCARP* [98] were used for computing the spread of the depolarization wave with different propagation models as well as ECGs with the finite element and the infinite volume conductor method. The algorithms described by Stenroos *et al.* [107] were used for calculating ECGs with the boundary element method. As recommended by Schuler *et al.* [152], the surface mesh bounding the atria was downsampled to a resolution of 2.5 mm for computing the transfer matrix. Furthermore, Laplacian smoothing was applied to the transmembrane voltage sources to ensure a continuous wave propagation on the coarse mesh.

### 4.2.3 Evaluation Metrics

From the source distribution obtained from simulations using different propagation models, APDs at 90 % repolarization ( $APD_{90}$ ) were calculated for each node in the mesh. Also at

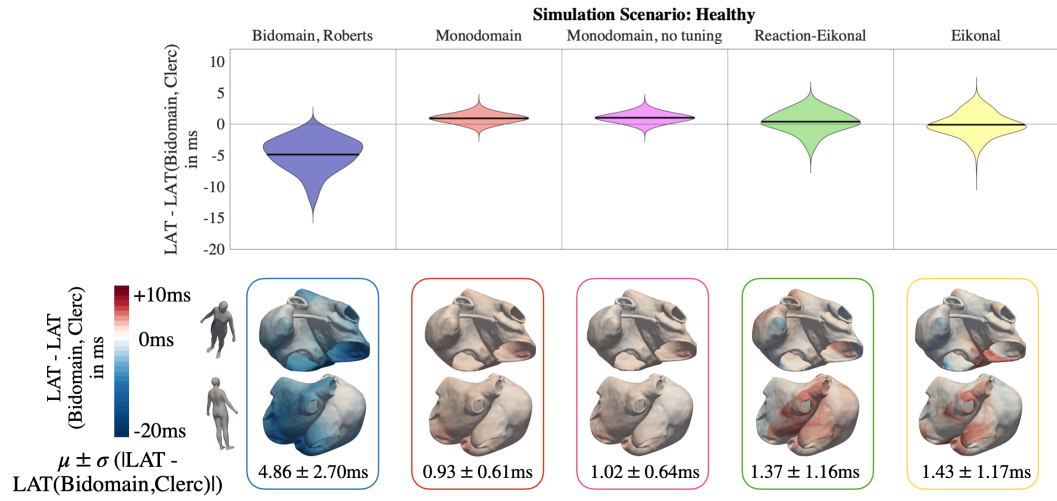


**Figure 4.4: Local activation time (LAT) results in sinus rhythm for healthy (non-fibrotic) tissue for different propagation models.** The top panel shows the distribution of the signed LAT differences taking the bidomain simulations executed with the Clerc conductivity ratios as a reference. From left to right, the violin plots show the results for the bidomain (Roberts conductivities), the monodomain (with and without explicit conductivity tuning), the RE<sup>+</sup> and the Eikonal simulations. The bottom panel shows the signed LAT differences mapped on the atrial geometry for each propagation model in the above order. Mean and standard deviation of the absolute LAT differences are shown in the bottom row for each case.

each vertex in the geometry, LATs were extracted defined as the timestep with the steepest AP upstroke. For both, APDs and LATs, the accuracy of each propagation model simulation was quantified as the absolute difference to the respective value for each metric obtained from the bidomain simulation with the Clerc conductivities.

To assess fidelity of simplified forward calculation methods along with different propagation models, the Pearson correlation coefficient of the respective ECG results with the ECGs obtained by solving the forward problem with the finite element method based on the bidomain source distribution computed with the Clerc conductivities was evaluated.

## 4.3 Results

### 4.3.1 Propagation Models

The effect of different propagation models on the activation sequence (LATs) is visualized in Figure 4.4. The maximum activation time in the healthy reference scenario solved with the bidomain model was 102 ms. In the top panel, the distributions of the signed differences between the examined propagation models' LATs and the bidomain results obtained with Clerc conductivity ratios evaluated at all mesh nodes are visualized as violin plots. In the bottom panel, the difference to the bidomain results are mapped onto the atrial geometry.

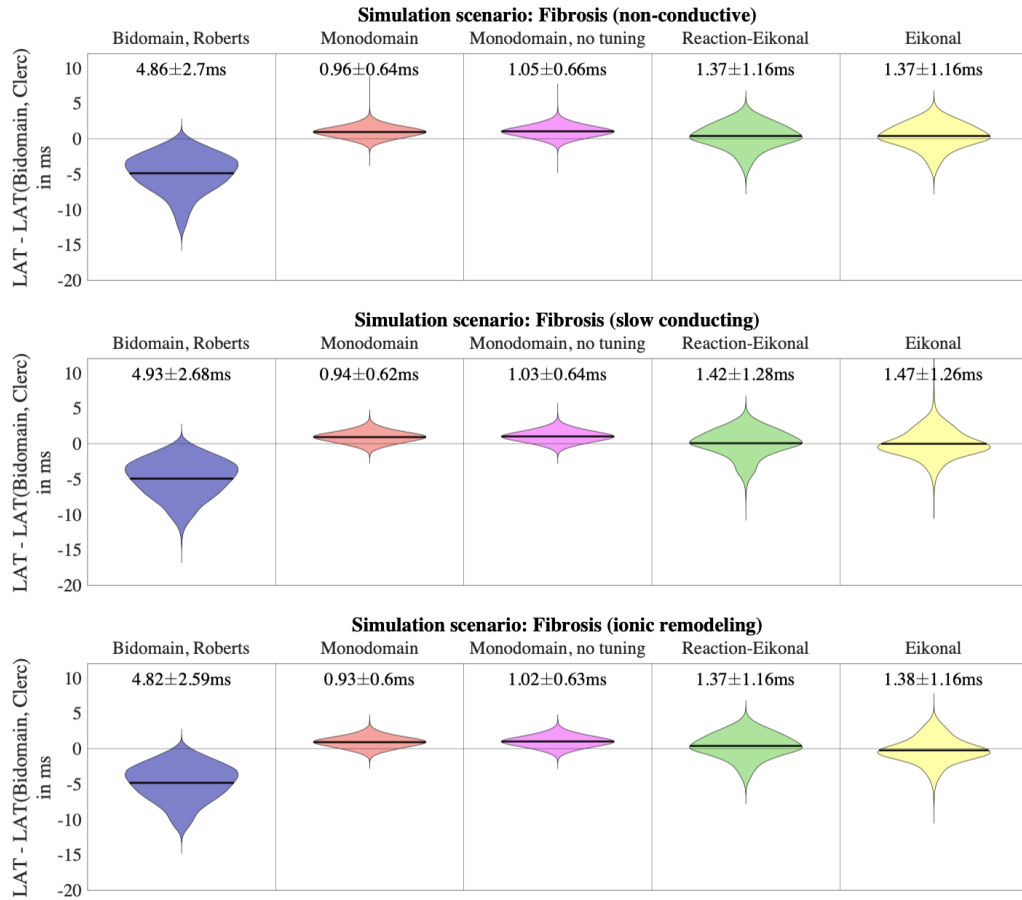
The mismatch in LATs was most pronounced for the bidomain scenario with Roberts conductivities and much smaller for the simplified propagation models. For the Roberts conductivity ratios, the LATs were systematically smaller than the ones resulting from the reference bidomain simulation with the Clerc conductivity settings. Furthermore, the error increased with the spread of the depolarization wave front leading to small deviations close to the sinus node exit site, but errors of up to -14 ms at the latest activated areas at the posterior wall of the left atrium and the coronary sinus in the right atrium. The mean and standard deviation of the absolute errors between the bidomain and monodomain LATs with and without explicit conductivity tuning were  $0.93 \pm 0.61$  ms and  $1.02 \pm 0.64$  ms. With the temporal resolution of the sampled simulated myocyte APs being 1 ms and the LATs being calculated as the point in time marking the steepest AP upstroke, in particular the LAT results for the monodomain simulation with additional conductivity tuning were below the accuracy with which the LATs were determined.  $RE^+$  and Eikonal LAT differences quantified to  $1.37 \pm 1.16$  ms and  $1.43 \pm 1.17$  ms, respectively. The signed LAT error to the bidomain results was distributed similarly across the atrial tissue among these two propagation models (see Figure 4.4 bottom panel).

The LAT results in the simulation scenarios involving fibrosis remodeling were only slightly different (see Figure 4.5) compared to the sinus rhythm results depicted in Figure 4.4. The largest differences occurred for the Eikonal propagation model in the simulation scenario where fibrosis was modeled as slow conducting tissue. There, the absolute error to the bidomain results quantified to  $1.47 \pm 1.26$  ms compared to  $1.43 \pm 1.17$  ms in sinus rhythm without the inclusion of fibrosis.

$APD_{90}$  results are visualized for the simulation scenario with fibrosis modeled as ionic conductance rescaling in Figure 4.6. For the monodomain simulations, the mean and standard deviation of the absolute  $APD_{90}$  discrepancies to the bidomain results obtained with Clerc conductivity ratios were below the temporal resolution of the AP time course of 1 ms. Absolute errors to the bidomain simulation with Roberts conductivity ratios and the  $RE^+$  results quantified to  $2.92 \pm 3.07$  ms and  $1.35 \pm 1.69$  ms, respectively. In both cases, the highest errors occurred in regions around the fibrotic tissue patches.  $APD_{90}$  results for the Eikonal simulation were characterized by an absolute error to the bidomain simulation results of  $25.1 \pm 20.72$  ms. Furthermore, the AP signal trace obtained from a tissue strand simulation and used as a template to infer the transmembrane voltage distribution for the Eikonal LATs is visually clearly distinguishable from the bidomain AP especially in fibrotic regions (see Figure 4.6 bottom panel).

The APD results in the simulation scenarios involving other fibrosis remodeling methodologies as well as in the healthy control case are visualized in Figure 4.7. The largest differences occurred for the Eikonal propagation model in the simulation scenario where fibrosis was modeled as slow conducting tissue.

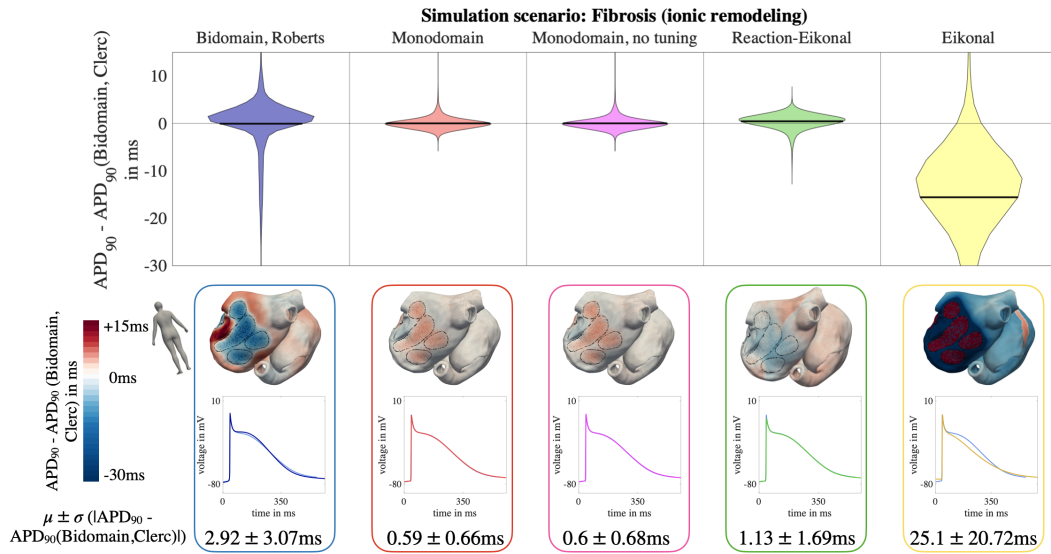
ECGs obtained from the transmembrane voltage distributions in the simulation scenario with fibrosis modeled as ionic rescaling (as depicted for  $APD_{90}$  in Figure 4.6) and using the boundary element forward calculation method are visualized in Figure 4.8. The 12-lead ECG is displayed for a duration of 450 ms whereby the signal sections in the interval



**Figure 4.5: LAT differences between different propagation models and the bidomain simulation results obtained with the Clerc conductivities.** The top row shows the mean  $\pm$  standard deviation of the absolute differences to the bidomain LATs.

[0 ms, 150 ms] and [150 ms, 450 ms] represent the P wave (panel (a) in Figure 4.8) and the atrial repolarization (panel (b) in Figure 4.8), respectively. The latter is typically not visible in the clinical ECG of a full heartbeat since the repolarization phase of the atria temporally coincides with the ventricular activation and the respective signal parts are thus buried within the QRS complex.

The observed discrepancies in the AP signal course between the bidomain and Eikonal simulation (see Figure 4.6) also reflect in the ECG. As can be seen in Figure 4.8, the repolarization signal obtained with the Eikonal and bidomain propagation model differ markedly. In lead aVL, the polarity of the repolarization wave was even inverted. Apart from the atrial repolarization in case the ECG signal was obtained with the Eikonal model and precomputed AP templates, the choice of the propagation model did not noticeably influence the ECG as the remaining signals in Figure 4.8 show only minor differences to one another. Furthermore, the correlation coefficients between the bidomain ECG obtained with the Clerc conductivity ratios and the other examined propagation models are summarized in



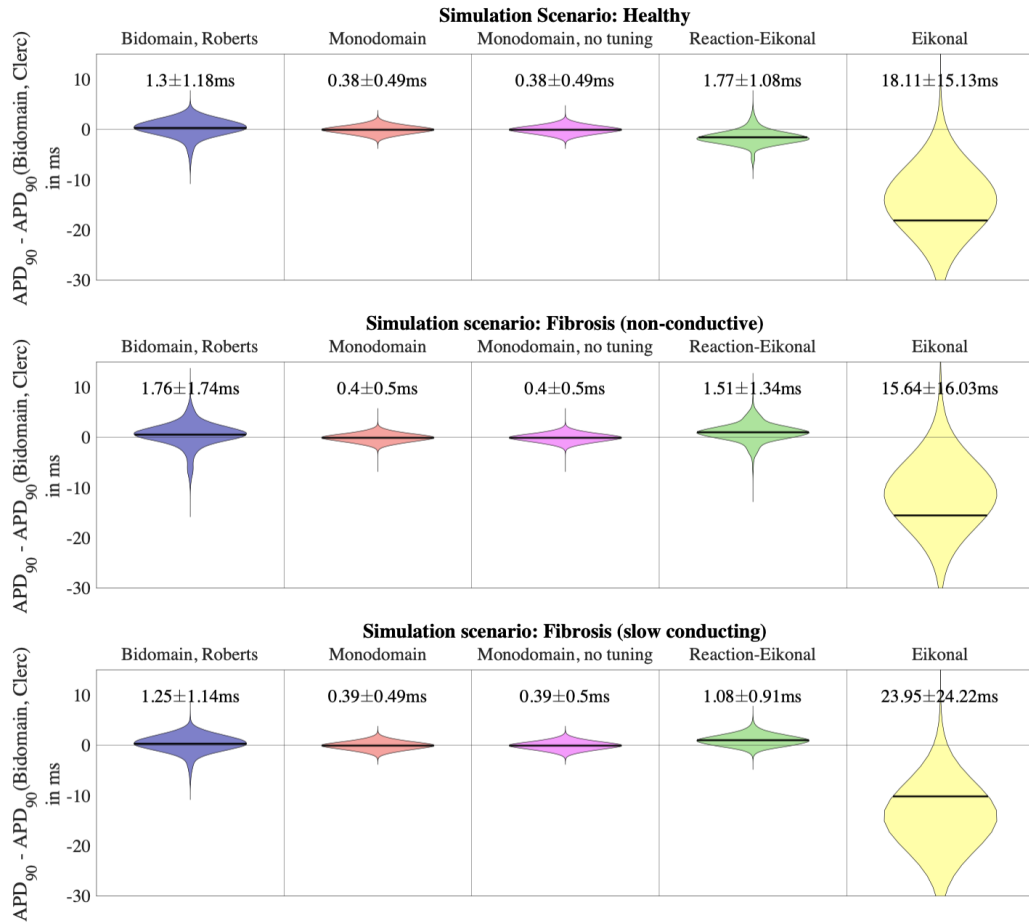
**Figure 4.6: APD<sub>90</sub> results in sinus rhythm with fibrotic substrate replacing 22% of the left atrial myocardial tissue modeled as rescaled ionic conductances.** The violin plots in the top panel represent the distribution of APD<sub>90</sub> discrepancies to the bidomain results for all investigated propagation models. In the bottom panel, the signed APD<sub>90</sub> differences are mapped onto the atrial geometry. Fibrotic regions are encircled with black dashed lines. The APs are shown for one node within the fibrotic area on the posterior left atrial wall. Bidomain APs are visualized in light blue, the other signal trace was obtained with the respective propagation model. The numbers in the bottom line show the mean and standard deviation of absolute APD<sub>90</sub> differences with respect to the bidomain simulation results.

Table 4.3 for the intervals [0 ms, 150 ms] (P wave), [150 ms, 450 ms] (repolarization) and [0 ms, 450 ms] (entire signal). The lowest correlation coefficient for the P wave occurred for the bidomain simulation with Roberts conductivity ratios. For all simplified propagation models, the P wave correlation coefficients were above 0.92. Except for the Eikonal model, the correlation coefficient of the ECG signal sections representing the repolarization phase wave was above 0.99.

ECGs only marginally differed between the investigated fibrosis remodeling scenarios as shown in Figure 4.9. Also the comparison of ECG metrics in the other simulation scenarios led to similar results compared to those visualized and described for the fibrosis case with ionic conductance rescaling above. Resulting P waves, Ta waves and feature distributions in the remaining simulation scenarios are shown for all propagation drivers and forward calculation methods in the appendix (section A).

### 4.3.2 Forward Calculation Methods

ECGs calculated with different forward calculation methods based on the same source distribution stemming from the bidomain simulation with Clerc conductivity ratios are depicted in Figure 4.10 for the simulation scenario with fibrosis modeled as slow conducting tissue.



**Figure 4.7:**  $APD_{90}$  differences between the investigated propagation models and the bidomain simulation results obtained with the Clerc conductivities. The top row shows the mean  $\pm$  standard deviation of the absolute differences to the bidomain LATs.

The correlation coefficients covering the ECG signal parts of the P wave between the gold standard finite element method (FEM) approach and each of the boundary element method (BEM) and infinite volume conductor (IVC) method quantified to 0.98 and 0.83 for fibrosis modeled as slow conducting tissue (see Table 4.4).

Especially the IVC method yielded too high ECGs amplitudes in the precordial leads and inaccurately captured atrial repolarization in the inferior leads II, III and aVF.

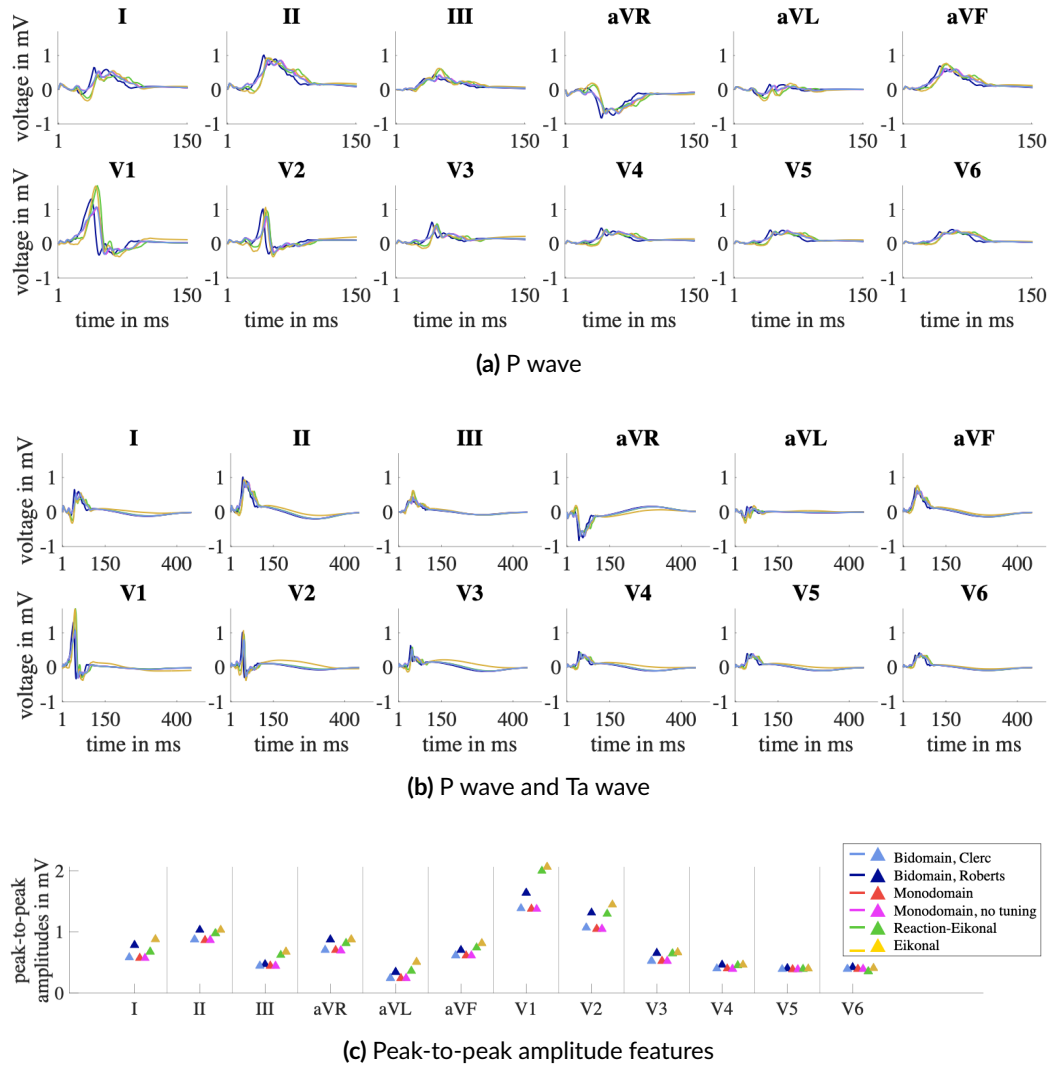


Figure 4.8: ECGs calculated with the same forward calculation method (BEM) but different propagation models (color coded). Transmembrane voltages resulted from the simulation scenario with fibrosis modeled as ionic conductivity rescaling. In panel (a) and (b) the P wave and P wave followed by a Ta wave are shown, respectively. In panel (c), lead specific peak-to-peak amplitude features extracted from the P wave signals are visualized.

## 4.4 Discussion

### 4.4.1 Main Findings

In this study, atrial APD<sub>90</sub>, LATs and ECGs computed with the bidomain, monodomain, RE<sup>+</sup> and the Eikonal propagation models as well as with the finite element, the boundary element and the infinite volume conductor forward calculation methods were compared to one another.

**Table 4.3:** Correlation coefficients between the ECGs obtained with the bidomain and simplified propagation models when solving the forward problem with BEM in the simulation scenario of fibrosis modeled as ionic conductance rescaling. Columns represent depolarization (P wave), repolarization (Ta wave) and the entire signal.

|                       | [0 ms, 150 ms] | [150 ms, 450 ms] | [0 ms, 450 ms] |
|-----------------------|----------------|------------------|----------------|
| Bidomain, Clerc       | 1              | 1                | 1              |
| Bidomain, Roberts     | 0.8590         | 0.9904           | 0.9028         |
| Monodomain            | 0.9942         | 0.9998           | 0.9961         |
| Monodomain, no tuning | 0.9931         | 0.9998           | 0.9954         |
| Reaction-Eikonal      | 0.9211         | 0.9953           | 0.9428         |
| Eikonal               | 0.9203         | 0.6233           | 0.8791         |

**Table 4.4:** Correlation coefficients between the ECGs obtained with the FEM and simplified forward calculation methods when calculating the spread of the excitation wavefront with the bidomain model in the simulation scenario of fibrosis modeled as slow conducting tissue. Columns represent depolarization (P wave), repolarization (Ta wave) and the entire signal.

|                                  | [0 ms, 150 ms] | [150 ms, 450 ms] | [0 ms, 450 ms] |
|----------------------------------|----------------|------------------|----------------|
| Finite Element Method            | 1              | 1                | 1              |
| Boundary Element Method          | 0.8507         | 0.9818           | 0.8947         |
| Infinite Volume Conductor Method | 0.8299         | 0.8107           | 0.8548         |

The largest deviations in LATs were observed between the bidomain simulations with Clerc and Roberts conductivity ratios. As the absolute LAT errors increase with the propagating wavefront, discrepancies in LATs can be traced back to more pronounced bath loading effects occurring with the Roberts conductivity settings (compare Figure 4.11, left panel). With a higher ratio between extracellular bulk and isotropic bath conductivities, the depolarization wave propagates faster in close vicinity to the interface between blood pool and endocardial wall leading to earlier LATs throughout the cardiac tissue. Due to the thin atrial wall, the bathloading effect is visible transmurally and thus results in globally faster conduction velocities in the bidomain simulations with the Roberts conductivity setup. However, in this work, conductivities were tuned as described in section 4.2.1 without a bath attached to one face of the strand meshes. Incorporating the bath already in the tuning process would have led to more similar results between the bidomain simulation results obtained with tuned Clerc and Roberts conductivities. This systematic underestimation of LATs also reflects in the ECG. The bidomain simulation with the Roberts conductivity settings yielded the smallest P wave correlation to the bidomain ECGs with the Clerc conductivity ratios and markedly shorter P wave duration. Also Sebastian *et al.* [153] found that the choice

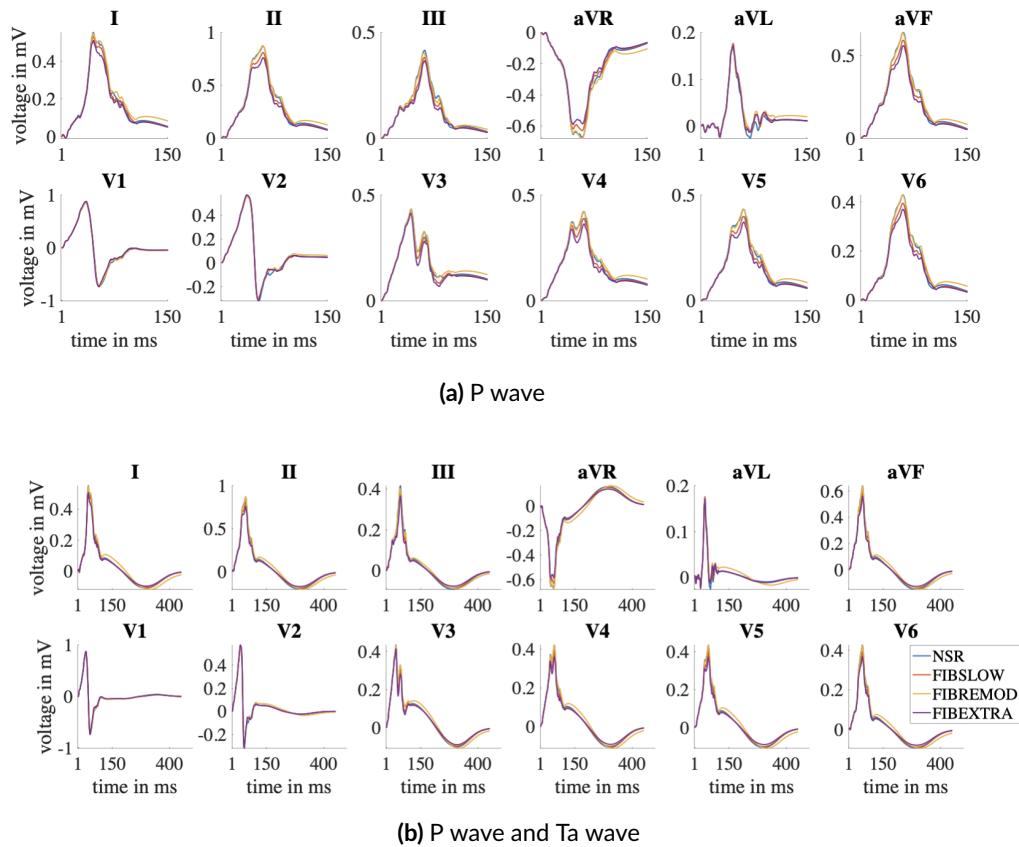


**Figure 4.9:** ECGs resulting from a full bidomain simulation for different fibrosis modeling approaches. Top panel: P wave, bottom panel: P wave and Ta wave. The blue, red, yellow and purple curve show the 12-lead surface ECG for the healthy case (NSR) and the fibrotically infiltrated atrial geometry with fibrosis modeled as slow conducting tissue (FIBSLOW), ionic conductance rescaling (FIBREMOD) and the percolation approach (FIBEXTRA), respectively.

of conductivity ratios in the intra- and extracellular domain as well as in longitudinal and transversal fiber direction had a marked effect on CV and LATs. Intra- and extracellular conductivity values were derived by Clerc and Roberts *et al.* in animal experiments on specimen from excised trabecular cardiac bundles. Measuring intra- and extracellular current flow using microelectrodes allowed for a computation of the resistance and in turn the conductivity in longitudinal and transversal fiber direction in both, the extra- and intracellular space. Considering the complex and cumbersome in and ex vivo experiments to derive these parameters, fixed ratios between  $\sigma_i$  and  $\sigma_e$  along and perpendicular to the myocardial fiber orientation need to be assumed when personalizing computer models. As a consequence, the high uncertainty of the ratio between  $\sigma_i$  and  $\sigma_e$  which cannot be measured patient-specifically with reasonable efforts further justifies the application of simplified models that do not involve uncertainties in non-measurable entities and only cause minor differences in LATs, ECGs and  $APD_{90}$ .

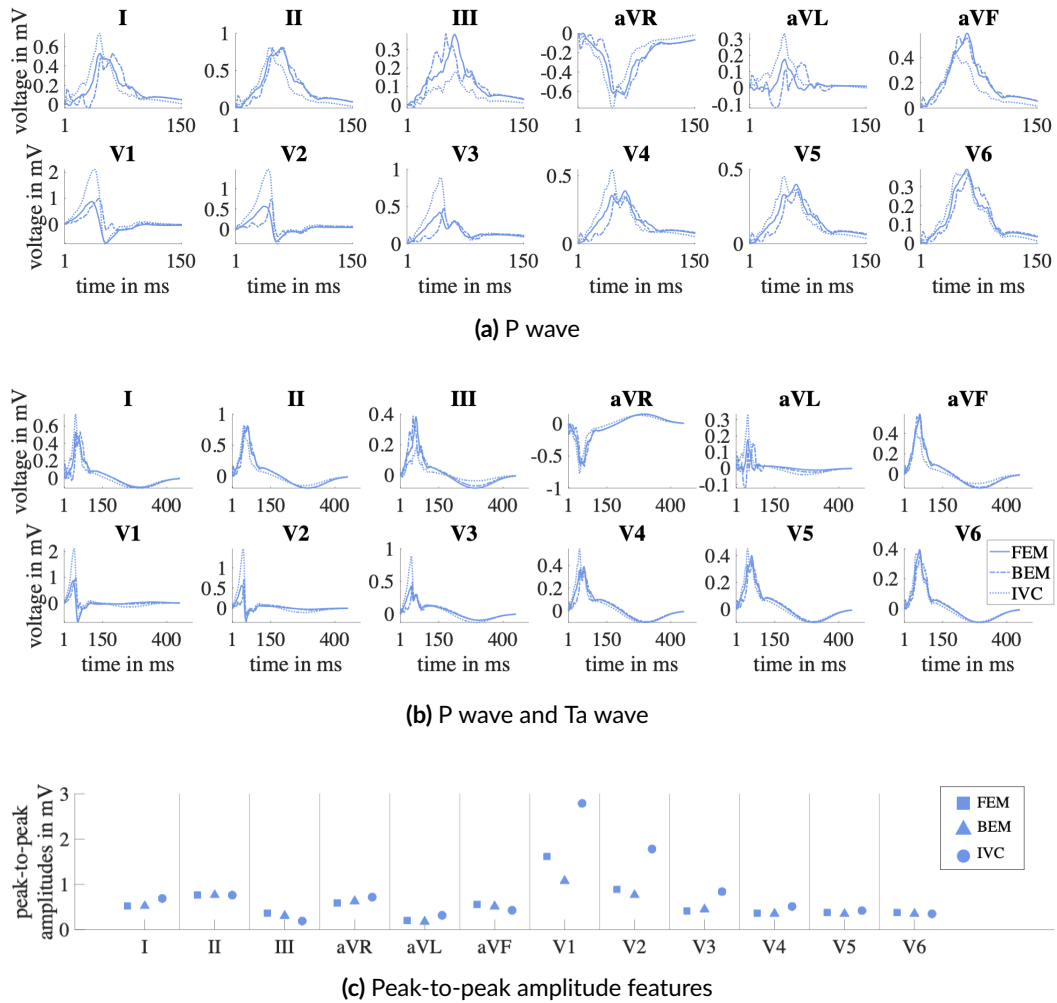


**Figure 4.10:** ECGs calculated with the same propagation driver (bidomain) but different forward calculation methods for the simulation scenario with fibrosis modeled as slow conducting tissue. ECGs calculated with FEM, BEM and IVC results are represented by the solid, dashed and dotted lines, respectively. Peak-to-peak amplitude features extracted from the ECGs calculated with FEM, BEM and IVC are represented with triangle, square and circle markers, respectively.

Among all investigated simplified model solutions, the monodomain model yielded the most accurate results regarding activation times, repolarization behavior and ECGs. However, explicit conductivity tuning for the monodomain model neither had a notable effect on LATs, nor APD<sub>90</sub>, nor on the 12-lead ECG.

Mean and standard deviation of the absolute LAT differences to the bidomain results quantified to  $1.37 \pm 1.16$  ms and  $1.43 \pm 1.17$  ms for the RE<sup>+</sup> and the Eikonal model, respectively, which differed only slightly due to numerical jitter. The distribution of LAT discrepancies to the bidomain results mapped on the atrial geometry was similar for the Eikonal and the RE<sup>+</sup> model (see Figure 4.4). The LATs of the simplified propagation models were especially higher compared to the bidomain results in regions on the posterior left atrial

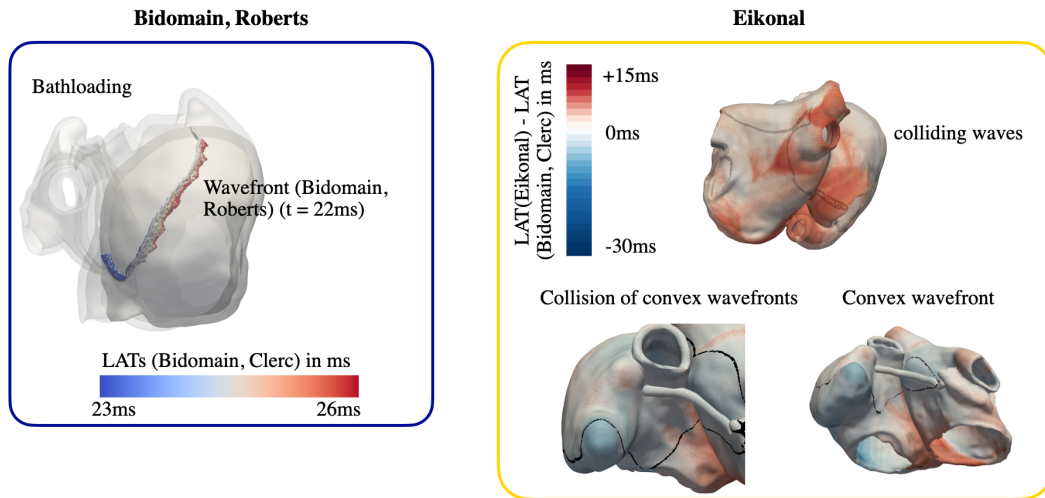


**Figure 4.11: Visualization of LAT discrepancies between the bidomain results and other propagation models.** The left panel shows the wavefront position obtained with the bidomain simulation ran with Roberts conductivities at  $t=22$  ms. The more pronounced bathloading effects for the Roberts conductivity ratios becomes visible by color coding the activation wave front with activation times obtained with the bidomain simulation and Clerc conductivity settings. In this case, nodes along the wavefront at the endocardium in close proximity to the interface between blood pool and myocardial tissue were excited at a later time than the ones at the epicardium. The right panel shows the signed LAT differences between the Eikonal and the bidomain simulation. The top panel shows the atrial geometry from the posterior view where wavefronts collide and cause an acceleration of the wavefront in the bidomain, but not in the Eikonal model. The bottom panel shows the effect of convex wavefronts at the right atrial appendage as well as at the connection between the Bachmann's bundle and the left atrium.

wall. In these late activated areas, different wavefronts collide causing an acceleration of the wave in the bidomain model, which is not captured in the mathematical description of the (reaction-)Eikonal model. Source-sink mismatch effects caused by convex wavefronts entailing conduction slowing in the bidomain model cause smaller LATs in the Eikonal simulation results. This effect is especially visible in the area where Bachmann's bundle connects to the anterior wall of the left atrium (compare Figure 4.11, right panel), i.e. where a small source (Bachmann's bundle) meets a large sink (the left atrium). At the apex of the right atrial appendage, two convex wavefronts traversing the tissue from the lateral and the septal right atrial wall collide and cause Eikonal LATs to be smaller than the ones resulting from the bidomain simulation. The P waves computed with the reaction-Eikonal and the Eikonal source distribution showed similar correlation coefficients of 0.921 and 0.920 to the bidomain results. However, when evaluating repolarization dynamics,  $RE^+$  clearly led to more precise results than the Eikonal model. This reflects on the one hand in smaller  $APD_{90}$  discrepancies to the bidomain simulation results. The small  $APD_{90}$  discrepancies between the monodomain and  $RE^+$  simulation results might have occurred due to differences in the activation pattern or a mismatch between the diffusion term and the  $I_{f_{oot}}$  current in the case of curved wavefronts or wave collisions causing different AP upstrokes and amplitudes which subsequently lead to subtle APDs changes. On the other hand, the  $RE^+$  model is capable of faithfully replicating both the P wave as well as the atrial repolarization phase in the ECG,

whereas with the Eikonal model, only the P wave highly resembles the bidomain results. Using precomputed AP templates to obtain the transmembrane voltage source distribution for the Eikonal LAT results,  $APD_{90}$  results were systematically smaller compared to the bidomain results in regular bulk tissue regions and systematically higher in fibrotic regions. The more precise representation of repolarization behavior in simulation results using the  $RE^+$  model is due to local APD balancing caused by the diffusion term. Consequently, also the Ta wave in the ECG obtained with the source distribution derived from the Eikonal results only showed a correlation coefficient of 0.62 to the bidomain ECG.

ECGs calculated with the BEM highly resembled the ECGs obtained with the FEM. P wave correlation coefficients to the FEM approach quantified to 0.94 and 0.93 for the simulation scenario with fibrosis modeled as slow conducting and non-conductive patches, respectively. In the former scenario, surface transmembrane voltages can be used as a source model for the forward calculation, whereas in the latter, volumetric sources such as primary impressed currents were necessary to model the effect of passive conduction barrier not contributing to the electrical source distribution in the heart. If the surface transmembrane voltages had been used as sources for the forward calculation in this case as well, an artefact in form of an offset in the isoelectric line in the P wave would have been induced. The IVC method instead yielded more inaccurate ECGs results. Especially in the septal and anterior leads, the ECG amplitudes were overestimated by a factor of  $>2$  compared to the FEM results. On the one side, this observation can be traced back to the method's assumption that the atria are immersed in an infinite medium of a homogeneous conductivity, which does not allow considering a heterogeneous conductivity setup in the torso. On the other hand, the high ECG errors occurred predominantly in leads measured at electrode locations on the body surface in close proximity to the cardiac sources. Thus, neglecting the attenuating effect that the bounded torso volume conductor introduces, causes a more pronounced effect on the resulting ECGs in V1-V3.

Simulations were run on a 16 core CPU machine (Intel Xeon Gold 6230, 2.1 GHz). The full bidomain and the pseudo-bidomain simulation of a duration of 450 ms were completed in 25 and 1.5 hours, respectively. Computation time for the  $RE^+$  setup was 1.4 hours on a 6 core machine. The computation of the transfer matrix for the BEM approach in the case of a heterogeneous torso volume conductor with seven surfaces bounding the atria, the torso and other organs took 2 hours on a 4 core CPU machine (Intel Core i5, 2.4 GHz). The speed-up in computation times when using simplified propagation models is comparable to a ventricular setup. Computational performance improved by one order of magnitude when using the monodomain model [99] and up to three orders of magnitude when using the Eikonal model [104, 125] compared to bidomain. However, increasing the number of cores the simulations are ran on could change the results regarding algorithmic efficiency as different models might exhibit different scalability properties when parallelized to multiple threads or processes [154]. Solvers with strong scaling capabilities have been shown to provide the basis for fast simulation runs of the biophysically detailed monodomain model and of forward calculation methods without any cutbacks on anatomical and electrophysiological properties [155, 156]. In the simulations in this study, the degrees of freedom

in terms of number of nodes and elements in the mesh was the same for all propagation models. High resolutions in time and space are required for numerical convergence of the bi- and monodomain solution [92]. As described by Woodworth *et al.* [157], a high mesh resolution is a necessary requirement for CV convergence, especially for low conductivities (see also Figure 4.12 and Figure 4.13). On the other side, (reaction)-Eikonal models are capable of faithfully estimating activation time sequences on coarser meshes [104, 158]. The computational complexity of the Eikonal model depends on the method used to solve it [159], but is approximately  $\mathcal{O}(n \log(n))$  with  $n$  being the number of nodes in the mesh. These properties could be taken advantage of to further reduce computational cost when running simulations based on these simplified models. Computational savings using the BEM approach are on the one hand due to the decreased problem complexity when discretizing the domain with surface instead of volume elements [106]. On the other hand, coarser resolution meshes can be applied which is the key influencing factor for an improved computational efficiency over FEM [160].

#### 4.4.2 Related work

In this study, the differences in activation and repolarization times were examined when using different propagation models in atrial electrophysiology, which, to the best of our knowledge, has not been done before in a comprehensive way. However, comparable studies have partly already been conducted for the ventricles and four-chamber heart models. Potse *et al.* [127] found that activation using bidomain was 2 % faster compared to the monodomain approach for a complete cardiac cycle. Also in this study, the monodomain activation times were on average 1 ms higher than those obtained from the bidomain simulation. Considering the total time of 102 ms for a complete activation of both atria, the discrepancies between mono- and bidomain resulting in this study correspond to a relative error of approximately 1 % , too. Pashaei *et al.* [161, 162] as well as Wallman *et al.* [125] found that the differences in activation times are small for a ventricular simulation setup when comparing biophysically detailed approaches and the Eikonal model. Neic *et al.* [104] compared extracellular potential fields, electrograms and ECGs calculated with the RE and the bidomain model for the ventricles and concluded that the simplified model can replicate the gold standard results with high fidelity. The results in this work confirm the findings from previous studies mainly conducted for ventricular simulation setups. Gassa *et al.* [163] investigated the suitability of an RE model to generate re-entrant activity on a bi-atrial geometry and succeeded in replicating the wave patterns resulting from a monodomain simulation. It was also shown in a preceding study of this work that the Eikonal-based models can produce activation times and ECGs resembling full bidomain simulation results with high fidelity in an atrial model without cellular remodeling placed in a homogeneous torso volume conductor [164]. The setup described in this chapter was extended to heterogeneous scenarios covering cellular and conductivity heterogeneity in both the torso and the atria and similar results were obtained.

Previous studies have also investigated the application of simplified forward calculation methods to computed ECGs. Schuler *et al.* [152] suggest the calculation of ECGs based on

the BEM with coarse resolution surface meshes bounding the heart and the torso whereby parameters to blur the cardiac sources are optimized beforehand to avoid discontinuous wave propagation. In this way, they obtained body surface potentials in accurate accordance with the bidomain simulation results for a ventricular setup. However, one major drawback of the BEM approach is the impossibility of accounting for anisotropic conductivity in the myocardium [106]. However, the P wave correlation coefficients was found to quantify to  $>0.93$  showing that the isotropic assumption yields similar ECGs compared to the bidomain results. For the IVC method instead, not only the assumption of isotropic myocardial conductivities but also of a homogeneous torso volume conductor has to be made. Moreover, the simplified assumption that the atria is immersed in a medium of infinite spatial extent does not hold true. Although the general P wave morphology was preserved, the ECG still substantially differs regarding peak-to-peak amplitudes in the precordial leads and atrial repolarization in the inferior leads as it reflects in the results of this study and was reported in previous work [105]. For the application field of computing intracardiac electrograms, the reader is referred to the review by Sánchez *et al.* [103].

### 4.4.3 Limitations

In this work, four different simulation scenarios were investigated comprising a healthy baseline case and three atrial models infiltrated with fibrosis, which was modeled either as slow conducting patches, non-conductive conduction barriers or ionic conductance rescaling. For the spatially distributed fibrotic areas (patchy and diffuse), none of the fibrosis remodeling scenarios had a marked effect on the ECG compared to the healthy baseline case. Ionic conductance rescaling, slow conducting fibrotic patches and percolation reflect in the ECG as a slight prolongation of the repolarization phase and an offset in the isoelectric line, a prolongation of the P wave and a decrease in peak-to-peak P wave amplitudes, respectively. Even though all these effects on the ECG are small, they would show up in a more pronounced way if different fibrosis remodeling approaches were combined [122]. However, it was intentionally decided to investigate the effect of different propagation models and forward calculation methods in each of these simulation scenarios separately to shed light on which fibrosis remodeling aspects can be accurately captured by the simplified model solutions.

In the simulation setup described above, neither motion nor contraction of the atria were considered for the sake of reducing model complexity and computational cost. Moss *et al.* showed that a fully coupled electro-mechanical model does not have any influence on simulation results regarding atrial activation and that resulting P waves exhibit negligible differences to the ones computed on a non-deforming model [165]. However, the atrial repolarization results of this study might be affected to a larger extent by the lack of a coupled model as previous studies reported a substantial impact of mechanical feedback on electrophysiological behavior in the ventricles [166, 167], especially during the repolarization phase [165, 168].

CVs were derived from the values reported in [140]. Based on them, conductivities were computed using *tuneCV* [100] as described in section 4.2.1 using strand meshes. However,

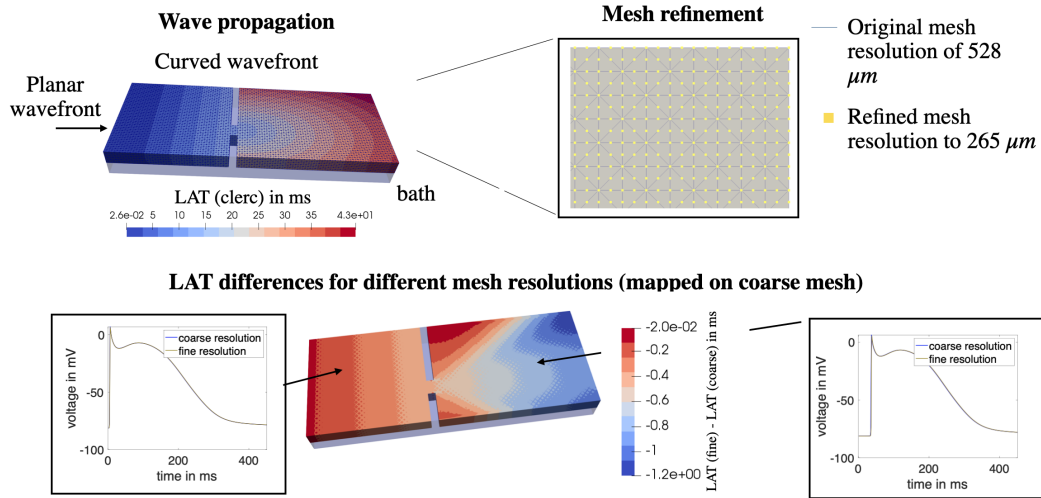


**Figure 4.12: Experiment for quantifying the error in LATs due to a coarser mesh resolution in the bidomain model.** The top panel shows the  $5\text{ cm} \times 2\text{ cm} \times 2.8\text{ mm}$  block mesh with a resolution of  $528\ \mu\text{m}$ . The mesh resolution on the same geometry was refined to  $265\ \mu\text{m}$  by linearly subdividing the tetrahedral elements (top right panel). The excitation was initiated by pacing from the left side of the block. When the planar wave passes through the isthmus, it propagates with a curved wavefront onwards. The bottom panel shows the signed LAT differences between the nodes in the coarse and the fine mesh. Two action potentials at nodes on the right and the left end of the block are visualized for the fine and the coarse resolution mesh.

no bath loading effects, mesh and wavefront curvature were considered when tuning the CVs, which might lead to mismatching CVs and conductivities assigned to different regions in the more complex atrial geometry. Adding a bath in the experiments set up for the tuning process could lead to more similar LAT and ECG results between the bidomain results with Clerc and Roberts conductivities on the bi-atrial geometry. Moreover, performing the tuning with a bath attached to the strand geometries would lead to different monodomain conductivities for the setups without explicit conductivity tuning while the conductivity values in case of explicit conductivity tuning for the monodomain simulation would remain unchanged. Conductivities in transverse and longitudinal direction needed to be scaled by a factor of 54 and 12, respectively. The tuning procedure caused the original transversal vs. longitudinal conductivity ratios reported by Clerc and Roberts *et al.* to change while keeping intra- vs. extracellular conductivity ratios constant.

The average edge length of the atrial geometry was  $523\ \mu\text{m}$ . To quantify the numerical error arising due to the mesh resolution, additional experiments were conducted on a  $5\text{ cm} \times 2\text{ cm} \times 2.8\text{ mm}$  block mesh with a resolution of  $528\ \mu\text{m}$  and a refined resolution of  $265\ \mu\text{m}$  by linearly subdividing the elements (see Figure 4.12, top panel).

Using the same numerical settings as for the experiments on the bi-atrial geometry, a simulation of a planar wave passing through an isthmus and then propagating with a curved wavefront was run. Conductivities were adjusted using *tuneCV* [100] as described in section 4.2.1 to the CV in the regular atrial bulk tissue region. Maximum LAT differences

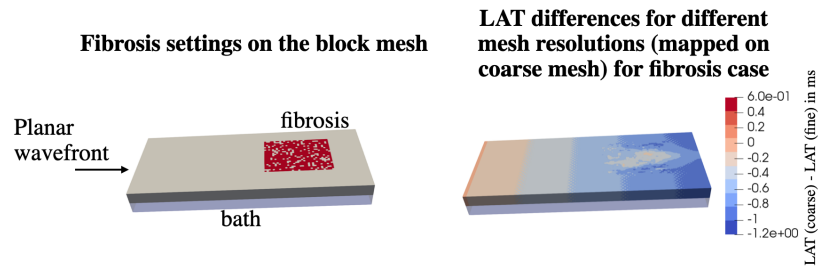


**Figure 4.13: Experiment for quantifying the error in LATs due to a coarser mesh resolution in the bidomain model in case of fibrotically infiltrated tissue.** The left panel shows the model setup with a fibrotic patch of 80% density and a planar wave propagating along the block. The right panel shows the color-coded differences in LATs for the coarse and the fine mesh.

between the experiments on the coarse and the fine mesh were 1.2 ms. Considering the total activation time in the block of 43 ms, the error introduced by the coarse mesh resolution was 2%. The root mean squared errors between two APs resulting from the simulations on the coarse and the fine mesh were 0.0186 mV and 0.0491 mV for the two nodes marked in Figure 4.12. When adding a fibrotic region to the block, the maximum absolute LAT error between the experiments on the fine and the coarse mesh was 1.2 ms ( $\sim 2\%$ ) as well (see Figure 4.13) for a planar wave propagating along fiber direction. The latter is approximately also the case in the bi-atrial simulation setup where the depolarization wavefront traverses the elliptically shaped fibrotic patches along their main axis growing predominantly in fiber direction. However, if a notable transverse wave propagation had to be represented, the chosen mesh resolution of  $523\mu\text{m}$  would have been too coarse to capture the wave propagation at a velocity of 0.15m/s. Thus, the mesh resolution chosen for the atrial model in this study might introduce an error of 2%, which is equivalent to an absolute LAT error of  $\sim 2$  ms on the bi-atrial mesh. Due to the small root mean squared error between the APs of the coarse and the fine mesh, no additional discretization error affecting  $\text{APD}_{90}$  is expected.

## 4.5 Conclusion

The results presented in this chapter show that the Eikonal model is capable of faithfully producing LATs and P waves compared to full bidomain simulations with a reduction of computation times by a factor of up to three orders of magnitude. However, propagation models neglecting diffusion terms lack the fidelity in terms of repolarization as shown by  $\text{APD}_{90}$  deviations. Thus, RE models are needed, e.g., in cases where repolarization dynamics are of significant importance such as e.g. for re-entry mechanism studies. ECGs calculated with the BEM accurately resemble the FEM results for both P waves and the ECG in the repolarization phase. When computing ECGs with the IVC method, the systematic overestimation of peak-to-peak P wave amplitudes especially in the precordial leads should be taken into account when evaluating P wave features.



---

PART III

---

MULTI-SCALE GENERATION OF  
VIRTUAL COHORTS OF  
COMPUTATIONAL MODELS



---

# Development and Evaluation of a Bi-atrial Statistical Shape Model

In this chapter, the construction and evaluation of a bi-atrial statistical shape model (SSM) as well as the generation of simulation-ready volumetric atrial geometries based thereon are described.

*The content of this chapter is taken from a paper that has been published open access under licence CC-BY 4.0 in Medical Image Analysis [169]. Most passages have been quoted verbatim from the publication.*

## 5.1 Introduction

A wide range of machine learning approaches have already been proposed for classifying cardiovascular pathologies based on the 12-lead electrocardiogram (ECG) [24, 170–172]. The limitations in clinically recorded data [21, 24, 173–175] for training purposes of such a classifier as explained in section 1.1 call for simulated synthetic ECG as a source for large, representative and well controlled datasets. These datasets can be used to directly deduce diagnostic criteria visually [176] or to train machine learning classifiers to discriminate between different cardiac diseases and healthy individuals [47, 177]. The advantage of using simulated over clinical data lies not only in the precisely known ground truth of the underlying pathology that was defined for the simulation, but also in the possibility to generate a virtually infinite amount of signals for each pathology class.

Nevertheless, atrial, ventricular and thoracic geometrical models are needed for conducting electrophysiological simulations to obtain the 12-lead ECG. In this regard, SSMs allow to compile a wide range of realistic geometries that represent the variability observed in the cohort used to build the model. While SSMs of the human ventricles [178] and torsos [179] exist and are publicly available, an open shape model of both atria covering all

relevant anatomical structures for electrophysiological simulations (atrial body, appendages, pulmonary veins (PVs)) is still lacking to date to the best of our knowledge.

Table 5.1.: Previously published statistical shape models of the human atria.

| Model                           | Chambers     | Number of subjects                                             | Comment                                                   |
|---------------------------------|--------------|----------------------------------------------------------------|-----------------------------------------------------------|
| Corrado <i>et al.</i> [180]     | left atrium  | 130 MR segmentations of AF patients                            | left atrial appendage excluded                            |
| Biegging <i>et al.</i> [66]     | left atrium  | 254 MR segmentations of AF patients (DE-CAAF study [181])      |                                                           |
| Cates <i>et al.</i> [182]       | left atrium  | 137 MR segmentations of AF patients                            | spatial resolution reduced to 1,024 correspondence points |
| Depa <i>et al.</i> [183]        | left atrium  | 16 MR segmentations                                            |                                                           |
| Varela <i>et al.</i> [184]      | left atrium  | 144 MR segmentations of AF patients                            | left atrial appendage excluded                            |
| Rodero <i>et al.</i> [185]      | four chamber | 19 MR segmentations of asymptomatic individuals                | left atrial appendage excluded                            |
| Ecabert <i>et al.</i> [186]     | four chamber | 28 MR segmentations at different cardiac phases of 13 patients |                                                           |
| Hoogendoorn <i>et al.</i> [187] | four chamber | 138 CT segmentations                                           |                                                           |
| Loijonen <i>et al.</i> [188]    | four chamber | 25 MR segmentations of healthy subjects                        |                                                           |
| Ordas <i>et al.</i> [189]       | four chamber | 100 CT segmentations of healthy and pathological subjects      |                                                           |
| Unberath <i>et al.</i> [190]    | four chamber | 20 CT segmentations                                            | 4D statistical shape model including cardiac contraction  |
| Zhuang <i>et al.</i> [191]      | four chamber | 37 MR segmentations                                            |                                                           |

Different statistical atlases of the human whole heart anatomy [185–191] have been constructed for segmentation of magnetic resonance (MR) or computed tomography (CT) images by means of active shape modeling approaches and are summarized in Table 5.1. However, those models are usually built based on a small number of sample segmentations or were not made publicly available. Furthermore, different SSMs of only the left atrium (LA) have been presented in various studies either for the purpose of simulations [180] or for characterizing changes in shape of the LA [66, 182–184] in patients with atrial fibrillation (AF). These LA models are built based on a solid number of instances, but lack the right atrium (RA) and often also the left atrial appendage (LAA). However, these anatomical structures are not only indispensable for the use case of ECG simulations. They are also of particular importance when investigating the mechanisms of typical atrial flutter in the RA or bi-atrial flutter and fibrillation. Additionally, the LAA is highly relevant for studies examining blood clot formation causing stroke [192], LAA occlusion as potential therapy [193] and the role of the LAA in the onset and maintenance of AF [194].

Due to the lack of ready-to-use models of the atria, a bi-atrial SSM would cater the need of generating geometrical atrial models representing inter-subject anatomical variability. These could be employed to gain a comprehensive understanding of the underlying mechanisms of the onset and perpetuation of re-entrant activity during atrial flutter and fibrillation not only in personalized computer models [33, 195–197] but also in a large patient cohort [54, 198]. Thus, including the shape of the RA in the model as well as making the bi-atrial SSM available to the community, enables large-scale simulation of atrial signals. Although the focus of the work presented in this chapter is the application of the SSM for ECG simulations, its field of application is not limited to this particular use case. The bi-atrial model can also be exploited for other *in silico* approaches like continuum-mechanics and fluid simulations. Furthermore, active shape modeling approaches [199] using the novel bi-atrial SSM could facilitate automated segmentation of the atria from CT or MR datasets.

In this chapter, the development of an SSM comprising both atria based on manual segmentations of 47 CT and MR scans is described. Furthermore, a workflow to generate a volumetric atrial model based on an instance derived from the SSM is proposed. A major added value of this work for the community is the provision of the bi-atrial SSM under the creative commons license CC-BY 4.0 together with 100 exemplary volumetric models derived from it including fiber orientation, inter-atrial bridges, material tags and solutions to Laplace’s equation [200].

## 5.2 Methods

The geometric representation as well as the variation in shape among a set of individual three dimensional objects can be described by SSMs (see section 3.2 and Figure 3.2). Point distribution models [109] are the most common subclass of SSMs and require a vectorized point-based representation  $\mathbf{s}_n$  of any individual geometry  $\Gamma_n$  comprising  $M$  consistently

sampled surface points  $[\mathbf{x}_n, \mathbf{y}_n, \mathbf{z}_n]^T$ :

$$\mathbf{s}_n = [x_{n,1}, y_{n,1}, z_{n,1}, \dots, x_{n,M}, y_{n,M}, z_{n,M}]^T \quad (5.1)$$

Assuming that the spatial variations of the surface points follow a multivariate normal distribution, a compact representation of the sample mean and sample covariance matrix describing the shape variations can be obtained by applying a principal component analysis (PCA) to the observations  $\mathbf{s}$  (see section 3.3 for further details). In this way, all  $N$  individual shapes  $\Gamma$  can be represented by a linear combination of  $N - 1$  basis functions  $\mathbf{v}$ :

$$\mathbf{s}_n = \bar{\mathbf{s}} + \sum_{k=1}^{N-1} r_{n,k} \cdot \sigma_k \cdot \mathbf{v}_k, \quad (5.2)$$

with  $\bar{\mathbf{s}}$  being the mean shape vector as well as  $\sigma$  and  $\mathbf{v}$  representing the eigenvalues and eigenvectors of the covariance matrix, respectively.  $r_{n,k}$  represent the weighting coefficients for the individual eigenvectors. To obtain this parametric representation of the shape variations from clinical MR or CT data, a number of preprocessing steps have to be performed (see Figure 3.2 and Figure 5.1): i) segmenting the images, preferably in a (semi-)automatic manner, ii) rigidly aligning the resulting shapes in space, iii) establishing a dense correspondence between the individual shapes to obtain the shape vectors  $\mathbf{s}^C$  that were then subject to PCA.

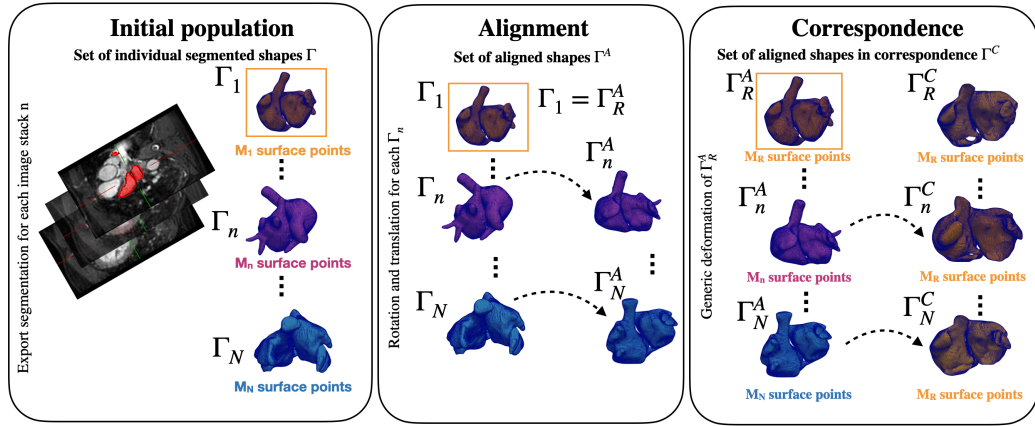


Figure 5.1: Construction of a statistical shape model of the atria.

### 5.2.1 Acquisition of the Initial Model Population

Three independent multi-center, multi-vendor databases [201–203] were used to build the SSM. Their properties are summarized in Table 5.2. The images originate either from healthy subjects or from patients suffering from AF. Since all of the challenges focused on the

**Table 5.2:** Summary of datasets used to generate the statistical shape model.

| Dataset | Source                                                     | Number of subjects | Voxel resolution                           |
|---------|------------------------------------------------------------|--------------------|--------------------------------------------|
| 1       | Left atrium segmentation challenge [203]                   | 30 MRI             | 1.25 x 1.25 x 2.7 mm                       |
| 2       | Left atrium fibrosis and scar segmentation challenge [201] | 8 MRI              | 1.25 x 1.25 x 2.5 mm<br>1.4 x 1.4 x 1.4 mm |
| 3       | Left atrial wall thickness challenge [202]                 | 9 CT               | 0.8 x 1 x 0.4 mm                           |

segmentation of the LA, 23 of the originally available images had to be excluded due to an incomplete capture of the inferior right atrial body or an inadequate signal-to-noise ratio. Since a PCA description was relied on for representing the atrial shape variability with which only continuous changes of vertex locations are representable, only subjects with 4 PVs were considered. The number of PVs attached to a subject's atrium is discrete and the absence or the presence of an additional PV is not characterized by a continuous transition which is why only data samples of patients with 4 PVs were included in this study. According to Marom *et al.* [204], this PV configuration is representative for the majority of the population with 71 % and 86 % of all subjects in their study exhibiting two ostia on the right and left side of the LA body, respectively.

In order to obtain the individual instances of both atria, a semi-automatic segmentation of the blood pool representing the endocardial surface of the left and the right atrium from MR and CT images was performed using CemrgApp [205]. 2D region growing in several selected slices as well as 3D interpolation were applied to each image stack. To reduce the impact of noise or image artefacts on the segmentation outcome, details were manually corrected. Figure 5.2 shows examples of incorrect segmentation results due to insufficient region growing performance (left column) and 3D interpolation (middle column) that made a manual correction indispensable. Automated segmentation with region growing especially failed in 2D planes where both the LA and the left ventricle are visible, as the mitral valve exhibits the same image intensity as the LA and the left ventricle. Therefore, a cutting plane between atrium and ventricle was inserted manually. The drawbacks of 3D interpolation were particularly affecting the areas around the PVs where the interpolated surface tends to close small gaps between the PVs and the atrial body. For 20 images in dataset 2, a segmentation of the LA was provided. However, the LAA was truncated in close proximity to the left atrial body [203] in these segmentations. Since the variability of the LAA shape was aimed to be incorporated in the model, the LA segmentations of dataset 2 were adapted to include the full volume of the LAA as shown in Figure 5.2 (right column). The resulting segmentations were exported as triangular meshes.

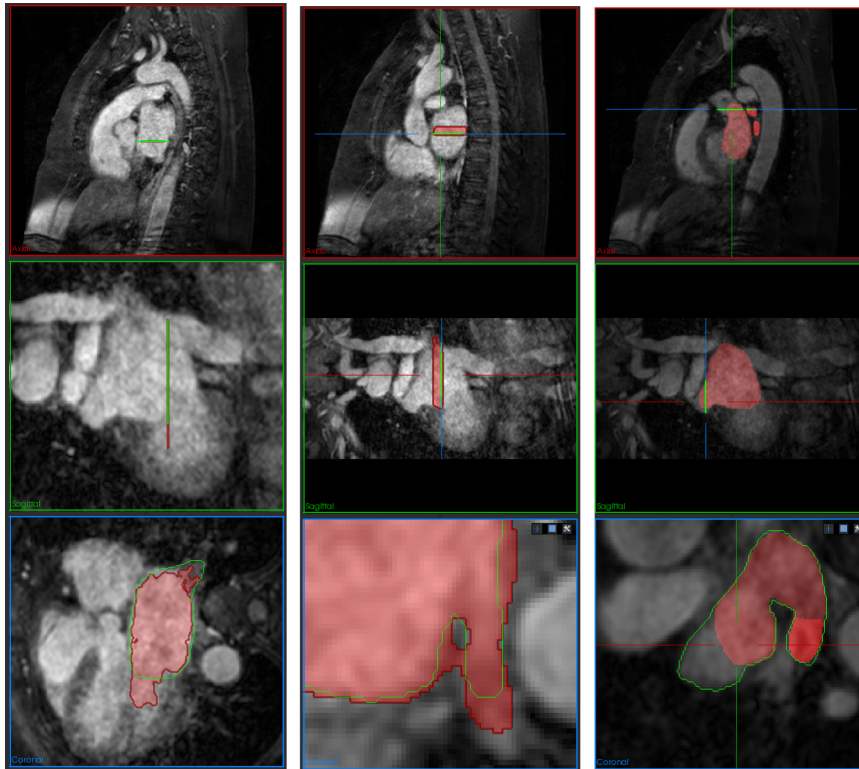


**Figure 5.2:** Segmentation inaccuracy due to different automated segmentation methods. The different rows represent the axial, sagittal and the coronal plane, respectively. The images in the left, middle and right column show the segmentation errors due to region growing, 3D interpolation and a partly excluded LAA in the ground truth data colored in red, respectively. The green contours mark the manual corrections tailored to the correction of inaccurately found automated segmentations.

### 5.2.2 Rigid Alignment

After segmenting the individual instances  $\Gamma_n$  of the atria, the resulting isosurfaces exported from CemrgApp were rigidly aligned in space to avoid a representation of translation and rotation parameters in the eigenmodes of the SSM [206]. This was performed automatically by means of the iterative closest point (ICP) algorithm that provides a solution to the orthogonal Procrustes problem [110]. Surface-to-surface distances were calculated with the *vtkDistancePolyDataFilter* (Kitware, Clifton Park, New York, USA) between each pair of individual instances  $\Gamma_n$ . The reference template was chosen as the surface holding the smallest mean distance to all other instances (compare Figure 5.3).

In each iteration  $i$ , candidate correspondences  $[\hat{x}_n, \hat{y}_n, \hat{z}_n]_{R,i}^T$  between a target mesh  $\Gamma_n$  and the reference mesh  $\Gamma_R$  were found by attributing the point with the smallest Euclidean distance in  $\Gamma_R$  to each node in  $\Gamma_n$ . Procrustes analysis was then used to estimate the linear transformation  $T_i$  – consisting of rotation and translation – which yields the best match of the candidate correspondence points  $[\hat{x}_n, \hat{y}_n, \hat{z}_n]_{R,i}^T$  with the reference points  $[x_R, y_R, z_R]^T$ . After applying the estimated transformation  $T_i$  to the points in mesh  $\Gamma_n$ :

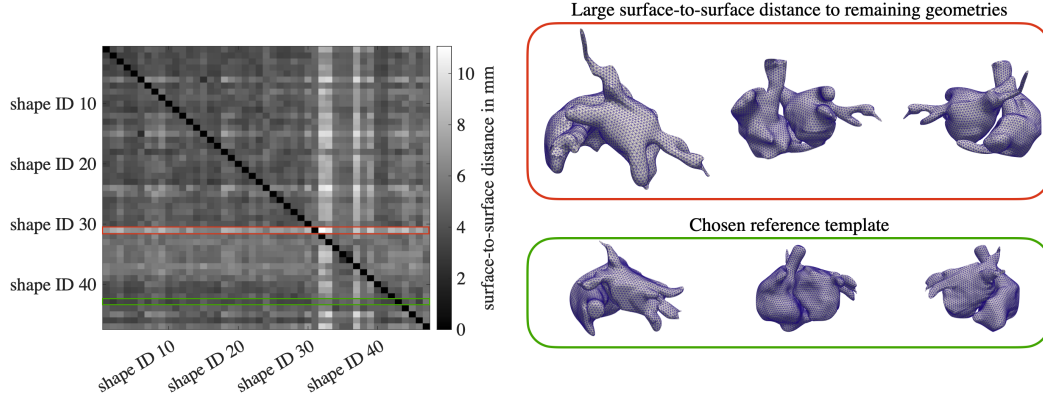


**Figure 5.3:** Surface-to-surface distance of each pair of individual instances. The green surface held the smallest mean distance to the remaining atria in the dataset and was chosen as a reference for the alignment and morphing process. The red boxed geometry outlines an example in three different views of an instance holding a notably larger surface-to-surface distance to the other data samples.

$$\tilde{\Gamma}_{n,i+1} = \mathbf{T}_i \cdot \tilde{\Gamma}_{n,i}, \quad \text{with } \tilde{\Gamma}_{n,0} = \Gamma_n, \quad (5.3)$$

new candidate correspondences  $[\hat{\mathbf{x}}_n, \hat{\mathbf{y}}_n, \hat{\mathbf{z}}_n]_{R,i+1}^T$  are recursively found between the transformed mesh  $\tilde{\Gamma}_{n,i+1}$  and  $\Gamma_R$  at each iteration  $i$  and used for solving the Procrustes problem. If after several recursive calls of the function, either the maximum number of 150 iterations is exceeded or the convergence criterion is fulfilled, an optimal transformation matrix for the alignment of both shapes  $\Gamma_n$  and  $\Gamma_R$  is found resulting in a set of  $N$  rigidly aligned shapes  $\Gamma^A$ .

### 5.2.3 Dense Correspondence Retrieval

Each aligned individual instance  $n$  comprises  $M_n$  surface points  $[x_{n,1}^A, y_{n,1}^A, z_{n,1}^A, \dots, x_{n,M_n}^A, y_{n,M_n}^A, z_{n,M_n}^A]^T$ . In order to describe the variations in shape of the aligned instances  $\Gamma^A$  by means of a point distribution model, correspondence between the vertex IDs among all individual shapes have to be established. Establishing correspondence requires to retrieve concordant points in all shapes  $\Gamma^A$ , so that the  $N$  aligned shapes are not only represented by the same amount of surface points  $M$  but also that each point  $[x_{n,m}^A, y_{n,m}^A, z_{n,m}^A]$  with a specific ID  $m$  represents the same morphological point in any arbitrary shape  $n$ . For this purpose, Gaussian process morphable models (GPMMs) [111] available as a built-in library in Scalismolab [207] were used to subject a reference shape  $\Gamma_R^A$  to a generic deformation in such a way that the deformed shape  $\tilde{\Gamma}_{R,n}^A$  matches the individual aligned shape  $\Gamma_n^A$  in the best possible way. This process then yields a set  $\Gamma^C$  of aligned shapes that are characterized by homologous, corresponding surface points. For this process, three independent generic deformations were defined by Gaussian process (GP) models. Gaussian kernels described the similarity between two distinct points  $\mathbf{x}$  and  $\mathbf{x}'$ :

$$k(\mathbf{x}, \mathbf{x}') = s \cdot \exp\left(-\frac{(\mathbf{x} - \mathbf{x}')^2}{l^2}\right) \quad (5.4)$$

The kernels were approximated by the leading eigenfunctions of their Karhunen-Loève expansion as described in [111]. They were further employed to fit the orientation of the left and right pulmonary veins (LPV, RPV), the atrial body, as well as the LAA and right atrial appendage (RAA). The separation into three different models (atrial body, appendages, PVs) served two different purposes. On the one hand, the high anatomical variability of the appendages could be accounted for by allowing smaller inter-dependencies spanning between the points located on the appendages. On the other hand, the generic model varying the points located on the PVs was designed such that only the orientation of the PV ostia but not their length was affected. Built-in functions of Scalismo [207] were used to successively fit the three anatomical regions of each aligned observation  $\Gamma_n^A$  with a custom PV model and a generic deformation for the appendages and the atrial body. The optimization problem of fitting the GP model  $\tilde{\Gamma}_{R,n}^A$  to the individual aligned shapes  $\Gamma_n^A$  was solved using the *Registration* built-in class in Scalismo with a limited-memory Broyden-Fletcher-Goldfarb-Shanno (L-BFGS) optimization [208, 209] minimizing the mean squared error between the vertex coordinates of the deformed model  $\tilde{\Gamma}_{R,n}^A$  and the target shape  $\Gamma_n^A$ . To accurately fit the PVs, a kernel representing the orientation of the four PVs in anterior-posterior direction in its first four eigenvectors was constructed (Figure 5.4). This custom kernel was built by manually moving each of the four PVs of the reference shape  $\Gamma_R^A$  in two different directions at a time using Meshmixer (Autodesk, San Rafael, CA, USA). Disabling the mesh refinement option during this process ensured that the resulting eight shapes differed from one another only in their PV orientation and were in correspondence. Therefore, they could directly be applied to construct the custom PV model (Figure 5.4). The length of the PVs was intentionally not fitted since this quantity highly depends on the segmentation approach and does therefore not represent a proper observed anatomical variation considering the heterogeneous input data used in this study. A low rank approximation of a GP model was realized using the *LowRankGaussianProcess* class in Scalismo with an empirically chosen variance of  $s_b = 50, l_b = 40$  at points representing the general atrial body ( $b$ ) and  $s_a = 20, l_a = 20$  at the appendages to account for the higher anatomical variability in the appendage ( $a$ ) regions.

### 5.2.4 Principal Component Analysis

The vertices at the distal parts of the superior and inferior caval veins, the coronary sinus, the PVs, as well as the mitral valve and the tricuspid valve were discarded from the  $N$  aligned shape vectors in correspondence  $\mathbf{s}^C$  to limit the model creation to atrial components relevant for electrophysiological simulations. Applying a PCA to these cut shape vectors in correspondence  $\mathbf{s}^C$  yields their mean shape  $\bar{\mathbf{s}}$  and  $N - 1$  basis functions  $\mathbf{v}$  along with their respective variances  $\sigma^2$ . In this way, an exact reconstruction of any individual shape instance  $\Gamma_n^C$  is feasible by determining the coefficients  $\mathbf{r}_n$  in equation 5.2 with an ordinary least squares

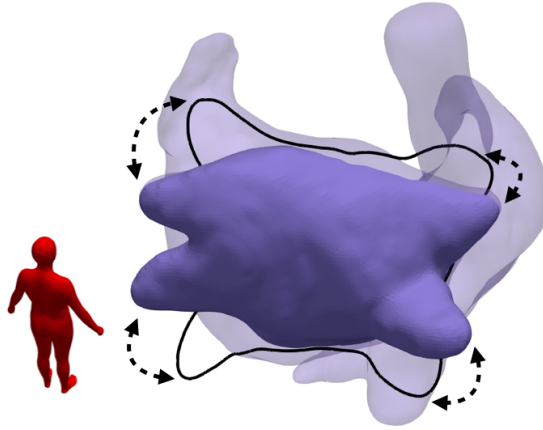


**Figure 5.4:** Morphable model for establishing correspondence at the PVs. The arrows indicate the movement of the respective vertices in the model for a variation of the four leading eigenvectors by  $-3\sigma$  and  $+3\sigma$ . The LA body and the RA shape are not affected by this PV model and are visualized in a semi-transparent manner.

estimation. Furthermore, additional arbitrary variation shapes  $\mathbf{\Gamma}_{var}$  in the span of the  $N - 1$  basis vectors  $\mathbf{v}$  can be derived by varying  $\mathbf{r}$ . Under the assumption that the values of  $\mathbf{r}$  are normally distributed among the observed instances  $\mathbf{\Gamma}_n^C$ , keeping  $\mathbf{r}$  in the interval  $[-3, +3]^{N-1}$  yields realistic artificially generated shapes within the empirically observed variability.

### 5.2.5 Generation of Arbitrary Volumetric Atrial Models

The bi-atrial SSM represents the mean shape of the atrial endocardial surface and the variation of all point coordinates in space so that any arbitrary variation mesh  $\mathbf{\Gamma}_{var}$  can be derived from it. However, a volumetric model of the atria, including inter-atrial bridges, anatomical labels and fiber orientations is required to perform electrophysiological simulations and to obtain realistic body surface P waves. A workflow was developed (see Figure 5.5) to fully automatically create a volumetric model based on an arbitrary endocardial surface. Since a segmentation of the epicardial surface from conventional MR images is usually not feasible due to an insufficient spatial resolution and a limited signal to noise ratio, the epicardial surface was augmented in a postprocessing step assuming a homogeneous atrial wall thickness.

To approximate the epicardial surface, the endocardial surface of the variation mesh  $\mathbf{\Gamma}_{var}$  was dilated by 3 mm [210] at each point along the normal direction calculated as the mean of the adjacent triangle normals. Both surfaces were merged and intersections and holes between epi- and endocardium were corrected and closed automatically using the iso2mesh toolbox [211]. The closed surface was afterwards remeshed using Instant Meshes [131] and transformed into a volumetric tetrahedral mesh with an average edge length of 1 mm using Gmsh [212]. Contact and integrity between left and right atrium were preserved by

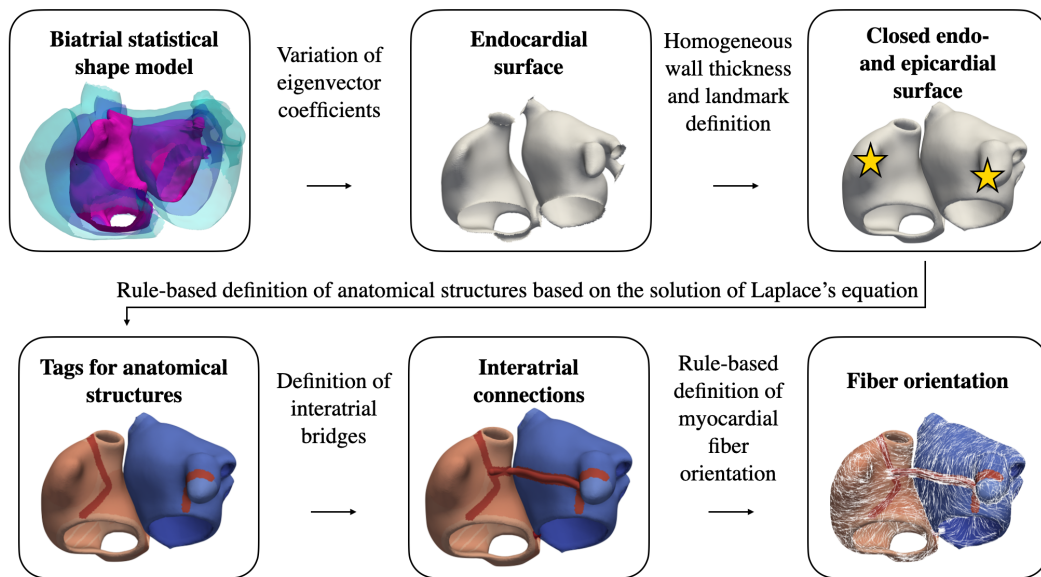


**Figure 5.5: Workflow for augmenting an endocardial surface derived from the statistical shape model with tags for anatomical structures, interatrial connections and myocardial fiber orientation.**

duplicating the epicardial nodes belonging to the septum in regions where the left and the right epicardial surfaces spatially overlapped. The affected endocardial nodes were subsequently moved in negative direction of the surface normals to ensure a homogeneous wallthickness of 3 mm. The algorithms described by Azzolin *et al.* [195], Piersanti *et al.* [135] and Wachter *et al.* [213] were used to automatically augment the models with Bachmann's bundle, a coronary sinus and an upper and middle posterior inter-atrial connection between the LA and RA as well as myocardial fiber orientation and anatomical labels. The augmented anatomical structures are visualized in Figure 5.5. The only manual input required for augmenting the volumetric geometry with the aforementioned structures consists of 4 seed points defining the tips of the appendages and landmarks for the Bachmann's bundle connection. They were defined once on the mean shape and were tracked through the deformations for any arbitrary variation mesh. In this way, it was ensured that the seed points were consistently chosen among all variation meshes.

## 5.2.6 Parameterization of Electrophysiological Simulations

100 random instances were derived from the bi-atrial SSM by drawing the eigenvector coefficients  $\mathbf{r}$  of Eq. 5.2 from a Gaussian distribution in the  $[-3, +3]\sigma$  range. A fast iterative simulation was carried out for solving the Eikonal equation on these 100 geometries to obtain the spread of electrical activation and derive local electrical activation times for each node. Sinus rhythm activation was initiated from a sinus node exit site located at the junction of the superior caval vein and the RAA [149]. The atrial wall was separated into seven different anatomical regions: regular right and left atrium, inter-atrial connections, valve

**Table 5.3:** Conduction velocity (CV) along the transversal fiber direction in mm/s and anisotropy ratios (AR) in different atrial regions.

| Atrial Region            | CV <sub>⊥</sub> (mm/s) | AR   |
|--------------------------|------------------------|------|
| Right atrium             | 739                    | 2.11 |
| Left atrium              | 946                    | 2.11 |
| Inter-atrial connections | 1093                   | 3.36 |
| Valve rings              | 445                    | 2.11 |
| Pectinate muscles        | 578                    | 3.78 |
| Crista terminalis        | 607                    | 3.0  |
| Inferior isthmus         | 722                    | 1    |

rings, pectinate muscles, crista terminalis and inferior isthmus. The conduction velocity (CV) along the fiber directions and the anisotropy ratio in the different regions were chosen as reported previously [149] and are given in in Table 5.3.

### 5.3 Results

The bi-atrial SSM is provided under the Creative Commons license CC-BY 4.0 together with 100 exemplary volumetric models derived from it including fiber orientation, inter-atrial bridges and anatomical labels [200]. Furthermore, solutions to Laplace’s equation with various boundary conditions as proposed by Piersanti *et al.* [135] are provided to facilitate the derivation of universal atrial coordinates [214]. The SSM is available as an h5 file encoding information about the mean shape’s spatial vertex locations and their triangulation. Also the eigenvectors and -values resulting from applying the PCA are included. The 100 geometries were generated by sampling the eigenvector coefficients  $\mathbf{r}$  from a Gaussian distribution in the  $[-3, +3]\sigma$  range. These anatomical models are provided in VTK file format including fiber orientation as 3D vectors and material tags as scalar values in the cell data section.

The shape statistics in the SSM resulting from applying PCA to the individual instances in correspondence are quantitatively shown in section 5.3.1. Furthermore, three standard evaluation criteria for evaluating the SSM quality proposed by Davies *et al.* [64] were considered: generalization, specificity, and compactness. The *generalization* metric addressed in section 5.3.3 refers to the ability of the SSM to recreate an instance whose shape vector was excluded from the dataset used to create the SSM. The *specificity* metric (section 5.3.4) assesses the goodness of the model in terms of generating realistic shapes. Furthermore, the *compactness* (section 5.3.5) metric of the model increases the more the set of eigenvectors can be reduced while still being able to describe the majority of the total shape variance present in the dataset.

**Table 5.4:** Summary of datasets used to generate the statistical shape model.

| Eigenmode | Most prominent shape changes                                                                                                                                   |
|-----------|----------------------------------------------------------------------------------------------------------------------------------------------------------------|
| 1         | total volume for both atria                                                                                                                                    |
| 2         | asymmetric prominence of both appendages<br>asymmetry of the left and right atrial volume<br>relative position of the left and right atrium towards each other |
| 3         | relative orientation of the left pulmonary veins towards each other<br>relative orientation of the left and right atrium towards each other                    |
| 4         | distance between the left and right atrium<br>tilt angle of the appendages                                                                                     |
| 5         | symmetric prominence of both appendages<br>pointedness of the right appendage                                                                                  |
| 6         | orientation of the right superior pulmonary vein<br>volume of the left atrium                                                                                  |
| 7         | volume of the left atrial appendage                                                                                                                            |
| 8         | orientation of the right pulmonary veins                                                                                                                       |

### 5.3.1 Shape Statistics

Applying a PCA to the cut shape vectors in correspondence  $s^C$  as described in section 5.2.4 yields their mean shape  $\bar{s}$  comprising 62,818 triangular cells and 31,745 vertices with an average edge length of 0.929 mm. Furthermore, the eigenvectors and eigenvalues of the bi-atrial model were obtained. Figure 5.6 shows the shape changes caused by varying the coefficients of the first eight eigenvectors. A qualitative description of the most prominent shape changes encoded in each of the eigenmodes – as outlined in grey in Figure 5.6 – is listed in Table 5.4.

### 5.3.2 Correspondence

The quality of the bi-atrial SSM was evaluated by assessing the mean vertex-to-nearest neighbor distances between the meshes in correspondence and their respective original node locations. For the 47 meshes used to build the SSM, this mean distance across the dataset was  $1.60 \pm 0.25$  mm. The mean vertex-to nearest neighbor distance per atrial region is visualized for all instances in Figure 5.7. The smallest morphing errors occurred in the appendages. In the bottom panel of Figure 5.7, two examples for a small and a large surface-to-nearest neighbor distance in the left atrium are visualized.

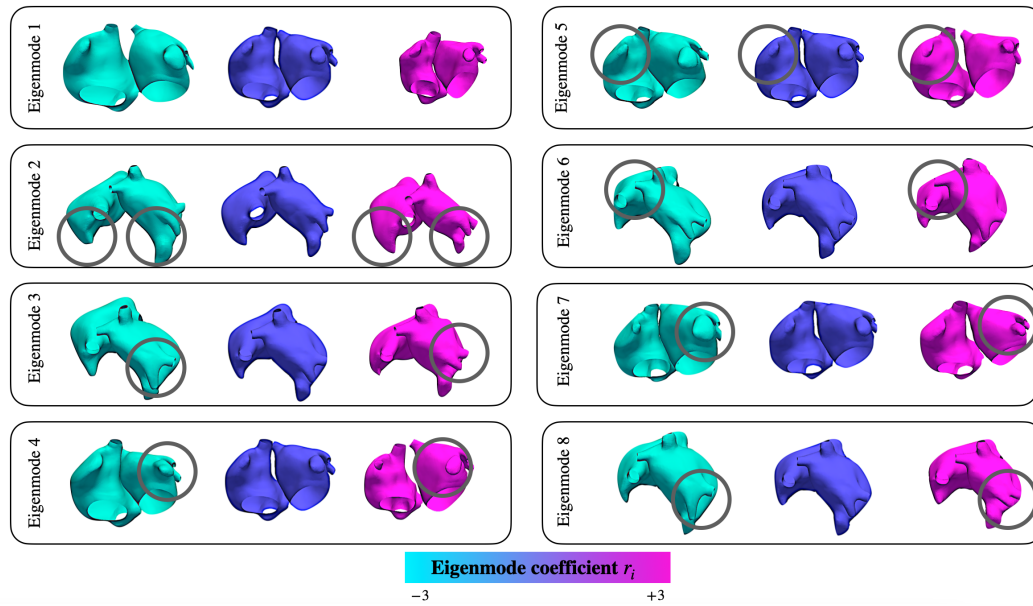


Figure 5.6: Eigenmodes of the bi-atrial shape model. The eight leading eigenmodes are displayed. The different colors represent the applied eigenvector coefficients which were varied for each mode independently.

### 5.3.3 Generalization

To evaluate the generalization quality of the SSM, leave-one-out cross-validation was used and  $N$  datasets with  $N - 1$  meshes each were defined by leaving out the final observation. Each of those was used to compute a reduced SSM. The excluded shape was reconstructed with the reduced SSM by determining the eigenvector coefficients using ordinary least squares. The similarity between the original excluded shape and the approximated one was assessed in terms of the Euclidean distance between the corresponding vertices. Figure 5.8 shows the distribution of this error metric for all instances in the dataset. The median of the vertex to vertex distance was below 1.56 mm among all shapes which compares to the order of magnitude of the MRI cross-plane resolution (0.4 mm - 2.7 mm). Instance 4, 11 and 43 hold the lowest Euclidean distances between the vertices of its original and reconstructed shape, whereas instance 47 is characterized by considerably high error values. Especially the 75th and the 95th percentile bounds comprise large vertex to vertex distances. Vertices showing larger deviations were located predominantly on the anterior wall and the appendages of both atria (compare Figure 5.8).

### 5.3.4 Specificity

The specificity of the bi-atrial model was evaluated by generating 1000 random shapes according to Eq. 5.2 by uniformly sampling  $\mathbf{r}$  in the interval  $[-3, 3]$ . The similarity between

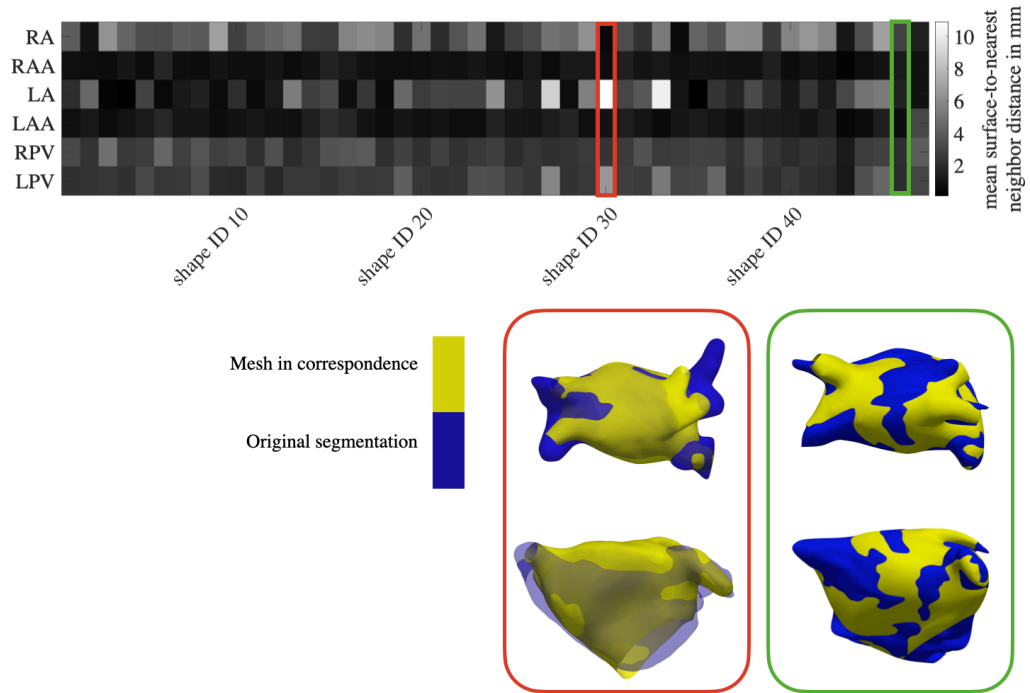


**Figure 5.7: Correspondence results.** Surface-to-nearest neighbor distance in mm evaluated per region between the surfaces in correspondence and the original segmentation. Two examples for large and small correspondence retrieval errors (red and green boxes, respectively) are visualized in the bottom panel for the segmented left atrium (blue surface) and the morphed template (yellow surface). RA: right atrium, RAA: right atrial appendage, LA: left atrium, RPV: right pulmonary veins, LPV: left pulmonary veins.

these random shapes and the respective closest shapes in the underlying dataset  $\Gamma^C$  used to build the SSM was assessed in terms of the root mean squared error (rmse) of all vertex-to-vertex distances between the randomly generated and the original shape. The rmse ranged from 4.65 to 10.83 mm among all 1000 random instances with a mean  $\pm$  standard deviation of  $7.79 \pm 1.00$  mm.

### 5.3.5 Compactness

Figure 5.9 depicts the total variance of the dataset explained by the model when including only a limited number of leading eigenvectors. 90 and 95% of the total shape variance in the individual segmented shapes can be covered by the SSM when considering only the first 18 and 24 eigenvectors, respectively.

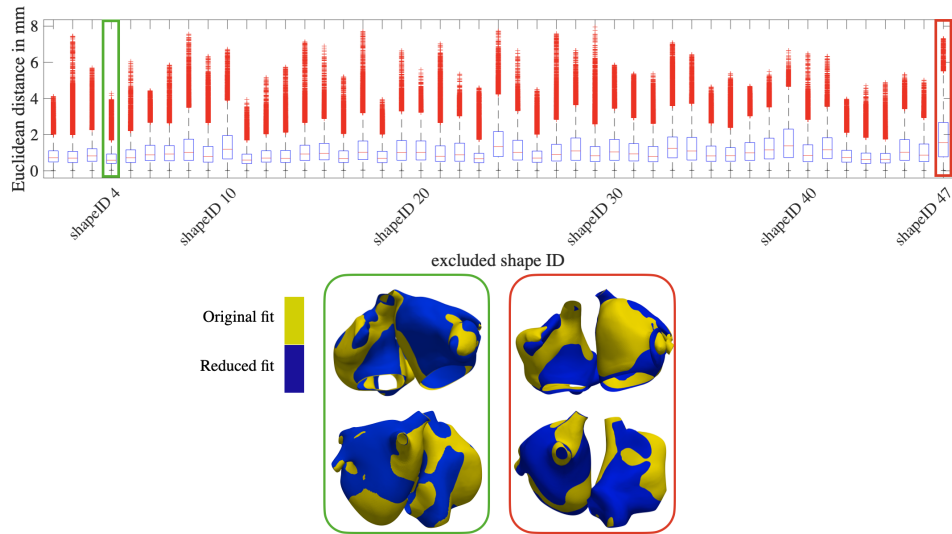


**Figure 5.8:** Euclidean distance between vertices of the original and reconstructed shapes in mm. Two examples for small and large Euclidean distances (green and red box, respectively) are shown in the bottom panel. The blue surface represents the instance approximated with a reduced SSM built without this particular shape, the yellow surface the original correspondence results.

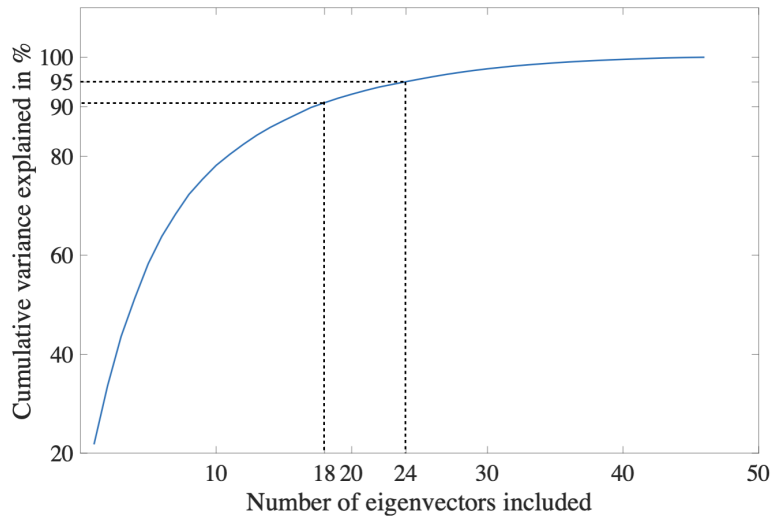


**Figure 5.9:** Cumulative variance covered for different numbers of leading eigenvectors included.

### 5.3.6 Validation with Electrophysiological P wave Simulations

Calculating the P wave on the 100 random geometries derived from the constructed SSM as described in section 5.2.6 yields the signals for the Einthoven, Goldberger and Wilson

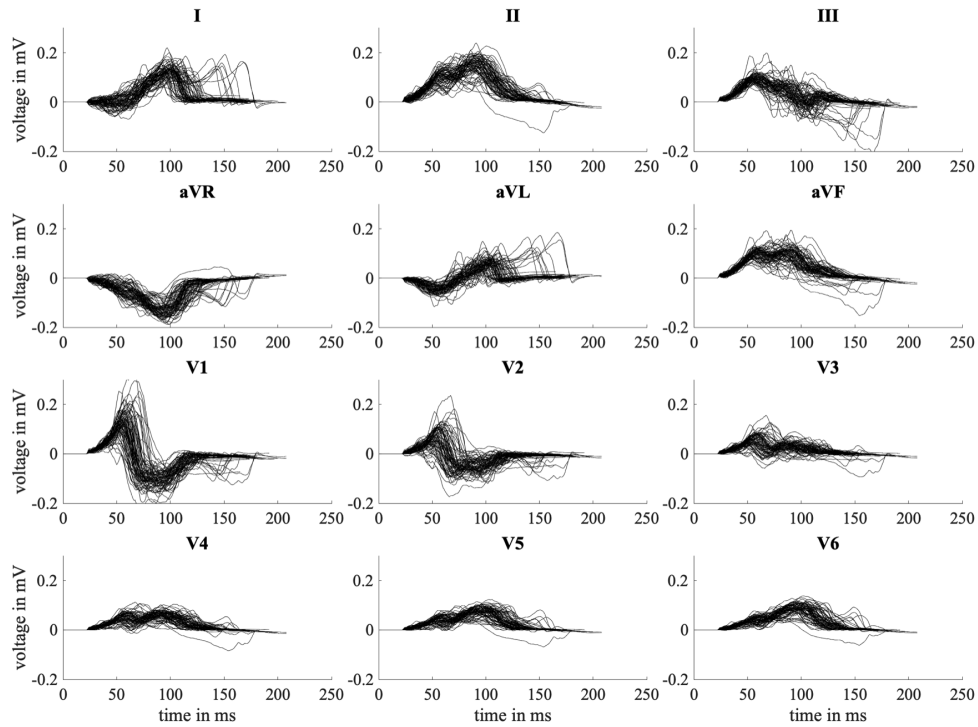


**Figure 5.10:** P waves of the 12-lead ECG calculated on 100 geometries derived by modifying the eigenvector coefficients of the constructed bi-atrial shape model.

leads shown in Figure 5.10. The P wave duration was extracted for each of the 12-lead ECGs simulated on 100 random instances as the mean P wave durations across all 12 leads. The values of the P wave durations - arising from simulations in which only the atrial anatomy was varied - ranged from 85 ms to 186 ms with a mean and standard deviation of  $114.82 \pm 20.19$  ms. The probability density of the P wave durations extracted from the simulation results are visualized in Figure 5.11 in yellow. The distribution of P wave durations in the Copenhagen ECG study was reconstructed based on the values reported in Nielsen *et al.* [215] and are shown in blue in Figure 5.11. The interval of 90-111 ms characterizing P wave durations of subjects stratified with a low AF risk is marked in red.

## 5.4 Discussion

The main result of this study is a point distribution model incorporating the shape variations of the right and the left atrium as well as their appendages and the PVs. Moreover, a workflow was proposed for building a volumetric atrial model from an endocardial surface derived from the SSM. Together with 100 example volumetric geometries generated by a Gaussian variation of the principal component coefficients in the  $[-3, +3]\sigma$  range including fiber orientation, inter-atrial bridges and anatomical labels, the SSM is openly available [200].

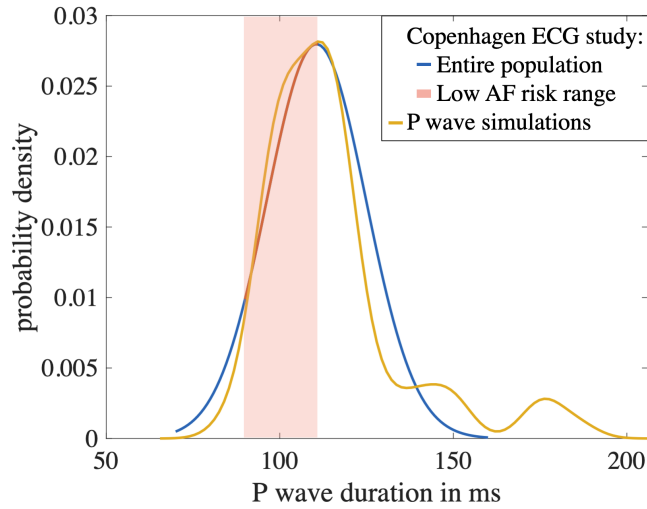


**Figure 5.11:** Probability density functions of P wave durations in the Copenhagen ECG study (blue) and in the simulation study (yellow). The area highlighted in red represents the value range of patients holding a low AF risk (90-111 ms) as reported by [215].

Electrophysiological simulations covering atrial excitation spread and propagation of electrical potentials to the body surface were conducted on these 100 example shapes. The resulting P wave durations obtained with the proposed SSM of  $114.82 \pm 20.19$  ms are in agreement with the P wave durations of 100-105 ms reported for individuals with a very low AF risk in an extensive cohort study based on 285,933 ECGs [215]. On the one hand, this suggests that the constructed model is capable of producing a large variety of variation shapes leading to realistic ECG feature values when compared to clinical recordings. On the other hand, it implies that the additional P wave duration variability observed in individuals with increased AF risk (92-116 ms range covering 20-80% percentiles in Nielsen *et al.* [215]) is either due to pathological anatomical variability not represented in the healthy dataset used to build this SSM or due to non-anatomical, functional changes such as CV slowing due to fibrotic infiltration of the atrial tissue [216].

In the constructed model, 24 eigenvectors are necessary to explain 95% of the total variance of the dataset. In the LA-only SSM built by Corrado *et al.* [180], the first 15 eigenmodes cover 95% of the entire shape variance. Cates *et al.* [182] reported that only 8 eigenvectors account for 95% of the total variance. However, these two models do neither consider the LAA nor the RA which explains the higher complexity of this model and in turn the need to include more eigenvectors to cover the majority of the shape variance. By allowing only a variation of the PVs orientation in anterior-posterior direction during correspondence retrieval, changes in the PV lengths and diameters were prevented to be reflected in the model's eigenmodes, which was reported as a possible limitation of the model by Cates *et al.* [182].

Varying the first eigenvector in the LA SSM published by Varela *et al.* [184] causes a variation of the total LA volume as it is also the case in this model (Figure 5.6). Also

Corrado *et al.* [180] and Cates *et al.* [182] reported a change of the total LA size in the first eigenmode. In the latter, the first mode represents a dilation of the LA mainly in anterior-posterior direction, which is also the case for the third eigenmode of the SSM built by Corrado *et al.* [180], where the first eigenmode rather represents an elongation of the LA in medial-lateral direction. Cates *et al.* [182] also constructed a separate SSM of the LAA and found that its first shape parameter corresponds to a change in the LAA length which is as well described by the third eigenmode of the constructed model in this work.

The shape variations encoded in the leading eigenmodes of the novel bi-atrial SSM are consistent with previously published LA-only SSMs as far as the LA is concerned. This demonstrates that the model is able to reflect the same main shape variations even though it is based on a dataset of less than half the size compared to the other models. The second eigenmode of the model represents the asymmetry between right and left atrial volume. This further manifests the novel insights into inter-subject atrial geometry variations revealing with the constructed model since this shape change cannot be captured with two separate RA and LA SSMs.

The generalization results demonstrate that this model is able to accurately predict the shape of a previously unseen atrial geometry. The specificity results of  $7.79 \pm 1.00$  mm leave room for improvement. However, the low specificity scores do not result from unanatomical characteristics of the generated shapes. They occur rather due to the small dataset of 47 instances available for selecting the closest shape during evaluation. Considering the MR slice thickness of predominantly  $2.7$  mm (Tab. 5.2), a specificity rmse of  $7.79$  mm is in the range of less than 2 voxel diameters with segmentation uncertainty adding to it [202]. The specificity evaluation of the model therefore indicates that randomly generated shapes produce valid shapes with an accuracy in the range of the error susceptibility during segmentation.

The atria segmented for this study originate from datasets comprising images of not only healthy subjects but also patients with a known history of AF. LA enlargement has been linked with an increased risk for this arrhythmia [176, 217, 218]. To ensure that the model is not based on a biased dataset with predominantly enlarged left atria, the LA volume (excluding LAA and PV ostia) of the  $N$  segmented geometries ( $82.16 \pm 19.16$  ml) was compared to reference values. Pritchett *et al.* [219] considered all age and BMI groups in healthy individuals. Translating their 2D measurements to 3D volumes as suggested by Al Mohaisen *et al.* [220] yields a  $[-3, +3]\sigma$  range of 10-130 ml with the largest LA volume in this dataset (122 ml) being within that range. In this way, the dataset could have been kept as large as possible. For the same reason, no geometries segmented from different image modalities or different spatial resolutions were excluded, which might however impact the shape statistics of the SSM. The largest slice thickness (2.7 mm) is in the range recommended in Salerno *et al.* [221] and relied on in previous studies [180, 182]. This indicates that the coarsest spatial resolution in the training dataset was still sufficient to allow covering all relevant anatomical structures during segmentation. Regarding segmentation, the ground truth LA shapes provided publicly available along with the datasets and the automated segmentation workflows in CemrgApp were relied on to the furthest extent possible. However,

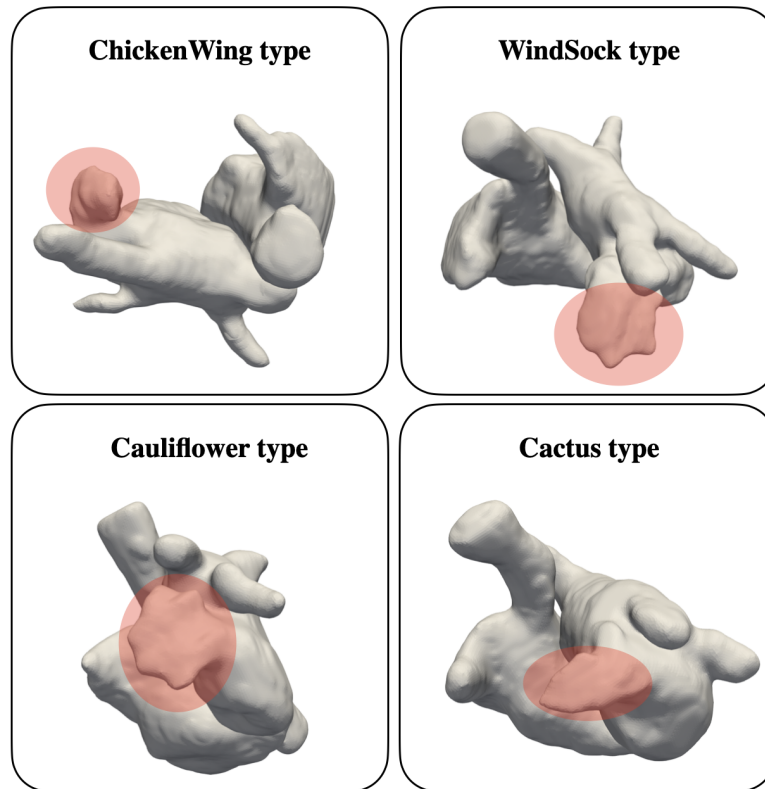


**Figure 5.12:** Examples from the dataset used in this work assigned to the different LAA shape clusters as proposed by [222]. The ChickenWing type differs from the other types by a sharp bend, the WindSock type is characterized by secondary lobes only in inferior direction, the Cactus type in inferior and superior direction. The Cauliflower type doesn't exhibit any clear primary lobe.

since manual corrections were indispensable in some cases (see Figure 5.2), inter- and intra-observer variabilities might still have had an impact on the final segmentation outcome.

Due to the highly complex shape and the natural clustering of the LAA, the shape of this structure was categorized for all 47 subjects into four classes as proposed by Wang *et al.* [222]. 11 %, 47 %, 36 % and 6 % of the segmented shapes were assigned to the ChickenWing, WindSock, Cauliflower and Cactus morphology classes, respectively. Examples from this dataset assigned to each of the four shape clusters are shown in Figure 5.12. The distribution of the LAA shape in the four categories are in accordance with the frequency of occurrence of the 612 LAA shapes studied by Wang *et al.* [222] in each class. This demonstrates that the dataset used in this work also exhibits similar variability concerning the LAA shape as observed in larger cohort studies.

PCA representation was chosen to describe the atrial shape variability and thereby assumed the changes in the atrial shape to be Gaussian distributed which does not hold true for the entire inter-patient shape variability [66, 222]. For the sake of comparability with previously published models and for reproducibility, it was intentionally decided to follow this state-of-the-art approach. Furthermore, the reference shape for the rigid alignment and

the correspondence retrieval was chosen to be the geometry with the smallest mean vertex to nearest neighbor distance to the other shapes. The choice of the reference mesh for ICP only influences the alignment results regarding the final orientation of all aligned meshes. Since the mean vertex-to-nearest neighbor distances between the meshes in correspondence and the original instances quantified to  $1.60 \pm 0.25$  mm, it can be inferred that the fitting algorithm for correspondence retrieval performed sufficiently well. Therefore, the choice of the reference shape should not have any major influence on the correspondence estimate. In contrast, with the particular choice of the reference mesh, it was facilitated that the deformed atlas is still capable of representing finer structural changes present in other models and prevent that finer structures that would only be present in the atlas are over-represented in the final SSM.

To showcase a potential application, multiscale electrophysiological simulations were conducted on 100 instances of the shape model. This proof of concept was deliberately based on a simple model not considering locally heterogeneous atrial wall thickness [202, 210, 223], disease-induced remodeling of membrane dynamics [224] or diffusive aspects during cardiac depolarization. Also only one torso shape and no rotation and translation of the atria within the torso are considered. The pipeline to generate volumetric models and simulation setups from the SSM is prepared for such extensions, though. Even though the shape variability covered by the model only comprises anatomical variants that were present in the dataset, i.e. healthy and AF patients without considerably enlarged left atrial volumes, the geometries can still be used for simulations of pathologies not affecting the atrial anatomy but reflecting in non-healthy functional anomalies, for example conduction blocks or ionic remodeling processes. Future studies focusing on repolarization could replace the simplistic Eikonal coupling employed here with a reaction-Eikonal scheme as suggested by Neic *et al.* [104].

The main advantage of the novel bi-atrial SSM consists in the automated generation of a large number of atrial geometries. In this way, the cumbersome and time-consuming process of anatomical model generation involving MRI segmentation and defining bundles and fiber orientation can be facilitated and expedited.

Potse *et al.* [225] examined the influence of electrical and structural remodeling on the maintenance of complex reentrant activity. With the proposed bi-atrial SSM, also the influence of the general atrial anatomy on the perpetuation and initialization of AF can be quantified.

Saha *et al.* [226] investigated the effect of endo-epicardial activation delay on the P wave morphology. However, only one atrial geometry was used to deduce models of different atrial wall thicknesses in this study and the authors state the lack of using different geometries as a limitation of their work. The same limitation is listed in the study of Pezzuto *et al.* [227] aiming at quantifying the beat-to-beat variability of P waves in patients with AF. With the SSM, a larger number of different volumetric atrial models is easily acquirable.

By means of the bi-atrial SSM, scale-large cohort studies using computer models for simulating atrial activity become feasible. Luongo *et al.* [228, 229] found a significant influence of the number of atrial anatomies included on the classification of different types of atrial flutter with a machine learning approach. With the proposed SSM, a large number

of geometries can be deduced and used as a basis for in silico big data approaches such as to produce extensive datasets for machine learning applications. The provided instances are ready to be used off the shelf in available computational simulation environments such as openCARP for electrophysiology [98, 230], openFOAM for fluid dynamics [231], FEniCS for continuum-mechanics [232] or life<sup>x</sup> for coupled electro-mechanical simulations [136, 233].

---

# Generation and Calibration of a Multiscale Population of Atrial Models

In this chapter, the generation and subsequent calibration of atrial computational models comprising anatomical variability of the atria as well as electrophysiological variability on cellular and tissue scale are explained.

*This project was carried out during a research stay at University of Oxford, Oxford, UK, in collaboration with Albert Dasí, Alfonso Bueno-Orovio and Blanca Rodriguez. Albert Dasí designed and conducted the study for generating and calibrating the population of cell models and provided all data used to enrich the atrial computational models with cellular variability. Blanca Rodriguez and Alfonso Bueno-Orovio provided guidance and supervision on all aspects of the project.*

## 6.1 Introduction

Large-scale datasets of cardiac signals obtained through multiscale electrophysiological simulations carry the potential to provide systematic insights into vulnerability, maintenance and termination of cardiac arrhythmias in entire subpopulations of patients. As such, they have been applied in various previous studies as an underlying database for e.g. disease classification and prediction with machine learning algorithms [47, 229] or for developing new pharmacological therapy options in *in silico* clinical trials [54, 198]. In these fields of applications, simulated datasets are particularly preferable over clinical data as they can represent a wide range of inter-patient variability and are not affected by ground truth label

and signal quality distortions arising due to expert annotation uncertainties or interfering noise sources.

For single-cell simulations, populations of candidate cellular models are typically generated by varying cell model parameters within wide ranges [54, 234]. Subsequently, a calibration of this initial model cohort is indispensable to not only ensure that the virtual cohort is composed of an extensive amount of instances, but also that the simulated signals comply with real-world inter-subject variability from experimental findings [235]. In this regard, biomarkers are extracted from both the simulated and experimental action potentials and calcium transients and are used to prune model instances not in line with clinical observations.

For 3D geometries representing atrial anatomy, statistical shape models can form the basis for sampling various anatomical endocardial instances representing the variability in shape encoded in the atlas [169]. Augmenting these models with a homogeneous wall thickness, tags for anatomical structures, rule-based myocardial fiber orientation and interatrial connections allows for generating 3D atrial models ready to use for electrophysiological simulations [52].

A combination of electrophysiological variability in form of populations of cell models and anatomical variability presents a promising approach to compose a large and diverse cohort of atrial models. As reported by Rodero *et al.* [185], only considering anatomical variability for cohort simulations is insufficient for representing the entire signal variability occurring in clinical practice. Thus, it is advisable to additionally include functional variability, for example in the form of conduction velocity (CV) and anisotropy changes, for compiling an initial model cohort (see section 6.2.1). In a step-wise approach, clinical reference ranges for anatomical properties as well as local activation times (LATs) and action potential and electrocardiogram (ECG) biomarkers are employed to exclude parameter combinations yielding simulation results that do not comply with the signal variability observed in clinical recordings [236] (see section 6.2.2).

## 6.2 Methods

### 6.2.1 Generation of the Initial Candidate Model Population

Figure 6.1 shows an overview of different types of electrophysiological and anatomical variability that were considered to compile the initial candidate model cohort.

Cellular electrophysiological variability was realized by scaling maximum ionic conductances of 12 key parameters in the Courtemanche *et al.* [91] cell model by up to  $\pm 50\%$  of their baseline value [237]. These parameters include the ultrarapid, rapid and slow delayed-rectifier  $K^+$  current density ( $G_{Kur}$ ,  $G_{Kr}$  and  $G_{Ks}$ ), transient outward  $K^+$  current density ( $G_{to}$ ),

$G_{K1}$ ,  $G_{CaL}$ ,  $G_{Na}$ ,  $Na^+/K^+$  pump ( $G_{NaK}$ ),  $Ca^{2+}/Na^+$  exchanger ( $G_{NCX}$ ) and the sarcoplasmic reticulum  $Ca^{2+}$  release ( $G_{rel}$ ), leak ( $G_{leak}$ ) and uptake ( $G_{up}$ ) currents.

To include atrial anatomical variability in the population, 4,000 atrial endocardial surfaces were derived by varying the leading 24 eigenmodes of the bi-atrial statistical shape model (SSM) (see chapter 5) with a latin hypercube sampling scheme. By including 24 eigenmodes, 95 % of the total atrial shape variation in the SSM were accounted for (see section 5.3.5). An interposed calibration step ensuring realistic left and right atrial volumes (see section 6.2.2) preceded the selection of 100 distinct atrial shapes that were continued to use for generating the volumetric instances constituting the anatomical basis for the initial candidate model population.

On tissue scale, 15 spatially distinct atrial regions could be robustly annotated on the geometrical models using the pipeline developed by Azzolin *et al.* [52] to which heterogeneous conduction properties in terms of CVs and anisotropy ratios can be assigned (see Figure 6.3). A sensitivity analysis was carried out to identify key CV parameters affecting the body surface P wave [238] and in turn, reduce the number of CV and anisotropy parameters to be varied for generating the cohort. In table 6.1, the ranges, in which CV and anisotropy were varied for the sensitivity analysis, are summarized. As an input for sensitivity analysis, a set of 17,280 combinations of different regional CVs and anisotropy ratios was compiled using latin hypercube sampling. The Eikonal equation was solved using the Fast Marching method and the sinus rhythm ECG was subsequently obtained as described in section 3.1.2.3. In contrast to the simulations covering cellular electrophysiological variability for the generation of the candidate population, only the baseline Courtemanche *et al.* [91] action potential was used as a template in all atrial regions for the sensitivity analysis. The forward problem was solved using the boundary element method (BEM) (see section 3.1.3.2). Additionally, a baseline 12-lead ECG P wave was calculated by applying the reference set of CVs and anisotropy ratios as summarized in table 6.1. For each of the 17,280 P waves resulting from the latin hypercube CV and anisotropy sampling, the L2 norm of the difference to the baseline ECG was calculated. This value was used as an output parameter for the sensitivity analysis to examine which regional CV and anisotropy parameters can cause a marked change in the ECG compared to baseline model parameters. Sensitivity was quantified by calculating correlation coefficients between the input model parameters (CV and anisotropy ratios in 15 atrial regions) and the cost function (L2 norm distance to the baseline P wave).

CV and anisotropy parameters with a sensitivity coefficient above 0.1 were selected to generate a set of 2,000 CV and anisotropy combinations using latin hypercube sampling to be combined with cellular and anatomical variability as will be explained in section 6.2.2. Functional parameters in regions with lower sensitivity coefficients were kept constant at their reference value listed in Table 6.1.

Each of the 100 volumetric atrial instances were randomly joined with 20 combinations of cell models and CV settings. Thus, the initial candidate population counted 2,000 multiscale model instances that were subject to additional calibration steps based on LATs as well as ECG biomarkers and morphology.

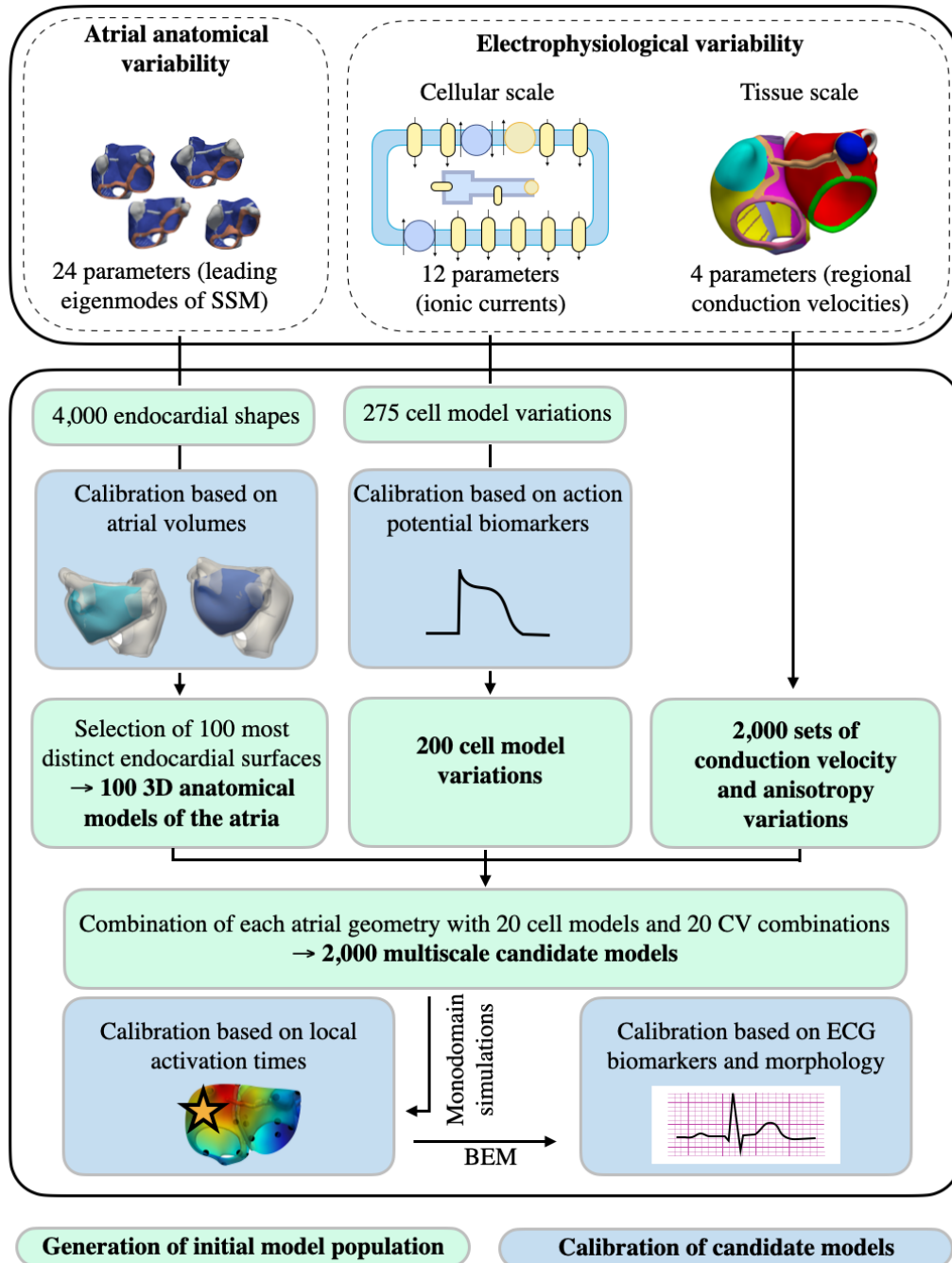


Figure 6.1: Electrophysiological and anatomical variability characterizing the initial candidate model cohort.

**Table 6.1:** Reference ranges for region-wise heterogeneous CVs and anisotropy ratios ( $AR = CV_{\parallel} / CV_{\perp}$ ).

| Atrial Chamber | Region                      | Longitudinal conduction velocity ( $CV_{\parallel}$ ) |                    | Anisotropy ratio (AR) |             | Baseline ECG     |      | Reference                                                                                |
|----------------|-----------------------------|-------------------------------------------------------|--------------------|-----------------------|-------------|------------------|------|------------------------------------------------------------------------------------------|
|                |                             | Lower bound (mm/s)                                    | Upper bound (mm/s) | Lower bound           | Upper bound | $CV_{\parallel}$ | AR   |                                                                                          |
| Left           | Pulmonary veins             | 800                                                   | 1600               | 1.2                   | 3.2         | 1377             | 1.94 | Volpato <i>et al.</i> [239], Maesen <i>et al.</i> [240]                                  |
|                | Bulk tissue                 | 430                                                   | 1470               | 1.2                   | 3.2         | 1377             | 1.94 | Maesen <i>et al.</i> [240], Fukumoto <i>et al.</i> [241], Hori <i>et al.</i> [242]       |
|                | Mitral valve                | 430                                                   | 1470               | 1.2                   | 3.2         | 1377             | 1.94 | Maesen <i>et al.</i> [240], Fukumoto <i>et al.</i> [241], Hori <i>et al.</i> [242]       |
|                | Appendage                   | 430                                                   | 1470               | 1.2                   | 3.2         | 1377             | 1.94 | Maesen <i>et al.</i> [240], Fukumoto <i>et al.</i> [241], Hori <i>et al.</i> [242]       |
| Right          | Bulk tissue, lateral wall   | 570                                                   | 1570               | 1.2                   | 3.2         | 1377             | 1.94 | Maesen <i>et al.</i> [240], Krueger <i>et al.</i> [141], Hassankhani <i>et al.</i> [243] |
|                | Bulk tissue, septal wall    | 370                                                   | 1620               | 1.2                   | 3.2         | 1377             | 1.94 | Maesen <i>et al.</i> [240], Krueger <i>et al.</i> [141], Hassankhani <i>et al.</i> [243] |
|                | Appendage                   | 530                                                   | 1050               | 1.15                  | 1.84        | 1377             | 1.94 | Hansson <i>et al.</i> [244]                                                              |
|                | Crista terminalis           | 850                                                   | 1818               | 1.18                  | 3.56        | 1818             | 2.56 | Loewe <i>et al.</i> [245], Saffitz <i>et al.</i> [246], Liu <i>et al.</i> [247]          |
|                | Pectinate muscles           | 700                                                   | 1879               | 1.2                   | 3.24        | 1879             | 3.24 | Loewe <i>et al.</i> [245], Krueger <i>et al.</i> [141]                                   |
|                | Tricuspid valve             | 570                                                   | 1570               | 1.2                   | 3.2         | 1377             | 1.94 | Maesen <i>et al.</i> [240], Krueger <i>et al.</i> [141], Hassankhani <i>et al.</i> [243] |
|                | Superior/Inferior vena cava | 570                                                   | 1570               | 1.2                   | 3.2         | 1377             | 1.94 | Maesen <i>et al.</i> [240], Krueger <i>et al.</i> [141], Hassankhani <i>et al.</i> [243] |
| Bridges        | Bachmann's bundle           | 1900                                                  | 3100               | 3                     | 8           | 2310             | 3    | Krueger <i>et al.</i> [141], Loewe <i>et al.</i> [245], Volpato <i>et al.</i> [239]      |
|                | Upper posterior bridge      | 1900                                                  | 3100               | 3                     | 8           | 2310             | 3    | Krueger <i>et al.</i> [141], Loewe <i>et al.</i> [245], Volpato <i>et al.</i> [239]      |
|                | Lower posterior bridge      | 1900                                                  | 3100               | 3                     | 8           | 2310             | 3    | Krueger <i>et al.</i> [141], Loewe <i>et al.</i> [245], Volpato <i>et al.</i> [239]      |
|                | Coronary sinus bridge       | 1900                                                  | 3100               | 3                     | 8           | 2310             | 3    | Krueger <i>et al.</i> [141], Loewe <i>et al.</i> [245], Volpato <i>et al.</i> [239]      |

**Table 6.2:** Scaling factors for  $G_{to}$ ,  $G_{CaL}$  and  $G_{Kr}$  in 6 different atrial regions to account for spatially heterogeneous ionic properties in the 3D simulations.

| Atrial Region         | $G_{to}$ | $G_{CaL}$ | $G_{Kr}$ |
|-----------------------|----------|-----------|----------|
| Right atrium          | 1        | 1         | 0.625    |
| Left atrium           | 1        | 1         | 1        |
| Crista terminalis     | 1.35     | 1.6       | 0.9      |
| Pectinate muscles     | 1.05     | 0.95      | 0.9      |
| Left atrial appendage | 0.65     | 1.05      | 2.75     |
| valve rings           | 1.05     | 0.65      | 3        |

## 6.2.2 Calibration of the Initial Model Population

Instances of the cell model were calibrated against experimental data obtained from patients under sinus rhythm and atrial fibrillation (AF) [198]. The retained ionic models were employed as baseline models for generating the multiscale population of atrial computational models. When coupling an ionic model with an anatomical geometry, selected ionic conductances were additionally scaled in different atrial areas to account for region-wise cellular heterogeneities (see Table 6.2).

Reference ranges for left and right atrial volumes were taken from literature reports based on large cohort studies analyzing extensive patient datasets [17, 248]. Likewise, threshold values for atrial volumes associated with an increased risk for AF were extracted from previous studies. The generated 4,000 atrial shapes were compared to the reference volume ranges and only instances with left and right atrial volumes inside these ranges were retained for the selection of 100 instances with maximum Dice coefficients to each other. The Dice coefficient served as a similarity metric to choose the most distinct instances for which 3D atrial volumetric geometries were created as described by Azzolin *et al.* [195].

To compile an initial population of 2,000 atrial models covering the different types of above mentioned variability, each atrial geometrical model was randomly combined with 20 calibrated cellular models and CV settings.

Monodomain simulations were carried out to calculate the spread of the electrical depolarization wavefront and to derive LATs from them. The approach described in section 4.1 was relied on to convert the chosen CVs into conductivities defined based on the intra- vs. extracellular conductivity ratios reported by Clerc [142]. Thereby it is important to note, that the monodomain conductivities were calculated based on the baseline Courtemanche *et al.* [91] cell model without taking ionic variability resulting from including cellular heterogeneity in the population into account. Thus, the effective CV in each tissue region could deviate by up to around  $\pm 70$  mm/s from the chosen target CV on tissue level mainly driven by marked in- or decreased sodium conductances. Subsequently, the forward problem was solved with the infinite volume conductor method (see section 3.1.3.3), using the electrode positions defined on the mean shape of the human body SSM developed by Pishchulin *et*

*al.* [179]. Calibration on tissue level was performed by comparing the simulated activation times at 22 anatomical landmarks (see Figure 6.2) in both atria to clinical reference ranges reported by Lemery *et al.* [249]. Additionally, the maximum activation times in both the left and right atrium were added for the calibration on tissue scale based on LATs.

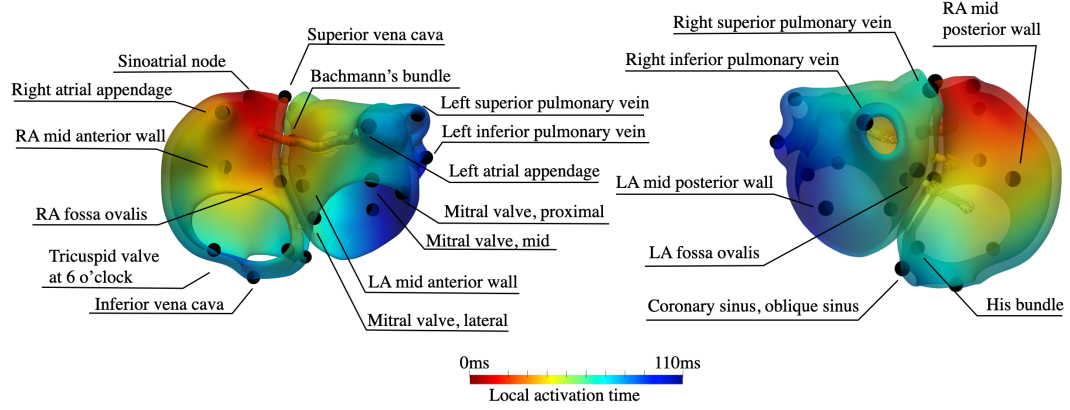


**Figure 6.2: Landmarks for calibration of the candidate multiscale model population based on LATs.** 22 landmarks were selected on the left and right atrium. For these, clinical reference intervals of activation times in normal sinus rhythm were reported. They were employed to exclude model combinations with LAT values outside these ranges.

Finally, the forward calculated ECGs were employed for a final calibration step to exclude model instances out of range regarding P wave duration and ECG morphology. A principal component analysis (PCA)-based approach was used to identify multiscale model instances leading to unrealistic ECG morphology which is explained in greater detail in the following.

The PTB-XL dataset [16] served as the reference for clinical ECG signals. For each of the 9,528 healthy subjects in this database, a representative P wave template was calculated by averaging all detectable P waves over the entire recording time as described by Pilia *et al.* [250]. These P wave templates of all 12 leads were then concatenated to one signal vector (see Figure 6.8) as implemented by Welle *et al.* [251]. These signal vectors were subsequently subject to a PCA yielding a mean vector  $\vec{\mu}_{clin}$  and eigenvalues and -vectors  $\lambda_{clin}$  and  $\vec{v}_{clin}$ . These quantities span an eigenspace representing the P wave morphology occurring in the clinical signals (compare Figure 6.8). The P waves of all retained simulated signals were concatenated likewise and approximated with the first 48 eigenvectors  $\vec{v}_{clin}$  accounting for 95% of the total variance in the clinical dataset using least squares estimation to obtain  $\vec{c}_{sim}$ :

$$E\hat{C}G_{sim} = \vec{\mu}_{clin} + \sum_{i=1}^{48} c_{i,sim} \cdot \lambda_{i,clin} \cdot \vec{v}_{i,clin} \quad (6.1)$$

Afterwards, the reconstruction errors  $\varepsilon$  of the approximated and the actual simulated signals were evaluated by the root mean squared error (rmse) between them as

$$\varepsilon = \sqrt{\frac{1}{N} \sum_{i=1}^N (EC\hat{G}(t_i) - ECG(t_i))^2} \quad (6.2)$$

with  $t_i$  being the discretized time step values,  $N$  the total number of sampled values in the concatenated ECG vectors,  $EC\hat{G}$  the approximated and  $ECG$  the actually simulated signal vector (compare Hotelling filter [252]). Simulation runs leading to an error  $\varepsilon > 0.1$  were not accepted in the final population (see Figure 6.11 for an example).

## 6.3 Results

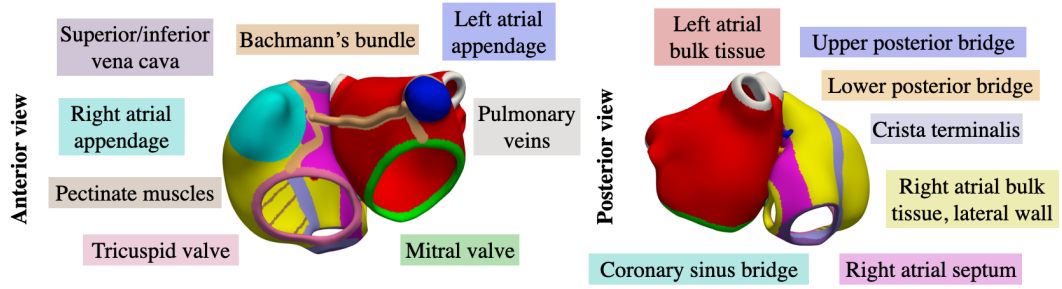
### 6.3.1 Sensitivity Analysis for Tissue-scale Electrophysiological Model Parameters

In Figure 6.3 (b), the absolute sensitivity coefficients for regionally heterogeneous CV and anisotropy ratios are visualized. It is apparent that CV variation in left atrial bulk tissue, right atrial bulk tissue (lateral and septal wall) and crista terminalis had the most pronounced effect on the ECG. Anisotropy ratios played a minor role and did not cause as much of a change in the ECG as CV. CV in the four above mentioned regions were considered to compile a set of 2,000 CV variations by latin hypercube sampling their values in the ranges reported in Table 6.1. CV in the remaining 11 and anisotropy values in all 15 regions were kept constant at their baseline values.

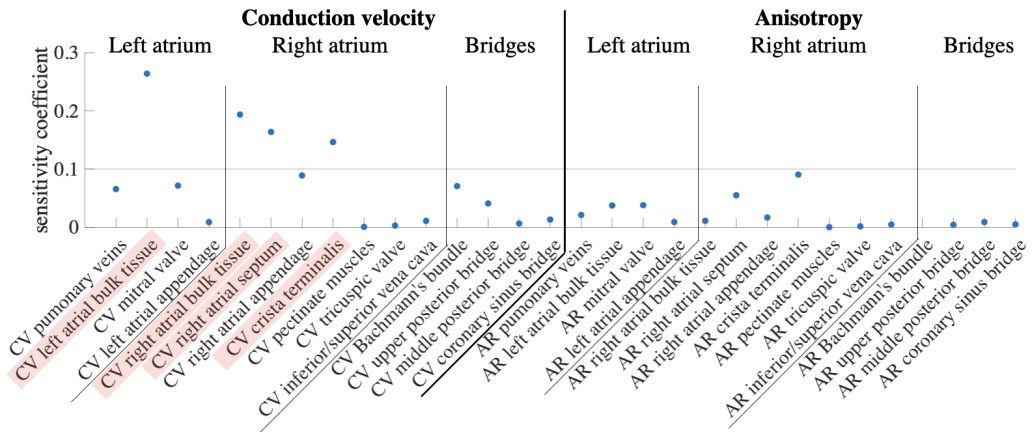
### 6.3.2 Cohort Calibration

#### 6.3.2.1 Atrial Volumes

Applying the clinical reference indices of [26 ml, 112 ml] and [34 ml, 148 ml] [248] for the left and the right atrial volumes, respectively, as lower and upper bounds to calibrate the anatomical model population leaves 3,925 out of the initially generated 4,000 endocardial surfaces fulfilling the clinical volume requirements (black enclosed areas in Figure 6.4). Dividing the atrial volumes bounded by the endocardial surface by the body surface area of the mean torso that was used for the ECG calculation in this study ( $1.9 \text{ m}^2$ ), allows for their comparison with clinical thresholds for identifying patients with enlarged atrial volumes associated with an increased AF risk. Out of the retained 3,925 calibrated endocardial shapes, 739 models were characterized by both left and right atrial volumes above the threshold of  $34 \text{ ml/m}^2$  and  $42 \text{ ml/m}^2$  [88], respectively, and could thus be considered predisposed to develop AF based on their anatomical properties.



(a) Tags for locally heterogeneous conductivity regions.



(b) Sensitivity coefficients for conduction velocity and anisotropy variation in 15 different anatomical regions.

**Figure 6.3:** Absolute correlation coefficients between CVs and anisotropy ratios in 15 different atrial regions and the L2-norm to the baseline ECG.

Calculating the Dice coefficient as a similarity metric between each pair of the retained 3,925 anatomical instances leads to the selection of 100 endocardial surfaces to be further processed through the pipeline developed by Azzolin *et al.* [195] to obtain simulation-ready volumetric atrial geometries (see Figure 6.3). Figure 6.5 depicts 5 examples of fully processed atrial anatomical models from the dataset of 100 volumetric instances. Each of these were subsequently paired randomly with 20 cell models and 20 sets of regionally heterogeneous CVs and employed to conduct monodomain simulations (see section 3.1.2.2) to obtain LATs and transmembrane voltage distributions. The latter were further projected onto the body surface using the infinite volume conductor method 3.1.3.3 to obtain the 12-lead (pseudo-)ECG.

### 6.3.2.2 Local Activation Times

Evaluating the LAT results from the 2,000 simulations (100 geometries  $\times$  20 cell models and 20 CV settings) with respect to clinically reported ranges for LATs in normal sinus

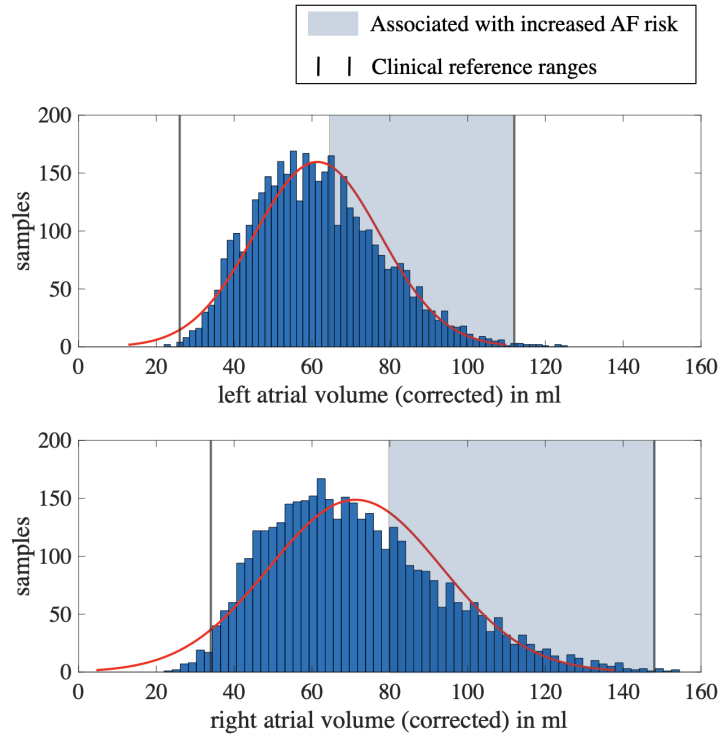


**Figure 6.4:** Left (top panel) and right atrial volumes (bottom panel) for an anatomical model cohort comprising 4,000 endocardial surface instances derived from the SSM. The red curve represents a fitted normal distribution on the data samples. The black intervals indicate value ranges of atrial volumes occurring in clinical practice. The volume intervals shaded in blue visualize the ranges that are reported to be associated with an increased risk for AF.

rhythm [249], resulted in 1,652 model combinations with LAT results inside the clinical reference intervals. In Figure 6.6, the distribution of LATs at each of the landmarks are shown for all 20 CV and cell model combinations paired with one specific geometry (atriaID\_062). For this atrial anatomical model, one of the 20 simulation runs yielded an LAT at the left superior pulmonary vein and a latest left atrial activation time above the clinically measured upper bound. This multiscale model was subsequently excluded for the calibrated population, the remaining 19 instances were accepted.

Figure 6.7 shows the percentage of the entire 2,000 simulation results that are distributed inside the clinical  $\mu \pm \sigma$ ,  $\mu \pm 2\sigma$  and  $\mu \pm 3\sigma$  (from top to bottom) ranges mapped on 22 regions around each of the considered landmarks (compare Figure 6.2) on the mean shape. It is apparent that the highest percentage of model combinations had to be pruned due to LAT simulation results outside the clinically reported intervals at the RA mid posterior wall, the LA mid anterior wall, the left pulmonary veins, the mitral valve (septal wall) and the sinoatrial node. However, the percentage of model instances with LATs outside the  $\mu \pm 3\sigma$  range is small and quantified to only 17.4 % (348 out of 2,000).

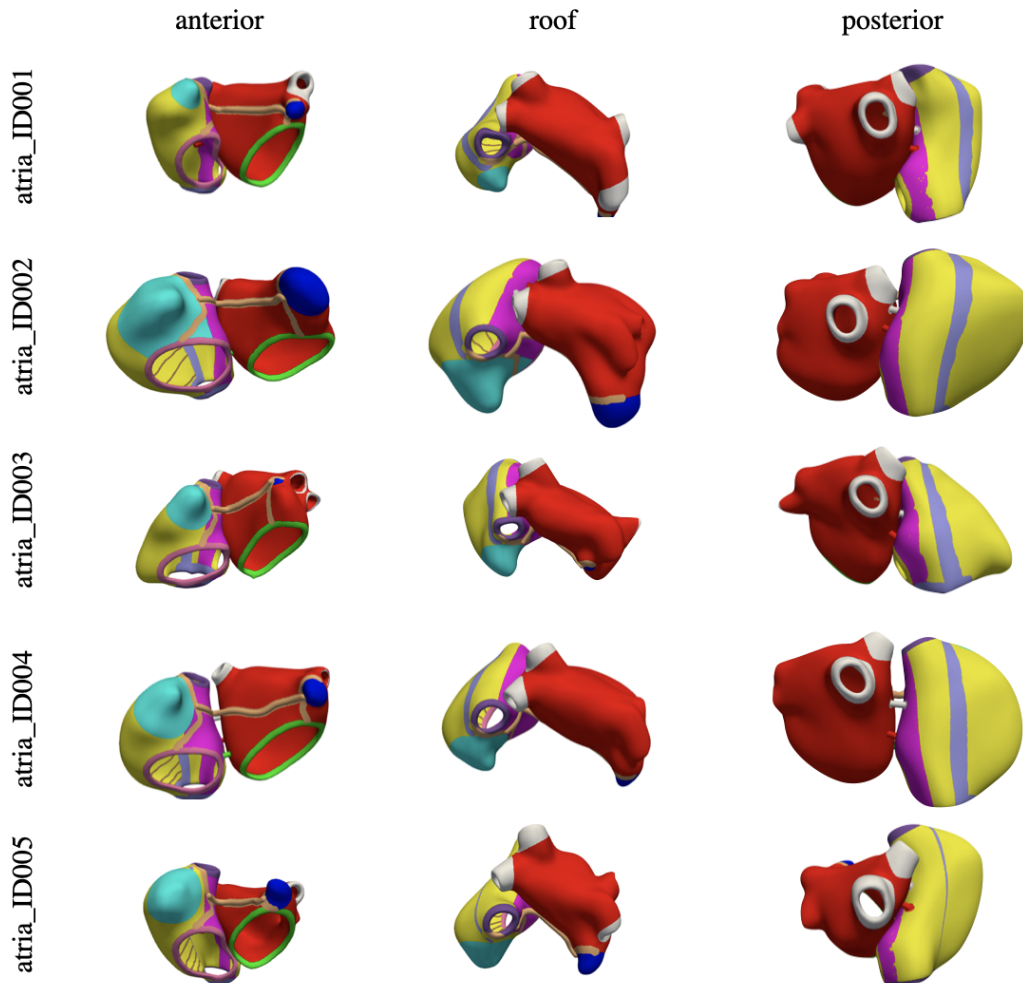


**Figure 6.5:** 5 exemplary simulation-ready volumetric instances of the atria. In each row, one atrial anatomical model is shown from the anterior, roof and posterior point of view in the right, middle and left column, respectively. The colors represent the regions that can be allocated heterogeneous conduction properties as explained in Figure 6.3.

### 6.3.2.3 P wave Features and Morphology

Mean and standard deviation of the P wave duration for the multiscale model instances passing the LAT calibration step was  $126.55 \pm 27.78$  ms. Applying the interval of [78, 144] ms as lower and upper bound for the P wave duration calibration step [215, 253], leads to 1,435 remaining model instances provisionally accepted into the population.

Lastly, P wave morphology was analyzed in a final calibration iteration. In Figure 6.8, the mean P wave in all 12-leads in the clinical dataset is shown in red. The  $[-3\sigma, +3\sigma]$  range of the first, second and third eigenmode are visualized in grey. They account for 15 %, 14 % and 12 % of the total signal variance in the clinical dataset. The first eigenmode mostly represents a change in the P wave amplitude in lead II, aVR and V5 as well as a change in

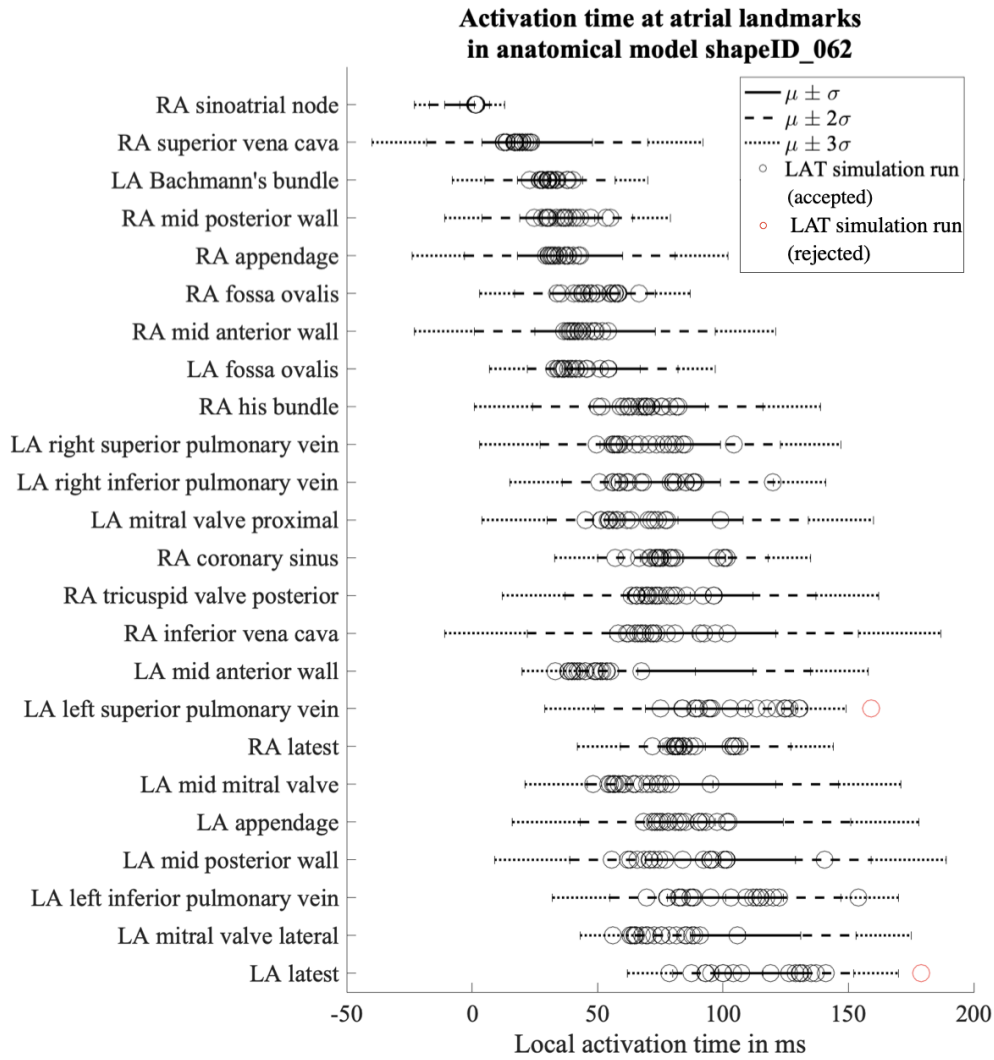


**Figure 6.6: Calibration of multiscale model combinations of one exemplary geometry based on LATs on predefined atrial landmarks.** 22 landmarks and the latest activation times in the left and right atrium are shown in each row. The clinically measured  $\mu \pm \sigma$ ,  $\mu \pm 2\sigma$  and  $\mu \pm 3\sigma$  ranges are shown with the solid, dashed and dotted line, respectively. LATs simulated for accepted and rejected instances are visualized in black and red, respectively. RA = right atrium, LA = left atrium, LAT = local activation time

polarity in lead III, aVL and aVF. The second and third eigenmode predominantly affect the amplitude and morphology of lead V5 and V6, respectively.

The reconstruction errors  $\varepsilon$  (equation 6.2) are depicted for each lead separately in Figure 6.9. Marked reconstruction errors only occurred for the precordial leads V1, V2 and V3 (Figure 6.9). A simplified forward calculation method was chosen to generate the large scale dataset of 2,000 simulated ECGs in a reasonable amount of time. As this approach is known to overestimate amplitudes in the ECG leads measured in close proximity to the sources (see chapter 4, in particular Figure 4.10c), a threshold  $\bar{\varepsilon}$  for the rmse averaged over



**Figure 6.7: Statistics of calibrating all 2,000 multiscale model combinations based on LATs.** The rows show the percentage of simulated LATs inside the clinical reference ranges (from top to bottom:  $\mu \pm \sigma$ ,  $\mu \pm 2\sigma$ ,  $\mu \pm 3\sigma$ ) for each landmark (yellow dots) represented as a region around it on the mean shape geometry.

all leads except for V1-V3 of 0.1 was chosen:

$$\bar{\varepsilon} = \frac{1}{9} \sum_i \varepsilon(i), \quad i \in [\text{I, II, III, aVR, aVL, aVF, V3} - \text{V6}] \quad (6.3)$$

In this way, 764 of the up until this point remaining 1,435 multiscale model combinations were accepted in the population.

In Figure 6.10, 20 12-lead ECGs calculated for the 20 different CV and ionic model setups in one of the 100 atrial geometries are visualized. The signal traces in black passed all calibration steps and were accepted in the final population of multiscale models. The blue, cyan and red curves represent instances that were rejected due to nonfulfilling LAT, P wave duration and P wave morphology criteria, respectively.

Table 6.3 summarizes the number of model instances generated for the initial candidate population and the amount that has passed each individual calibration step.

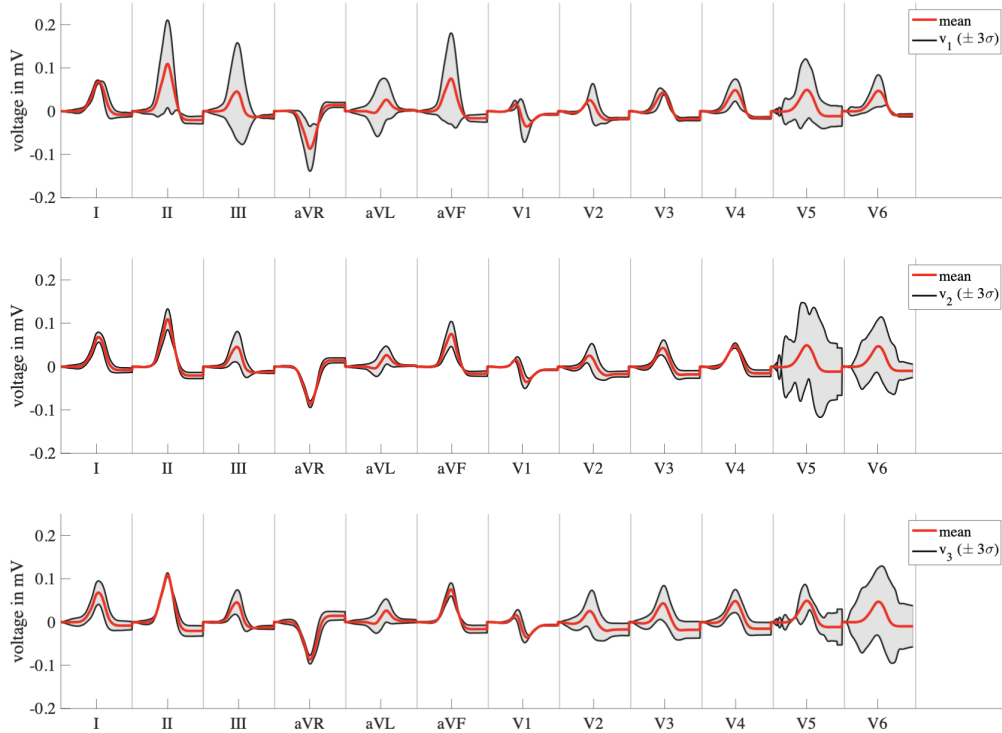


**Figure 6.8:** Concatenated P waves of the 12-lead ECG. The mean of the clinical dataset is shown in red, the  $[-3, +3]\sigma$  range of the first, second in third principle component from top to bottom row, respectively, is exemplary shaded in grey.

**Table 6.3:** Number of candidate models and accepted instances for each calibration step. Anatomical and ionic models were generated and calibrated independently from each other. Calibration based on local activation times, P wave duration and P wave morphology was performed consecutively leaving 764 accepted instances out of 2,000 initially generated candidate models.

| Calibration step            | Candidate population | Accepted   | Rejected |
|-----------------------------|----------------------|------------|----------|
| Action potential biomarkers | 275                  | 200        | 75       |
| Atrial volumes              | 4,000                | 3,925      | 75       |
| Local activation times      | 2,000                | 1,652      | 348      |
| P wave duration             | 1,652                | 1,435      | 217      |
| P wave morphology           | 1,435                | <b>764</b> | 671      |

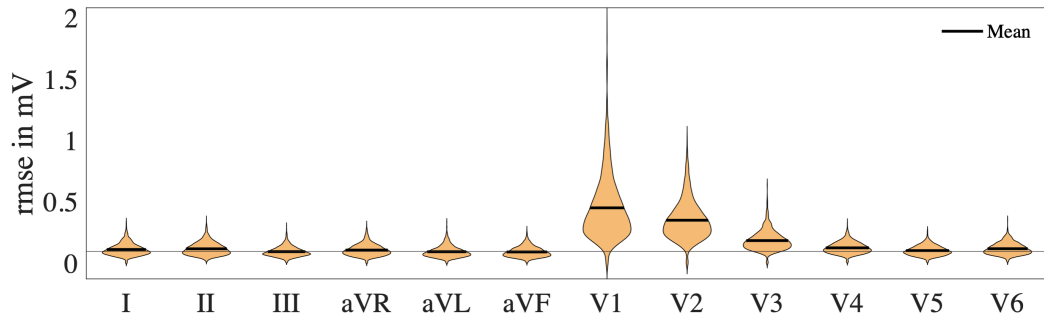


**Figure 6.9:** Lead-wise root mean squared errors (rmse) between simulated and approximated signals in a reduced eigenspace derived from PCA on clinical ECGs. The thin solid line shows the threshold of 0.1 applied for excluding model instances exhibiting ECG characteristics not complying with typical clinical ECG morphology.

## 6.4 Discussion

### 6.4.1 Main findings

In the work presented in this chapter, a cohort of atrial models comprising anatomical and functional variability on both tissue and cellular scale was generated and calibrated. 100 atrial geometries with calibrated left and right atrial volumes were each paired with 20 CV settings and 20 cellular models to generate a candidate model population consisting of 2,000 instances. Calibrating this candidate cohort based on LATs and ECG biomarkers leaves a total of 764 multiscale models to be used in future for electrophysiological simulations focusing e.g., on *in silico* drug trials on 3D atrial models. The variability encoded in this population account for three key parameters that are known to contribute to the initiation, maintenance and termination of AF, as the condition for a re-entry to be sustained reads as follows [254]:

$$PL \geq CV \cdot ERP \quad (6.4)$$

with PL being the path length, CV the conduction velocity and ERP the effective refractory period. In the calibrated population of models, these quantities are modulated by a change of the atrial anatomy, CV variation itself and different ionic conductances driving the repolarization behavior of the cell, respectively.

Sensitivity analysis of CV and anisotropy ratio in 15 spatially distinct regions revealed that three out of the four regions where a change in CV had a pronounced effect on the ECGs were located in the right atrium (RA). This is in line with the findings from Loewe *et al.* [140] reporting that around 70 % of the total P wave integral is attributable to electrical activation of the RA. Furthermore, the left atrium (LA) was subdivided into spatially coarser regions, i.e., the majority of the tissue volume was allocated only to the LA bulk tissue class, whereas the RA was additionally also composed of a septal region and crista terminalis which account for

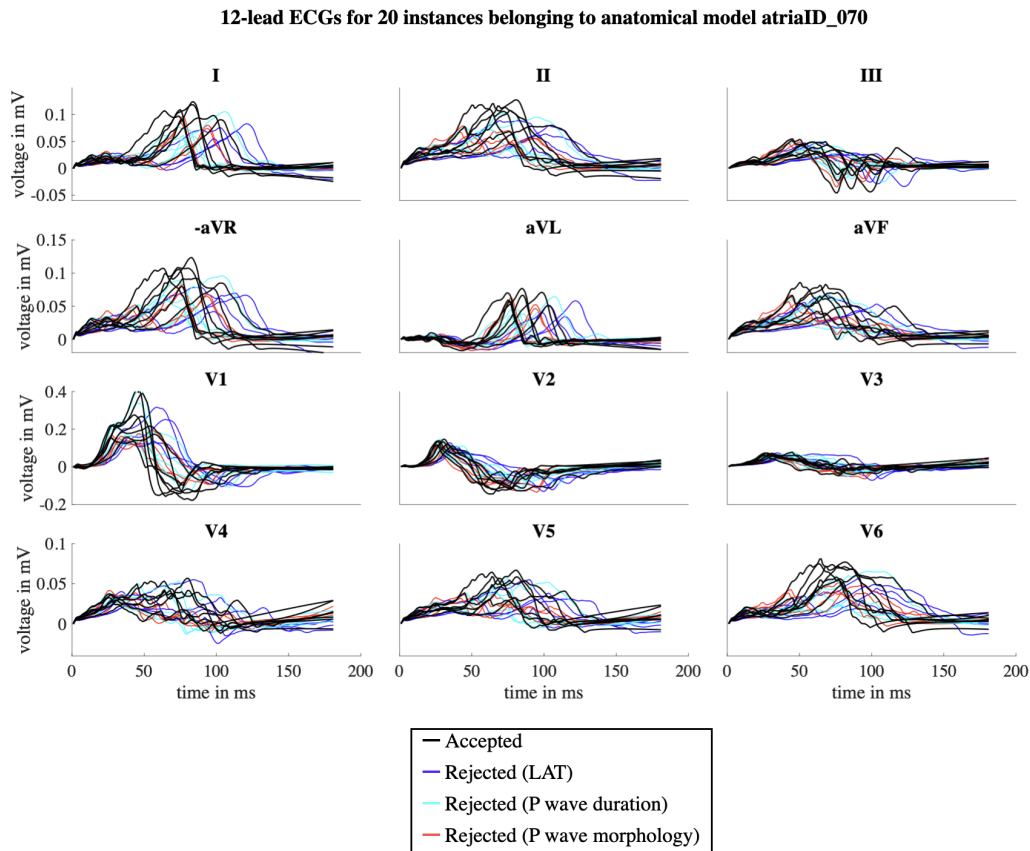


**Figure 6.10:** 12-lead ECGs calculated on the anatomical model instance atriaID\_070 combined with 20 different CV and ionic model combinations. ECGs that were rejected for the final population based on LATs, P wave duration and ECG morphology are visualized in blue, cyan and red, respectively. ECGs of multiscale models passing all calibration steps are shown in black.

large fractions of the total RA myocardial tissue volume themselves. Sensitivity analysis also highlighted that anisotropy plays a minor role compared to longitudinal CV in the genesis of the ECG. This could potentially be traced back to the fact that longitudinal CVs were defined and divided by the prescribed anisotropy ratios to obtain transversal CVs. Furthermore, conduction in the atria is in any case already highly anisotropic, so that longitudinal CVs clearly dominate the preferred direction of wave propagation and transversal CV mediated by varying anisotropy ratios does not have a strong influence on the depolarization spread.

Out of the initially generated 4,000 instances of the endocardial wall, the largest left atrial volume was 125 ml and was in the same ballpark as the largest volume of the individual segmented MR instances based on which the atrial SSM was built (compare chapter 5). However, when indexing the atrial volumes to the body surface area (BSA) calculated analytically for the torso geometry used to compute the ECGs in this study, a total of 739 models had LA volumes above the threshold for diagnosing left atrial dilation associated with an increased AF risk. However, using a different torso geometry and thus another resulting BSA or accounting for under- or overestimation when approximating BSA with

only height, weight and gender as it is clinically routinely done, the number of anatomical models characterized by an increased AF risk based on volume properties could deviate markedly.

A total of 348 out of the 2,000 multiscale model combinations were excluded due to non-fulfilled LAT calibration requirements, whereas additional 671 were pruned due to non-realistic ECG morphology. After the LAT calibration, 217 additional models had P wave durations outside the clinical reference ranges. The highest percentage of model combinations not accepted in the population during this calibration step exhibited LATs in the RA mid posterior wall. The exact position of this landmark is not specified in more detail by Lemery *et al.* [249] and thus, a slightly different placement of this point in the *in silico* model cohort could have led to different results. The relatively low number of models leading to non-realistic P wave durations could be traced back to the fact that latest right and left atrial activation times were already considered in the course of the LAT-based calibration step. In this way, models potentially leading to too long simulated P wave durations were already excluded by the time ECG biomarkers were computed for the ongoing calibration process. Usually, other ECG biomarkers for which clinical reference ranges are reported comprise peak-to-peak amplitudes and P wave terminal force in V1. However, both of these features are amplitude based and heavily depend on the signal acquisition procedure, electrode contact and the torso shape. As too many confounding factors affect these biomarkers, they were not employed in any of the calibration steps in this study.

A novel approach for calibrating computational models particularly based on the ECG morphology was presented. In this calibration step, the largest number of model instances were rejected for the population (617 rejected instances compared to 348 and 217 rejected instances after LAT and P wave duration calibration). This highlights the importance of considering the entire P wave morphology in addition to only selected ECG biomarkers, such as P wave duration. Even though model combinations could lead to P wave durations inside clinical reference ranges, they do not necessarily exhibit typical ECG signal time courses provoked potentially through unrealistic CV combinations in different atrial regions. This might indicate that even if CV values are globally selected in reasonable intervals, certain local and region-wise CV distributions could still lead to unrealistic ECG phenotypes which are identifiable with the novel P wave morphology calibration procedure. To understand why and which certain model instances were not accepted into the final population, a clustering approach could reveal whether specific anatomical or functional parameters yield unrealistic ECG signals. Interpreting the eigenmodes resulting from applying PCA to clinical ECGs disclose the most prominent signal variability occurring in clinically measured ECGs. The first eigenmode affected the polarity of lead III, aVL and aVF while the morphology in the remaining limb and augmented leads remained unchanged, indicating that the first eigenmode could represent a change of the electrical heart axis among different patients. The amplitude change in V2 in the third eigenmode could besides physiological reasons also be caused by inconsistent electrode placement for different patients. The striking amplitude variation in V5 for eigenmode 1 and 2 as well as in V6 for eigenmode 3 was surprising and could have been arisen due to incorrectly delineated P waves in these leads.

The evaluation of the coefficients  $c_{i,sim}$  (see equation 6.1) opens up new possibilities for future work. By comparing them to the distribution of the scores resulting from PCA on clinical ECGs, one could assess if the simulated ECGs are representative for a wide range of clinical signals or if a certain type of ECG morphology is not covered by the variability in the virtual cohort so far.

The monodomain propagation model (see section 3.1.2.2) was used to calculate the LATs and the transmembrane voltage distribution for the 2,000 model instances of the candidate population. The Eikonal model has been shown to reproduce LAT results with high fidelity compared to biophysically more detailed models (see chapter 4) in normal sinus rhythm simulations. For the 17,280 simulations carried out for the sensitivity analysis (see Figure 6.3), these properties were made use of to allow for an efficient computation of the resulting ECGs. However, the simulations for the 2,000 candidate model instances were intentionally carried out using the computationally more expensive monodomain model to ensure that the mesh quality is sufficiently high for simulations with propagation models capable of producing re-entry simulations. In this way, the proposed calibrated model population is ready to use for the intended purposes comprising testing the efficacy of different channel blockers or ablation targets on arrhythmia termination *in silico*.

Future work could also comprise separating the retained and calibrated multiscale atrial models extended with fibrotic tissue variants into a healthy and AF cohort. In this way, an ensuing validation step regarding arrhythmia vulnerability of both subpopulations could be conducted by evaluating dominant frequency maps after inducing reentry. Another application of the proposed population could be to identify key model properties contributing to arrhythmia susceptibility in the cohort and evaluate whether either slow conduction velocity, ionic remodeling, enlarged atrial volumes or a combination of them is the main driver for rotational activity.

## 6.4.2 Related work

Several previous studies have focused on generating, calibrating and validating populations of cellular models. Muszkiewicz *et al.* [237] showed that calibrated cell model populations yielded action potentials which biomarkers overlapped with those obtained from clinical experiments. They concluded that the population of ionic models are thus representative for a wide range of action potential morphology. Furthermore, they highlighted the need of a calibration step as cell models with ionic conductances set to their baseline values were not able to reproduce action potential biomarkers within experimental ranges, in contrast to other instances of the model population even characterized by substantial parameter variations. Britton *et al.* [255] generated a large population of human ventricular computational cell models to identify key ionic properties leading to abnormal repolarization behavior. Sánchez *et al.* [198] calibrated populations of cell models under sinus rhythm and chronic AF conditions. They identified key ionic conductances underlying the inter-patient variability of action potential biomarkers in both populations aiming at a better understanding towards the mechanisms behind differences in arrhythmogenesis and response to treatment

of both cohorts. Vagos *et al.* [256] followed a similar approach and found that the healthy and chronic AF populations exhibit substantial deviations in sensitivity of the ionic current parameters to pro-arrhythmic action potential biomarkers. In contrast to the generation and calibration of the multiscale model population presented in this chapter, a large number of ionic model instances had to be excluded in the calibration steps of the above mentioned studies. Britton *et al.* [54] reported that only 213 out of 10,000 initially generated cell model instances exhibited action potential biomarkers complying with experimental results when varying ionic conductances by  $\pm 100\%$  of their baseline values. In the study presented in this chapter, a larger fraction of the candidate population (764 out of 2,000 multiscale models) passed the LAT and ECG calibration steps. This relates to the fact that cell model populations have to be created assuming a large variation of ionic conductance parameters as these quantities cannot be measured *in vivo* or are affected by the isolation process during voltage clamp experiments [255]. In contrast, CV can be directly derived from clinical LAT measurements and therefore, more precise clinical intervals are available to draw the parameter values for the initial model population from. Even more straight forward is the generation of anatomical models. The SSM was built based on 47 patient-specific atrial models. Thus, selecting the PCA coefficients in the  $[-3\sigma, +3\sigma]$  interval leads to endocardial geometries within the eigenvector space of the SSM, theoretically exhibiting already realistic atrial geometrical variations as they also occur in the 47 underlying SSM geometries.

The latin hypercube sampling scheme was used to generate the model parameters for the ionic and anatomical models as well as for generating locally heterogeneous CV variations. This approach is well established and has been used in various previous studies [54, 255]. However, more sophisticated approaches for generating *in silico* populations exhibiting coinciding biomarker distributions with clinical data have been published. Lawson *et al.* [257] proposed a method to iteratively tune model parameters such that the resulting computed biomarker distribution can be compared to a set of measured values in a step-wise approach. This method is computationally more efficient than brute force sampling and calibration until *in silico* and *in vivo* data distributions match. Even though this sampling technique will lead to a more representative population of models for actual clinical data, it will also imply an under-representation of rare and unusual action potential morphologies. However, the ability to investigate the mechanisms in outlier models is one of the main advantages of using simulated over clinical data where these morphologies do not occur in sufficient numbers to infer statistical information, e.g. regarding drug response. For this reason, model parameters were sampled using the established latin hypercube approach for generating the multiscale population of models.

Regarding tissue scale atrial electrophysiology, only a limited number of previous studies have focused on the generation and validation of virtual cohorts covering various types of variability. In these, the generated populations usually either consisted of only a small amount of anatomical instances as they had to be built based on patient-specific segmentations or lacked a validation step. In the work from Corrado *et al.* [258], 10 atrial anatomical models were generated and validated against LATs acquired during an S1-S2 pacing protocol. Roney *et al.* [259] generated 100 patient-specific anatomical models of only the left atrium

with the aim to predict long-term AF recurrence after catheter ablation for each individual patient. However, no explicit validation step of the computer models with clinically measured biosignals, such as LATs or ECGs, was presented. Rodero *et al.* [185] showed that only modifying anatomical properties in a four chamber human heart model was not sufficient to explain the entire range of variability regarding electromechanical function occurring in clinical data. Therefore, the multiscale population of models presented in this chapter was generated by additionally incorporating functional variability on tissue and cellular scale.

### 6.4.3 Limitations

Sensitivity analysis on CV and anisotropy model parameters was performed based on simulations with the baseline Courtemanche cell model on the mean shape geometry. Other anatomical shapes of the atria, e.g., with bigger appendages, might have led to different results as sensitivity analysis might have identified different CV regions affecting the P wave. However, the CV variation in the four regions chosen based on the sensitivity results in this study is consistent with spatially heterogeneous conducting regions considered in other studies (compare chapter 9 and chapter 8).

For the multiscale population of atrial models, only one torso geometry and no additional variation in terms of the atrial rotation angles were considered. When including thoracic shape variability, a variation of the first two eigenmodes of the SSM developed by Pishchulin *et al.* [179] would be sufficient to describe a large cohort. These two eigenmodes reflect in torso shape changes associated with height, weight and gender differences. The ensuing eigenmodes represent a change in body posture which are not particularly relevant for the simulation outcomes and do not represent pertinent variability in a large population. Furthermore, no fibrotic remodeling was included in selected tissue regions on the atria up until now which are indeed crucial to assess arrhythmia vulnerability and to test the efficacy of different channel blockers.

The forward calculation was performed using the infinite volume conductor method which was shown to cause a prominent amplitude overestimation in lead V1-V3 (see chapter 4). Consequentially, these leads were not considered when calibrating the population based on the ECG simulation results. However, applying instead the boundary element method (see section 3.1.3.2) would allow for using all 12 leads as an additional source of evidence for accepting only model instances with morphology and biomarkers in the entire 12-lead ECG within clinical ranges. A threshold of 0.1 for the averaged rmse  $\bar{\epsilon}$  was applied to decide between accepted and rejected model instances during the P wave morphology calibration step. This threshold was chosen empirically based on exemplary reconstructed simulated signals in the clinical ECG eigenspace. In Figure 6.11, two examples for an accepted and rejected ( $\bar{\epsilon} = 0.08$  and  $\bar{\epsilon} = 0.12$ ) simulation run are shown. Choosing a different threshold for  $\bar{\epsilon}$  would clearly have led to a different number of instances retained for the final multiscale model population.

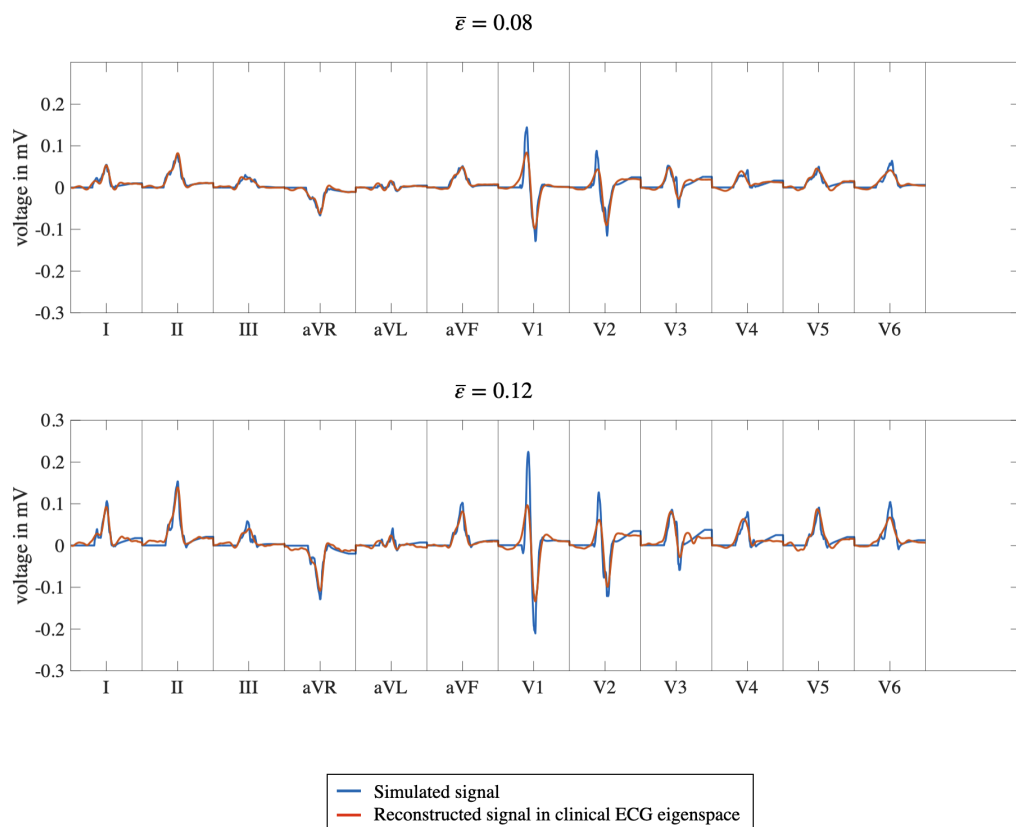


**Figure 6.11:** Two examples of simulated signals (blue lines) and their least squares reconstruction with in the clinical ECG eigenspace. The example in the top panel shows an ECG of a model instance that was accepted in the population as  $\bar{\epsilon} < 0.1$ , the example in the bottom panel was rejected.



---

# Simulation of a Large-scale ECG Dataset of Healthy Subjects and Selected Pathologies

In this chapter, the simulation of 10,000 12-lead electrocardiogram (ECG) signals of 10 seconds length for healthy subjects and patients with selected cardiac pathologies is presented. These are of a comparable format to clinically measured ECGs and could therefore be directly employed as an extension to clinically recorded signals for deep learning applications.

*This study was carried out within the scope of a project supported by the EMPIR programme co-financed by the participating states and from the European Union's Horizon 2020 research and innovation programme under grant MedalCare 18HLT07. Methodology and results were developed, generated and discussed in close collaboration with Karli Gillette, Matthias Gsell and Gernot Plank from Medical University of Graz, Graz, Austria. Karli Gillette simulated and provided the QRS(T) segments for the healthy cohort and all ventricular pathologies.*

## 7.1 Introduction

Unless a four chamber heart model constitutes the underlying geometry for electrophysiological simulations, basic simulation protocols applied for example within the openCARP [98] simulation framework allow for generating single beat P waves or QRS(T) complexes and lack the possibility to represent intra-patient variability in the ECG over time. This impedes the direct and straight forward usage of simulated ECGs as an extension to clinically measured datasets in the machine learning context since the simulated single beat ECG

waveforms are not of a comparable format to clinically recorded ECG time series of at least multiple seconds.

Thus, a synthesization pipeline was developed to stitch P waves and QRST segments simulated independently of one another together. The synthesized heartbeat was then extended to a 10 s ECG time series while accounting for heart rate variability within a patient or subject. In this way, a dataset of 10,000 simulated ECGs was generated with samples equally distributed among a healthy control group and patients with each of the following cardiac pathologies: interatrial conduction block (IAB), left atrial enlargement (LAE), arrhythmogenic fibrotic atrial cardiomyopathy (FAM), 1st degree atrioventricular block (AVB), right bundle branch block (RBBB), left bundle branch block (LBBB) and myocardial infarction (MI).

## 7.2 Methods

### 7.2.1 Simulation Protocol and Parameter Settings

The simulation parameters for P wave simulations of the healthy cohort and the atrial pathologies (FAM, LAE and IAB) are explained in detail in chapter 8, chapter 9 and by Bender *et al.* [260]. For the ventricular pathologies (LBBB, RBBB, MI) and AVB, P waves of the healthy sinus rhythm control group were used in the subsequent synthesization process (see section 7.2.2). Parameter ranges and modeling methodology for the ventricles are described by Gillette *et al.* [34, 261]. For the healthy control group and each of the pathologies listed above, 1,300 synthetic ECGs were simulated and synthesized, summing up to a total of 10,400 *in silico* ECGs.

80 geometrical models of the atria underlain the simulation of the healthy control group, as well as the FAM and IAB cohorts. They were generated by drawing the eigenvector coefficients of the bi-atrial statistical shape model (SSM) (see chapter 5) from a Gaussian distribution in the  $[-3\sigma, +3\sigma]$  interval (see chapter 8). For the LAE cohort, 45 additional anatomical models were generated by optimizing the SSM's eigenvector coefficients such that the left atrial volumes were uniformly distributed between 48 and 65 ml which is explained in greater detail in chapter 9. Conduction velocity was assigned to different atrial regions and varied within physiological intervals for all pathology classes and the control group. Fibrosis was modeled as described in chapter 8, key parameters considered in fibrotic remodeling scenarios are summarized in section 8.2.1.2. The atria were placed in a torso volume conductor for which geometrical models were also derived from a human body SSM [179]. The reference position of the atria inside the thorax was defined based on the mean location and orientation of eight patient-specific atrial models in their respective torso geometry [141]. The rotation angle and translation parameters of the heart within the torso around and along all three coordinate axes were varied relative to the reference position in ranges of  $[-15^\circ, +15^\circ]$  and  $[15 \text{ mm}, +15 \text{ mm}]$ , respectively. The Eikonal model was solved with the Fast Iterative (for LAE, FAM and the healthy control group) and the Fast

Marching method (for IAB) to calculate local activation times (LATs) and based thereon, the transmembrane voltage distribution with a Courtemanche *et al.* [91] action potential template as described in section 3.1.2.3. The forward problem was solved with the boundary element method (BEM) (for LAE and IAB) and the infinite volume conductor method (for FAM and the healthy control group) to obtain P waves of the 12-lead ECG. Further details on the simulation protocol and parameter settings for the FAM and healthy cohort, the LAE cohort and the IAB cohort are elaborated on in chapter 8, chapter 9 and in the study from Bender *et al.* [260].

## 7.2.2 Synthesization of P waves and QRST segments

The pipeline for synthesizing single beat P waves and QRST segments from individual simulation runs is outlined in Figure 7.1. ECG segments of atrial and ventricular activity

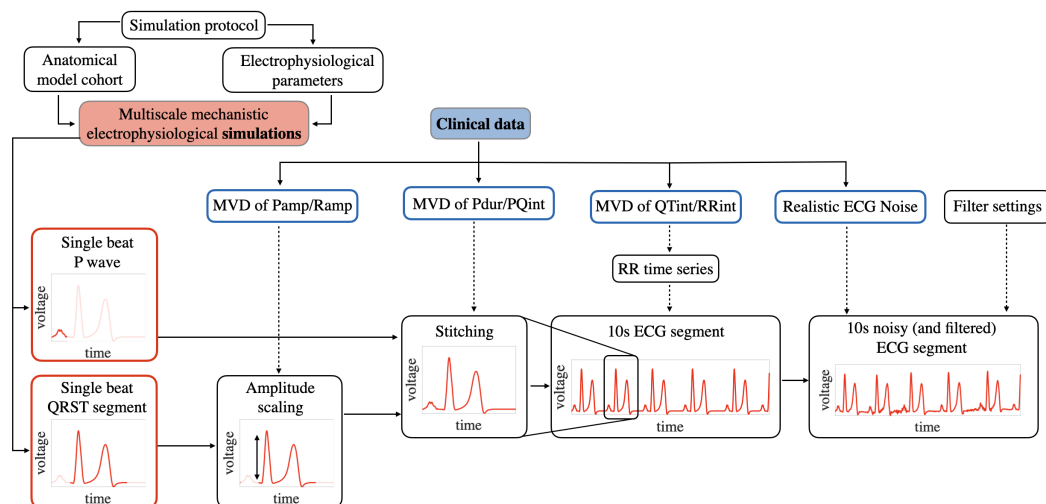


**Figure 7.1: Synthesization pipeline for stitching P waves and QRST segments from separate simulations runs together and generate a 10 s ECG time segment.** Multivariate normal distributions (MVDs) were set up using ECG timing and amplitude features extracted from clinical signals. In this way, R peak amplitudes were first scaled to match the simulated P wave amplitude, a realistic PQ segment was chosen complying with the simulated P wave duration and a mean heart rate was defined based on the QT interval of the simulated QRST segment. An RR time series was generated based on a heart rate variability model to concatenate the resulting single heartbeat to a 10 s signal trace which can optionally be superimposed with realistic ECG noise and band-pass filtered using the recommended cut-off frequency settings.

were generated in separate simulation runs independently from one another. Thus, it was not explicitly ensured that heart and torso geometries for the resulting atrial and ventricular signals are compatible. In particular, P wave and R peak amplitudes were likely to mismatch since also different forward calculation methods were employed for atrial and ventricular simulations. Thus, an amplitude scaling step marked the beginning of the synthesization

process. For that purpose, a multivariate normal distribution (MVD) was set up for P wave amplitude and R peak amplitude extracted from 918 ECGs of healthy subjects in the Physionet Computing in Cardiology 2020 Challenge Database [262] as described previously [263]. The resulting distribution is visualized in Figure 7.2.

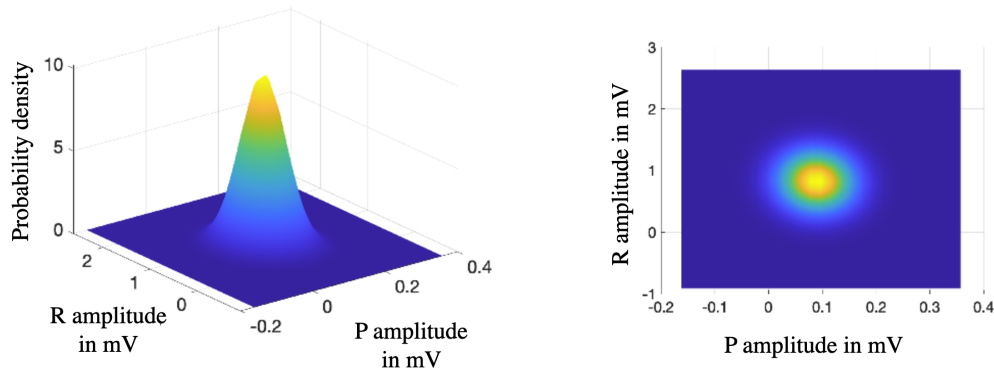


**Figure 7.2: Multivariate normal distribution for R peak and P wave amplitudes.** The left panel shows the probability of specific combinations of R peak and P wave amplitudes in lead II. The right panel represents the same information as a 2D projection with probability densities color coded in the same way as in the figure on the left hand side.

From the P wave simulation result to be synthesized with a QRST segment, the P wave amplitude in lead II was calculated and in this way, a realistic scaling factor for multiplying the respective simulated QRST segment was drawn from the MVD. Likewise, an MVD for P wave duration and PQ interval extracted using ECGdeli [250] from the same clinical database [262] was constructed to sample a time interval for the PQ segment matching the simulated P wave duration. For the AVB pathology class, the PQ segment was constrained to be sampled so that the PR interval quantified to at least 200 ms. The scaled QRST segment could be stitched together with the simulated P wave by inserting a sigmoid function of a length determined by the PQ segment in between. This single simulated heartbeat was then further processed and extended to a 10 s ECG time series as explained in section 7.2.3.

### 7.2.3 Realizing Beat-to-beat Variability Through a Heart Rate Variability Model

Building on an MVD of QT intervals and mean RR intervals, the mean heart rate of the simulated and synthesized ECG signal was determined based on the QT interval extracted from the ventricular simulation outcome. This mean RR interval was used to generate a time series of RR intervals with the heart rate variability model proposed by Kantelhardt *et al.* [264]. Their model considers transient correlation of successive heartbeats and stochastic variation underlying the regulation and change in heart rate over time. By scaling the

QRST segment so that the QT interval matches the single RR interval for every heartbeat and adding a sigmoid TP segment to fill up the remaining ECG samples in between two beats, the 10 s time series of the ECG was constructed. This was subsequently superimposed with realistic ECG noise [265] and filtered with a low- and high-pass filter with their cut-off frequencies set to 150 Hz and 0.5 Hz, respectively.

### 7.2.4 Assessing Fidelity of Simulated Signals

6 timing features (P wave duration, PR interval, QRS duration, QT interval, T wave duration and RR interval) and 5 amplitude features in each lead (P wave amplitude, Q-, R- and S peak amplitudes, T wave amplitudes) were extracted from the resulting simulated database comprising 1,300 signals per pathology class or healthy control group. The same features were extracted from the PTB XL database [16]. This dataset has neither been used before in any calibration step preceding the P wave and QRST simulations in this study nor in the generation of the MVDs and could thus serve as an independent validation resource to assess fidelity of the simulated signals by comparing the resulting feature distributions.

## 7.3 Results

Example ECGs of the *in silico* cohorts for the healthy control group (red curves) and the atrial pathologies (blue curves) are shown in Figure 7.3. Examples for ventricular pathological signals are to be found in appendix B in Figure B.1. Simulated signals exhibit P wave alterations compared to the healthy case characteristic for the specific disease: In LAE signals, the overall P wave duration is slightly prolonged and also P wave terminal force, calculated in clinical practice as the product of interval and amplitude of the negative deflection in lead V1, is increased compared to the healthy control group. Also in IAB signals, P wave duration is increased. Additionally, a change in morphology, polarity and amplitude is visible especially in lead III and aVL. Signal variations in FAM ECGs are more subtle and comprise a marginal increase of P wave duration and a small decrease in P wave amplitude, mostly visible in the anterolateral leads V5 and V6.

The feature distributions for all timing features and the amplitude features in lead II for the simulated and clinical healthy control group are depicted in Figure 7.4. It gets apparent from Figure 7.4, that the features extracted from the simulated cohort lie within the ranges of those extracted from clinical signals. Large deviations, however, are visible in the T wave amplitude that ranged until 1 mV in the simulated cohort, whereas the largest values in the clinical signals did not exceed 0.5 mV.

In Figure 7.5, the distributions of characteristic features used for a diagnosis of each atrial disease are compared to the respective distribution of the healthy control group. It is evident, that the trend in feature shifts between healthy control and the pathological cases is consistent between the simulated and clinical LAE cohorts. In the IAB cohort, amplitudes in the lateral limb leads tend to be smaller compared to the respective quantities in the

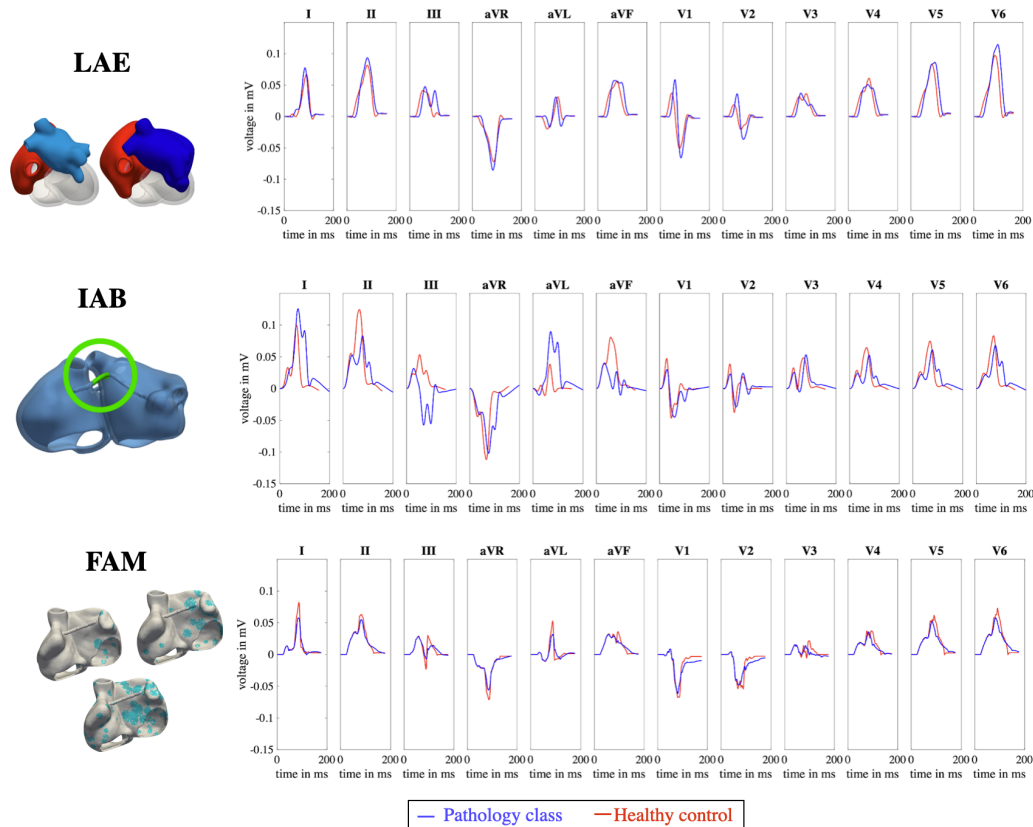


**Figure 7.3:** Example 12-lead P waves for the atrial pathology classes. Red and blue curves represent simulated signals of the healthy control and the LAE, IAB and FAM pathologies from top to bottom row.

healthy control group. Characteristic features for the FAM class comprise P wave amplitude in the anterolateral leads that statistically exhibit smaller values than the ones extractable from the healthy cohort. However, for FAM and IAB, no clinical signals were available in PTB XL. A comparison with measured P wave features from another clinical data source is shown in detail for the FAM class in section 8.3.2. A quantitative validation of IAB P wave timing, amplitude and morphology features was carried out by Bender *et al.* [260] (see section 7.4). Feature distributions for the AVB class and the ventricular pathologies are shown in appendix B in Figure B.2.

## 7.4 Discussion

In the study presented in this chapter, a large scale dataset of 10,000 simulated 12-lead ECGs each of 10 s length was compiled and validated against clinical signals. The synthetic database will be published and made openly available to the community together with a complete list of parameters underlying the generation of each signal. Besides a healthy

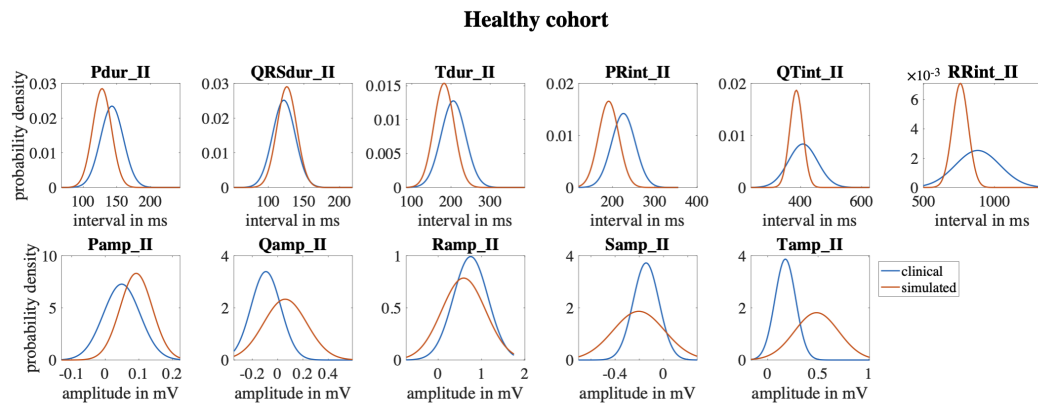


**Figure 7.4: Feature distributions for the healthy control group.** Red and blue curves represent the probability density of the extracted feature values from the simulated and clinical ECGs, respectively. The top row shows the interval features, the bottom row the amplitude features calculated in lead II.

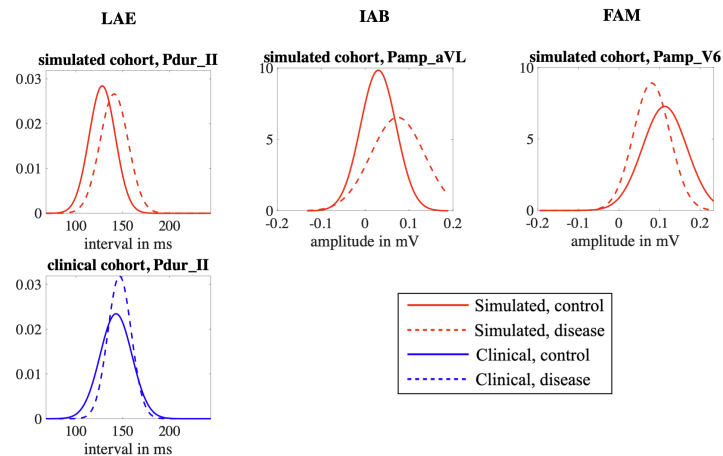


**Figure 7.5: Feature distributions for the atrial pathologies compared to the healthy control group.** Red and blue curves represent the probability density of the extracted feature values from the simulated and clinical ECGs, respectively. Dashed and solid lines show the distributions of the pathologies (from left to right: LAE, IAB, FAM) and healthy control, respectively.

control group, pathologies covered in this *in silico* dataset comprise FAM, LAE and IAB as examples for atrial diseases, AVB as an example for atrioventricular conduction disorders, as well as LBBB, RBBB and MI as examples for ventricular pathologies. These pathologies reflect in altered ECG signal characteristics of different degrees. Thus, the generated ECGs are particularly suitable as a benchmark dataset to develop machine learning algorithms for automated signal analysis and arrhythmia classification, even for difficult classification tasks requiring the detection of subtle signal variations. The simulated dataset fulfills important properties essential for developing such ECG-based computer assisted diagnostic tools: It contains a large number of signals in contrast to most data sources of clinically recorded ECGs [262], the number of samples per pathology class is equally distributed and the ground

truth of the underlying pathology did not need to be annotated by cardiologists, but was instead defined by parameter changes in the underlying simulation run and are thus precisely known. As such, the presented dataset can be employed for transfer learning tasks, i.e., to pre-train a machine learning classifier on simulated data and fine-tuning it using the actual clinical ECGs. In this way, the learning process can be considerably expedited and streamlined, as the network can build on prior knowledge and experience instead of learning dependencies in the input data from scratch. However, an important prerequisite for successful pre-training of a network is a small domain gap between the dataset for initializing the network's weights and the actual data the network's performance should be optimized for. Therefore, an explicit validation step ensuring that the *in silico* ECGs are representative and realistic compared to clinically measured signals is indispensable. Moreover, the presented database allows for full traceability of altered ECG characteristics with regard to underlying cellular, anatomical and tissue properties, as parameter sets defined for each simulation run are available for each ECG signal.

In the study presented in this chapter, the validation of the simulated ECGs was performed by annotating fiducial points in the 12-lead signal, delineating single waveforms and extracting common timing and amplitude features therefrom. The comparison with clinical ECG features extracted in the same way showed that simulated ECG features lied mostly within the range of the clinical intervals in the healthy case. However, simulated T waves showed too high amplitudes compared to clinical feature statistics, most likely having occurred due to too high action potential duration gradients in apico-basal direction mapped onto the  $\tau_{close}$  parameter in the Mitchell-Schaeffer ionic model [266]. The comparison of feature statistics also shows that the simulated data do not cover the full range of the feature variation in the clinical case. Especially RR intervals exhibited a much more narrow distribution around a mean of 750 ms compared to clinical features. However, the mean RR interval in the *in silico* dataset was defined using an MVD based on the simulated QT interval, for which the feature distribution was also smaller and shifted to smaller time values compared to the clinical case. It can thus be concluded that the simulated feature statistics are consistent in themselves and do not exhibit unrealistic feature combinations within the same signal. Simulated signals not covering the entire range of clinically measurable feature values might have occurred due to insufficient simulation parameter variation not exploiting the full physiological ranges.

In the pathological cases, the shift and change of feature statistics compared to the healthy control case was compared among simulated and clinical data. For all pathologies where corresponding data was available in the clinical PTB XL dataset, the changes in feature statistics were consistent between *in silico* and clinically measured ECGs (compare Figure 7.5 and Figure B.2). PTB XL lacked the respective signals for the FAM and the IAB pathology class, inhibiting a similar approach for the ECGs in these classes. However, a detailed comparison of simulated and clinical P wave features for the FAM class was carried out using a different clinical dataset in chapter 8. The change in P wave amplitude in V6 as shown in Figure 7.5 (left panel) can be attributed to the chosen fibrosis remodeling methodology, as 50 % of the elements in fibrotic patches were modeled as passive conduction barriers not contributing to the overall source distribution in the heart and thus causing a

decreased P wave amplitude on the body surface. Bender *et al.* [260] presented the generation and validation of simulated P waves for the IAB pathology class and discussed the resulting feature variations in detail. They found that P wave amplitude variation in lead aVL as visible in Figure 7.5 (middle panel) arose specifically due to conduction blockage in Bachmann's bundle and the accompanying retrograde activation of the left atrium.

The 10 s time series of synthetic ECGs were generated by concatenating P waves and QRST segments simulated independently from one another. Different methods for solving the forward problem of electrocardiography were employed for the atrial and ventricular simulations and moreover, different torso volume conductors were used in the simulation runs of atrial and ventricular signals which were later concatenated to the ECG time series. Even though an amplitude scaling step was introduced to prevent the generation of an ECG heartbeat exhibiting non-matching amplitudes of P waves and QRS complexes, it is not ensured that the chosen atrial and ventricular anatomical and electrophysiological parameters underlying the generation of one specific ECG signal are compatible.

Anzlinger [267] presented a different approach for synthesizing single beat P waves and QRST segments to a time series of 10 s ECGs. They extracted intra-patient variability in various ECG features from clinical data and sampled scaling factors for amplitude and time intervals to vary single P waves and QRST segments to be concatenated to the resulting time series signal. However, this approach lacks the possibility of representing correlating RR intervals of subsequent beats. Furthermore, mutually dependent ECG features, e.g. QT- and RR intervals, were not accounted for, potentially leading to inconsistent ECG feature distributions within the same patient or subject. Therefore, the heart rate variability model developed by Kantelhardt [264] was implemented for this study to generate realistic RR interval time series and MVD feature distributions were generated based on an independent clinical ECG dataset to take dependencies of intra-patient feature variations into account.



IMPROVING NON-INVASIVE RISK  
STRATIFICATION OF ATRIAL  
FIBRILLATION THROUGH  
MACHINE LEARNING AND *IN  
SILICO* ECG DATA



---

# Estimation of Left Atrial Fibrosis

In this chapter, the capability of neural networks applied to simulated and clinical P waves to estimate the volume fraction of fibrotic substrate in the atria is examined. In this way, the potential of the 12-lead electrocardiogram (ECG) as a non-invasive and cost-effective tool for the early detection of fibrotic atrial cardiomyopathy can be gauged to ultimately stratify atrial fibrillation (AF) propensity.

*The content of this chapter is taken from a paper and two conference proceedings that have all been published open access under licence CC-BY 4.0 in Journal of Clinical Medicine [122], Current Directions in Biomedical Engineering [268], and Computing in Cardiology [269]. Most passages in this chapter have been quoted verbatim from the publications.*

## 8.1 Introduction

The clinical picture of AF is characterized by disorganized reentrant waves traversing the atrial tissue and causing an irregular heart rhythm (see section 2.3). The maintenance of the arrhythmia requires either sustained rapid ectopic foci firing or a single ectopic focus acting as an AF driver in regions of vulnerable atrial substrate. Hence, fibrotic tissue having undergone structural and electrical remodeling processes provides the necessary substrate to contribute to the perpetuation of AF [270, 271]. Disease mechanisms contributing to fibrotic remodeling of atrial tissue include an increased deposition of collagen strands and other extracellular matrix proteins in the interstitial space. The accumulation of collagenous septa implies the separation and electrical decoupling of myocytes and thus restricts the electrical depolarization wave to propagate via alternate conduction pathways. With increased conduction anisotropy, slowed conduction due to down-regulated gap junction proteins, and the formation of unidirectional conduction blocks, fibrotic patches provide an arrhythmogenic substrate for the initiation and maintenance of functional and anatomical re-entry patterns.

Quantifying the amount of these arrhythmogenic substrate areas could thus be an important means for individual risk stratification of new-onset AF and arrhythmogenic fibrotic atrial cardiomyopathy (FAM) [272, 273]. Moreover, it could serve as a basis for suggest-

ing susceptible patients for AF screening, choosing an appropriate treatment strategy, and reducing the risk of accompanying co-morbidities [81].

Catheter ablation is a common treatment option in clinical practice for the purpose of blocking certain conduction pathways in the atria that are suspected to contribute to the onset and maintenance of the arrhythmia. However, the optimal choice of these ablation targets beyond pulmonary vein isolation is challenging and calls for a personalized approach. AF recurrence rates between 20 and 60% in patients with large arrhythmogenic substrate areas in the atria [274] underline the need to tailor therapy to the substrate [275–278]. Accordingly, scarring of additional targets in those patients was suggested to improve the ablation outcome [31, 279–281]. Quantifying the amount of atrial fibrosis non-invasively using the ECG could thus contribute to select patients suitable for ablation and contribute to a more effective treatment of AF [279].

High intensity areas on late Gadolinium enhancement magnetic resonance imagings (LGE-MRIs) as well as low bi- and unipolar electrogram voltages [80, 216, 282] recorded during electrophysiological studies are currently drawn on to identify the amount and spatial location of scars and fibrosis on the atrial endocardial wall. However, LGE-MRI is a cost-intensive imaging technique for which technical parameters have to be carefully selected. Additionally, segmentation of magnetic resonance (MR) images is cumbersome and challenging [201]. Furthermore, electroanatomical mapping is an invasive and time-consuming procedure with inter-electrode spacing and electrode sizes being additional confounding factors influencing electrogram voltages [283].

To circumvent these shortcomings, the 12-lead ECG as a commonly available and easily usable tool in clinical practice could feature a way to quantify the fibrotic left atrial volume fraction and in consequence predict the propensity to future AF incidents [284]. The duration of the P wave in the 12-lead ECG has been shown to correlate with the amount of left atrial (LA) low-voltage substrate in AF patients if a low threshold for determining P wave on- and offsets are chosen [273, 285–287]. P wave terminal force in V1 (PTF V1) has been identified as sensitive to a change in conduction velocity in the atria [176], which is typically caused by fibrotic substrate in AF patients. Also P wave dispersion, i.e., the difference between latest and earliest detectable P wave offset across all 12 ECG leads, has been shown to be a measure for locally heterogeneous conducting tissue regions [272]. Other ECG-based predictors for the onset of AF and for the presence of low-voltage areas include P wave amplitude [288, 289], P wave area in V3 [290] and root mean squared (rms) voltage in the terminal P wave signal parts [291].

However, these P wave-derived features are not only affected by fibrotic infiltration of atrial tissue. P wave duration (PWd) and dispersion are also influenced by changes in conduction velocity and atrial anatomy [169] that both vary between different subjects within healthy reference ranges [215, 292, 293]. Furthermore, PTF V1 is highly dependent on the placement of the electrodes on the thorax [294]. Lastly, different thoracic geometries yield different P wave amplitudes, which might additionally be impaired by loose electrode contact.

Therefore, the aim of the study presented in this chapter was to quantify which changes in P wave morphology, amplitude and duration can be attributed specifically to fibrotic infiltration of atrial tissue. Furthermore, it was investigated if these effects on the P wave can be separated from confounding changes induced by healthy anatomical variation of the atria and the thorax as well as different electrode positions. For that purpose, various anatomical model combinations were composed constituting of different geometries for atria and torsos as well as different orientation angles of the atria within the torso. Electrophysiological simulations with inclusion of fibrotic regions in the atria of different volume fraction were conducted in sinus rhythm wherefore a set of different baseline conduction velocities (CVs) in healthy reference ranges were imposed to also account for functional variation within the virtual cohort. Subsequently, changes in P wave features caused by geometry and rotation angle variations (section 8.3.1) were compared to those caused by local atrial substrate modifications (section 8.3.2). The results thereof were employed to estimate the fibrotic LA volume fraction from simulated P wave features with neural networks in section 8.2.4.

For a successful clinical translation of the proposed ECG-based fibrosis estimation method, the network needs to fulfill the requirement of low sensitivity to inaccurately extracted feature values which is addressed in section 8.3.3.4. This is because the proposed regression model would rely on features extracted from simulated P waves of the 12-lead ECG. Those features might be easily and robustly extractable from noise-free simulated signals, but their values are subject to several disturbances in the clinical use case. It was therefore quantified how sensitive the network would be towards inaccurately determined feature values and to what extent the network's estimation of the fibrotic volume fraction would still be reliable if the feature values were superimposed with noise (see section 8.3.3.4).

Finally, to investigate the expediency and applicability of the proposed methods in a realistic clinical use case, the developed network is applied to measured clinical ECGs (see section 8.2.2).

## 8.2 Methods

### 8.2.1 *In silico* Database

#### 8.2.1.1 Virtual Patient Cohort

In order to generate a large-scale dataset of P waves representing a virtual patient cohort characterized by different anatomical properties, various atrial and thoracic geometries were derived from statistical shape models (SSMs). The bi-atrial SSM described in detail in chapter 5 [169] was used to generate 80 random volumetric instances of the atria augmented with homogeneous wall thickness, rule-based fiber orientation [213], tags for anatomical structures and inter-atrial connections [200]. An exemplary instance is shown in Figure 5.5.

Furthermore, 25 thoracic geometries were generated by varying the two leading eigenvectors of the model developed by Pishchulin *et al.* [179] systematically in the  $[-2, 2]\sigma$  range. The first two eigenvectors account for approximately 80% of the total shape variance. The first two eigenmodes, i.e., the shape variability resulting from a variation of only the respective eigenvector, are visualized in Figure 8.1. A variation of both of them reflects in a change of the torso size in superior-inferior direction and in anterior-posterior direction in both the chest and the abdominal regions. In this way, height, weight and gender variation could be accounted for in the virtual cohort.

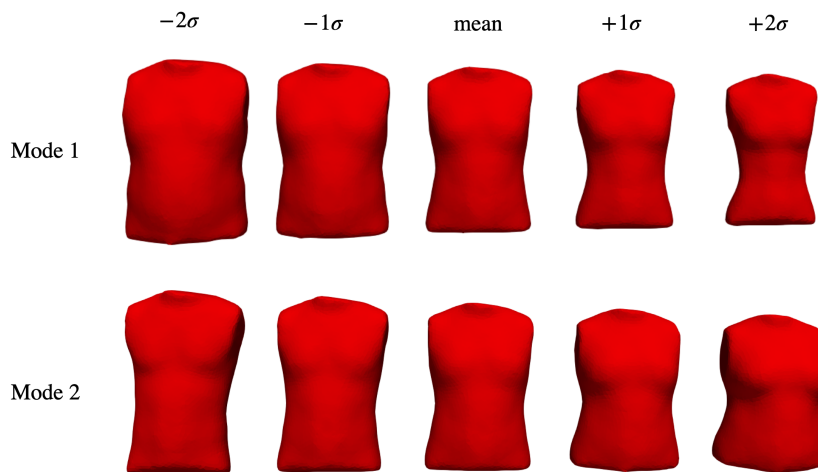


**Figure 8.1: Representation of eigenmodes of the upper body statistical shape model.** The first eigenmode (top row) reflects in a change of the torso size predominantly in the abdominal region, the second one (bottom row) in the chest region.

Each of the 80 atrial geometries were rotated by  $-20^\circ$ ,  $0^\circ$  and  $+20^\circ$  around the x-, y- and z-axes [295] leading to 27 permutations of different orientation angles for each individual atrial geometry. Combinations of every rotated atrial geometry placed in each of the 25 thoracic geometries were realized and thus a set of 54,000 anatomical models were obtained. The different model and parameter combinations are illustrated in Figure 8.2. For each of these combinations, electrophysiological simulations were conducted in sinus rhythm and the 12-lead ECG was extracted at the standardized electrode positions. The sinus rhythm simulations were repeated with electrical and structural remodeling of different degrees for all model combinations. For that purpose, the ionic and tissue parameters were modified as described in section 8.2.1.2 in selected tissue patches covering 0%, 5%, 10%, 15%, 20%, 25%, 30%, 35%, 40% and 45% of the total LA myocardial volume. In this way, the virtual cohort comprised a total of 540,000 (80 atria geometries  $\times$  25 torso geometries  $\times$  27 rotation angles  $\times$  10 volume fractions covered by fibrosis) anatomical model combinations of healthy subjects and FAM patients. These were subject to the electrophysiological simulations described in section 8.2.1.3 to finally obtain 642,400 12-lead ECG signals evaluated and processed for the analysis described in sections 8.2.3 and 8.2.4.

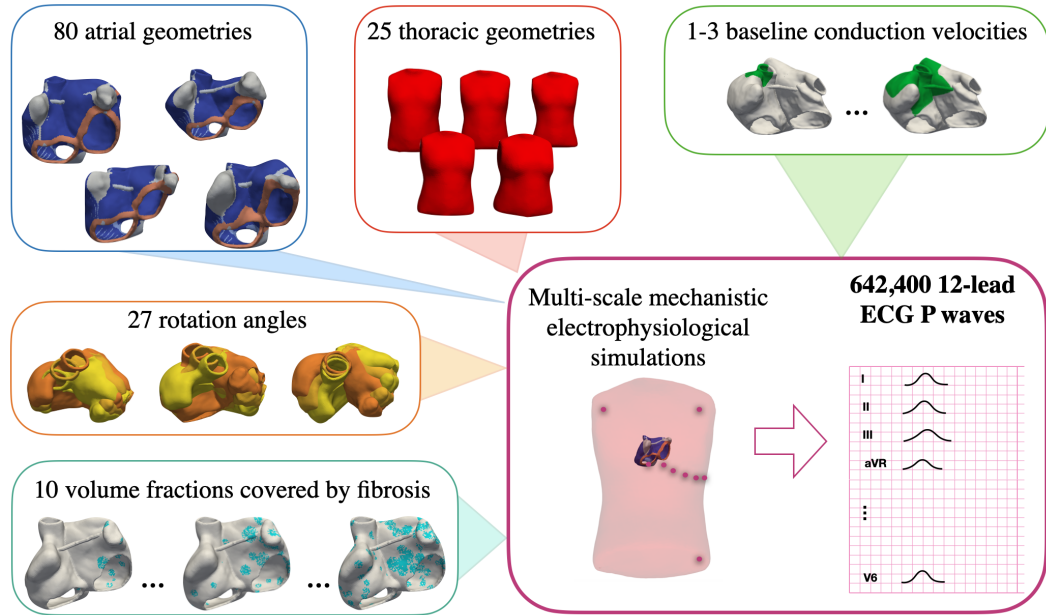


**Figure 8.2:** Representation of the different model combinations. A total of 642,400 P waves were simulated for a virtual patient cohort characterized by anatomical and functional variability as well as fibrosis covering different volume fractions of the atrial tissue.

### 8.2.1.2 Modeling Methodology of Fibrotic Tissue

For each atrial model, variants with fibrosis covering 0%, 5%, 10%, 15%, 20%, 25%, 30%, 35%, 40% and 45% of the total LA myocardium volume were created. Subsequently, the volume fraction of right atrial fibrosis was defined for each case according to the findings from Akoum *et al.* [296] (Table 8.1).

**Table 8.1:** Volume fraction of fibrosis in the right atrium for each Utah stage as reported by Akoum *et al.* [296].

| Utah Stage | Fibrotic LA volume fraction | Fibrotic RA volume fraction |
|------------|-----------------------------|-----------------------------|
| Utah I     | 0 - 5%                      | $1.27 \pm 0.38\%$           |
| Utah II    | 5 - 20%                     | $4.65 \pm 0.70\%$           |
| Utah III   | 20 - 35%                    | $9.40 \pm 2.16\%$           |
| Utah IV    | >35%                        | $12.66 \pm 3.0\%$           |

Considering the patchiness of fibrosis observed in AF patients [297], several disconnected patches on the atrial surface were defined as fibrotic accumulating to the total left atrium (LA) volume fraction of fibrosis. Each of these individual fibrotic patches was defined by a center seed point and a radius around it. The total number of seed points and the sizes

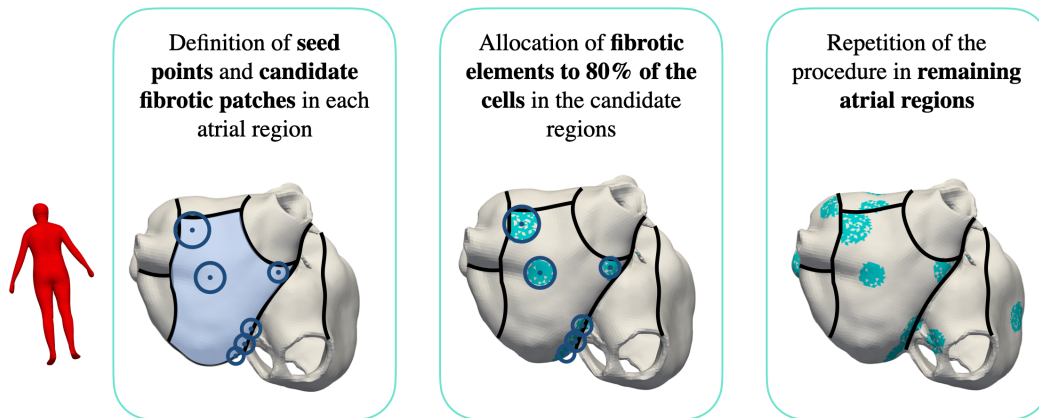


**Figure 8.3: Definition of the spatial distribution of fibrotic tissue.** The atrial geometry was first separated into 6 subregions for the left and 2 subregions for the right atrium as reported by Akoum *et al.* [296] and Higuchi *et al.* [145] indicated by the black separation lines. The stage of fibrosis to be modeled was then set (15% in this example) and the number of seed points and radii around them were chosen pseudo-randomly by ensuring that within each of these subregions, the total volume of fibrotic elements accumulated to the spatial fibrosis distribution found in clinical studies [145, 296]. 80% of the cells in these candidate regions were defined as fibrotic (middle column) and this process was repeated for all subregions (right column).

of the radii were chosen depending on the total volume fraction of fibrosis to be covered. The positions of the seed points for the patchy fibrotic regions were defined by taking the spatial distribution of fibrotic atrial substrate as reported by Higuchi *et al.* [145] for the left and Akoum *et al.* [296] for the right atrium into account. Radii randomly chosen in a range of [3, 6] mm around these seed points determined the candidate regions of fibrosis in the atria. To not only account for the patchy nature of fibrotic tissue, but also for its diffuse appearance, around 80% of the cells within the candidate regions defined above were assigned to the fibrotic substrate (compare Figure 8.3 (middle and left column)). In these substrate regions, the simulation parameters were adjusted as described in the following to account for structural and electrical fibrotic remodeling.

Fibrosis infiltrating the regular myocyte tissue structure cause adjacent myocytes to be electrically decoupled and thus act as passive barriers to the propagating wavefront. The concept of percolation [128] was drawn on to account for this phenomenon in the simulations. 50% of the cells within the fibrotic regions were therefore defined as belonging to the extracellular matrix. Hence, these cells impair the normally straight conduction across the tissue and constrain the intracellular depolarization wave to pass around the fibrotic barriers [81]. In the remaining 50% of the cells belonging to the fibrotic regions, maximal ionic conductances were rescaled as suggested by Roney *et al.* [82] to account for cytokine-induced remodeling (50%  $g_{K1}$ , 60%  $g_{Na}$ , 50%  $g_{CaL}$ ) [48]. Furthermore, conduction velocities were reduced by 80% in transversal and 50% in longitudinal direction, which in turn caused anisotropy ratios to be increased by a factor of 2.5. In this way, local CV heterogeneities and anisotropic wavefront propagation was accounted for facilitating functional reentry in AF patients [298].

### 8.2.1.3 Electrophysiological Simulations

For each atrial model and volume fraction covered by fibrosis, simulations were performed by solving the anisotropic Eikonal equation with the fast iterative method [158]. For all simulations, excitation was initiated from a sinus node trigger located at the junction of the superior caval vein and the right atrial appendage [149]. The atrial wall was separated into five different anatomical regions: bulk right and left atrium, inter-atrial connections, pectinate muscles, crista terminalis and inferior isthmus. For each of these regions, the anisotropy ratio and baseline (B) conduction velocity in transversal ( $\perp$ ) fiber direction  $CV_{\perp,B}$  were chosen as reported previously [149] (Table 8.2). For simulations involving fibrotic tissue areas, two additional anatomical regions were included as described in section 8.2.1.2: Non-conductive elements were characterized by a conduction velocity of  $CV_{\perp} = 0$  mm/s and CV was reduced by 80% in slow conducting cells. Anisotropy ratio in slow conducting tissue was increased by a factor of 2.5 compared to baseline.

**Table 8.2:** Conduction velocities in transversal fiber direction and anisotropy ratios.

| Tissue region              | $CV_{\perp,B}$ in m/s  | Anisotropy ratio |
|----------------------------|------------------------|------------------|
| Bulk right and left atrium | 0.591                  | 2.090            |
| Crista terminalis          | 0.591                  | 2.843            |
| Pectinate muscles          | 0.461                  | 3.780            |
| Inter-atrial connections   | 0.645                  | 3.339            |
| Inferior isthmus           | 0.540                  | 1                |
| Fibrosis (non-conductive)  | 0                      | NA               |
| Fibrosis (slow conducting) | $0.2 \cdot CV_{\perp}$ | $2.5 \cdot AR$   |

To additionally account for functional variability within the virtual cohort, 1-3 different CV values in the interval  $[-20\%, +20\%] \cdot CV_{\perp,B}$  were sampled in each region assuming a uniform distribution for each of the 540,000 anatomical model combinations described in section 8.2.1.1.

By solving the Eikonal equation, the spread of electrical activation in sinus rhythm was computed and local activation times (LATs) were obtained at each node. By shifting a Courtemanche *et al.* [91] action potential template in time according to the calculated LATs as proposed by Kahlmann *et al.* [299], the transmembrane voltage distribution on the atria was obtained. A remodeled Courtemanche action potential as described in section 8.2.1.2 was used for cells in slow conducting fibrotic areas representing cytokine-induced remodeling.

For each model combination explained in section 8.2.1, the atria were assumed to be embedded in an infinite volume conductor of conductivity  $\sigma_s = 0.2$  S/m [139]. The extracellular potentials were extracted at the respective electrode positions [300] and used to derive the P wave of the standard 12-lead ECG. For analyzing the influence of the V1 electrode position

on PTF V1, the 12-lead ECG was also extracted from the electrophysiological simulations with the reference atria and torso geometry for varying positions of the V1 electrode. The latter was varied within a radius of 6 cm around the standard V1 electrode position.

The raw ECGs simulated in this way were subject to feature extraction (see section 8.2.3) to systematically evaluate the influence of healthy anatomical, functional and pathological variation on ECG features (see sections 8.3.1 and 8.3.2) and assess whether these features carry diagnostically relevant information to estimate the LA volume fraction of fibrosis with neural networks (see section 8.3.3). To systematically investigate the influence of inaccurately extracted features, Gaussian noise was added directly to the extracted feature values as described in detail in section 8.3.3.4. For the translational study described in section 8.2.2, realistic ECG noise as generated by Petrenas *et al.* [265] was added to the simulated signals before applying high- and lowpass filters with cut-off frequencies of 0.5 Hz and 150 Hz as recommended by Kligfield *et al.* [301], respectively.

## 8.2.2 Clinical Database

From 27 AF patients who underwent an electroanatomical mapping procedure at Städtisches Klinikum Karlsruhe and University Hospital Essen, bipolar electrograms as well as 12-lead ECGs in sensed paced rhythm were recorded (see Figure 8.4, left panel). The patients' age ranged between 49 and 84 years ( $67.19 \pm 8.64$  years) and 11 out of the 27 patients were women. Patients provided informed consent and the study was approved by the institutional review boards. Detecting the activity at the pacing site from the electrograms allowed to select time windows of normal sinus rhythm activity in the ECG traces (green highlighted intervals in Figure 8.4). ECGdeli [250] was applied to automatically delineate the P waves in the 12-lead ECGs in sinus rhythm. Furthermore, the fraction of fibrotic substrate in the left atrial endocardium was calculated for each patient by identifying the areas where bipolar peak-to-peak voltage in the intracardiac electrograms was below 0.5 mV. P waves were also delineated using ECGdeli in the 12-lead sinus rhythm ECGs of 7,185 healthy subjects from the public PTB-XL dataset [16] (see Figure 8.4, right panel).

In this way, a total of 68,282 single clinical P waves from 7,185 subjects in the control group and 42,227 single P waves from 27 patients with an extent of fibrotic left atrial areas between 7.05 % and 77.28 % were used as clinical input for the machine learning classifiers.

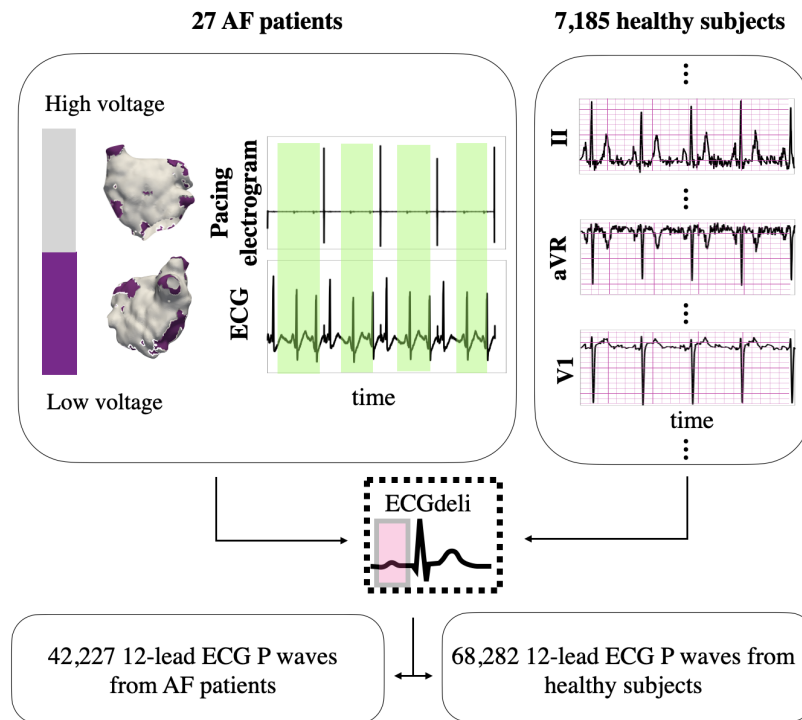


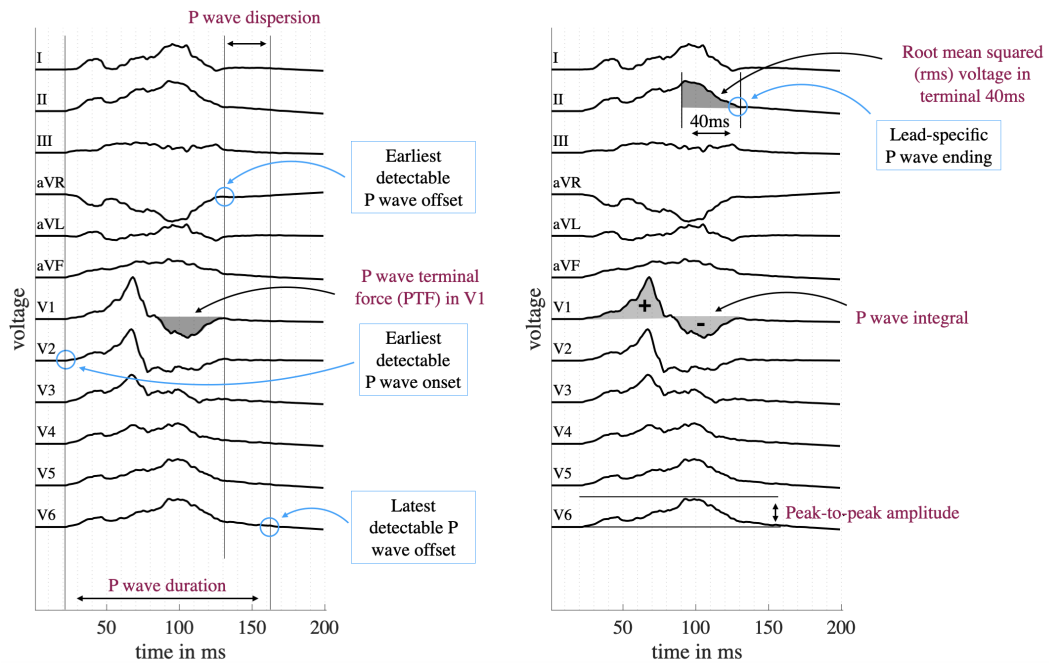
**Figure 8.4: Clinical ECG data from 27 AF patients and 7,185 healthy individuals applied for clinical translation of the fibrosis estimation methods.** Time periods of normal sinus rhythm activity were extracted from the ECG recordings in sensed paced rhythm (green intervals in the left panel) and ground truth fibrotic volume fraction was calculated as the surface area fraction where bipolar voltage was below a threshold of 0.5mV. The delineation tools from ECGdeli allowed to extract P waves from the AF and healthy ECG recordings which were subsequently fed into the feature extraction pipeline (right panel).

### 8.2.3 ECG Analysis and Feature Extraction

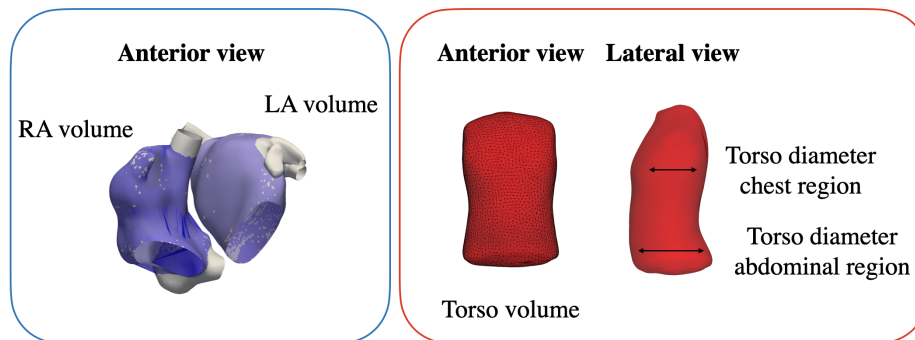
For each of the resulting 642,400 simulated and 110,509 clinical P waves of the 12-lead ECG, the following features were calculated: duration, dispersion, terminal force in V1, peak-to-peak amplitude in each lead, P wave integral as well as the rms voltage in the entire signal and terminal 20, 30 and 40 ms of the ECG signal trace. These features have been shown to correlate with the presence of fibrotic atrial tissue in previous work [176, 273, 288–291] and are visualized in Figure 8.5.

In some of these previous studies, it was also shown that not only fibrosis but also anatomical and functional variability prevailing in a healthy cohort have an impact on ECG features. Therefore, the network performance was anticipated to decrease for samples with extraordinary high and low LA volumes. Thus, 5 additional non-invasive features representing LA and RA volume, torso volume and torso diameter in anterior-posterior direction in the chest and the abdominal region were optionally included when training the network.

PWd was calculated as the time difference between the latest detectable P wave offset and the earliest detectable P wave onset across all 12 leads. For that purpose, the P wave onset and offset was retrieved for each channel individually. In simulated signals, only the actual electrical activity originating from the depolarization of the atria reflects in the simulated P waves and no interfering noise sources superimpose the simulation outcome. Therefore, the P wave endings and beginnings were annotated with simple thresholds defined above the isoelectric line for the simulated cohort. ECGdeli [250] annotations for retrieving P wave on- and offsets had to be relied on for the clinical dataset. P wave dispersion was subsequently derived by computing the time difference between the latest and earliest detected P wave ending across all 12 leads. To calculate PTF V1, the time difference between the detected P wave ending in V1 and the signal crossing the isoelectric line between positive and negative deflection was multiplied with the minimum amplitude in V1. The peak-to-peak amplitudes were obtained by subtracting the minimum from the maximum P wave signal value in all 12 leads individually. P wave integral in each lead was approximated with the trapezoidal rule. The root mean square voltages were calculated as the square root of the accumulated squared voltage values in the respective time interval extending in negative time direction from the individually detected P wave offset in each lead. Features that were extracted from only selected or all leads at once are visualized in Figure 8.5 (left panel), along with features that were extracted for each of the 12 leads individually (right panel) and anatomical measures (bottom panel).



(a) P wave features extracted from all leads at once or only for selected leads (left) and from all leads separately (right).



(b) Features for anatomical measures of the atria (left) and the torso (right).

**Figure 8.5: Feature extraction.** The top panel shows the P wave derived features (purple) that were extracted from the simulated and clinical ECGs. Blue marked samples represent characteristic bounds automatically detected in the ECG trace as a basis to compute the P wave derived features. The bottom panel shows the additional features representing anatomical atrial and thoracic measures.

## 8.2.4 Regression using Neural Networks

To evaluate whether and to what extent the influence of healthy inter-individual anatomical variability on the P wave can be separated from changes caused by atrial fibrosis, a regression neural network was set up. The built-in function fitting neural network in MATLAB was used with 2 hidden layers comprising 10 and 5 neurons each. The network's dimensions

were increased compared to the algorithms applied in Nagel *et al.* [122] to account for the increased problem complexity arising from providing 60 additional features as input parameters to the network. In total, 75 P wave-derived features described in detail in section 8.2.3 and optionally 5 additional features for anatomical measures could serve as input for the network:

- **P wave features extracted from only selected or all leads at once**
  - P wave terminal force in V1
  - P wave duration
  - P wave dispersion
  
- **P wave features extracted for all 12 leads individually**
  - P wave integral
  - root mean squared voltage in terminal 40 ms
  - root mean squared voltage in terminal 30 ms
  - root mean squared voltage in terminal 20 ms
  - root mean squared voltage in the entire signal
  - peak-to-peak amplitudes
  
- **Anatomical measures**
  - left atrial volume
  - right atrial volume
  - torso volume
  - torso diameter in anterior-posterior direction in the abdominal region
  - torso diameter in anterior-posterior direction in the chest region

Bayesian regularization was chosen as a training algorithm to predict the volume fraction of LA fibrosis as an output. To evaluate the network's performance, 6-fold cross validation was applied wherefore P wave feature data were split into 6 subsets. P waves generated with one specific atrial geometry (in case of simulated data) or extracted from the ECG of one specific patient (in case of clinical data) were never assigned to different training and testing sets in one split but instead kept all in the same set ('pseudo-random split') as proposed by Luongo *et al.* [228]. This procedure ensured that the network is blinded to previously unseen atrial geometries and patient data during testing and does not link P wave features in the test set to nearly the same feature values seen in the training set caused, e.g., only by a slight rotation of the atria in case of simulated data. Luongo *et al.* [228] also found that excluding thoracic instead of atrial geometries during training still leads to good generalization results, which is why it was decided to allocate the pseudo-random splits using certain atrial geometries exclusively during testing.

For each split, the simulated and clinical data were divided into 6 sets by combining clinical P wave features of 1796-1797 healthy subjects and 4-5 AF patients with features extracted from the simulated dataset generated based on 13-14 different atrial geometries. Thus, the entire dataset was divided into groups of 67%, 17% and 17% for training, validation, and testing, respectively. 6-fold cross-validation was performed by employing one of these subsets at a time as a test set and using the remaining 5 sets for training and validation. Through this procedure, it was ensured that P wave features extracted from one patient are only included in either of the training, validation or test set, and that the testing of the trained network is only performed based on the P waves from patients the network has never seen before.

The network was trained 10 times for each of the 6 pseudo-random train-validation-test configurations for a maximum of 1000 epochs each. Its performance was assessed by taking the mean of the absolute root mean squared error (rmse) between the predicted and the actual volume fraction of LA fibrosis among all 10 training iterations.

The network was trained and tested using different input feature and data source configurations to shed light on the following research questions:

#### RESEARCH QUESTIONS

A: Does the network benefit from being provided simulated data as an additional input data source when estimating the atrial fibrotic extent with clinical ECGs?

B: Does the addition of realistic ECG noise and the application of different low-pass filter settings on simulated training data have an impact on the network performance when trained on a hybrid dataset?

C: Do anatomical measures of the atria and the torso complementing P wave-derived features as additional input data contribute to an improved network performance?

D: To what extent is the network's estimation of fibrotic volume fraction still reliable if input feature values are corrupted by noise?

To quantify the added value that simulated data can contribute to improving the estimated fibrotic volume fraction (A), the machine learning regression model outcome was compared

when trained once by only using features from the clinical ECGs and once by additionally providing simulated data during training.

The influence of filter settings and the preceding superposition of simulated data with realistic ECG noise (B) was assessed by comparing the network output on the same clinical test set when either trained with only clinical data or with a hybrid dataset for which the simulated data were subject to different preprocessing steps (noise-free and without filtering, addition of noise and 150 Hz low-pass filtering, addition of noise and 40 Hz low-pass filtering).

The impact of additional input data consisting of anatomical measures (C) on the network performance was evaluated by training the network once by only using simulated P wave-derived features and once by extending these simulated features with the anatomical measures from the geometries that were employed for the respective simulation run. Building on the analysis described in section 8.3.1, it could be reasonable to assume that specific P wave features are highly dependent on the anatomical properties of the (virtual) patient and thus, the network's performance would decrease systematically for samples with extraordinary high and low atrial volumes or anatomical torso measures. It was therefore evaluated if a potential systematic under- and overestimation for data samples of low and high atrial and torso sizes can be avoided and compensated for by additionally providing features representing anatomical measures as input to the network. As values for the anatomical measures were not available for the clinical ECG data, the analysis was carried out on simulated data only.

An important aspect for a successful clinical translation consists of the network's sensitivity towards inaccurately determined feature values. Although the ECG features are easily and robustly extractable from noise-free simulated signals, their values are subject to several disturbances in the clinical use case. Especially determining PWd is prone to errors since sensitive thresholds are necessary to accurately capture all signal parts belonging to the ECG [122]. Also measuring the volume of the atria, potentially serving as an additional input feature quantifiable non-invasively via echocardiography, is oftentimes inaccurate [88]. It was therefore investigated to what extent the network's estimation of fibrotic volume fractions is still reliable if the feature values were corrupted by noise (D). Furthermore, the analysis could shed light on key features that require accurate feature extraction methods for reliably estimating the amount of fibrosis with the proposed network. To recreate the clinical use case of inaccurately extracted features in a systematic way and controlled environment, the simulated P wave features and the anatomical measures were superimposed with noise. For each feature, 11 noise vectors were realized consisting of Gaussian noise with zero mean and a standard deviation ( $\sigma_N$ ) set to different fractions  $n$  with  $n \in [0, 0.05, 0.1, \dots, 0.5]$  of the standard deviation of the respective feature distribution ( $\sigma_S$ ). By choosing Gaussian noise, it was possible to account for different levels of imprecisely extracted values occurring when applying automated feature extraction software.

The different network configurations set up to address the different aspects described above are summarized in Table 8.3.

**Table 8.3: Different configurations to set up the regression neural network to estimate the amount of LA fibrosis.** Each of them serve the purpose to address the impact of a hybrid training dataset (A), of filter settings and superimposed noise in simulated data (B), additionally using anatomical measures (C) and inaccurately extracted features (D).

| Research question | Network configuration | Training/validation data                         | Testing data            | Input features                                                             |
|-------------------|-----------------------|--------------------------------------------------|-------------------------|----------------------------------------------------------------------------|
| A                 | 1                     | clinical                                         | clinical                | 75 P wave features                                                         |
|                   | 2                     | clinical<br>+ simulated (noise, 150Hz low-pass)  | clinical<br>+ simulated | 75 P wave features                                                         |
| B                 | 1                     | clinical                                         | clinical                | 75 P wave features                                                         |
|                   | 2                     | clinical<br>+ simulated (noise, 150Hz low-pass)  | clinical<br>+ simulated | 75 P wave features                                                         |
|                   | 3                     | clinical<br>+ simulated (noise, 40Hz low-pass)   | clinical<br>+ simulated | 75 P wave features                                                         |
|                   | 4                     | clinical<br>+ simulated (no noise, no filtering) | clinical<br>+ simulated | 75 P wave features                                                         |
| C                 | 5                     | simulated (no noise, no filtering)               | simulated               | 75 P wave features                                                         |
|                   | 6                     | simulated (no noise, no filtering)               | simulated               | 75 P wave features, 5 anatomical measures                                  |
| D                 | 6                     | simulated (no noise, no filtering)               | simulated               | 75 P wave features, 5 anatomical measures                                  |
|                   | 7                     | simulated (no noise, no filtering)               | simulated               | 75 P wave features, 5 anatomical measures superimposed with Gaussian noise |

## 8.3 Results

The resulting P wave features were analyzed regarding three different aspects: First, the influence of anatomical variability and electrode positions on the P wave features were compared to those caused by the presence of atrial fibrosis (section 8.3.1). Afterwards, it was investigated to what extent the volume fraction of fibrotic substrate resulted in altered P wave features (section 8.3.2). In section 8.3.3, it was analyzed if the effect of healthy anatomical variations on P wave features can be separated by a neural network from the feature changes resulting from the presence of fibrosis.

### 8.3.1 Influence of Geometries, Rotation Angles and Electrode Positions on P wave Features

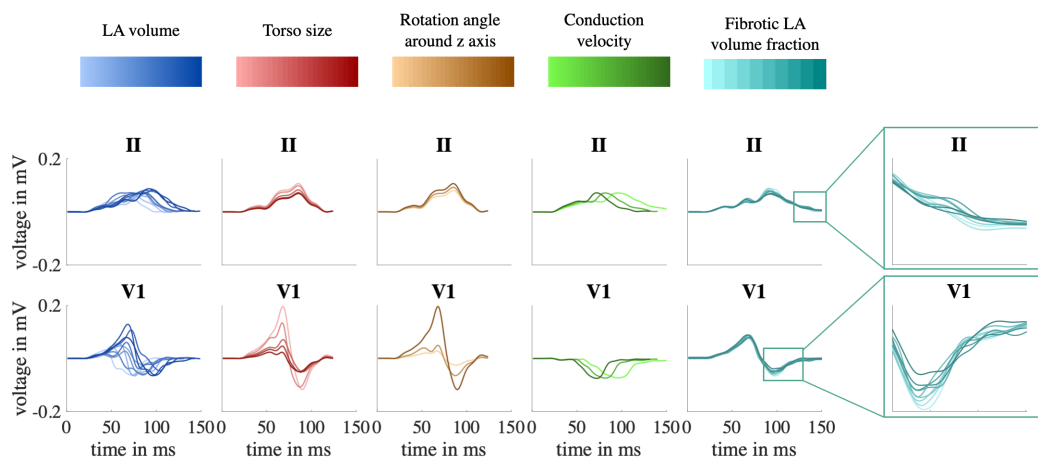


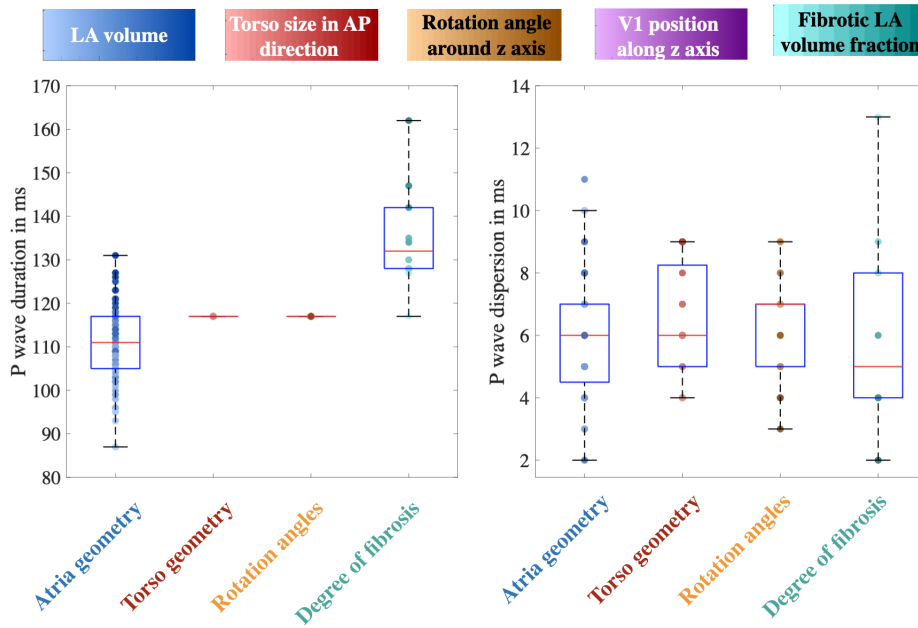
**Figure 8.6: Exemplary ECGs resulting from a variation of anatomical and functional simulation parameters.** From left to right: atrial geometry (small to large LA volumes range from light to dark blue), torso size (small to large torso diameters range from light to dark red), rotation angle (small to large rotation angles around the z axis range from light to dark orange), conduction velocity (small to large values range from light to dark blue) and fibrotic LA volume fraction (small to large LA fibrotic volume fractions range from light to dark turquoise).

Exemplary P waves (lead II and V1) for systematic variations of the atrial and thoracic geometry, the rotation angle, conduction velocity and fibrotic volume fraction are shown in Figure 8.6. The color code represents the dominant change underlying a variation of the respective factor, e.g., LA volume as a key property of atrial geometry alterations. The other dominant properties were the torso size in anterior-posterior direction, the rotation angle around the z-axis, conduction velocity and fibrotic LA volume fraction for the torso geometry, orientation angles, tissue-scale functional variability and fibrotic infiltration, respectively.

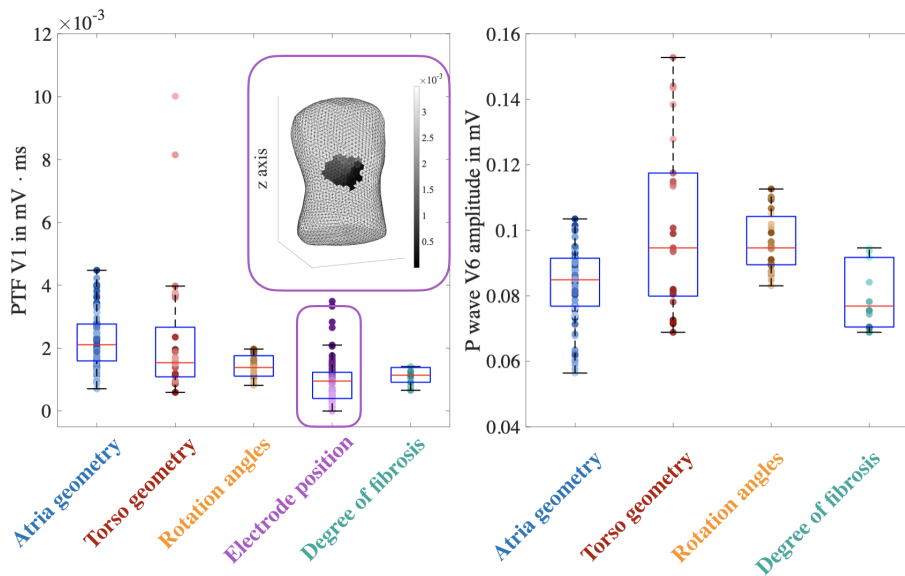
The atrial geometry caused the largest deviations in P wave morphology. A change in torso size reflects predominantly in a variation of P wave amplitudes. Increasing CV values caused PwD to decrease.

The visual observations above based on exemplary simulated P waves were extended by systematically evaluating P wave features of the complete *in silico* dataset. The individual influence of anatomical variations and the placement of electrodes on these features was assessed by varying one of these factors at a time while keeping the remaining ones constant at their reference value. In this way, the variance of each P wave feature resulting from a change of the atrial geometry, the torso geometry, the atrial rotation angle and in the case of PTF V1 also the position of the V1 electrode was analyzed quantitatively.

Figure 8.7 shows the P wave feature distributions. To gauge the potential of one specific P wave feature to be a predictor for the fibrotic atrial volume fraction, also the P wave feature values resulting from fibrotic infiltration in the reference geometry are shown aside.



(a) Influence of anatomical factors on P wave derived timing features (duration and dispersion).



(b) Influence of anatomical factors on PTF V1 and P wave amplitude in lead V6.

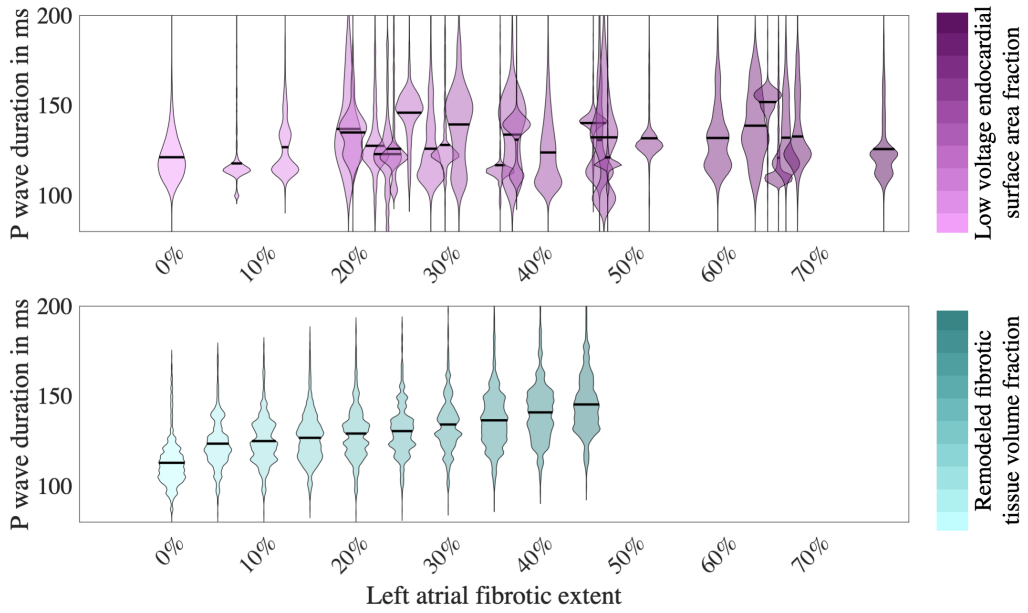
**Figure 8.7: Influence of anatomical variations and electrode position on P wave features.** The effect of atrial geometry, thoracic geometry, atrial rotation angles, V1 electrode placement and the fibrotic LA volume fraction on (a) PWD (top left), P wave dispersion (top right) and (b) PTF-V1 (bottom left), P wave amplitude in V6 (bottom right). The colored sample points indicate one major change resulting from a variation of the respective influencing factor which consist of the total LA volume (small to large LA volume from light to dark blue), the torso diameter in anterior-posterior direction (small to large diameter from light to dark red), the rotation angle around the z-axis (small to large angle from light to dark orange), the position of the V1 electrode along the inferior-superior direction (inferior to superior direction from light to dark purple) and the fibrotic LA volume fraction (0%-45% from light to dark turquoise).

Figure 8.7b reveals that all examined factors have an impact on the value of PTF V1. The largest variance is however caused by a change in the torso geometry. Thoracic variations characterized by a low diameter in anterior-posterior direction and atrial variations holding large LA volume values yielded increased PTF V1 values, with some of them even above the threshold of 4 mV·ms which is typically used when diagnosing structural heart abnormalities. The influence of the exact V1 electrode position on PTF V1 is visualized directly on the top right hand corner of Figure 8.7b. A rather superior placement of the V1 electrode on the thorax caused increased PTF V1 values. The interquartile ranges in Figure 8.7b show that the fibrotic LA volume fraction had a smaller effect on PTF V1 than any anatomical variation. PWd was not affected by torso size and rotation angle (Figure 8.7a, left panel). On the other hand, large LA volumes yielded P waves with durations up to 130 ms. Electrical and structural remodeling of fibrotic tissue resulted in PWds up to 160 ms. Due to the proximity of the V6 electrode to the LA lateral wall characterized by a high probability for the presence of fibrosis [145], the peak-to-peak amplitude is shown for lead V6 in Figure 8.7b. All four analyzed factors affected this feature, while the torso geometry caused the largest variation. P wave dispersion was mostly affected by the atrial geometry (Figure 8.7a, right panel). The maximum dispersion was 11 ms for the healthy anatomical variations and 13 ms in the presence of fibrosis.

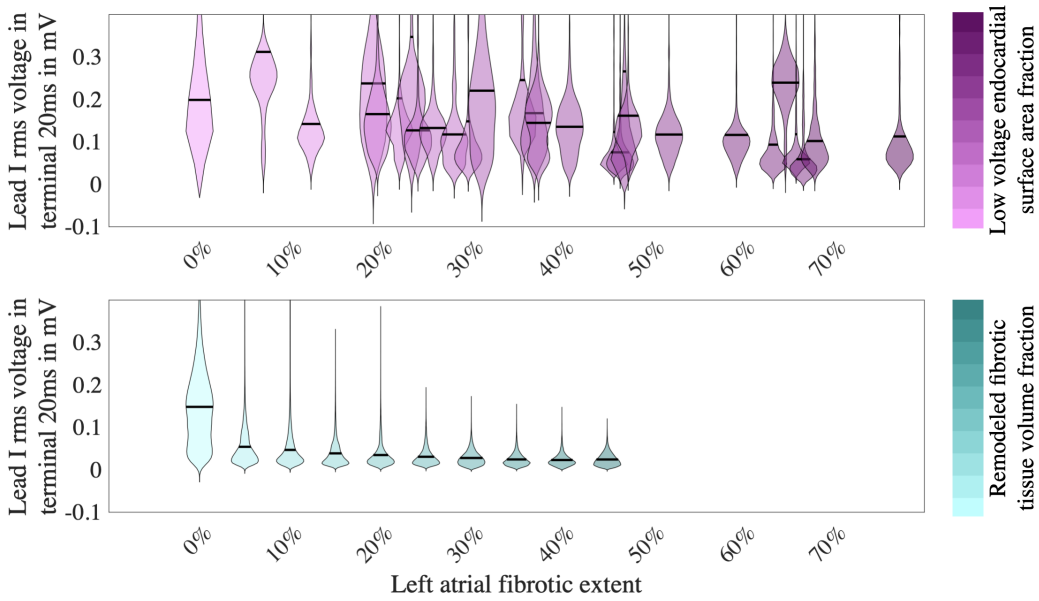
### 8.3.2 Effect of the Fibrotic LA Volume Fraction on P wave Features

To examine to which extent the specific volume fraction of local atrial substrate modification causes graded changes in the P wave features, each set of 12-lead ECGs belonging to one particular volume fraction of fibrosis was analyzed at a time. As an example for the group of lead independent features, the distribution of PWd among the simulated and clinical cohort is shown in Figure 8.8a. When considering all anatomical and functional variations in the simulated dataset of 642,400 ECGs as it is the case in Figure 8.8a, the value ranges of all features overlap between the healthy and all diseased cohorts. Of the three lead independent features (PWd, dispersion and PTF V1), PWd was the most discriminative single feature.

As an example for the lead dependent set of P wave features, the rms voltage values in the terminal 20ms of the P wave in lead I are shown in Figure 8.8b for each patient and degree of fibrosis. Feature values systematically decrease in the simulated cohort for an increasing left atrial fibrotic extent. In the clinical cohort a similar trend, albeit less pronounced, is visible.



(a) Distribution of P wave duration among the clinical (top panel) and simulated cohort (bottom panel).



(b) Distribution of P wave amplitude in lead I among the clinical (top panel) and simulated cohort (bottom panel).

Figure 8.8: Influence of left atrial fibrotic extent on P wave derived features.

### **8.3.3 Estimating the Amount of Fibrosis with Neural Networks**

The network set up as explained in section 8.2.4 was trained for the four different scenarios explained in section 8.2.4. In Table 8.4, the rmse values of the regression model for the different training scenarios summarized in Table 8.3 are outlined. The results for these training options, each designed to address the individual research questions, are unraveled in detail in the following sections.

Table 8.4: Regression model performance for different network configurations evaluated on clinical and simulated test sets.

| Network configuration | Training/validation data            | Network performance (rmse on clinical data) | Network performance (rmse on simulated data) |
|-----------------------|-------------------------------------|---------------------------------------------|----------------------------------------------|
| 1                     | clinical                            | 17.56%                                      | -                                            |
| 2                     | hybrid (noise and 150 Hz filtering) | 16.57%                                      | 11.66%                                       |
| 3                     | hybrid (noise and 40 Hz filtering)  | 17.51%                                      | 13.91%                                       |
| 4                     | hybrid (no noise and no filtering)  | 17.10%                                      | 13.26%                                       |
| 5                     | simulated                           | 36.12%                                      | 8.69%                                        |
| 6                     | simulated + anatomical measures     | -                                           | 7.92%                                        |
| 7                     | simulated (noisy features)          | -                                           | see Figure 8.13                              |

### 8.3.3.1 Impact of Hybrid Training Data on Fibrosis Estimation Accuracy on Clinical Data

When providing the regression neural network with all 75 extracted P wave features, the LA fibrotic volume fraction on a clinical test set was estimated with an absolute rmse averaged over all 6 cross-validation runs of 16.57% and 17.56% in case the network was trained on a hybrid and only on a clinical dataset, respectively.

Figure 8.9 shows the distribution of predicted volume fraction of fibrosis for the test sets included in the different cross-validation runs when trained on a hybrid (bottom panel) and only on a clinical dataset (top panel).

When trained on a hybrid dataset, the network performance was increased especially for patients with a fibrotic extent in the range of [0%, 45%] which corresponds to the interval of fibrotic volume fraction that was defined for the simulations (compare data samples outlined in green in Figure 8.9). On the contrary, training on clinical data only yielded superior results for patients with an extraordinary high extent of fibrosis outside the ranges that were included in the simulated dataset (compare data samples outlined in red in Figure 8.9). When only considering clinical data with a low voltage area fraction <45 % as in the simulated dataset, the network performance error was comparable to the results in the simulated test sets and quantified to 12.28 %.

The performance metric of the neural network is shown in Figure 8.10 when trained on a hybrid dataset (dots) or on clinical data only (triangles). The marker color indicates whether the ECGs in the test set for performance evaluation were extracted as a subset of the simulated (cyan) or the clinical (magenta) ECGs.

In any case except for split 6, the estimation of the fibrotic extent was more accurate if simulated data were additionally included in the training set. The improvement when training the network with the hybrid dataset averaged over all clinical test sets was around 1%.

### 8.3.3.2 Influence of Noise and Filter Settings Applied to Simulated Data on Network Performance

The influence of adding realistic ECG noise [265] to the simulated data and subsequently filtering the signals choosing different cut off frequencies for the low-pass filter is shown for the test sets of all 6 cross-validation runs in Figure 8.11. The solid line represents the turning point for which training on a hybrid dataset yielded improved regression results over training on clinical data only.

Adding noise and selecting a low-pass cut off frequency of 150 Hz yielded the best performance for 3 out of 6 test sets each belonging to one cross-validation run (green boxes in Figure 8.11). As these filter settings were also applied for the analysis described in section 8.3.3.1, it was shown that these filter settings also yielded improved results for 2 further test sets over the case where only clinical data was used. Only for split 6, training on clinical data resulted in a smaller rmse. Out of the three low-pass filter options, a cut off frequency of 40 Hz applied to the simulated data led to the poorest performance (compare

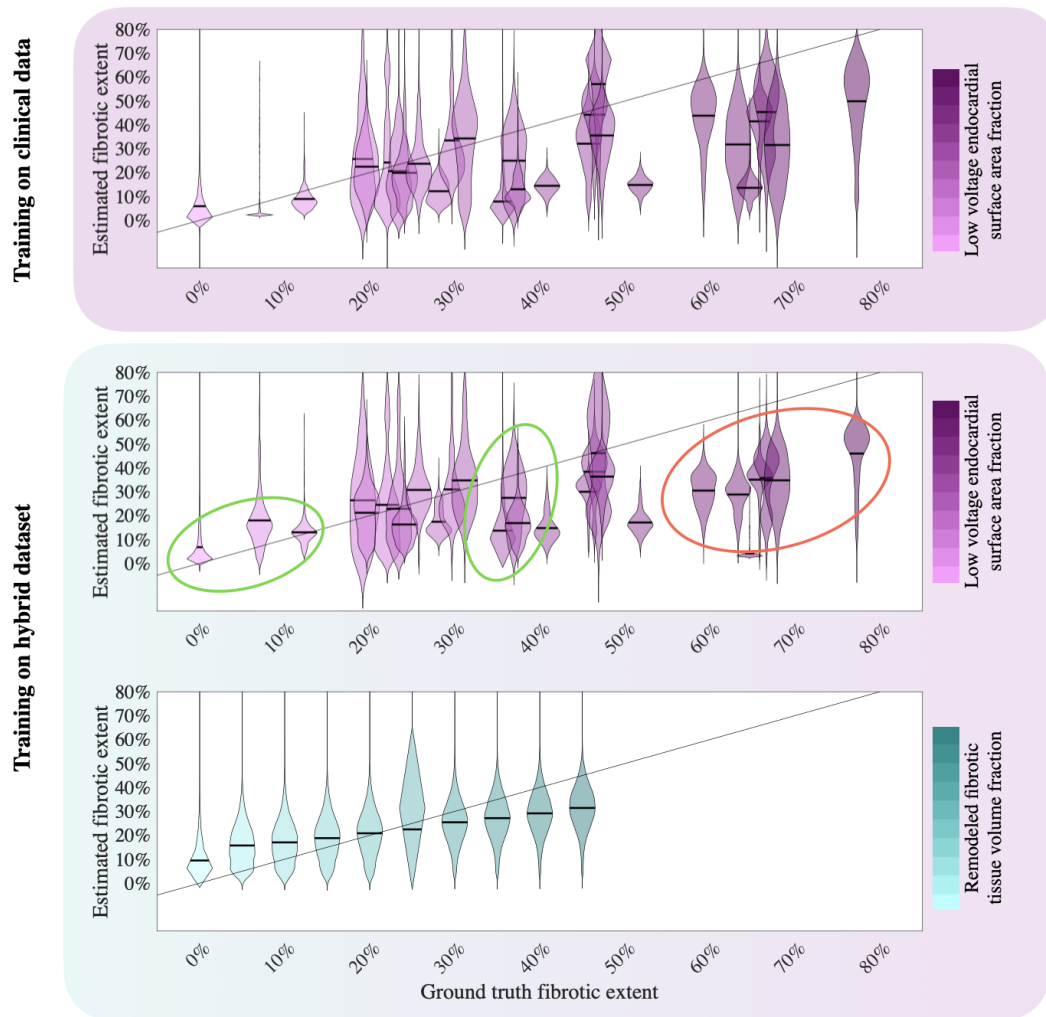


**Figure 8.9:** Network performance for predicting the volume fraction of atrial fibrosis evaluated on a clinical test set when trained only on clinical data (top panel). The distribution of predicted vs. ground truth left atrial fibrotic extent when trained on a hybrid dataset is shown in the bottom panel in case of clinical (magenta) and simulated test data (cyan).

dark pink dots in Figure 8.11), as the averaged rmse over all 6 test sets was 17.51% in contrast to 16.57% when setting the cut-off frequency to 150 Hz and 17.56% when only training on clinical data.

### 8.3.3.3 Added Value of Anatomical Measures as Additional Input Data

In Figure 8.12, the estimated and ground truth fibrotic volume fraction output by a network trained with and evaluated on the simulated data are shown when only providing 75 P wave derived features as input to the network. The scatter points represent selected samples in the test splits and their face colors encode their respective total LA volume (top panel) and torso volume (bottom panel).

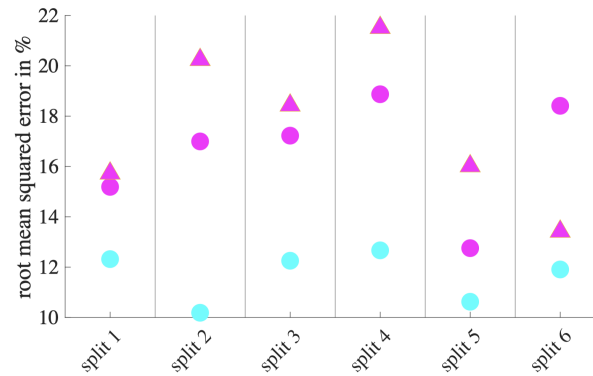


**Figure 8.10:** Performance of a neural network trained on a hybrid dataset (dots) and on clinical data only (triangle) when evaluated separately on a simulated (cyan) and clinical test set (magenta).

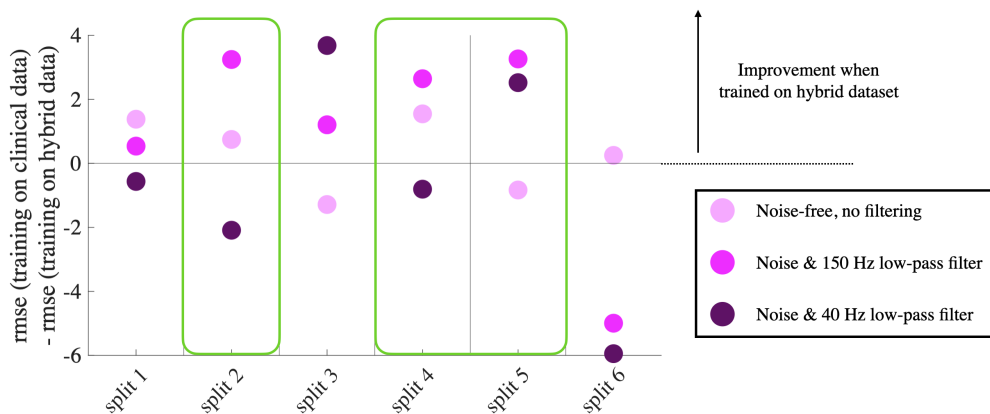


**Figure 8.11: Influence of superimposed noise and low-pass filter cut off frequencies on network performance.** The difference in the network's rmse between training on clinical data and on a hybrid dataset is shown for all 6 cross-validation runs for different filter configurations applied to simulated data (faded pink: noise-free, without filtering; pink: superimposed noise and subsequent low-pass filtering with 150 Hz, purple: superimposed noise and subsequent low-pass filtering with 150 Hz).

The visualization indicates that the prediction performance decreased for samples with extraordinary high and low LA and torso volumes. Especially, a systematic under- and overestimation for low and high LA volumes, respectively, prevailed. Thus, 5 additional non-invasively measurable features representing LA and RA volume, torso volume and torso diameter in anterior-posterior direction in the chest and the abdominal region were included for training the network. In this case, the rmse between the predicted and ground truth volume fractions covered by fibrosis decreased from 8.69% to 7.92% .

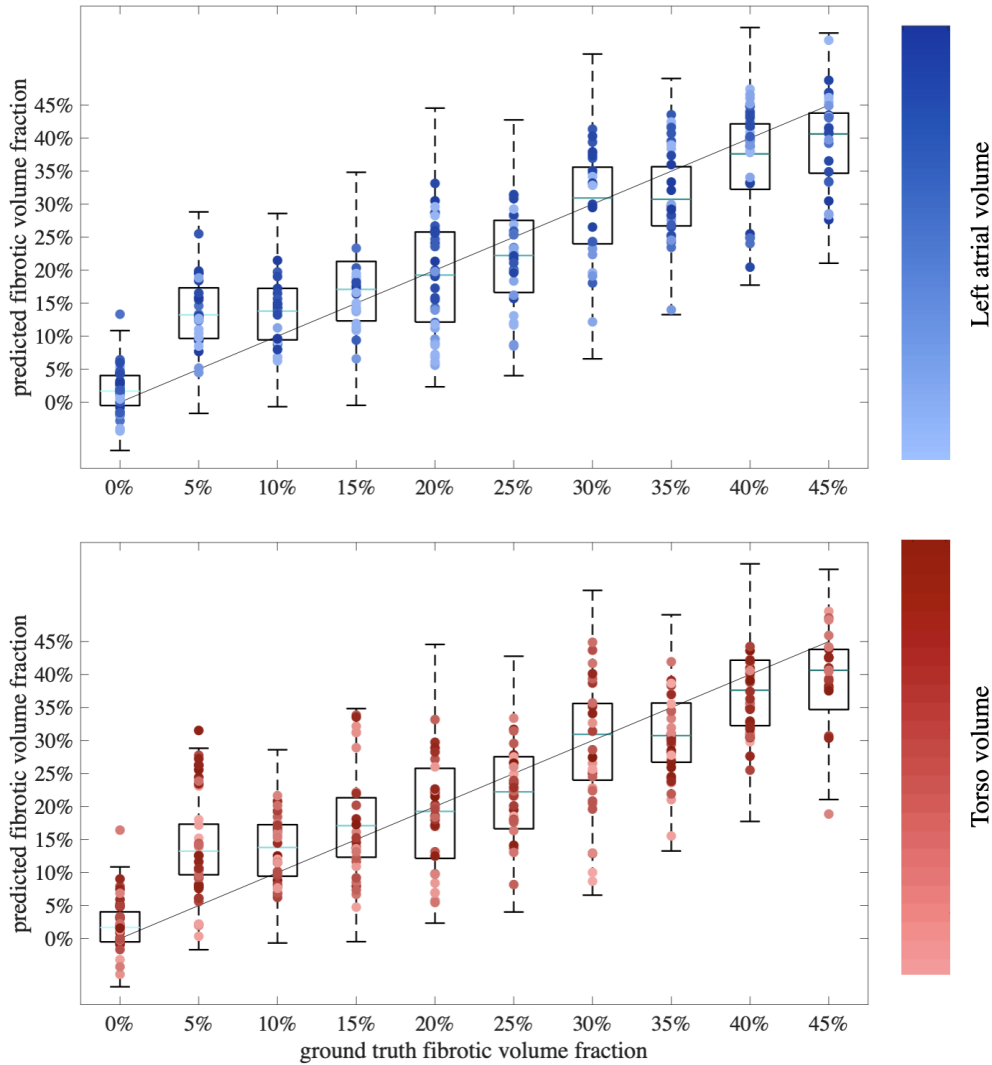
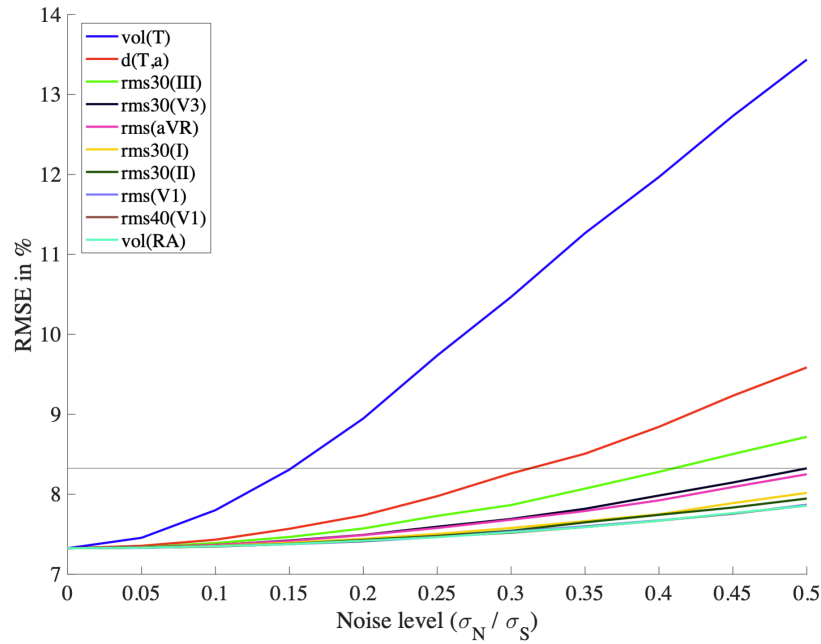


Figure 8.12: Network performance for predicting the volume fraction of atrial fibrosis only based on P wave derived features. The color code represents the LA volume (top) and torso volume (bottom) of each individual sample point (light: small volume; dark: high volume). The solid black line represents perfect prediction.

### 8.3.3.4 Network Sensitivity to Inaccurately Extracted Features

Figure 8.13 shows the rmse of the network output averaged over all cross-validation test sets depending on the applied noise level  $n$  to the input feature values. The decrease of the network performance is depicted for 10 out of the 80 input features for which the network’s rmse was affected the most. The absolute rmse estimated by the network increased by 1% compared to the noise-free baseline case for a noise level of  $\sigma_N / \sigma_S = 0.2$  for the torso volume (corresponding to an absolute noise standard deviation of  $\sigma_N = 0.0028 \text{ m}^2$ ) and a noise level of  $\sigma_N / \sigma_S \approx 0.3$  for the torso diameter in anterior-posterior direction in the



**Figure 8.13: Sensitivity of the network towards inaccurately extracted features.** The rmse of the network is shown for different levels of noise added to the specific feature values one at a time. The solid horizontal line represents a drop of the network performance of 1% compared to the noise-free baseline case.

abdominal region ( $\sigma_N = 14.36$  mm). Besides the anatomical measures, a distortion of rms voltage features predominantly in the terminal 30 ms of the P wave caused the most marked decrease in network performance compared to the noise-free baseline case.

## 8.4 Discussion

### 8.4.1 Main Findings

In this work, a total of 642,400 simulated 12-lead ECGs of healthy subjects and patients with different LA volume fractions covered with fibrosis were generated. Different atrial and thoracic anatomical models derived from SSMs as well as varying orientation angles of the atria within the torso are hallmarks of the virtual cohorts. Additionally, different regionally heterogeneous sets of CVs were applied representing inter-individual CV variation in healthy subjects causing additional P wave feature variability in all model cohorts. P wave features including duration, PTF V1, peak-to-peak amplitudes, rms voltages in the terminal 40, 30 and 20 ms, P wave integral and dispersion were calculated for each signal. The influence of anatomical properties on these features' variances was compared to the variance caused by

fibrotic infiltration of the atrial tissue of various degrees. None of the investigated features showed distinct ranges for the diseased cohort and different healthy anatomical variations.

The intervals of all feature values occurring from anatomical and functional variations were greater than or equal to the variability in case of fibrotic infiltration of atrial tissue (compare Figure 8.7). The atrial geometry variation caused altered P wave morphologies resulting in varying values for all features, whereas the torso geometry variation mainly affected P wave amplitudes. Nevertheless, all investigated features were characterized by a systematic change in their values for an increasing volume fraction of fibrotic atrial tissue (compare Figure 8.8a and 8.8b).

The electrodes for the lateral ECG leads V5 and V6 are located closest to the LA lateral wall. According to the findings reported by Highuchi *et al.* [145], which the distribution of fibrosis in the computational models was based on, the presence of fibrotic tissue in this region holds a considerable high probability. Therefore, the amplitude decrease in V5 and V6 [122] that were found for an increasing volume fraction of LA fibrosis can be explained by a growing amount of passive fibrotic elements not contributing to the overall source distribution in the left pulmonary vein (PV) antrum and the LA lateral wall. Rms voltages in the terminal 40, 30 and 20 ms systematically decreased for an increasing extent of atrial fibrosis which occurs due to delayed activation of fibrotic patches causing low voltage ECG signal parts ensuing the normal depolarization of healthy myocardial tissue. Accordingly, also PWd systematically increased with the amount of LA fibrosis. Thereby, a careful choice of the threshold for detecting the P wave ending in each lead is crucial as already reported by Jadidi *et al.* [273]. In this simulation study, a simple amplitude threshold of  $1.5 \cdot 10^{-4}$  mV could have been chosen. However, when changing this threshold value to  $3 \cdot 10^{-3}$  mV, PWd doesn't show the steady increase for different fibrotic LA volume fractions as shown in Figure 8.8a. In this case, the low voltage signal parts at the end of the P wave caused by delayed activation of fibrotic regions in the LA are ignored, which results in underestimation of PWd. This implies that a sufficiently high signal-to-noise ratio is required for clinically recorded signals in order to apply sensitive thresholds to accurately measure PWd.

A neural network provided with the aforementioned features of the simulated data succeeded in estimating the volume fraction of atrial fibrosis with an average error of 8.69% fibrotic LA volume. When also including anatomical measures for atria or torso, the rmse of the regression network could be improved and decreased to 7.92% fibrotic volume. Thus, the results of this simulation study suggest that it is beneficial to provide the network with additional anatomical measures non-invasively acquirable by estimating the torso volume with measurements of the torso perimeter and the atrial diameter based e.g. on echocardiographic recordings to further increase the prediction accuracy. By comparing the overlapping interquartile ranges in Figure 8.8a to those in Figure 8.12, it can be inferred that the volume fraction of fibrotic substrate can be estimated more accurately with ECG-based machine learning approaches than by isolatedly considering single P wave features, such as e.g., P wave duration. Therefore, the network indeed seems to be capable of separating the effects of anatomical variability from the influence of fibrotic substrate on the P wave.

The impact of inaccurately determined features – as it is likely the case in a clinical setting – was investigated by adding Gaussian noise to the robustly and accurately extractable feature values from simulated data. It was found that the network's rmse increased the most if noisy values for the torso volume, torso diameter and the rms voltages in the terminal sections of the P wave were provided to the network independent on how the data were split for training, testing and validation. Likely reasons for these findings could involve that the presence of fibrotic tissue reflects in a decrease of the P wave amplitudes that are also affected by the torso volume and could not be properly compensated for if this entity was extracted inaccurately. Furthermore, the reduced CV in the fibrotic regions causes rms voltages in the terminal P wave intervals to decrease. For this reason, these features are important to separate the changes in P wave features resulting from fibrotic infiltration of atrial tissue from those caused by healthy anatomical variations and thus must be accurately measured. The network was able to generalize well to ECGs simulated with unseen atrial and torso geometries if ECGs generated with different geometries, but similar atrial and thoracic volumes were included during training [122].

Moreover, the feasibility of non-invasively estimating the amount of fibrosis in the atria by using features from clinical 12-lead ECGs as an input to a feedforward neural network was demonstrated. The rmse between the estimated and the ground truth fibrotic volume fraction on a test set composed of clinical signals was 17.56% when using only clinically recorded ECGs during training of the network. The error was reduced to 16.57% by additionally including simulated data during training. Non-matching absolute values in the feature distributions between the simulated and clinical cohort, for example in case of PWD (compare Figure 8.8a) could likely be a reason for the limited, though visible, added value that simulated data carry when used as an additional input dataset. However, measuring P wave duration automatically in clinical data remains challenging, especially in FAM patients where low voltage signal parts are not uncommon to occur after the presumably detected P wave ending. Averaging multiple P waves of the same patient could provide a possibility to reduce noise in the signal and to potentially more accurately determine the P wave ending. However, as ECGs of only 27 patients were available in the clinical dataset of this study, averaging over multiple beats was not performed for the sake of keeping the P wave dataset as large as possible. An incorrectly detected P wave offset also affects other P wave features in the set of network input data. Among them are the rms voltages in the terminal P wave intervals which also turned out to impair the network performance notably if not assigned their correct values (compare section 8.3.3.4). Compared to current state-of-the-art methods to quantify the fibrotic extent in the atria, the ECG-based estimation can be a reasonable indicator for fibrosis infiltrating the atrial myocardium, but does not provide quantitatively as accurate results as invasive mapping procedures or expensive imaging techniques.

Adding noise to the simulated data prior to feature extraction was important to reduce the estimation error with the hybrid training dataset as this seems to contribute to closing the domain gap between clinical and simulated ECGs. When including features directly extracted from the raw simulated ECGs during training, the network's performance declined from 16.57% (150 Hz low-pass cut off frequency) to 17.10% (without added noise and

filtering) which is comparable to the performance in case the network is only trained on clinical data. Furthermore, choosing appropriate filter settings for all signals was necessary for a successful fibrosis estimation. Applying a low-pass filter with a cut-off frequency of 40 Hz instead of the chosen 150 Hz, the network performance could only be improved for 2 out of 6 splits when additionally providing simulated data for training. This highlights the need of preserving subtle ECG characteristics that might arise due to delayed and scattered depolarization of the tissue in fibrotic areas and the necessity of recording clinical signals of high quality.

## 8.4.2 Related Work

Yoshizawa *et al.* [272] reported that new-onset AF could be estimated using P wave amplitude in lead II and P wave dispersion features with a sensitivity of 69.1 % and specificity of 88.2 % in their clinical study comprising 68 AF patients and the same number of controls. Lankveld *et al.* [289] drew on several time- and frequency domain features to predict AF recurrence rates after pulmonary vein isolation (PVI) in 93 patients with an area under the curve (AUC) of 0.76. In the clinical study conducted by Nakatani *et al.* [288], a combination of several P wave amplitudes led to a sensitivity of 69 %, a specificity of 88 % and an AUC of 0.77 for predicting the presence of low voltage areas  $\geq 10$  % in 50 AF patients. Jadidi *et al.* [273] found that a PwD above 150 ms – provided a very low threshold is set for detecting the P wave offset – was a predictor for advanced LA low voltage substrate with a sensitivity of 94.3 % and a specificity of 91.7 %. Conte *et al.* [302] report that PwD and beat-to-beat variability of P wave morphologies held the highest discriminative power to identify patients holding an increased risk of AF occurrence.

Especially sensitivity and AUC results for discriminating between the healthy and the FAM group were higher in this simulation study compared to the findings in previous clinical studies [122]. Possible reasons could involve the number of P waves included in this work (642,400 simulated P waves compared to  $\leq 100$  ECG recordings in clinical studies) leading to a larger database for the network to learn relations between P wave features and fibrotic LA volume fraction. Moreover, it was found that additional anatomical measures improve the estimation outcome. On the other hand, it was investigated in this study whether detecting fibrotic substrate extent in the atria is feasible, whereas most clinical studies focused on predicting AF recurrence rates and new-onset AF episodes. Even though the latter are reported to correlate with the amount of the fibrotic LA volume fraction, there is no clear 1:1 relation between them complicating the comparison between this study and those conducted by Yoshizawa *et al.* [272] and Lankveld *et al.* [289]. Besides that, the chosen set of investigated P wave features in this study resembles but does not exactly equal the one used in previous clinical studies. The set of features was indeed chosen based on previous findings, but a combination of a vast number of features was used compared to clinical studies [272, 289]. In contrast, beat-to-beat alterations were not evaluated in this study as proposed by Conte *et al.* [302] since the simulation setup only allows for a single beat analysis.

### 8.4.3 Limitations

The analyses and results of this study are to large parts based on simulated data. Even though an established modeling methodology for fibrotic tissue was chosen covering versatile aspects of electrical and structural remodeling on cell and tissue level, other modeling methods could have led to different results [82]. In this context, future directions could involve to examine if the proposed method is capable of detecting fibrotic tissue in signals generated with any fibrosis remodeling methodology or if it is particularly sensitive towards either ionic remodeling, locally heterogeneous conduction velocities or percolation effects. Further future directions could include an investigation of how the specific location of fibrotic patches influences the accuracy of the estimation of left and right atrial fibrosis.

To generate simulated signals at scale, yet at a reasonable computational cost, the Eikonal model (see section 3.1.2.3) as a propagation driver and the infinite volume conductor (see section 3.1.3.3) as a simplified forward calculation method was drawn on. On the one hand, the Eikonal model is capable of faithfully reproducing LATs obtained with the bidomain model for sinus rhythm simulations on fibrotically infiltrated atrial models. Building on the analyses described in chapter 4, no substantial error is expected to have impaired the computed activation sequence and the ECGs derived therefrom. However, full bidomain, pseudo-bidomain or reaction-Eikonal [104] simulations could account for diffusion effects neglected when deriving the source distribution by only solving the Eikonal equation and shifting pre-computed action potentials in time. On the other hand, the infinite volume conductor was found to systematically overestimate P wave amplitudes in leads V1-V3 compared to the finite element method [303] (compare chapter 4). As this affects most of the features extracted from V1-V3 that were employed for the neural network, especially the amplitudes, a domain shift between the simulated and the clinical data for the affected features might have limited the benefits of providing more input variability through simulated signals during training. However, more sophisticated modeling approaches require considerable longer computation times compared to the methods employed in this study. The latter were therefore intentionally chosen for the sake of reducing computational cost to make the generation of a large database feasible.

The fibrosis distribution in the virtual patient cohort was set based on a spatial histogram of high image intensity ratios in late Gadolinium enhanced magnetic resonance images [145]. Thus, the simulation dataset is mainly characterized by fibrotic patches on the posterior left atrial wall. Opposite to this, the clinical electroanatomical voltage maps employed for extracting the ground truth fraction of fibrosis on the endocardium mainly exhibit low voltage areas on the anterior left atrial wall [304]. Furthermore, the fibrotic volume fractions defined for the virtual patient cohort ranged only up to 45 %, whereas the maximum surface area fraction of low voltage electrograms in the clinical dataset was 77.28 %. Therefore, the lack of P wave features pertaining to high fibrotic extents in the *in silico* training set could have caused the underestimation of fibrotic volume fractions in patients characterized by large low voltage areas in the clinical test set and therefore reduced the overall network performance.

This is also visible in Figure 8.9 as the estimated fibrotic extent complies with the ground truth values to a markedly higher degree for patients with low voltage areas  $<45\%$ .

Moreover, the impact of noise being added to simulated data was studied with regard to the added value that simulated signals can carry to enrich a clinical dataset on the one hand (also compare section 8.2.2) and regarding the sensitivity of the network output towards inaccurate feature values on the other hand. However, in the simulation study, only the network's sensitivity in case of noise being added to a single input feature was analyzed. In clinical practice though, measurement uncertainty usually affects multiple features at once. Therefore, clinical ECG recordings as input for the network require robust signal processing methods for extracting key features accurately. However, the impact of noise on robust and accurate feature extraction [305] was not particularly analyzed in this study. While noise and a QRS complex immediately following the P wave will definitely impede the feature extraction if averaging over several beats is not feasible, the focus of this study was not to develop robust feature extraction and signal processing methods. Instead, the intention was to probe the general potential of P wave features as predictors for the presence of atrial fibrosis provided that their values can be accurately extracted from the ECG.

Since a large-scale database of more than 700,000 12-lead ECG P waves from healthy and diseased simulated and clinical cohorts is now available, it could also be worth to use the signals directly as an input for a deep learning network to estimate the fibrotic LA volume fraction without prior feature extraction. Thereby, the network could directly learn relations between the different cohorts and derive rules to distinguish between them. Additionally, the effect of different ablation strategies (PVI vs. additional ablation targets) and their effect on the 12-lead ECG could be examined in a future study and reveal new insights regarding individual therapy planning on a sub-population level.

## 8.5 Conclusion

Given the results of the study presented in this chapter, the ECG constitutes a non-invasive and widely available tool in clinical practice to indicate left atrial volume fraction of fibrotic tissue up to an uncertainty of around 16%. Moreover, simulated signals of a virtual patient cohort covering anatomical, functional and pathological variability can contribute to reduce the estimation error.

---

# Detection of Left Atrial Enlargement

In this chapter, the benefits of extending clinical electrocardiograms (ECGs) by simulated training data derived from a bi-atrial statistical shape model (SSM) to improve the automated detection of left atrial enlargement (LAE) based on P waves of the 12-lead ECG are demonstrated.

*The content of this chapter is taken from conference proceedings that have been published in Lecture Notes in Computer Science (LNCS) [121]. Most passages in this chapter have been quoted verbatim from the publication and are adapted or reprinted by permission from Springer Nature Customer Service Centre GmbH: Springer Nature, Statistical Atlases and Computational Models of the Heart. Multi-Disease, Multi-View, and Multi-Center Right Ventricular Segmentation in Cardiac MRI Challenge (A Bi-atrial Statistical Shape Model as a Basis to Classify Left Atrial Enlargement from Simulated and Clinical 12-Lead ECGs, C. Nagel, M. Schaufelberger, O. Doessel, A. Loewe), Copyright: Springer Nature Switzerland AG (2022).*

## 9.1 Introduction

LAE is not only among the risk factors and an indicator for hypertensive heart disease [87, 306], but contributes also to the arrhythmogenesis and maintenance of atrial fibrillation (AF) [65, 86, 218]. Thus, an established LAE diagnosis could serve as a valuable risk marker for the early detection of AF which is crucial for choosing the appropriate patient-specific treatment therapy.

As an alternative to cardiac chamber size measurements with imaging techniques, a clinical diagnosis of LAE could initially also be informed by an evaluation of the 12-lead ECG [307–310]. The altered ECG signal characteristics in LAE patients comprise on one

side an increased duration and absolute amplitude in the negative deflection of the P wave in lead V1 [308, 309]. Furthermore, a dilation of the left atrium also reflects in an increased overall duration of the P wave in all leads since the depolarization wavefront needs to traverse a larger surface area [308]. Additionally, a bifid P wave with an interval  $\geq 40$  ms between both peaks in lead II is an indicator for P mitrale [310]. In contrast to imaging techniques applied to quantify the atrial chamber sizes, the ECG features an inexpensive, easily accessible and widely available tool in clinical practice. An automated analysis of ECG signals with e.g. machine learning techniques could facilitate the early diagnosis of LAE and in turn contribute to a proper risk stratification for AF [311, 312].

However, the application of machine learning algorithms to clinical ECGs for an automated disease classification entails several challenges. On the one hand, large clinical datasets are rarely available and also the diagnostic classes of interest are usually not balanced [313–315]. In spite of being the largest publicly available online ECG database to date, PTB-XL [16] comprises 9,528 12-lead ECGs from healthy individuals, but yet only 421 signals of LAE patients. A failure to meet the requirement of evenly distributed samples in the classes to be distinguished by the machine learning model, a classification bias is likely to be introduced at the expense of prediction accuracy for the minority class. Moreover, ground truth labels marking the underlying cardiac pathology have to be set manually by cardiologists. However, expert annotations are inevitably subject to inter- and intra-observer variabilities contributing to unreliably and inconsistently labeled signals that can severely impair the performance of a machine learning classifier [24].

These limitations call for simulated ECG signals as an additional data source with precisely known ground truth labels and arbitrarily selectable class distributions to overcome the above mentioned drawbacks of clinical signals. Especially for the use case of identifying LAE, a bi-atrial SSM carries the potential to produce a vast amount of atrial geometries with predefined and equally distributed left atrial volumes that can be employed for electrophysiological simulations to obtain simulated P waves of the 12-lead ECG. It was therefore investigated if synthetic P waves resulting from simulations carried out on anatomical models derived as instances from a bi-atrial SSM can improve the detection of clinical LAE ECGs.

## 9.2 Methods

### 9.2.1 Database

#### 9.2.1.1 Simulated Data

The bi-atrial SSM described in chapter 5 [169] was used to generate 95 anatomical models of the atria augmented with fiber orientation, inter-atrial connections and tags for anatomical structures. These models were made publicly available [200]. The eigenmode coefficients of the SSM were chosen such that the left atrial volumes of the 95 geometries were uniformly

distributed in a range of 30 - 65 ml, covering the left atrium (LA) volume range reported in a large clinical cohort study including a healthy control group and LAE patients [219]. For the computer models, left atrial volumes (LAVs) were calculated as the volume bounded by the surface of the left atrial body as shown in Fig. 9.1. The left atrial appendage as well as the pulmonary vein ostia were excluded for the volume assessment. The atrial SSM was built based on magnetic resonance (MR) and computed tomography (CT) segmentations but clinical LAV reference values are usually specified based on 2D echocardiography data. Therefore, each initially calculated LAV value of the virtual cohort was multiplied with a correction factor of 0.75 to account for the systematic underestimation of the atrial size using echocardiography compared to MR and CT measurements [316]. Examples of three atrial instances with a left atrial volume of 31 ml, 47 ml and 65 ml are shown in Fig. 9.1.

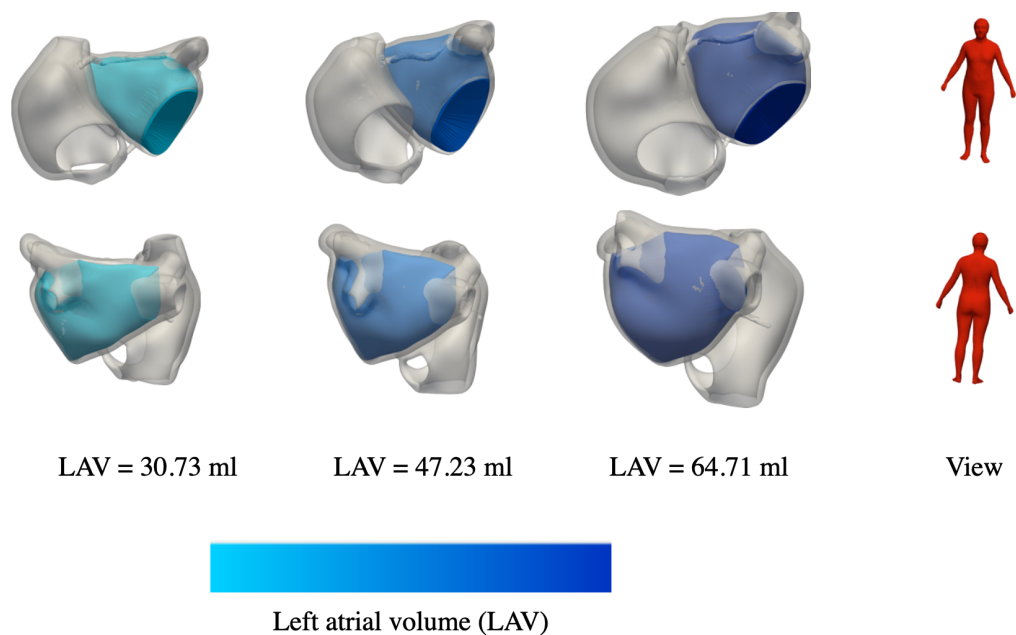


**Figure 9.1: Examples of three atrial geometries (endo- and epicardium) derived from the SSM with different LAV values.** Anterior and posterior point of views are shown in the top and bottom panel, respectively. The LAV is marked in blue and was calculated as the volume enclosed by the surface of the left atrial body excluding the left atrial appendage area and the pulmonary vein ostia. Figure adapted from Nagel *et al.* [121] with permission from the publisher.

For each atrial model, a baseline conduction velocity (CV) was assigned based on the values reported in [245] to 4 different atrial regions as listed in Table 9.1 and depicted in Figure 9.2. Nine variants of this CV setup were defined by modifying the velocities randomly in the interval [80 %, 120 %] of the baseline CV in each region. For each model and each CV setup, the Eikonal equation was solved using a mesh resolution of 1.22 mm with the Fast Iterative Method to obtain local activation times (LATs). Excitation was initiated at a sinus node exit site located at the junction of the right atrial appendage and the superior vena cava. Shifting a precomputed Courtemanche *et al.* [91] action potential in time according to

the resulting LATs yielded the spatio-temporal distribution of the transmembrane voltage in the atria [299]. Each atrial geometry was rotated by a random rotation angle drawn from a uniform distribution in a range of  $[-15, 15]^\circ$  around the x-, y- and z-axis [295] and were placed in two different torso geometries (see Fig. 9.4) derived from a human body SSM [179]. Torso 1 represents a male subject (body surface area (BSA) =  $1.7 \text{ m}^2$ ) and torso 2 a female subject (BSA =  $1.2 \text{ m}^2$ ). The ECG forward problem was solved by means of the boundary element method as implemented by Stenroos *et al.* [107] and 12-lead ECGs were extracted at the standardized electrode positions. In this way, 1900 (95 atrial geometries  $\times$  2 torso geometries  $\times$  10 CV settings) simulated ECGs were generated .

**Table 9.1:** Conduction velocities in transversal fiber direction ( $CV_{\perp}$ ) and anisotropy ratios (AR) for the baseline CV setup.

| Atrial Region     | $CV_{\perp}$ in m/s | $AR = CV_{\parallel}/CV_{\perp}$ |
|-------------------|---------------------|----------------------------------|
| Bulk tissue       | 0.59                | 2.11                             |
| Bachmann's bundle | 0.64                | 3.33                             |
| Crista terminalis | 0.59                | 2.84                             |
| Pectinate muscles | 0.46                | 3.78                             |

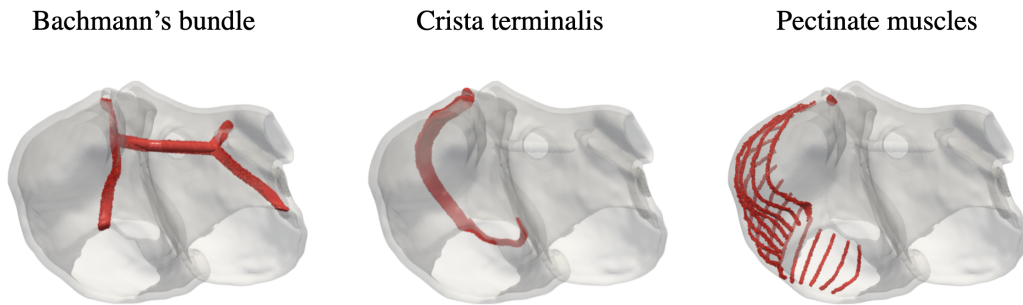


**Figure 9.2:** Example atrial geometry with three regions that are assigned different conduction velocities and anisotropy ratios. The bulk tissue makes up for the remaining areas in the left and right atrium. Figure adapted from Nagel *et al.* [121] with permission from the publisher.

Ground truth labels for the simulated dataset were set based on the left atrial volume indexed to the body surface area (LAV/BSA). Applying the cutoff value for LAV/BSA of  $34 \text{ ml/m}^2$  as recommended in the cardiac chamber size quantification guidelines [88] for 2D echocardiography derived data resulted in 1,050 healthy and 850 LAE signals in the simulated database. Left and right atrial volumes indexed to the body surface area are visualized in Fig. 9.4 for both torso models and all 95 atrial geometries.

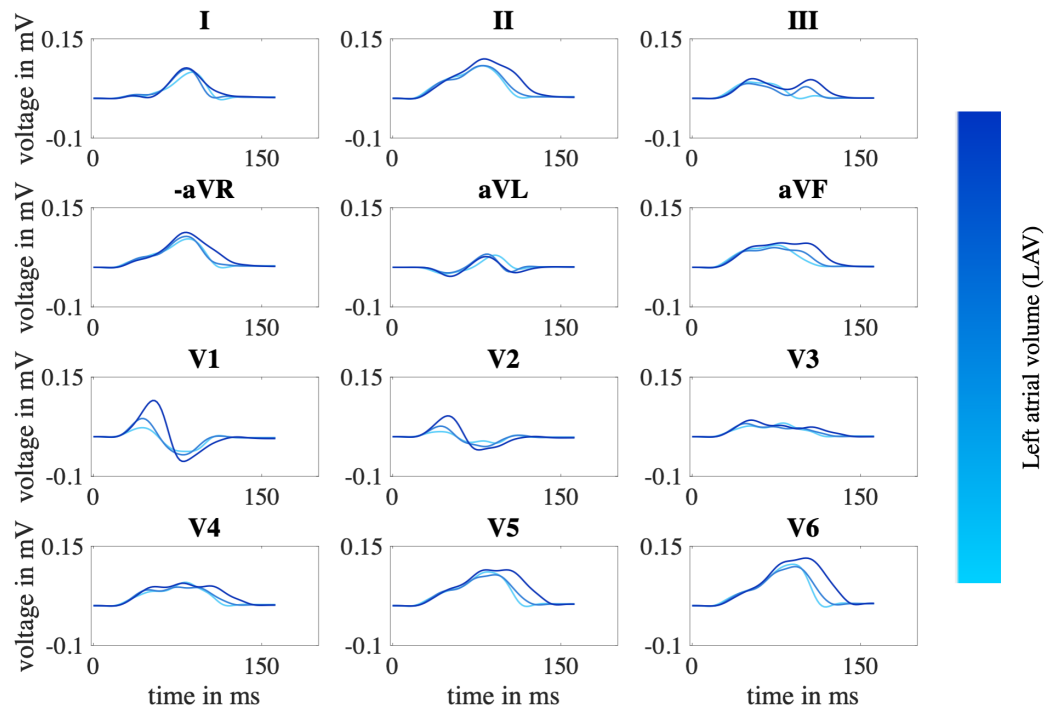


**Figure 9.3:** Examples for the P waves of the 12-lead ECG resulting from electrophysiological simulations conducted on the three models with different left atrial volumes as shown in Figure 9.1 calculated using constant rotation angles and the same torso model. Figure adapted from Nagel *et al.* [121] with permission from the publisher.

### 9.2.1.2 Clinical Data

Clinical ECGs of 10 seconds length from 9,485 healthy subjects and 421 LAE patients sampled at 500 Hz were extracted from the publicly available PTB-XL ECG database [16]. For 7,168 healthy and 309 LAE signals in this database, the certainty with which the expert cardiologist labeled the respective pathology, was specified as 100%. ECGdeli [250] was applied to extract the P waves from the time series of all healthy and LAE signals and to build a mean P wave template for each subject (see Figure 9.5)

## 9.2.2 Machine Learning Classifier

A long short-term memory (LSTM) network was trained to perform the binary classification between the healthy control group (NORM) and the left atrial enlargement cohort (LAE). The simulated P waves and the clinical P wave templates were filtered (0.5 Hz highpass cutoff frequency, 60 Hz lowpass cutoff frequency) and cut 40 samples (equivalent to 80 ms) before and 40 samples after the P wave peak in lead II occurred. In this way, it was ensured that the P waves are robustly and consistently extracted throughout the simulated and clinical dataset. The resulting time series signals of all 12 leads served as an input to the network.

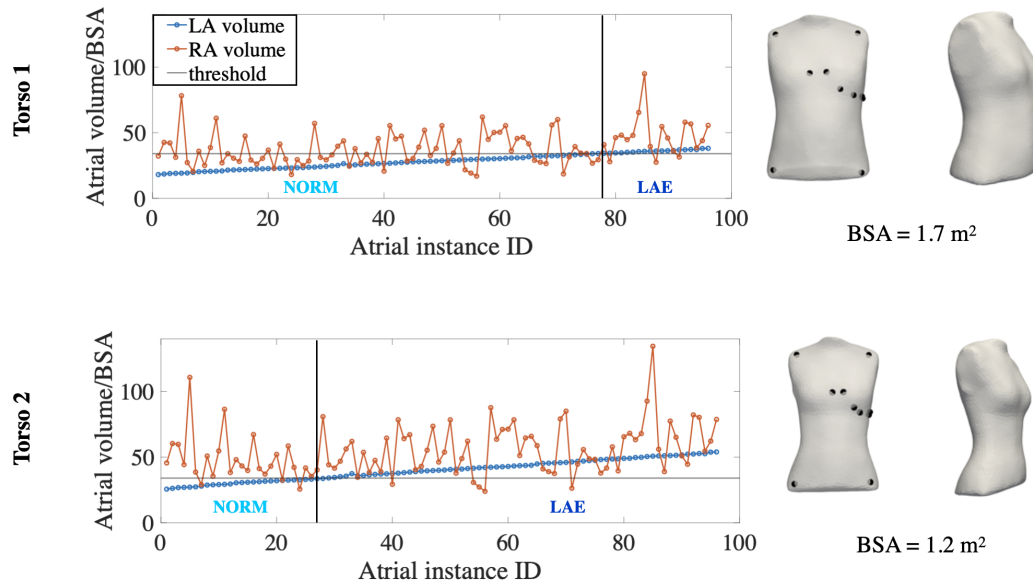


**Figure 9.4:** Left (blue) and right (red) atrial volumes indexed to the respective body surface area (BSA) for both torso models. Torso model 1 and 2 had a BSA of  $1.7 \text{ m}^2$  and  $1.2 \text{ m}^2$ , respectively, and are depicted together with the positions of the attached electrodes from the anterior and lateral view. Applying a threshold value of  $34 \text{ ml/m}^2$  to the LAV/BSA values yields the ground truth labels for the healthy (NORM) and the left atrial enlargement (LAE) cohorts. Figure adapted from Nagel *et al.* [121] with permission from the publisher.

70 %, 15 % and 15 % of the ECGs in both classes were split into a training, validation and test set, respectively. Three different training scenarios were considered. For scenario 1, only clinical signals with ground truth labels annotated with a certainty of 100 % were considered. For training scenario 2, the 1900 simulated P waves were additionally used as an input data source during training. The validation and test sets remained unchanged compared to scenario 1. In scenario 3, also the clinical NORM and LAE signals annotated with a certainty  $<100 \%$  by the expert cardiologist were added to the training split. The train, validation and test compositions for all training scenarios are summarized in Table 9.2. Accuracy, sensitivity, specificity metrics were calculated to evaluate the network performance of each training scenario, whereby the LAE signals were considered positive samples and the NORM signals negative samples (see section 3.4 and Figure 3.4). To avoid a bias of the network due to the larger number of samples in the NORM class in all training scenarios, the cross-entropy loss function was weighted by the inverse of the respective class support.

### 9.3 Results

Figure 9.6 depicts the confusion matrix for all training scenarios evaluated on the test set. Sensitivity, specificity and accuracy obtained for training scenario 1 were 0.83, 0.92 and 0.91, respectively. When additionally including simulated ECGs during training, as was the case

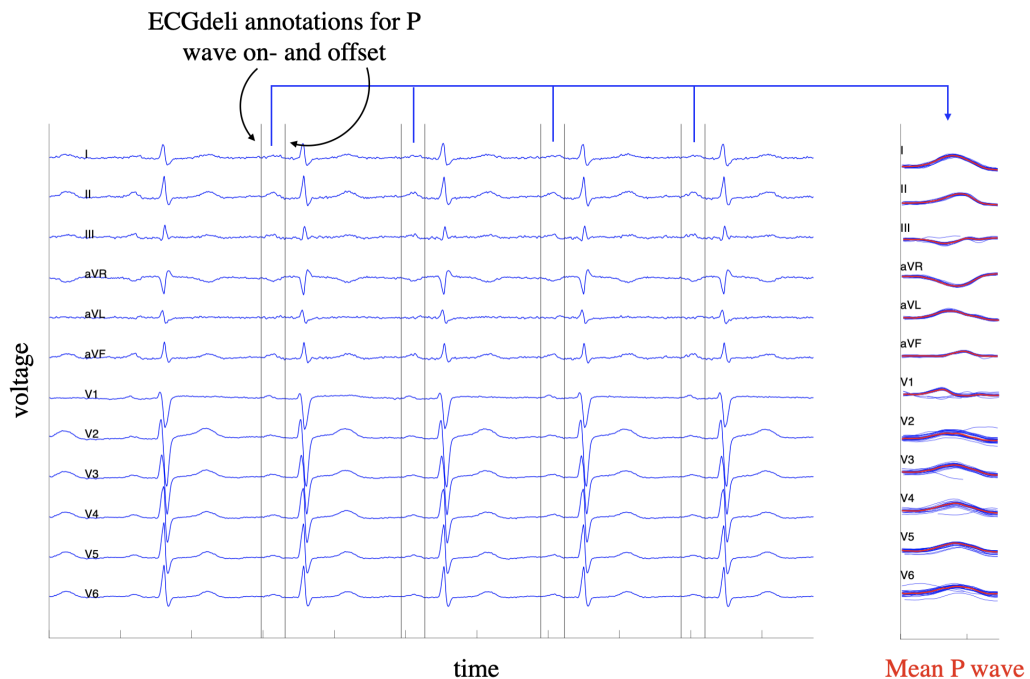


**Figure 9.5: Averaging single beat P waves for each 12-lead ECG in the clinical dataset.** This procedure was performed to obtain a mean P wave per subject and patient. An exemplary clinical 12-lead ECG is visualized in blue along with the ECGdeli annotations for P wave on- and offset in each beat. Averaging over all P waves detected in the signal trace resulted in a mean P wave template for each subject.

in scenario 2, the results for sensitivity, specificity and accuracy quantified to 0.87, 0.95 and 0.95, respectively. Thus, all three performance metrics improved when including simulated data for the training of the classifier. When extending the clinical training dataset of scenario 1 with additional clinical signals labeled with a certainty  $< 100\%$  in scenario 3, sensitivity, specificity and accuracy decreased to 0.78, 0.84 and 0.83 compared to the training scenario comprising only reliably labeled data.

## 9.4 Discussion

### 9.4.1 Main Findings

It was investigated whether the application of a bi-atrial SSM for generating a large synthetic ECG database can yield valuable additional input data for the training of a machine learning classifier to distinguish between clinical healthy and LAE ECGs. It was shown that the performance metrics of the network increased if simulated ECGs were added to reliably labeled clinical training data. The lowest scores for sensitivity, specificity and accuracy were achieved when additional clinical data with uncertain ground truth labels were included

**Table 9.2:** Number of samples in the healthy (NORM) and the left atrial enlargement (LAE) classes for different training scenarios. In scenario 1, a subset of the reliably labeled clinical data is used for training. For training scenario 2, simulated ECGs served as an additional input to the clinical training data from scenario 1. In scenario 3, clinical ECGs for which ground truth labels were specified with a certainty  $<100\%$  by the expert cardiologist were added to the training data. For all three cases, the same validation set and a test set comprising each 15% of the reliably labeled clinical data was used.

|           | Training Scenario 1 | Training Scenario 2 | Training Scenario 3 | Validation | Test       |
|-----------|---------------------|---------------------|---------------------|------------|------------|
| clinical  | NORM: 5018          | NORM: 5018          | NORM: 7335          | NORM: 1075 | NORM: 1075 |
|           | LAE: 216            | LAE: 216            | LAE: 328            | LAE: 47    | LAE: 46    |
| simulated | -                   | NORM: 1050          | -                   | -          | -          |
|           | -                   | LAE: 850            | -                   | -          | -          |
| total     | NORM: 5018          | NORM: 6068          | NORM: 7335          | NORM: 1075 | NORM: 1075 |
|           | LAE: 216            | LAE: 1066           | LAE: 328            | LAE: 47    | LAE: 46    |

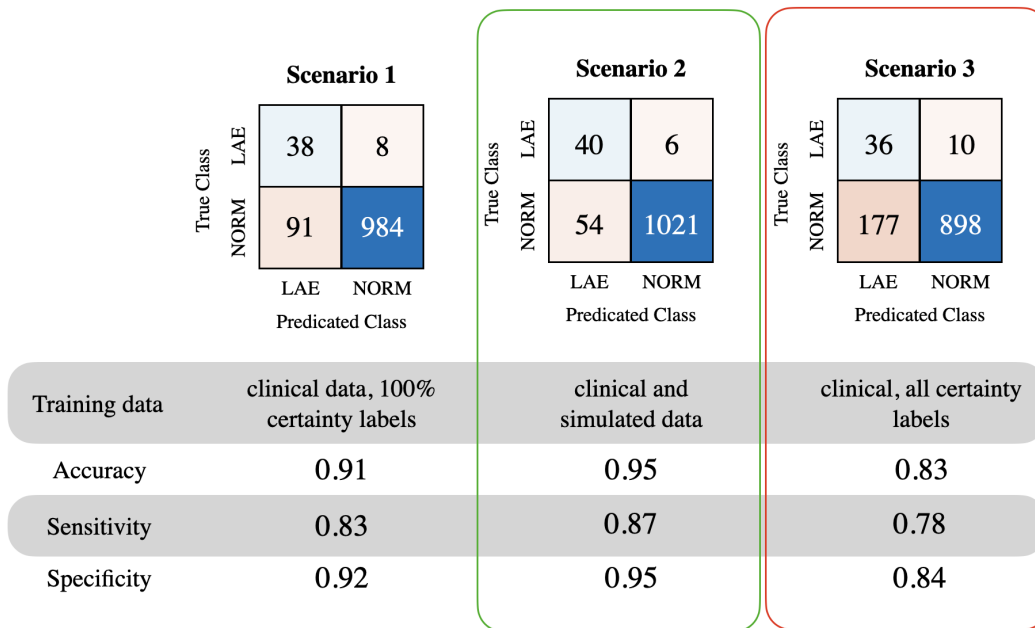


**Figure 9.6:** Confusion matrices and performance metrics resulting from predicting the labels of the test set with the network trained with each of the three training sets summarized in Table 9.2. Figure adapted from Nagel *et al.* [121] with permission from the publisher.

during training. Thus, expanding a clinical training dataset with simulated data can be preferable to either resigning oneself to a smaller clinical training split or extending the latter with additional unreliably tagged clinical data.

The advantage of deriving various *in silico* models of the atria from a SSM is on the one hand, that an arbitrary amount of geometries can be generated representing a large virtual

patient cohort. In this way, a large number of simulated ECGs can be generated contributing to the extension of the training data which otherwise typically only consist of a small amount of clinical signals. In this study, not only anatomical variability was incorporated by varying the atrial and thoracic geometries but also functional variability was added consisting of 10 different CV setups for each atrial model to capture inter-patient ECG variabilities to an even greater extent. On the other hand, the shape of the individual instances can be freely chosen by optimizing the eigenvector coefficients of the SSM. This implies that in the particular use case of identifying LAE based on 12-lead ECGs with machine learning techniques, the geometries can hold uniformly distributed left atrial volumes. In this way, the ground truth of the underlying pathologies for each signal is precisely known and also the distribution of the signals in the two classes can be chosen a priori. In doing so, the class imbalance for the training set was substantially reduced from 1:23 to 1:6. Furthermore, two different torso geometries were derived, representing a male and a female geometry. In this way, a one-to-one distribution of male and female ECGs in the simulated dataset prevailed contributing to a compensation of the gender bias in medical datasets.

The class imbalance during training was addressed by multiplying the cross-entropy loss function with the inverse of the class support. Considering sensitivity and specificity metrics in addition to evaluating the network's accuracy performance demonstrated that the class-wise accuracy was above 0.8 in all scenarios and thus, no notable overfitting towards the over-represented NORM class, especially in those scenarios where the classifier was only trained on clinical data, occurred.

### 9.4.2 Related Work

One key aspect for a successful and meaningful application of simulated ECGs to classification problems with clinical signals is assessing fidelity and comparability of the simulated data to the clinical ECGs and previously published simulation studies. In chapter 5 [169] it was shown that the P wave duration distribution originating from simulations on instances of the SSM with Gaussian distributed eigenvector coefficients is in accurate accordance with P wave durations reported in large clinical cohort studies of healthy subjects. The altered ECG signal characteristics in LAE patients reported in clinical studies and comprising an increased duration and absolute amplitude in the negative deflection of the P wave in lead V1 as well as an increased overall duration of P wave in all leads were also reflected in the simulation results (see Figure 9.3). However, a data-driven comparison between the synthetic and the clinical dataset for the healthy and LAE cases would further help to assess fidelity of the simulated ECGs (compare chapter 6).

In this study, the absolute amplitude and the duration of both, the positive and the negative deflection of the P wave in lead V1 increased with the left atrial volume (see Fig. 9.3). Andlauer *et al.* [176, 317] reported that left atrial concentric hypertrophy causes an increase in the absolute P wave amplitude of the negative deflection in V1, whereas left atrial dilation with a constant myocardial volume does not have a marked effect on the ECG morphology in V1. In contrast to the work presented in this chapter, the shape

of the right atrium remained constant which might explain the additional alterations in the positive deflection in V1 for the simulation results. Furthermore, for any stage of left atrial dilation, the myocardial volume was kept constant in the study conducted by Andlauer *et al.* [176], implying that the wall thickness decreased with an increasing left atrial volume. In the study shown in this chapter, a constant wall thickness of 3 mm was ensured for all atrial geometries, i.e. the myocardial volume increases with the left atrial size. This could thus explain the absolute increase of the negative amplitude in V1 for increasing LAV values as seen in Fig. 9.3 and reported for left atrial hypertrophy by Andlauer *et al.* [176].

### 9.4.3 Limitations

The network used for the classification was not explicitly optimized. A standard setup was used for a binary LSTM classifier. Tuning the network's hyperparameters or using a different network architecture might further improve the results. However, in this work, the focus was not on developing a robust classification method for healthy and LAE patients in the first place. Instead, the hypothesis that applying a bi-atrial SSM as a basis to generate a large database of synthetic simulation-derived electrophysiological signals with a predefined class distribution and precisely known ground truth labels can improve real-world classifier performance was put to test. It was shown that this approach can help to overcome the drawbacks of only using clinically recorded ECGs as the classifier performance improved when a combination of clinical and simulated data was employed during training.

Resorting to the Eikonal model and the boundary element method as simplified model solutions for normal sinus rhythm simulations has been shown to yield P waves of the 12-lead ECG resembling the full bidomain simulation results to a high degree [164, 303]. In this study, two torso models were used for the generation of the *in silico* database. As shown previously [122] and reported in chapter 8, the torso geometry mainly has an influence on the ECG amplitudes, whereas the P wave morphology is primarily dependent on the atrial geometry and functional variability. Therefore, 95 atrial geometries were considered with 10 different conduction velocity settings and only 2 different torso models representing a male and a female thoracic geometry were used. Since the torso models were derived from an SSM [179], the location of the electrodes could be consistently defined on both models and no electrode placement variability is reflected in the simulated dataset. Future directions could include the consideration of further patient characteristics such as the age, sex, weight and accompanying pathologies for an improved classification result [318]. Furthermore, adding more simulated data covering a larger torso variability and electrode placement variations to the training dataset could also yield improved results.

Even though the latest recommendations for diagnosing LAE were complied with by assessing LAV indexed to the BSA for each model combination to define the ground truth labels for the virtual patient cohort, these values are determined with approximation formulas in clinical practice and are therefore prone to errors. By including a multiplication factor in the analytical LAV calculation to account for the systematic underestimation of the atrial volume with 2D echocardiography compared to MR measurements, it was intended to correct

for the inaccuracies and establish comparability to the clinical reference volumes. However, this correction factor itself and also the calculation of the BSA might still not lead to the exact same values that would have been set in clinical practice. Thus, even though the ground truth labels in the simulation dataset are analytically correct, they could have varied if the volume indexed to the BSA was calculated with the clinical approximation functions based on height, weight and gender of the patient.

## 9.5 Conclusion

In conclusion, it was shown that the application of a bi-atrial SSM as a basis for generating synthetic ECGs can help to overcome the main drawbacks of clinically recorded signals for an automated classification of healthy and LAE ECGs with machine learning techniques: Firstly, an arbitrary number of atrial geometries can be derived leading in combination with functional electrophysiological variability to synthetic ECG signals representing a large virtual patient cohort. Secondly, the distribution of the synthetic ECGs in the different pathology classes can be freely chosen by drawing the eigenvector coefficients of the shape model from a custom statistical distribution so that left atrial volumes in the virtual cohort are uniformly distributed. Thirdly, reliable ground truth labels can be assigned to the simulated signals since diagnostic values for left atrial volumes and body surface areas are analytically calculable for the atrial and thoracic finite element models. These advantages finally contribute to an improved classification result of clinical healthy and left atrial enlargement ECGs when simulated data is added to the training set.



---

PART V

---

FINAL REMARKS



---

## Outlook

### 10.1 Application and Validation of Multiscale Populations of Atrial Models

Ideas for future projects involve applying an extensive population of atrial models for *in silico* clinical trials or for atrial fibrillation (AF) vulnerability studies. For this purpose, the model cohort presented in chapter 6 could be extended to systematically study differences in disease and treatment response among different cohorts, for example male vs. female subjects, or different age groups. Subsequently, vulnerability studies could reveal arrhythmogenic propensity of different subpopulations and unravel key model characteristics responsible for initiating and maintaining AF not only on a patient-specific level, but for entire subgroups of patients. Finally, the efficacy of different therapy options can be studied to investigate whether specific treatment strategies are particularly suitable for a specific subpopulation.

#### 10.1.1 Extension of the Model Population

The construction of separate atrial statistical shape models (SSMs) representing for example healthy and AF patients or male and female subjects can provide a means to particularly derive instances known to reflect specific shape characteristics of the respective group. Furthermore, mapping a scalar field showing the probability of low-voltage being present in different atrial regions across a clinical population onto the SSM as proposed by Nairn *et al.* [84, 304], could allow for directly generating endocardial instances with local arrhythmogenic substrate areas to be remodeled in the course of the simulations. To further enlarge the cohort, different torso shapes and rotation angles of the atria could be included into the population of models as explained in chapter 6. Thus, various cohorts of multiscale atrial computational models representing a wider range of variability can be derived, calibrated and grouped into different subpopulations based on various properties, as for example AF history, anatomical characteristics, age or gender.

Age is one of the major risk markers for AF development [319], which is why an independent analysis of AF inducibility for an advanced age group could provide mechanistic insights into the driving forces for AF in affected subjects. Likewise, AF incidence rates are reported to be higher in men than in women [320]. Predominantly, more round left atrial shapes are observed in men, potentially representing one of the causes for increased AF onsets in male patients [318]. A separate shape analysis for male and female AF patients could therefore contribute to systematically investigate the impact of gender-related atrial shape variability on the onset and termination of AF. Also for the cellular model population, a gender-specific analysis regarding their risk of AF development can be carried out as done in previous work [321]. Ionic parameters for the cell model population can be chosen to capture female and male electrophysiology, so that a sex-specific evaluation regarding their AF vulnerability can be carried out. The feasibility of generating atrial instances randomly (see chapter 6 and chapter 8) and with systematic constraints regarding atrial volumes (see chapter 9) as demonstrated in this thesis can be built on for generating and calibrating different multiscale model populations.

### 10.1.2 Vulnerability Study

By applying an arrhythmia inducibility protocol, such as the one proposed by Azzolin *et al.* [48] for example, AF vulnerability for each model in all subgroups can be studied systematically and comprehensively. Arrhythmia propensity can be quantified by the number of pacing sites from which reentry patterns could be induced, the dynamics of the induced episodes (duration and complexity) and the areas in which arrhythmia drivers anchor. The results of the arrhythmia vulnerability study can be evaluated to investigate whether there are specific subgroups that have an increased pro-arrhythmic risk compared to others. Work by Vagos *et al.* [256] suggests that ionic remodeling parameters are independent predictors for AF propensity. Furthermore, Jia *et al.* [65] showed that left atrial shape is associated with AF susceptibility. Both of these properties provide the necessary requirements for an arrhythmia to be sustained, namely a reduced conduction velocity, a shortened refractory period and an increased path length. With a population of multiscale models comprising the relevant variability, a fully integrated approach becomes feasible. Screening cohorts characterized both by different anatomical and functional properties systematically allows for identifying key remodeling parameters driving the arrhythmia and potentially dominate other factors. Subgroups more prone to arrhythmia development could be identified e.g. by means of fuzzy C-means or by Density-Based Spatial Clustering of Applications with Noise (DBSCAN) methods based on the arrhythmia propensity quantification results. Further methods to divide the model cohorts into subgroups characterized by their AF vulnerability could include decision trees as applied by Jia *et al.* [65] or sensitivity analysis as done by Vagos *et al.* [256]. Furthermore, electrocardiograms (ECGs) of the atrial normal sinus rhythm (P waves) and re-entry activity (f waves and F waves for fibrillation and flutter, respectively) can be computed for all instances in the model cohort. P waves could then serve as an input to machine learning techniques, taking either the raw ECG signals or selected features as an

input. The algorithms could be trained to estimate the number of inducing points and other arrhythmia markers found for the respective model in the course of the vulnerability study as a surrogate for the patient's individual risk to develop new-onset AF.

### 10.1.3 Treatment Efficacy Assessment

Based on the reentry simulations, the two major rhythm control options for treating AF can be applied. On the one hand, the efficacy of different pharmacological ion channel blockers and their doses [60, 322–324] for terminating reentry in all models can be investigated. On the other hand, it can be examined if there are systematic rules to place ablation lesions for different subgroups in the cohort to successfully terminate the arrhythmia and prevent recurrence. Ablation strategies to be tested could include pulmonary vein isolation or ablation of fibrotic areas with and without connection to non-conducting anatomical structures and a combination of the above. In this way, systematic rules for ablation target selection depending on anatomical and functional characteristics of the patients represented by the models could be retrieved. Furthermore, it can be investigated if the optimal ablation lines and drug doses can be identified based on the f waves computed for each individual model using similar machine learning strategies as described above. In this way, a non-invasive prediction of the optimal treatment strategy could precede catheter ablation and reduce procedure times.

## 10.2 ECG-based Differential Diagnosis of Atrial Fibrillation Related Pathologies

The ECGs generated in the studies and described in this thesis are representative for a healthy cohort (see chapter 6 and chapter 8) and patients with arrhythmogenic fibrotic atrial cardiomyopathy (FAM) (see chapter 8), left atrial enlargement (LAE) (see chapter 9) and interatrial conduction block (IAB) (see chapter 7). The changes in ECG characteristics between the healthy control group and each of the cohorts representing the above mentioned atrial pathologies, have been examined in detail and could individually be discriminated from the healthy signals using machine learning techniques. However, all of the examined atrial pathologies reflect partly in similar ECG changes, as for example P wave duration is increased in patients of all three above listed diseases. Thus, future projects could focus on investigating whether a differential diagnosis of healthy, FAM, LAE and IAB ECGs is feasible. In this way, risk stratification of AF can be performed more comprehensively and unveil the specific remodeling aspect driving the arrhythmia, whether it being structural (in case of FAM or IAB) or anatomical (in case of LAE). Thus, therapy planning can be further optimized and procedure times can be notably reduced by pointing towards the underlying arrhythmogenic mechanism prior to the actual intervention. For this purpose, the P wave databases generated in chapter 8, chapter 9 and by Bender *et al.* [260] could be employed initially to compute atrial ECG biomarkers without a necessary preprocessing step to delimit

the single waveforms of the 12-lead ECG affecting the accuracy of extracted P waves and features. Following, the 12-lead ECG curves described in chapter 7 could be used to train the machine learning algorithm directly to investigate if a differential diagnosis can be made automatically without extensive feature extraction steps preceding the development of the machine learning model. Also in this regard, the explicit benefit of simulated data in this multi-class classification task could be assessed by quantifying the improvement or decline in prediction accuracy in case the model is trained only on clinical data or on a hybrid ECG dataset.

---

## Conclusion

In summary, the main focus of this thesis was the large- and multiscale generation of atrial computational models for electrophysiological simulations leading ultimately to P waves of the 12-lead electrocardiogram (ECG). These are for example applicable as an extension to clinical signals in the machine learning context. To accelerate the generation of large synthetic P wave datasets, simplified propagation models and forward calculation methods were examined to later on choose the most appropriate simulation approach ensuring physiological accuracy of the resulting signals, yet at reasonable computational cost. To overcome the lack of anatomical variability in recent atrial cohort simulation studies, a bi-atrial statistical shape model (SSM) was developed and evaluated. Based thereon, a multiscale population of atrial computer models comprising not only anatomical variability, but also functional variability on both tissue and cellular scale, was compiled and calibrated. Two large-scale simulation studies were performed to investigate the added value of simulated ECG data enriching clinically recorded signals for classification and regression tasks with machine learning algorithms. These served the purpose to answer the overall research question underlying this thesis (see section 1.3), namely, whether the performance of a machine learning model for atrial fibrillation (AF) risk stratification trained on a hybrid dataset leads to improved results compared to training on clinical data only. The former training scenario yielded improved results for the ECG-based detection of both left atrial enlargement (LAE) and arrhythmogenic fibrotic atrial cardiomyopathy (FAM), with details outlined below. In this regard, it was investigated whether the inherent properties of electrophysiological simulations comprising the generation of large, balanced and reliably annotated data samples, can counteract the typical shortcomings prevailing in clinical datasets. Hence, two computational model cohorts were employed to generate P waves characterized by the presence of fibrotic substrate in the atria as well as by an enlarged left atrial volume. Both were used for the training of a machine learning model to predict the underlying structural and anatomical alterations in the atria which are predisposing factors for the development of AF. The main conclusion drawn from the studies conducted within the scope of this thesis and summarized above are as follows.

**For simulations of normal sinus rhythm in atrial electrophysiology with and with-**

**out the inclusion of fibrotic tissue, the Eikonal model and the boundary element method (BEM) can be employed to simulate P waves of a comparable accuracy to the gold standard simulation approaches at a reduced computational cost.**

Independent on the methodology to model fibrotic tissue, the Eikonal model combined with the BEM yielded P waves exhibiting correlation coefficients above 0.9 to the gold standard full-blown bidomain simulation. Pseudo-ECGs generated with the infinite volume conductor method failed to accurately reproduce P waves in the precordial leads and led to amplitude overshoot mainly visible in lead V1-V3. Only in simulation scenarios where repolarization dynamics are of significant importance, e.g., for reentry simulations, the diffusion term in simplified propagation models can no longer be neglected as this assumption resulted in action potential durations notably deviating from the bidomain results.

**A bi-atrial SSM can serve as a basis for including atrial anatomical variability in populations of computer models contributing to represent variability in ECG biomarkers and P wave morphology occurring also in large clinical cohorts.**

The atrial SSM was built using automatically found corresponding landmarks on 47 individual atrial image segmentations. It allows for deriving various endocardial surfaces that can be augmented to simulation-ready volumetric geometries representing atrial anatomy in a population. Atrial anatomy was shown to be a main contributing factor to varying P wave morphology in ECG simulations of virtual cohorts.

**If properly processed, simulated data can contribute to improve the prediction of fibrotic tissue volume fractions on clinical ECGs when provided as additional input to a shallow feature-based feedforward neural network.**

The fraction of left atrial fibrotic tissue can be estimated based on extracted P wave biomarkers from clinical signals with an absolute error of 17.5 % fibrotic volume by a shallow neural network. When adding simulated P wave features to the clinical training set, the estimation error can be reduced to 16.5 % fibrotic volume. In this way, adding features of simulated signals during training counteracted the disadvantages of small and imbalanced clinical datasets. It was also found that the degree of pre-processing the simulated signals, i.e. the addition of noise and the chosen cutoff frequency of a low-pass filter, was decisive for the quality of the network outcome. This is because the addition of noise and a high cutoff frequency for the lowpass-pass filter strike a balance in closing the domain gap to clinical signals and preserving subtle ECG characteristics attributable to the presence of fibrotic substrate in the atria.

**Key P wave biomarkers for estimating the volume fraction of left atrial fibrosis comprise mainly features relying on the detection of the P wave offset. This indicates that robust feature extraction methods are required for delineating the P wave ending in clinical signals.**

When adding noise directly to the extracted P wave features in the simulated database, the prediction accuracy of the neural network was impaired the most for biomarkers whose calculation was based on the P wave offset, such as P wave duration and the root mean squared

---

voltage in the terminal signal parts of the P wave in individual leads. Thus, the delineation of P waves, especially the detection of the P wave ending in clinical ECGs, requires robust, sophisticated and reliable methods to ensure an accurate calculation of P wave biomarkers for training the network.

**A deep learning network tailored at detecting LAE from clinical ECGs benefits from being provided simulated signals as an additional input data source during training. In contrast, adding further clinical data during training of which pathology labels were annotated with less than 100% certainty was detrimental to network performance.**

The accuracy of a long short-term memory (LSTM) network for performing the binary classification task between clinical healthy and LAE ECGs quantified to 0.95 when trained on a hybrid dataset, to 0.91 when trained on clinical data with 100% label certainty, and to 0.83 when trained on clinical data with all label certainties. Thus, adding simulated data for the training process of the classifier actually contributed to an improved performance, potentially due to the added signal variability of a more heterogeneous and diverse simulated dataset the network can be trained on. In contrast, extending the clinical dataset with further clinical ECGs of unreliably annotated ground truth labels was rather confounding and led to a declined classification outcome. Ultimately, this highlights the benefit of accurately known ground truth pathology labels for simulated signals definable by adjusting parameter settings in the underlying simulation run.



## P waves and Amplitude Features in Fibrosis Remodeling Scenarios

The following figures complement the results for P waves and peak-to-peak amplitude features computed with different propagation drivers and forward calculation methods in the remaining simulation scenarios not included in section 4.3.

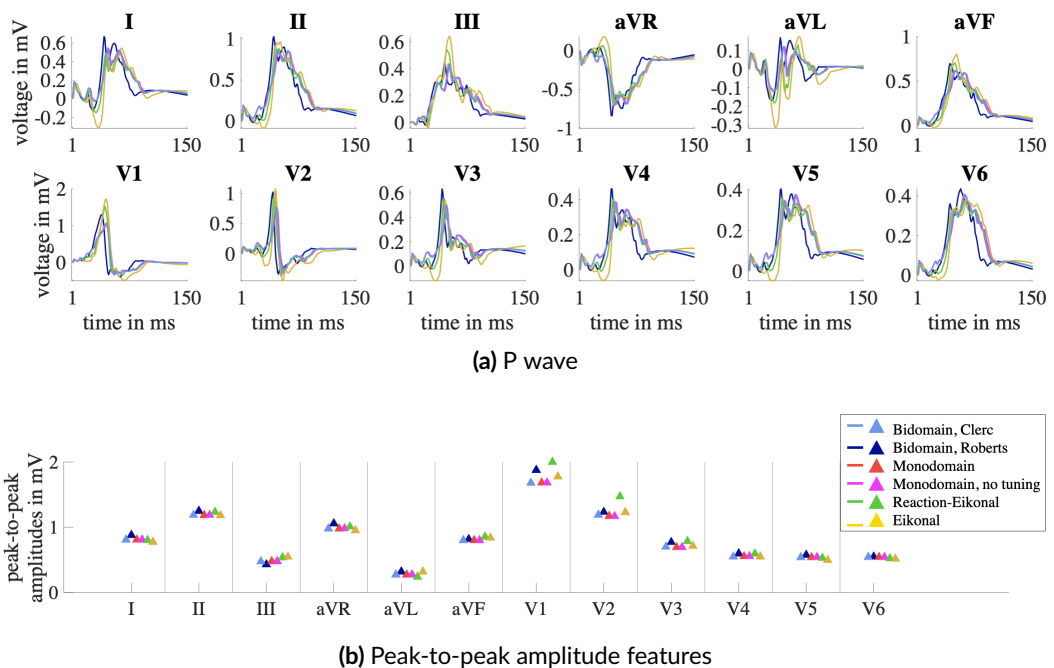


**Figure A.1:** ECGs (P waves) calculated with the same forward calculation method (BEM) but different propagation models (color coded) with the transmembrane voltages resulting from the simulation scenario with fibrosis modeled as slow conducting tissue. Peak-to-peak amplitude features extracted from the ECGs calculated with BEM and the respective propagation driver are represented with the colored triangle.

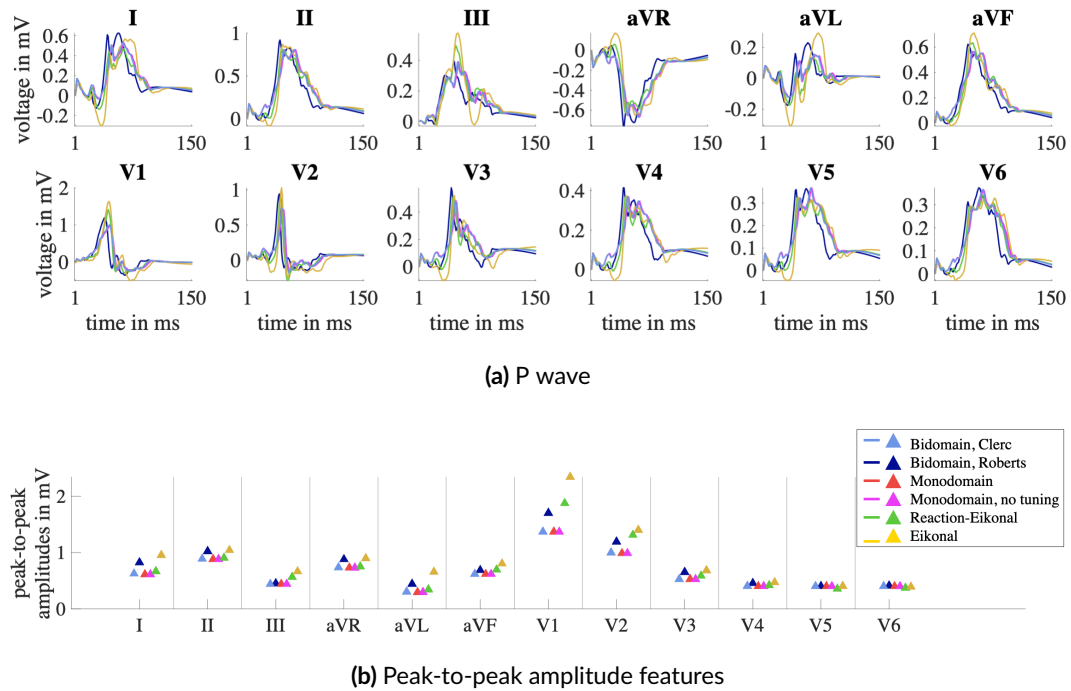
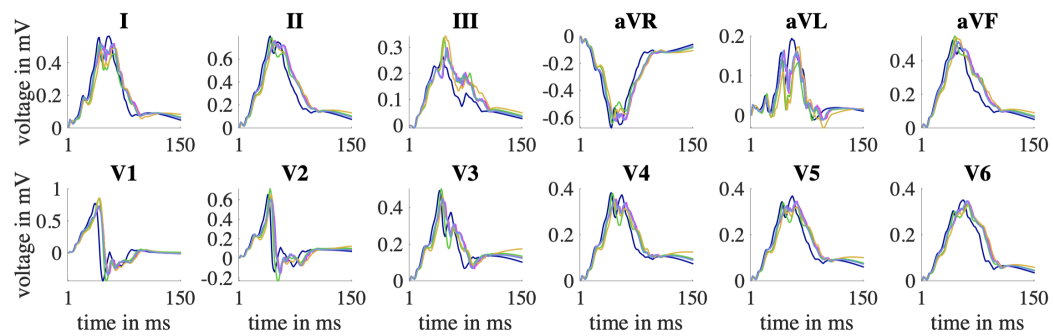
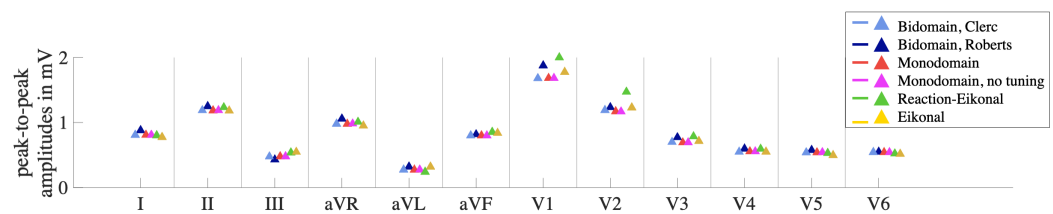


**Figure A.2:** ECGs (P waves) calculated with the same forward calculation method (BEM) but different propagation models (color coded) with the transmembrane voltages resulting from the simulation scenario with fibrosis modeled as slow conducting tissue. Peak-to-peak amplitude features extracted from the ECGs calculated with BEM and the respective propagation driver are represented with the colored triangle.



(a) P wave



(b) Peak-to-peak amplitude features

**Figure A.3:** ECGs (P waves) calculated with the same forward calculation method (BEM) but different propagation models (color coded) with the transmembrane voltages resulting from the simulation scenario with fibrosis modeled as slow conducting tissue. Peak-to-peak amplitude features extracted from the ECGs calculated with BEM and the respective propagation driver are represented with the colored triangle.

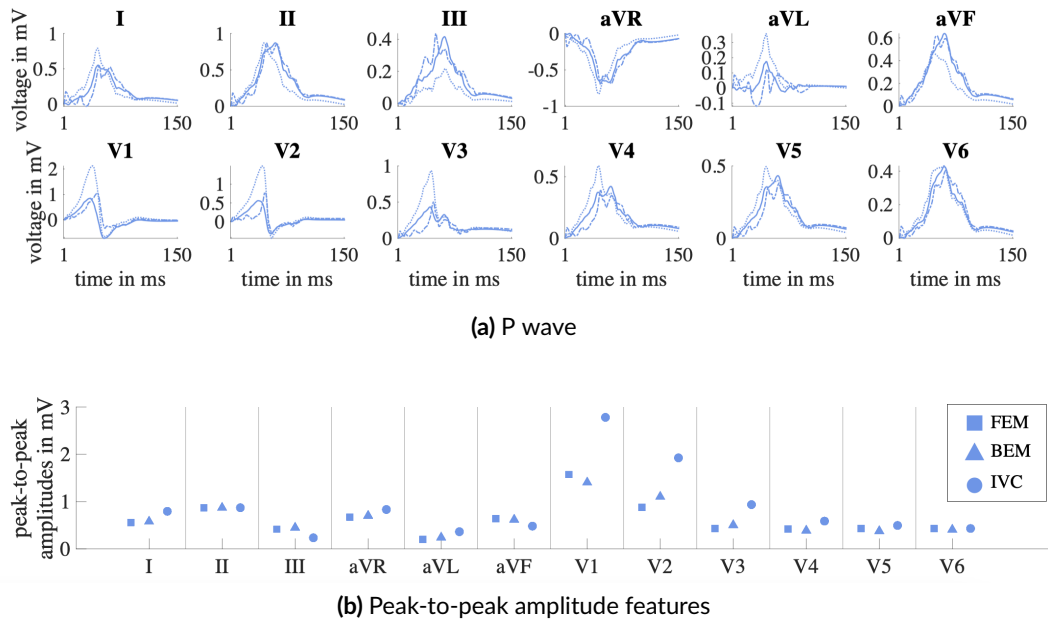


**Figure A.4:** ECGs (P waves) calculated with the same propagation driver (bidomain) but different forward calculation method for the healthy control simulation scenario. ECGs calculated with FEM, BEM and IVC results are represented by the solid, dashed and dotted lines, respectively. Peak-to-peak amplitude features extracted from the ECGs calculated with FEM, BEM and IVC are represented with square, triangle and circle markers, respectively.

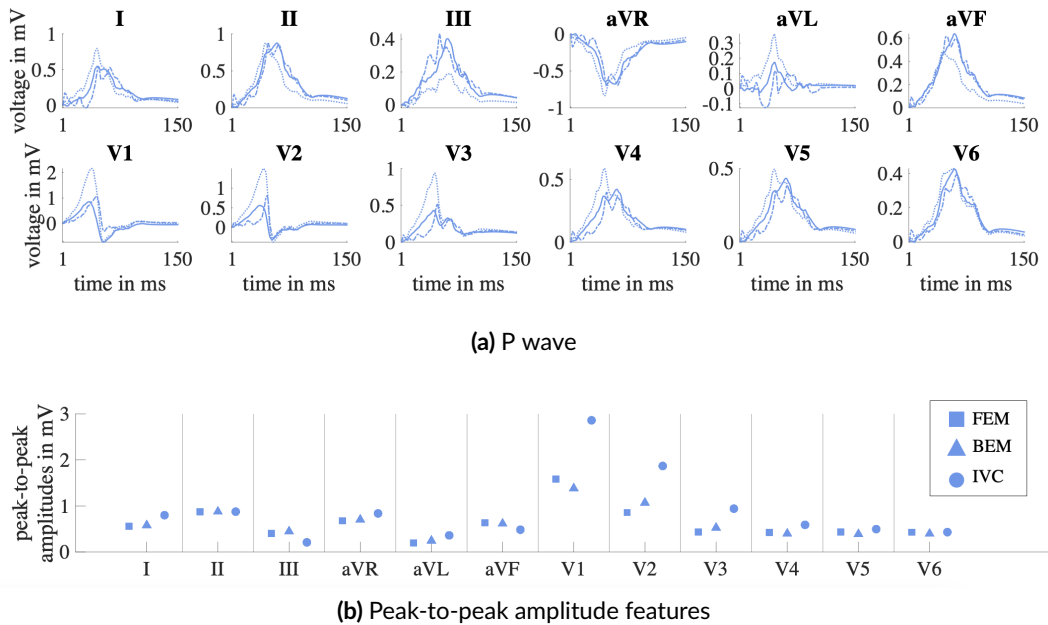
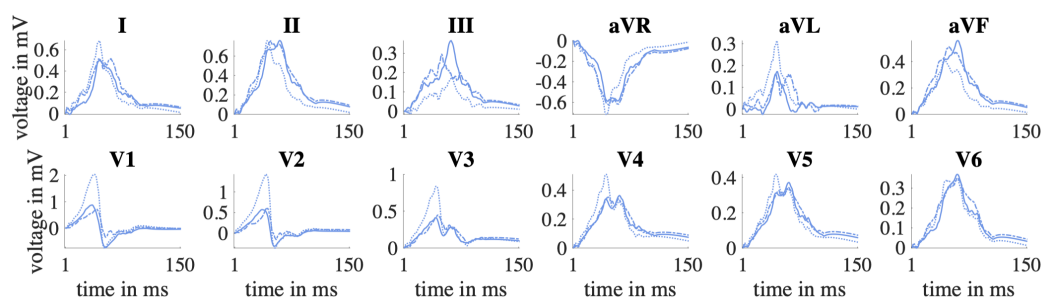
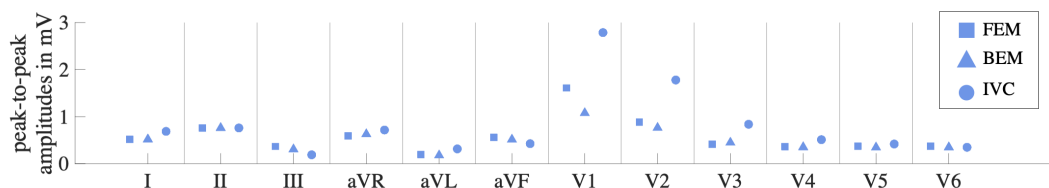


**Figure A.5:** ECGs (P waves) calculated with the same propagation driver (bidomain) but different forward calculation method for the simulation scenario with fibrosis modeled as ionic conductance rescaling. ECGs calculated with FEM, BEM and IVC results are represented by the solid, dashed and dotted lines, respectively. Peak-to-peak amplitude features extracted from the ECGs calculated with FEM, BEM and IVC are represented with square, triangle and circle markers, respectively.



(a) P wave



(b) Peak-to-peak amplitude features

**Figure A.6:** ECGs (P waves) calculated with the same propagation driver (bidomain) but different forward calculation method for the simulation scenario with fibrosis modeled as passive conduction barriers. ECGs calculated with FEM, BEM and IVC results are represented by the solid, dashed and dotted lines, respectively. Peak-to-peak amplitude features extracted from the ECGs calculated with FEM, BEM and IVC are represented with square, triangle and circle markers, respectively.

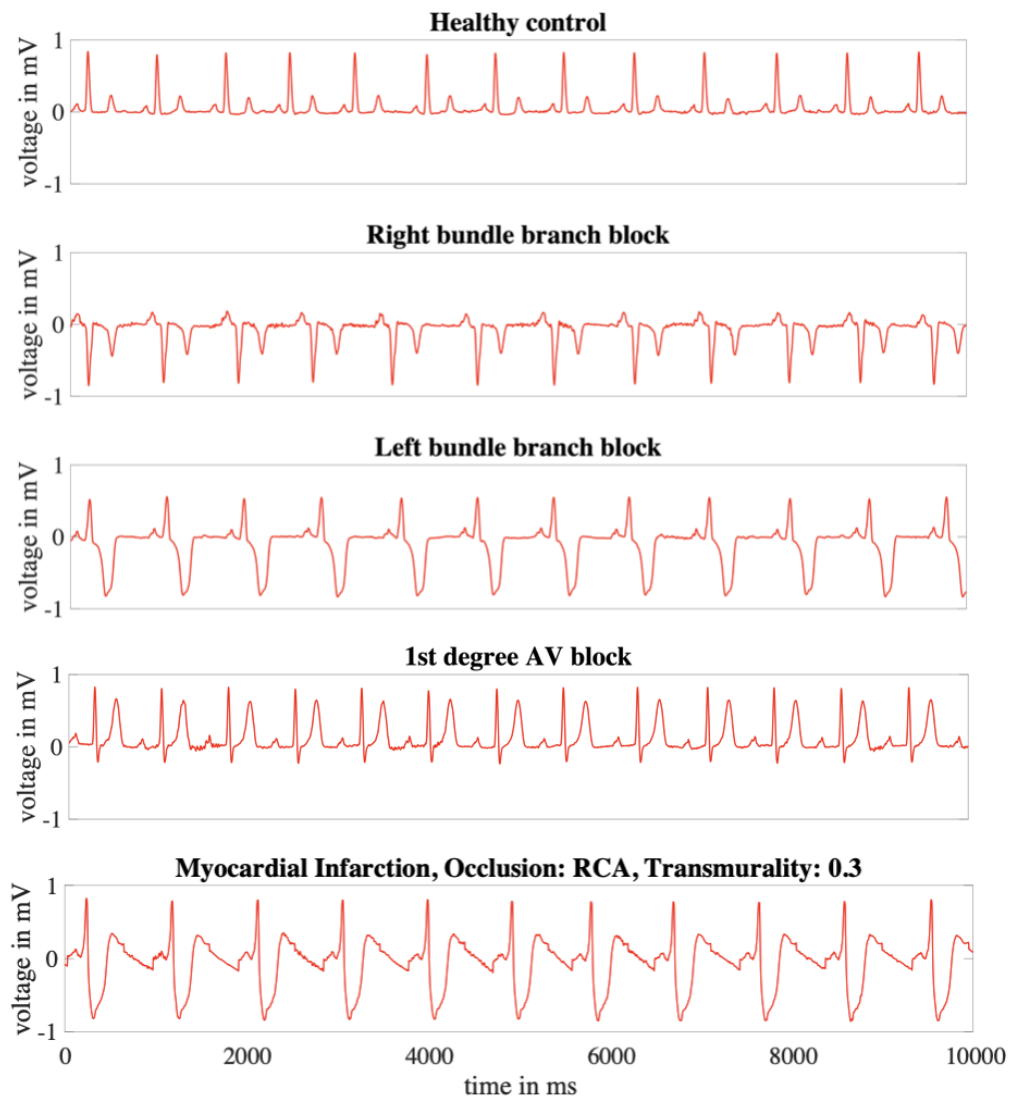


---

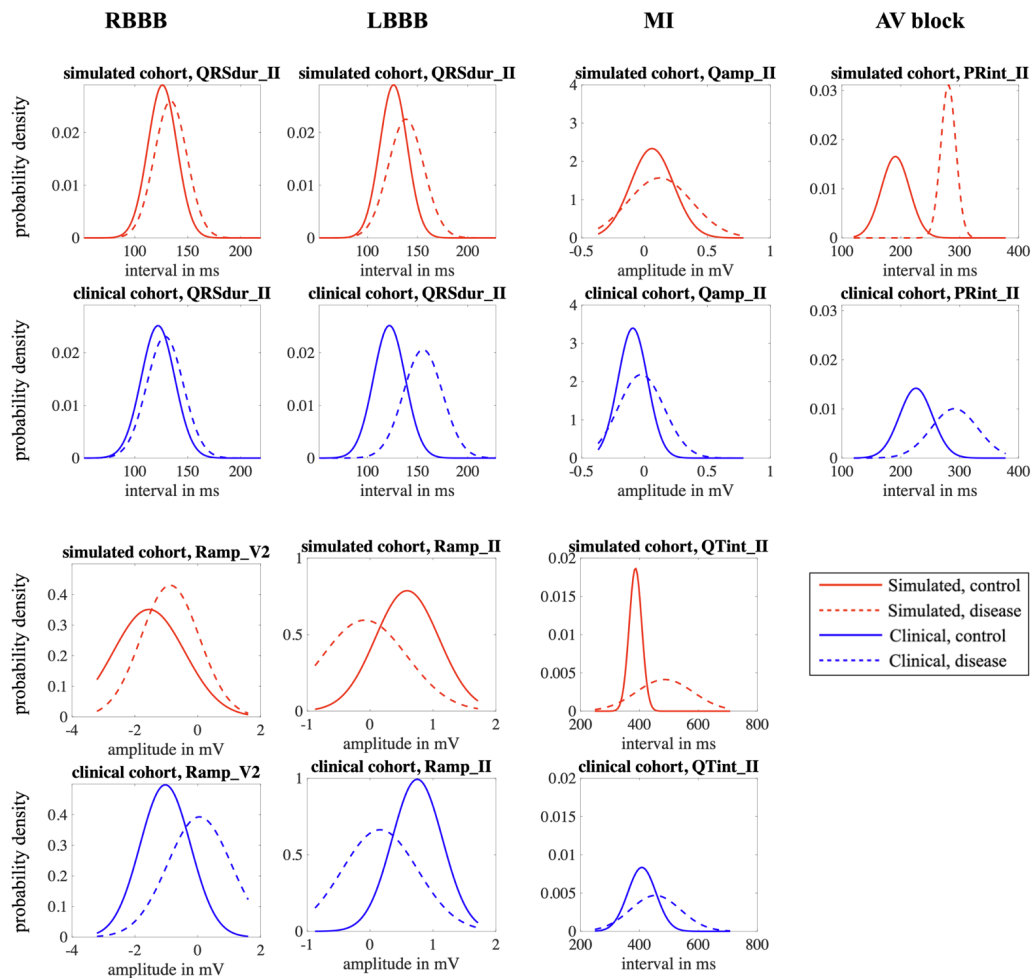
## Ventricular Pathologies in Large-scale ECG Dataset

Figure B.1 exemplarily shows lead II of one simulated and synthesized 10 s electrocardiogram (ECG) belonging to the healthy control, the right bundle branch block (RBBB), left bundle branch block (LBBB), atrioventricular block (AVB) and the myocardial infarction (MI) pathology class.

Figure B.2 shows the distributions of characteristic features extracted from ECGs of the RBBB, the LBBB, the AVB and the MI simulated and clinical cohort.



**Figure B.1:** Exemplary simulated and synthesized ECGs for ventricular pathologies and the healthy control.



**Figure B.2:** Feature distributions compared between the ventricular pathology classes and the healthy control.



# References

- [1] A. Zhang, L. Xing, J. Zou, and J. C. Wu, “Shifting machine learning for healthcare from development to deployment and from models to data,” *Nature Biomedical Engineering*, 2022. doi:10.1038/s41551-022-00898-y
- [2] A. Mincholé and B. Rodriguez, “Artificial intelligence for the electrocardiogram.” *Nat Med*, vol. 25, pp. 22–23, 2019. doi:10.1038/s41591-018-0306-1
- [3] A. Lyon, A. Mincholé, J. P. Martínez, P. Laguna, and B. Rodriguez, “Computational techniques for ECG analysis and interpretation in light of their contribution to medical advances.” *J R Soc Interface*, vol. 15, 2018. doi:10.1098/rsif.2017.0821
- [4] K. C. Siontis, P. A. Noseworthy, Z. I. Attia, and P. A. Friedman, “Artificial intelligence-enhanced electrocardiography in cardiovascular disease management,” *Nature Reviews Cardiology*, vol. 18, pp. 465–478, 2021. doi:10.1038/s41569-020-00503-2
- [5] M. Zoni Berisso, F. Lercari, T. Carazza, and S. Domenicucci, “Epidemiology of atrial fibrillation: European perspective,” *Clin Epidemiol*, vol. 6, pp. 213–220, 2014. doi:10.2147/CLEP.S47385
- [6] T. Wilke, A. Groth, S. Mueller, et al., “Incidence and prevalence of atrial fibrillation: an analysis based on 8.3 million patients,” *Europace*, vol. 15, pp. 486–493, 2013. doi:10.1093/europace/eus333
- [7] F. Rahman, G. F. Kwan, and E. J. Benjamin, “Global epidemiology of atrial fibrillation,” *Nature Reviews Cardiology*, vol. 11, pp. 639–654, 2014. doi:10.1038/nrcardio.2014.118
- [8] L. Staerk, J. A. Sherer, D. Ko, E. J. Benjamin, and R. H. Helm, “Atrial Fibrillation: Epidemiology, Pathophysiology, and Clinical Outcomes,” *Circulation Research*, vol. 120, pp. 1501–1517, 2017. doi:10.1161/CIRCRESAHA.117.309732
- [9] J. Kornej, C. S. Börschel, E. J. Benjamin, and R. B. Schnabel, “Epidemiology of Atrial Fibrillation in the 21st Century,” *Circulation Research*, vol. 127, pp. 4–20, 2020. doi:10.1161/CIRCRESAHA.120.316340
- [10] L. Y. Chen, A. L. P. Ribeiro, P. G. Platonov, et al., “P-Wave Parameters and Indices: A Critical Appraisal of Clinical Utility, Challenges, and Future Research-A Consensus Document Endorsed by the International Society of Electrocardiology and the International Society for Holter and Noninvasive Electrocardiology.” *Circ Arrhythm Electrophysiol*, p. CIRCEP121010435, 2022. doi:10.1161/CIRCEP.121.010435
- [11] J. Seitz, T. M. Durdez, J. Albenque, et al., “Artificial Intelligence Software Standardizes Electrogram-based Ablation Outcome for Persistent Atrial Fibrillation,” *Journal of Cardiovascular Electrophysiology*, 2022. doi:10.1111/jce.15657
- [12] S. Raghunath, J. M. Pfeifer, A. E. Ulloa Cerna, et al., “Deep Neural Networks Can Predict New-Onset Atrial Fibrillation From the 12-Lead ECG and Help Identify Those at Risk of

- Atrial Fibrillation–Related Stroke,” *Circulation*, vol. 143, pp. 1287–1298, 2021. doi:10.1161/CIRCULATIONAHA.120.047829
- [13] A. Barbarossa, F. Guerra, and A. Capucci, “Silent Atrial Fibrillation: A Critical Review.” *J Atr Fibrillation*, vol. 7, p. 1138, 2014. doi:10.4022/jafib.1138
- [14] E. Z. Soliman, R. J. Prineas, L. D. Case, Z.-m. Zhang, and D. C. Goff, “Ethnic distribution of ECG predictors of atrial fibrillation and its impact on understanding the ethnic distribution of ischemic stroke in the Atherosclerosis Risk in Communities (ARIC) study.” *Stroke*, vol. 40, pp. 1204–11, 2009. doi:10.1161/STROKEAHA.108.534735
- [15] P. A. Wolf, R. D. Abbott, and W. B. Kannel, “Atrial fibrillation as an independent risk factor for stroke: the Framingham Study,” *Stroke*, vol. 22, pp. 983–988, 1991.
- [16] P. Wagner, N. Strodthoff, R.-D. Bousseljot, et al., “PTB-XL, a large publicly available electrocardiography dataset.” *Sci Data*, vol. 7, p. 154, 2020. doi:10.1038/s41597-020-0495-6
- [17] C. Sudlow, J. Gallacher, N. Allen, et al., “UK Biobank: An Open Access Resource for Identifying the Causes of a Wide Range of Complex Diseases of Middle and Old Age,” *PLOS Medicine*, vol. 12, p. e1001779, 2015. doi:10.1371/journal.pmed.1001779
- [18] S. R. St. Pierre, M. Peirlinck, and E. Kuhl, “Sex Matters: A Comprehensive Comparison of Female and Male Hearts,” *Frontiers in Physiology*, vol. 13, 2022. doi:10.3389/fphys.2022.831179
- [19] A. Herraiz Martínez, C. Tarifa, V. Jiménez Sábado, et al., “Influence of sex on intracellular calcium homeostasis in patients with atrial fibrillation.” *Cardiovasc Res*, 2021. doi:10.1093/cvr/cvab127
- [20] A. W. Lee, D. P. O’Regan, J. Gould, et al., “Sex-Dependent QRS Guidelines for Cardiac Resynchronization Therapy Using Computer Model Predictions,” *Biophysical Journal*, vol. 117, pp. 2375–2381, 2019. doi:10.1016/j.bpj.2019.08.025
- [21] E. Puyol Anton, B. Ruijsink, S. K. Piechnik, et al., “Fairness in Cardiac MR Image Analysis: An Investigation of Bias Due to Data Imbalance in Deep Learning Based Segmentation,” *arXiv*, 2021. arXiv:2106.12387v2
- [22] N. Rieke, J. Hancox, W. Li, et al., “The future of digital health with federated learning,” *npj Digital Medicine*, vol. 3, 2020. doi:10.1038/s41746-020-00323-1
- [23] S. Kapoor and A. Narayanan, “Leakage and the Reproducibility Crisis in ML-based Science,” *eprint*, 2022. arXiv:2207.07048v1
- [24] A. Y. Hannun, P. Rajpurkar, M. Haghpanahi, et al., “Cardiologist-level arrhythmia detection and classification in ambulatory electrocardiograms using a deep neural network.” *Nat Med*, vol. 25, pp. 65–69, 2019. doi:10.1038/s41591-018-0268-3
- [25] E. Adib, F. Afghah, and J. J. Prevost, “Synthetic ECG Signal Generation Using Generative Neural Networks,” *eprint*, 2021. arXiv:2112.03268v1
- [26] I. J. Goodfellow, J. Pouget Abadie, M. Mirza, et al., “Generative Adversarial Networks,” *eprint*, 2014. arXiv:1406.2661v1
- [27] R. Doste, M. Lozano, G. Jimenez Perez, et al., “Training machine learning models with synthetic data improves the prediction of ventricular origin in outflow tract ventricular arrhythmias,” *Frontiers in Physiology*, vol. 13, 2022. doi:10.3389/fphys.2022.909372
- [28] A. Prakosa, M. K. Southworth, J. N. Avari Silva, J. R. Silva, and N. A. Trayanova, “Impact of augmented-reality improvement in ablation catheter navigation as assessed by virtual-heart simulations of ventricular tachycardia ablation,” *Computers in Biology and Medicine*, vol. 133, p. 104366, 2021. doi:10.1016/j.combiomed.2021.104366

- [29] H. Martinez Navarro, X. Zhou, A. Bueno Orovio, and B. Rodriguez, "Electrophysiological and anatomical factors determine arrhythmic risk in acute myocardial ischaemia and its modulation by sodium current availability," *Interface Focus*, vol. 11, p. 20190124, 2020. doi:10.1098/rsfs.2019.0124
- [30] P. M. Boyle, T. Zghaib, S. Zahid, et al., "Computationally guided personalized targeted ablation of persistent atrial fibrillation," *Nat Biomed Eng*, vol. 3, pp. 870–879, 2019. doi:10.1038/s41551-019-0437-9
- [31] L. Azzolin, M. Eichenlaub, C. Nagel, et al., "Personalized ablation vs. conventional ablation strategies to terminate atrial fibrillation and prevent recurrence," *EP Europace*, pp. 1–12, 2022. doi:10.1093/europace/euac116
- [32] K. N. Aronis, R. L. Ali, J. A. Liang, S. Zhou, and N. A. Trayanova, "Understanding AF Mechanisms Through Computational Modelling and Simulations," *AER*, pp. 210–219, 2019. doi:10.15420/aer.2019.28.2
- [33] J. Corral Acero, F. Margara, M. Marciniak, et al., "The 'Digital Twin' to enable the vision of precision cardiology," *Eur Heart J*, vol. 41, pp. 4556–4564, 2020. doi:10.1093/eurheartj/ehaa159
- [34] K. Gillette, M. A. Gsell, A. J. Prassl, et al., "A Framework for the Generation of Digital Twins of Cardiac Electrophysiology from Clinical 12-lead ECGs," *Medical Image Analysis*, p. 102080, 2021. doi:10.1016/j.media.2021.102080
- [35] C. L. Lei, S. Ghosh, D. G. Whittaker, et al., "Considering discrepancy when calibrating a mechanistic electrophysiology model," *Philosophical Transactions of the Royal Society A: Mathematical, Physical and Engineering Sciences*, vol. 378, p. 20190349, 2020. doi:10.1098/rsta.2019.0349
- [36] S. A. Niederer, Y. Aboelkassem, C. D. Cantwell, et al., "Creation and application of virtual patient cohorts of heart models," *Philosophical Transactions of the Royal Society A: Mathematical, Physical and Engineering Sciences*, vol. 378, p. 20190558, 2020. doi:10.1098/rsta.2019.0558
- [37] Z. Ebrahimi, M. Loni, M. Daneshtalab, and A. Gharehbaghi, "A review on deep learning methods for ECG arrhythmia classification," *Expert Systems with Applications: X*, vol. 7, p. 100033, 2020. doi:10.1016/j.eswax.2020.100033
- [38] A. Mincholé, J. Camps, A. Lyon, and B. Rodríguez, "Machine learning in the electrocardiogram," *Journal of Electrocardiology*, vol. 57, pp. S61–S64, 2019. doi:10.1016/j.jelectrocard.2019.08.008
- [39] S. Somani, A. J. Russak, F. Richter, et al., "Deep learning and the electrocardiogram: review of the current state-of-the-art," *EP Europace*, vol. 23, pp. 1179–1191, 2021. doi:10.1093/europace/euaa377
- [40] M. Varshneya, X. Mei, and E. A. Sobie, "Prediction of arrhythmia susceptibility through mathematical modeling and machine learning," *Proceedings of the National Academy of Sciences*, vol. 118, 2021. doi:10.1073/pnas.2104019118
- [41] M. V. Perez, K. W. Mahaffey, H. Hedlin, et al., "Large-Scale Assessment of a Smartwatch to Identify Atrial Fibrillation." *N Engl J Med*, vol. 381, pp. 1909–1917, 2019. doi:10.1056/NEJMoa1901183
- [42] Z. I. Attia, P. A. Noseworthy, F. Lopez Jimenez, et al., "An artificial intelligence-enabled ECG algorithm for the identification of patients with atrial fibrillation during sinus rhythm: a retrospective analysis of outcome prediction," *The Lancet*, vol. 394, pp. 861–867, 2019. doi:10.1016/S0140-6736(19)31721-0

- [43] S. Khurshid, S. Friedman, C. Reeder, et al., “ECG-Based Deep Learning and Clinical Risk Factors to Predict Atrial Fibrillation,” *Circulation*, vol. 145, pp. 122–133, 2022. doi:10.1161/circulationaha.121.057480
- [44] J. M. Ashburner, X. Wang, X. Li, et al., “Re-CHARGE-AF: Recalibration of the CHARGE-AF Model for Atrial Fibrillation Risk Prediction in Patients With Acute Stroke,” *Journal of the American Heart Association*, vol. 10, 2021. doi:10.1161/jaha.121.022363
- [45] J. C. L. Himmelreich, W. A. M. Lucassen, R. E. Harskamp, C. Aussems, H. C. P. M. van Weert, and M. M. J. Nielen, “CHARGE-AF in a national routine primary care electronic health records database in the Netherlands: validation for 5-year risk of atrial fibrillation and implications for patient selection in atrial fibrillation screening,” *Open Heart*, vol. 8, p. e001459, 2021. doi:10.1136/openhrt-2020-001459
- [46] M. Eichenlaub, B. Mueller Edenborn, H. Lehrmann, et al., “Non-invasive body surface electrocardiographic imaging for diagnosis of atrial cardiomyopathy,” *EP Europace*, vol. 23, pp. 2010–2019, 2021. doi:10.1093/europace/euab140
- [47] G. Luongo, L. Azzolin, S. Schuler, et al., “Machine learning enables noninvasive prediction of atrial fibrillation driver location and acute pulmonary vein ablation success using the 12-lead ECG,” *Cardiovascular Digital Health Journal*, vol. 2, pp. 126–136, 2021. doi:10.1016/j.cvdhj.2021.03.002
- [48] L. Azzolin, S. Schuler, O. Dössel, and A. Loewe, “A Reproducible Protocol to Assess Arrhythmia Vulnerability : Pacing at the End of the Effective Refractory Period.” *Front Physiol*, vol. 12, p. 656411, 2021. doi:10.3389/fphys.2021.656411
- [49] E. Passini, F. Margara, and B. Rodriguez, “Computational investigation of drug-induced effects on human cardiac electro-mechanics,” *EP Europace*, vol. 23, 2021. doi:10.1093/europace/euab116.513
- [50] A. Loewe, Y. Lutz, M. Wilhelms, et al., “In-silico assessment of the dynamic effects of amiodarone and dronedarone on human atrial patho-electrophysiology.” *Europace*, vol. 16, pp. iv30–iv38, 2014. doi:10.1093/europace/euu230
- [51] C. H. Roney, M. L. Beach, A. M. Mehta, et al., “In silico Comparison of Left Atrial Ablation Techniques That Target the Anatomical, Structural, and Electrical Substrates of Atrial Fibrillation,” *Frontiers in Physiology*, vol. 11, 2020. doi:10.3389/fphys.2020.572874
- [52] L. Azzolin, M. Eichenlaub, C. Nagel, et al., “AugmentA: Patient-specific Augmented Atrial model Generation Tool,” *medRxiv*, 2022. doi:10.1101/2022.02.13.22270835
- [53] S. Rocher, A. López, A. Ferrer, L. Martínez, D. Sánchez, and J. Saiz, “A Highly-Detailed 3D Model of the Human Atria,” in *IFMBE Proceedings*. Singapore: Springer Singapore, 2019, pp. 649–653. doi:10.1007/978-981-10-9035-6\_121
- [54] O. J. Britton, A. Bueno Orovio, K. Van Ammel, et al., “Experimentally calibrated population of models predicts and explains intersubject variability in cardiac cellular electrophysiology,” *Proc Natl Acad Sci U S A*, vol. 110, pp. E2098–105, 2013. doi:10.1073/pnas.1304382110
- [55] E. Passini, O. J. Britton, H. R. Lu, et al., “Human Drug Trials Demonstrate Higher Accuracy than Animal Models in Predicting Clinical Pro-Arrhythmic Cardiotoxicity.” *Front Physiol*, vol. 8, p. 668, 2017. doi:10.3389/fphys.2017.00668
- [56] A. Liberos, A. Bueno Orovio, M. Rodrigo, et al., “Balance between sodium and calcium currents underlying chronic atrial fibrillation termination: An in silico intersubject variability study.” *Heart Rhythm*, vol. 13, pp. 2358–2365, 2016. doi:10.1016/j.hrthm.2016.08.028

- [57] T. Brennan, M. Fink, and B. Rodriguez, "Multiscale modelling of drug-induced effects on cardiac electrophysiological activity," *Eur J Pharm Sci*, vol. 36, pp. 62–77, 2009. doi:10.1016/j.ejps.2008.09.013
- [58] N. Zenzemi, M. O. Bernabeu, J. Saiz, et al., "Computational assessment of drug-induced effects on the electrocardiogram: from ion channel to body surface potentials," *Br J Pharmacol*, vol. 168, pp. 718–733, 2013. doi:10.1111/j.1476-5381.2012.02200.x
- [59] E. Passini, A. Mincholé, R. Coppini, et al., "Mechanisms of pro-arrhythmic abnormalities in ventricular repolarisation and anti-arrhythmic therapies in human hypertrophic cardiomyopathy," *J Mol Cell Cardiol*, vol. 96, pp. 72–81, 2016. doi:10.1016/j.yjmcc.2015.09.003
- [60] A. Loewe, Y. Lutz, M. Wilhelms, E. P. Scholz, O. Dössel, and G. Seemann, "Optimization of pharmacotherapy for familial atrial fibrillation in a numerical model of human atrial electrophysiology," in *Computing in Cardiology*, vol. 41, 2014, pp. 745–748.
- [61] M. Viceconti, L. Emili, P. Afshari, et al., "Possible Contexts of Use for In Silico Trials Methodologies: A Consensus-Based Review," *IEEE Journal of Biomedical and Health Informatics*, vol. 25, pp. 3977–3982, 2021. doi:10.1109/JBHI.2021.3090469
- [62] C. Trovato, M. Mohr, F. Schmidt, E. Passini, and B. Rodriguez, "Cross clinical-experimental-computational qualification of in silico drug trials on human cardiac Purkinje cells for proarrhythmia risk prediction," *British Journal of Pharmacology*, vol. 81, pp. 41–47, 2022. doi:10.22541/au.164504834.41877071/v1
- [63] M. Viceconti, F. Pappalardo, B. Rodriguez, M. Horner, J. Bischoff, and F. Musuamba Tshinanu, "In silico trials: Verification, validation and uncertainty quantification of predictive models used in the regulatory evaluation of biomedical products," *Methods*, vol. 185, pp. 120–127, 2021. doi:10.1016/j.ymeth.2020.01.011
- [64] R. H. Davies, "Learning shape: optimal models for analysing natural variability," University of Manchester, Tech. Rep., 2002.
- [65] S. Jia, H. Nivet, J. Harrison, et al., "Left Atrial Shape Is Independent Predictor of Arrhythmia Recurrence after Catheter Ablation for Atrial Fibrillation: A Shape Statistics Study," *Heart Rhythm O2*, 2021. doi:10.1016/j.hroo.2021.10.013
- [66] E. T. Bieging, A. Morris, B. D. Wilson, C. J. McGann, N. F. Marrouche, and J. Cates, "Left atrial shape predicts recurrence after atrial fibrillation catheter ablation." *J Cardiovasc Electrophysiol*, vol. 29, pp. 966–972, 2018. doi:10.1111/jce.13641
- [67] A. J. Weinhaus, "Anatomy of the Human Heart," Cham, pp. 61—88, 2015. doi:10.1007/978-3-319-19464-6\_5
- [68] A. A. Young and A. F. Frangi, "Computational cardiac atlases: from patient to population and back," *Exp Physiol*, vol. 94, pp. 578–596, 2009. doi:10.1113/expphysiol.2008.044081
- [69] R. S. Stephenson, A. Atkinson, P. Kottas, et al., "High resolution 3-Dimensional imaging of the human cardiac conduction system from microanatomy to mathematical modeling." *Sci Rep*, vol. 7, p. 7188, 2017. doi:10.1038/s41598-017-07694-8
- [70] O. Monfredi, H. Dobrzynski, T. Mondal, M. R. Boyett, and G. M. Morris, "The anatomy and physiology of the sinoatrial node—a contemporary review," *Pacing Clin Electrophysiol*, vol. 33, pp. 1392–1406, 2010. doi:10.1111/j.1540-8159.2010.02838.x
- [71] S. Y. Ho and A. E. Becker, "Anatomy of electrophysiology," in *Hurst's The Heart*. Fuster, V.; Hurst, J. W.; O'Rourke, R. A.; Walsh, R. A.; King, S. B.; Poole-Wilson, P. A., 2008.

- [72] B. H. Smaill, I. J. LeGrice, D. A. Hooks, A. J. Pullan, B. J. Caldwell, and P. J. Hunter, “Cardiac structure and electrical activation: models and measurement,” *Clin Exp Pharmacol Physiol*, vol. 31, pp. 913–919, 2004.
- [73] R. E. Klabunde, *Cardiovascular Physiology Concepts*. Lippincott Williams & Wilkins, 2011. <https://openlibrary.org/books/OL34755472M>
- [74] M. Velleca, G. Costa, L. Goldstein, M. Bishara, and L. M. Boo, “A review of the Burden of Atrial Fibrillation: Understanding the impact of the New Millennium Epidemic across Europe,” *EMJ*, 2019.
- [75] G. Hindricks, T. Potpara, N. Dagres, et al., “2020 ESC Guidelines for the diagnosis and management of atrial fibrillation developed in collaboration with the European Association for Cardio-Thoracic Surgery (EACTS),” *Eur Heart J*, vol. 42, pp. 373–498, 2021. doi:10.1093/eurheartj/ehaa612
- [76] J. Dretzke, N. Chuchu, R. Agarwal, et al., “Predicting recurrent atrial fibrillation after catheter ablation: a systematic review of prognostic models,” *EP Europace*, vol. 22, pp. 748–760, 2020. doi:10.1093/europace/euaa041
- [77] E. Arbelo and N. Dagres, “The 2020 ESC atrial fibrillation guidelines for atrial fibrillation catheter ablation, CABANA, and EAST,” *EP Europace*, vol. 24, pp. ii3–ii7, 2022. doi:10.1093/europace/euab332
- [78] A. Verma, C.-y. Jiang, T. R. Betts, et al., “Approaches to catheter ablation for persistent atrial fibrillation.” *N Engl J Med*, vol. 372, pp. 1812–22, 2015. doi:10.1056/NEJMoa1408288
- [79] J. Seitz, C. Bars, G. Théodore, et al., “AF Ablation Guided by Spatiotemporal Electrogram Dispersion Without Pulmonary Vein Isolation: A Wholly Patient-Tailored Approach.” *J Am Coll Cardiol*, vol. 69, pp. 303–321, 2017. doi:10.1016/j.jacc.2016.10.065
- [80] A. Jadidi, M. Nothstein, J. Chen, et al., “Specific Electrogram Characteristics Identify the Extra-Pulmonary Vein Arrhythmogenic Sources of Persistent Atrial Fibrillation – Characterization of the Arrhythmogenic Electrogram Patterns During Atrial Fibrillation and Sinus Rhythm,” *Sci Rep*, vol. 10, p. 9147, 2020. doi:10.1038/s41598-020-65564-2
- [81] A. Xintarakou, S. Tzeis, S. Psarras, D. Asvestas, and P. Vardas, “Atrial fibrosis as a dominant factor for the development of atrial fibrillation: facts and gaps.” *Europace*, vol. 22, pp. 342–351, 2020. doi:10.1093/europace/euaa009
- [82] C. H. Roney, J. D. Bayer, S. Zahid, et al., “Modelling methodology of atrial fibrosis affects rotor dynamics and electrograms.” *Europace*, vol. 18, pp. iv146–iv155, 2016. doi:10.1093/europace/euw365
- [83] D. Nairn, C. Nagel, B. Müller Edenborn, et al., “Optimal Regional Voltage Thresholds for Identifying Ablation Targets in Patients with Atrial Fibrillation,” in *Computing in Cardiology Conference (CinC)*, vol. 48, 2021. doi:10.23919/CinC53138.2021.9662839
- [84] D. Nairn, M. Eichenlaub, H. Lehrmann, et al., “Spatial Correlation of Left Atrial Low Voltage Substrate in Sinus Rhythm versus Atrial Fibrillation: Identifying the Pathological Substrate Irrespective of the Rhythm,” *medRxiv*, 2022. doi:10.1101/2022.02.18.22271172
- [85] N. F. Marrouche, T. Greene, J. M. Dean, et al., “Efficacy of LGE-MRI-guided fibrosis ablation versus conventional catheter ablation of atrial fibrillation: The DECAAF II trial: Study design,” *J Cardiovasc Electrophysiol*, vol. 32, pp. 916–924, 2021. doi:10.1111/jce.14957
- [86] Y. Seko, T. Kato, T. Haruna, et al., “Association between atrial fibrillation, atrial enlargement, and left ventricular geometric remodeling,” *Scientific Reports*, vol. 8, 2018. doi:10.1038/s41598-018-24875-1

- [87] J. T. Miller, R. A. O'Rourke, and M. H. Crawford, "Left atrial enlargement: An early sign of hypertensive heart disease," *American Heart Journal*, vol. 116, pp. 1048–1051, 1988. doi:10.1016/0002-8703(88)90158-5
- [88] R. M. Lang, L. P. Badano, V. Mor Avi, et al., "Recommendations for cardiac chamber quantification by echocardiography in adults: an update from the American Society of Echocardiography and the European Association of Cardiovascular Imaging." *Eur Heart J Cardiovasc Imaging*, vol. 16, pp. 233–70, 2015. doi:10.1093/ehjci/jev014
- [89] J. T. Koivumäki, J. Hoffman, M. M. Maleckar, G. T. Einevoll, and J. Sundnes, "Computational cardiac physiology for new modelers: origins, foundations, and future," *Acta Physiologica*, 2022. doi:10.1111/apha.13865
- [90] S. A. Niederer, J. Lumens, and N. A. Trayanova, "Computational models in cardiology," *Nat Rev Cardiol*, vol. 16, pp. 100–111, 2018. doi:10.1038/s41569-018-0104-y
- [91] M. Courtemanche, R. J. Ramirez, and S. Nattel, "Ionic mechanisms underlying human atrial action potential properties: insights from a mathematical model," *American Journal of Physiology-Heart and Circulatory Physiology*, vol. 275, pp. H301–H321, 1998. doi:10.1152/ajpheart.1998.275.1.H301
- [92] P. Pathmanathan, M. O. Bernabeu, R. Bordas, et al., "A numerical guide to the solution of the bidomain equations of cardiac electrophysiology," *Progress in Biophysics and Molecular Biology*, vol. 102, pp. 136–155, 2010. doi:10.1016/j.pbiomolbio.2010.05.006
- [93] L. Tung, "A bi-domain model for describing ischemic myocardial DC potentials," PhD thesis, Massachusetts Institute of Technology, 1789.
- [94] P. C. C. Franzone, L. F. Pavarino, and S. Scacchi, *Mathematical Cardiac Electrophysiology*. Springer Cham, 2014. <http://openlibrary.org/book/OL28144166M>
- [95] J. Keener and J. Sneyd, "Mathematical Physiology," 2009. doi:10.1007/978-0-387-75847-3
- [96] K. H. Jæger and A. Tveito, "Deriving the Bidomain Model of Cardiac Electrophysiology From a Cell-Based Model; Properties and Comparisons," *Frontiers in Physiology*, vol. 12, 2022. doi:10.3389/fphys.2021.811029
- [97] E. J. Vigmond, R. Weber dos Santos, A. J. Prassl, M. Deo, and G. Plank, "Solvers for the cardiac bidomain equations," *Prog Biophys Mol Biol*, vol. 96, pp. 3–18, 2008. doi:10.1016/j.pbiomolbio.2007.07.012
- [98] G. Plank, A. Loewe, A. Neic, et al., "The openCARP simulation environment for cardiac electrophysiology." *Comput Methods Programs Biomed*, vol. 208, p. 106223, 2021. doi:10.1016/j.cmpb.2021.106223
- [99] M. J. Bishop and G. Plank, "Bidomain ECG simulations using an augmented monodomain model for the cardiac source." *IEEE Trans Biomed Eng*, vol. 58, 2011. doi:10.1109/TBME.2011.2148718
- [100] C. Costa, E. Hoetzel, B. Rocha, A. Prassl, and G. Plank, "Automatic Parameterization Strategy for Cardiac Electrophysiology Simulations," *CinC 2013*, 2013.
- [101] J. A. Sethian, "A fast marching level set method for monotonically advancing fronts," *Proc Natl Acad Sci U S A*, vol. 93, pp. 1591–1595, 1996.
- [102] A. Capozzoli, C. Curcio, and S. Savarese, "A Comparison of Fast Marching, Fast Sweeping and Fast Iterative Methods for the Solution of the Eikonal Equation," *Telfor Journal*, vol. 6, pp. 142–147, 2014.

- [103] J. Sánchez and A. Loewe, “A Review of Healthy and Fibrotic Myocardium Microstructure Modeling and Corresponding Intracardiac Electrograms,” *Frontiers in Physiology*, vol. 13, 2022. doi:10.3389/fphys.2022.908069
- [104] A. Neic, F. O. Campos, A. J. Prassl, et al., “Efficient computation of electrograms and ECGs in human whole heart simulations using a reaction-eikonal model,” *J Comput Phys*, vol. 346, pp. 191–211, 2017. doi:10.1016/j.jcp.2017.06.020
- [105] L. R. Bear, L. K. Cheng, I. J. LeGrice, et al., “Forward problem of electrocardiography: is it solved?” *Circ Arrhythm Electrophysiol*, vol. 8, pp. 677–84, 2015. doi:10.1161/CIRCEP.114.001573
- [106] M. Potse, B. Dube, and A. Vinet, “Cardiac anisotropy in boundary-element models for the electrocardiogram,” *Med Biol Eng Comput*, vol. 47, pp. 719–729, 2009. doi:10.1007/s11517-009-0472-x
- [107] M. Stenroos, V. Mäntynen, and J. Nenonen, “A Matlab library for solving quasi-static volume conduction problems using the boundary element method,” *Computer methods and programs in biomedicine*, vol. 88, pp. 256–263, 2007.
- [108] D. B. Geselowitz and T. W. Miller, “A bidomain model for anisotropic cardiac muscle,” *Annals of Biomedical Engineering*, vol. 11, pp. 191–206, 1983.
- [109] T. F. Cootes, C. J. Taylor, D. H. Cooper, and J. Graham, “Active shape models - Their training and application,” *Computer Vision and Image Understanding*, vol. 61, pp. 38–59, 1995.
- [110] Y. Chen and G. Medioni, “Object modelling by registration of multiple range images,” *Image and Vision Computing*, vol. 10, pp. 145–155, 1992. doi:10.1016/0262-8856(92)90066-C
- [111] M. Lüthi, T. Gerig, C. Jud, and T. Vetter, “Gaussian Process Morphable Models,” *IEEE Trans Pattern Anal Mach Intell*, vol. 40, pp. 1860–1873, 2018. doi:10.1109/TPAMI.2017.2739743
- [112] R. Bro and A. K. Smilde, “Principal component analysis,” *Anal. Methods*, vol. 6, pp. 2812–2831, 2014. doi:10.1039/c3ay41907j
- [113] C. M. Bishop, *Pattern Recognition and Machine Learning*. Berlin, Heidelberg: Springer-Verlag, 2006.
- [114] O.-J. Skrede, S. De Raedt, A. Kleppe, et al., “Deep learning for prediction of colorectal cancer outcome: a discovery and validation study,” *The Lancet*, vol. 395, pp. 350–360, 2020. doi:10.1016/s0140-6736(19)32998-8
- [115] G. Ian, B. Yoshua, and C. Aaron, *Deep Learning*. MIT Press, 2016.
- [116] S. S. Haykin, *Neural networks and learning machines*, vol. 10. Upper Saddle River, NJ: Pearson, 2009.
- [117] K. Hornik, M. Stinchcombe, and H. White, “Multilayer feedforward networks are universal approximators,” *Neural Networks*, vol. 2, pp. 359–366, 1989. doi:10.1016/0893-6080(89)90020-8
- [118] C. Nwankpa, W. Ijomah, A. Gachagan, and S. Marshall, “Activation Functions: Comparison of trends in Practice and Research for Deep Learning,” *eprint*, 2018. arXiv:1811.03378v1
- [119] N. S. Keskar, D. Mudigere, J. Nocedal, M. Smelyanskiy, and P. T. P. Tang, “On Large-Batch Training for Deep Learning: Generalization Gap and Sharp Minima,” *eprint*, 2016. arXiv:1609.04836v2
- [120] A. Maier, C. Syben, T. Lasser, and C. Riess, “A gentle introduction to deep learning in medical image processing,” *Zeitschrift für Medizinische Physik*, vol. 29, pp. 86–101, 2019. doi:10.1016/j.zemedi.2018.12.003

- [121] C. Nagel, M. Schaufelberger, O. Dössel, and A. Loewe, “A Bi-atrial Statistical Shape Model as a Basis to Classify Left Atrial Enlargement from Simulated and Clinical 12-Lead ECGs,” *Statistical Atlases and Computational Models of the Heart. Multi-Disease, Multi-View, and Multi-Center Right Ventricular Segmentation in Cardiac MRI Challenge*, vol. 13131, pp. 38–47, 2022. doi:10.1007/978-3-030-93722-5\_5
- [122] C. Nagel, G. Luongo, L. Azzolin, S. Schuler, O. Dössel, and A. Loewe, “Non-Invasive and Quantitative Estimation of Left Atrial Fibrosis Based on P Waves of the 12-Lead ECG-A Large-Scale Computational Study Covering Anatomical Variability.” *J Clin Med*, vol. 10, 2021. doi:10.3390/jcm10081797
- [123] G. Luongo, G. Vacanti, V. Nitzke, et al., “Hybrid machine learning to localize atrial flutter substrates using the surface 12-lead electrocardiogram,” *EP Europace*, vol. 24, pp. 1186–1194, 2022. doi:10.1093/europace/euab322
- [124] J. Camps, B. Lawson, C. Drovandi, et al., “Inference of ventricular activation properties from non-invasive electrocardiography,” *Medical Image Analysis*, vol. 73, p. 102143, 2021. doi:10.1016/j.media.2021.102143
- [125] M. Wallman, N. P. Smith, and B. Rodriguez, “A comparative study of graph-based, eikonal, and monodomain simulations for the estimation of cardiac activation times,” *IEEE Trans Biomed Eng*, vol. 59, pp. 1739–1748, 2012. doi:10.1109/TBME.2012.2193398
- [126] J. Sundnes, B. F. Nielsen, K. A. Mardal, X. Cai, G. T. Lines, and A. Tveito, “On the computational complexity of the bidomain and the monodomain models of electrophysiology,” *Ann Biomed Eng*, vol. 34, pp. 1088–1097, 2006. doi:10.1007/s10439-006-9082-z
- [127] M. Potse, B. Dubé, A. Vinet, and R. Cardinal, “A comparison of monodomain and bidomain propagation models for the human heart.” *Conf Proc IEEE Eng Med Biol Soc*, vol. 2006, pp. 3895–8, 2006. doi:10.1109/IEMBS.2006.259484
- [128] E. Vigmond, A. Pashaei, S. Amraoui, H. Cochet, and M. Hassagerre, “Percolation as a mechanism to explain atrial fractionated electrograms and reentry in a fibrosis model based on imaging data,” *Heart Rhythm*, vol. 13, pp. 1536–1543, 2016. doi:10.1016/j.hrthm.2016.03.019
- [129] L. Azzolin, C. Nagel, D. Nairn, et al., “Automated Framework for the Augmentation of Missing Anatomical Structures and Generation of Personalized Atrial Models from Clinical Data,” in *Computing in Cardiology Conference (CinC)*, vol. 48, 2021. doi:10.23919/CinC53138.2021.9662846
- [130] M. W. Krueger, G. Seemann, K. Rhode, et al., “Personalization of atrial anatomy and electrophysiology as a basis for clinical modeling of radio-frequency ablation of atrial fibrillation,” *IEEE Trans Med Imaging*, vol. 32, pp. 73–84, 2013. doi:10.1109/TMI.2012.2201948
- [131] W. Jakob, M. Tarini, D. Panozzo, and O. Sorkine Hornung, “Instant field-aligned meshes,” *ACM Transactions on Graphics*, vol. 34, pp. 1–15, 2015. doi:10.1145/2816795.2818078
- [132] T. Zheng, L. Azzolin, J. Sánchez, O. Dössel, and A. Loewe, “An automate pipeline for generating fiber orientation and region annotation in patient specific atrial models,” *Current Directions in Biomedical Engineering*, vol. 7, pp. 136–139, 2021. doi:10.1515/cdbme-2021-2035
- [133] M. D. Eggen, C. M. Swingen, and P. A. Iaizzo, “Analysis of fiber orientation in normal and failing human hearts using diffusion tensor MRI,” *2009 IEEE International Symposium on Biomedical Imaging: From Nano to Macro*, pp. 642–645, 2009. doi:10.1109/ISBI.2009.5193129
- [134] N. A. Trayanova, “Whole-Heart Modeling,” *Circulation Research*, vol. 108, pp. 113–128, 2011. doi:10.1161/circresaha.110.223610

- [135] R. Piersanti, P. C. Africa, M. Fedele, et al., “Modeling cardiac muscle fibers in ventricular and atrial electrophysiology simulations,” *Computer Methods in Applied Mechanics and Engineering*, vol. 373, p. 113468, 2021. doi:10.1016/j.cma.2020.113468
- [136] P. C. Africa, R. Piersanti, M. Fedele, L. Dede’, and A. Quarteroni, “life<sup>x</sup> - heart module: a high-performance simulator for the cardiac function. Package 1: Fiber generation,” *eprint*, 2022. arXiv:2201.03303v3
- [137] A. Neic, M. A. Gsell, E. Karabelas, A. J. Prassl, and G. Plank, “Automating image-based mesh generation and manipulation tasks in cardiac modeling workflows using Meshtool,” *SoftwareX*, vol. 11, p. 100454, 2020. doi:10.1016/j.softx.2020.100454
- [138] A. Reinke, D. Potyagaylo, W. H. W. Schulze, and O. Dössel, “Geometrical model and corresponding conductivities for solving the inverse problem of ECG,” in *Biomedizinische Technik / Biomedical Engineering*, vol. 59, no. s1, 2014, pp. 937–940.
- [139] D. U. J. Keller, F. M. Weber, G. Seemann, and O. Dössel, “Ranking the Influence of Tissue Conductivities on Forward-Calculated ECGs,” *IEEE TBME*, vol. 57, pp. 1568–1576, 2010. doi:10.1109/TBME.2010.2046485
- [140] A. Loewe, M. W. Krueger, P. G. Platonov, F. Holmqvist, O. Dössel, and G. Seemann, “Left and Right Atrial Contribution to the P-wave in Realistic Computational Models,” *LNCS*, vol. 9126, pp. 439–447, 2015. doi:10.1007/978-3-319-20309-6\_50
- [141] M. W. Krüger, “Personalized Multi-Scale Modeling of the Atria : Heterogeneities, Fiber Architecture, Hemodialysis and Ablation Therapy,” PhD thesis, KIT Scientific Publishing, 2013.
- [142] L. Clerc, “Directional differences of impulse spread in trabecular muscle from mammalian heart.” *The Journal of Physiology*, vol. 255, pp. 335–346, 1976. doi:10.1113/jphysiol.1976.sp011283
- [143] D. E. Roberts and A. M. Scher, “Effect of tissue anisotropy on extracellular potential fields in canine myocardium in situ,” *Circ. Res.*, vol. 50, pp. 342–351, 1982.
- [144] M. W. Krueger, A. Dorn, D. U. J. Keller, et al., “In-silico modeling of atrial repolarization in normal and atrial fibrillation remodeled state,” *Med Biol Eng Comput*, vol. 51, pp. 1105–1119, 2013. doi:10.1007/s11517-013-1090-1
- [145] K. Higuchi, J. Cates, G. Gardner, et al., “The Spatial Distribution of Late Gadolinium Enhancement of Left Atrial Magnetic Resonance Imaging in Patients With Atrial Fibrillation,” *JACC: Clinical Electrophysiology*, vol. 4, pp. 49–58, 2018. doi:10.1016/j.jacep.2017.07.016
- [146] S. Alonso and M. Bar, “Reentry near the percolation threshold in a heterogeneous discrete model for cardiac tissue,” *Phys Rev Lett*, vol. 110, p. 158101, 2013. doi:10.1103/PhysRevLett.110.158101
- [147] R. Ramos Mondragón, C. A. Galindo, and G. Avila, “Role of TGF-beta on cardiac structural and electrical remodeling,” *Vasc Health Risk Manag*, vol. 4, pp. 1289–300, 2008. doi:10.2147/vhrm.s3985
- [148] G. Avila, I. M. Medina, E. Jiménez, G. Elizondo, and C. I. Aguilar, “Transforming growth factor-beta1 decreases cardiac muscle L-type Ca<sup>2+</sup> current and charge movement by acting on the Ca<sub>v</sub>1.2 mRNA,” *American Journal of Physiology-Heart and Circulatory Physiology*, vol. 292, pp. H622–H631, 2007. doi:10.1152/ajpheart.00781.2006
- [149] A. Loewe, M. W. Krueger, F. Holmqvist, O. Dössel, G. Seemann, and P. G. Platonov, “Influence of the earliest right atrial activation site and its proximity to interatrial connections on P-wave morphology,” *Europace*, vol. 18, pp. iv35–iv43, 2016. doi:10.1093/europace/euw349

- [150] S. Y. Ho and D. Sánchez Quintana, “Anatomy and pathology of the sinus node,” *Journal of Interventional Cardiac Electrophysiology*, vol. 46, pp. 3–8, 2015. doi:10.1007/s10840-015-0049-6
- [151] E. J. Vigmond, M. Hughes, G. Plank, and L. J. Leon, “Computational tools for modeling electrical activity in cardiac tissue.” *J Electrocardiol*, vol. 36 Suppl, pp. 69–74, 2003. doi:10.1016/j.jelectrocard.2003.09.017
- [152] S. Schuler, J. D. Tate, T. F. Oostendorp, R. S. MacLeod, and O. Dössel, “Spatial Downsampling of Surface Sources in the Forward Problem of Electrocardiography,” in *Functional Imaging and Modeling of the Heart*, Lecture Notes in Computer Science, Y. Coudière, V. Ozenne, E. Vigmond, and N. Zemzemi, Eds., vol. 11504. Springer International Publishing, 2019, pp. 29–36. doi:10.1007/978-3-030-21949-9\_4
- [153] R. Sebastian, S. Ordas, G. Plank, B. Rodriguez, E. J. Vigmond, and A. F. Frangi, “Assessing influence of conductivity in heart modelling with the aim of studying cardiovascular diseases,” *Medical Imaging 2008: Physiology*, vol. 6916, p. 691627, 2008. doi:10.1117/12.770258
- [154] T. Cojean, F. Goebel, and M. Houillon, “Porting the OpenCARP Cardiac Electrophysiology Simulation Framework to GPU Architectures,” Fifth ISC Workshop on HPC Applications in Precision Medicine, 2022.
- [155] C. M. Augustin, A. Neic, M. Liebmann, et al., “Anatomically accurate high resolution modeling of human whole heart electromechanics: A strongly scalable algebraic multigrid solver method for nonlinear deformation.” *J Comput Phys*, vol. 305, pp. 622–646, 2016. doi:10.1016/j.jcp.2015.10.045
- [156] L. Cardone Noott, B. Rodriguez, and A. Bueno Orovio, “Strategies of data layout and cache writing for input-output optimization in high performance scientific computing: Applications to the forward electrocardiographic problem.” *PLoS One*, vol. 13, p. e0202410, 2018. doi:10.1371/journal.pone.0202410
- [157] L. A. Woodworth, B. Cansız, and M. Kaliske, “A Numerical Study on the Effects of Spatial and Temporal Discretization in Cardiac Electrophysiology.” *Int J Numer Method Biomed Eng*, p. e3443, 2021. doi:10.1002/cnm.3443
- [158] Z. Fu, R. M. Kirby, and R. T. Whitaker, “A Fast Iterative Method for Solving the Eikonal Equation on Tetrahedral Domains,” *SIAM J Sci Comput*, vol. 35, pp. c473–c494, 2013. doi:10.1137/120881956
- [159] A. Capozzoli, C. Curcio, A. Liseno, and S. Savarese, “A comparison of Fast Marching, Fast Sweeping and Fast Iterative Methods for the solution of the eikonal equation,” in *2013 21st Telecommunications Forum Telfor (TELFOR)*. IEEE, 2013. doi:10.1109/telfor.2013.6716321
- [160] S. Mukherjee and M. Morjaria, “On the efficiency and accuracy of the boundary element method and the finite element method,” *International Journal for Numerical Methods in Engineering*, vol. 20, pp. 515–522, 1984. doi:10.1002/nme.1620200309
- [161] A. Pashaei, D. Romero, R. Sebastian, O. Camara, and A. F. Frangi, “Comparison of Phenomenological and Biophysical Cardiac Models Coupled with Heterogenous Structures for Prediction of Electrical Activation Sequence,” *CinC 2010*, 2010.
- [162] A. Pashaei, D. Romero, R. Sebastian, O. Camara, and A. F. Frangi, “Fast Multiscale Modeling of Cardiac Electrophysiology Including Purkinje System,” *IEEE Transactions on Biomedical Engineering*, vol. 58, pp. 2956–2960, 2011. doi:10.1109/TBME.2011.2162841
- [163] N. Gassa, N. Zemzemi, C. Corrado, and Y. Coudière, “Spiral Waves Generation Using an Eikonal-Reaction Cardiac Electrophysiology Model,” *Functional Imaging and Modeling of the Heart*, vol. 12738, pp. 523–530, 2021. doi:10.1007/978-3-030-78710-3\_50

- [164] *Comparison of source models and forward calculation methods for atrial electrophysiology regarding activation times and electrocardiograms*, 2021.
- [165] R. Moss, E. M. Wülfers, S. Schuler, A. Loewe, and G. Seemann, “A Fully-Coupled Electro-Mechanical Whole-Heart Computational Model: Influence of Cardiac Contraction on the ECG,” *Front. Physiol.*, vol. 12, 2021. doi:10.3389/fphys.2021.778872
- [166] M. Salvador, M. Fedele, P. C. Africa, et al., “Electromechanical modeling of human ventricles with ischemic cardiomyopathy: numerical simulations in sinus rhythm and under arrhythmia,” *arXiv*, 2021. arXiv:2106.12811v1
- [167] M. Salvador, F. Regazzoni, S. Pagani, L. Dede’, N. Trayanova, and A. Quarteroni, “The role of mechano-electric feedbacks and hemodynamic coupling in scar-related ventricular tachycardia,” *arXiv*, 2021. arXiv:2110.15401v1
- [168] T. Gerach, S. Schuler, J. Fröhlich, et al., “Electro-Mechanical Whole-Heart Digital Twins: A Fully Coupled Multi-Physics Approach,” *Mathematics*, vol. 9, p. 1247, 2021. doi:10.3390/math9111247
- [169] C. Nagel, S. Schuler, O. Dössel, and A. Loewe, “A bi-atrial statistical shape model for large-scale in silico studies of human atria: model development and application to ECG simulations,” *Medical Image Analysis*, vol. 74, p. 102210, 2021. doi:10.1016/j.media.2021.102210
- [170] E. A. Perez Alday, A. Gu, A. Shah, et al., “Classification of 12-lead ECGs: the PhysioNet/Computing in Cardiology Challenge 2020,” *Physiological Measurement*, vol. 41, 2020. doi:10.1101/2020.08.11.20172601
- [171] N. Strodthoff, P. Wagner, T. Schaeffter, and W. Samek, “Deep Learning for ECG Analysis: Benchmarks and Insights from PTB-XL,” *IEEE Journal of Biomedical and Health Informatics*, vol. 25, pp. 1519–1528, 2021. doi:10.1109/JBHI.2020.3022989
- [172] A. Lyon, R. Ariga, A. Mincholé, et al., “Distinct ECG Phenotypes Identified in Hypertrophic Cardiomyopathy Using Machine Learning Associate With Arrhythmic Risk Markers.” *Front Physiol.*, vol. 9, p. 213, 2018. doi:10.3389/fphys.2018.00213
- [173] N. Pilia, S. Severi, J. G. Raimann, et al., “Quantification and classification of potassium and calcium disorders with the electrocardiogram: What do clinical studies, modeling, and reconstruction tell us?” *APL Bioeng.*, vol. 4, p. 041501, 2020. doi:10.1063/5.0018504
- [174] M. Roberts, D. Driggs, M. Thorpe, et al., “Common pitfalls and recommendations for using machine learning to detect and prognosticate for COVID-19 using chest radiographs and CT scans,” *Nature Machine Intelligence*, vol. 3, pp. 199–217, 2021. doi:10.1038/s42256-021-00307-0
- [175] P. Laguna, R. G. Mark, A. Goldberg, and G. B. Moody, “A database for evaluation of algorithms for measurement of QT and other waveform intervals in the ECG,” in *Computers in Cardiology 1997*, 1997, pp. 673–676.
- [176] R. Andlauer, G. Seemann, L. Baron, et al., “Influence of left atrial size on P-wave morphology: differential effects of dilation and hypertrophy,” *Europace*, vol. 20, pp. iii36–iii44, 2018. doi:10.1093/europace/euy231
- [177] G. Luongo, S. Schuler, M. W. Rivolta, O. Dössel, R. Sassi, and A. Loewe, “Semi-Supervised vs. Supervised Learning for Discriminating Atrial Flutter Mechanisms Using the 12-lead ECG,” in *Computing in Cardiology Conference (CinC)*, vol. 48, 2021. doi:10.23919/CinC53138.2021.9662849
- [178] W. Bai, W. Shi, A. de Marvao, et al., “A bi-ventricular cardiac atlas built from 1000+ high resolution MR images of healthy subjects and an analysis of shape and motion,” *Med Image Anal.*, vol. 26, pp. 133–145, 2015. doi:10.1016/j.media.2015.08.009

- [179] L. Pishchulin, S. Wuhrer, T. Helten, C. Theobalt, and B. Schiele, "Building statistical shape spaces for 3D human modeling," *Pattern Recognition*, vol. 67, pp. 276–286, 2017. doi:10.1016/j.patcog.2017.02.018
- [180] C. Corrado, O. Razeghi, C. Roney, et al., "Quantifying atrial anatomy uncertainty from clinical data and its impact on electro-physiology simulation predictions." *Med Image Anal*, vol. 61, p. 101626, 2020. doi:10.1016/j.media.2019.101626
- [181] N. F. Marrouche, D. Wilber, G. Hindricks, et al., "Association of atrial tissue fibrosis identified by delayed enhancement MRI and atrial fibrillation catheter ablation: the DECAAF study," *JAMA*, vol. 311, pp. 498–506, 2014. doi:10.1001/jama.2014.3
- [182] J. Cates, E. Bieging, A. Morris, et al., "Computational Shape Models Characterize Shape Change of the Left Atrium in Atrial Fibrillation." *Clin Med Insights Cardiol*, vol. 8, pp. 99–109, 2014. doi:10.4137/CMC.S15710
- [183] M. Depa, M. R. Sabuncu, G. Holmvang, R. Nezafat, E. J. Schmidt, and P. Golland, "Robust Atlas-Based Segmentation of Highly Variable Anatomy: Left Atrium Segmentation." *Stat Atlases Comput Models Heart*, vol. 6364, pp. 85–94, 2010. doi:10.1007/978-3-642-15835-3\_9
- [184] M. Varela, F. Bisbal, E. Zacur, et al., "Novel Computational Analysis of Left Atrial Anatomy Improves Prediction of Atrial Fibrillation Recurrence after Ablation." *Front Physiol*, vol. 8, p. 68, 2017. doi:10.3389/fphys.2017.00068
- [185] C. Rodero, M. Strocchi, M. Marciniak, et al., "Linking statistical shape models and simulated function in the healthy adult human heart," *PLOS Computational Biology*, vol. 17, p. e1008851, 2021. doi:10.1371/journal.pcbi.1008851
- [186] O. Ecabert, J. Peters, H. Schramm, et al., "Automatic model-based segmentation of the heart in CT images." *IEEE Trans Med Imaging*, vol. 27, pp. 1189–201, 2008. doi:10.1109/TMI.2008.918330
- [187] C. Hoogendoorn, N. Duchateau, D. Sánchez Quintana, et al., "A high-resolution atlas and statistical model of the human heart from multislice CT." *IEEE Trans Med Imaging*, vol. 32, pp. 28–44, 2013. doi:10.1109/TMI.2012.2230015
- [188] J. Lötjönen, S. Kivistö, J. Koikkalainen, D. Smutek, and K. Lauerma, "Statistical shape model of atria, ventricles and epicardium from short- and long-axis MR images." *Med Image Anal*, vol. 8, pp. 371–86, 2004. doi:10.1016/j.media.2004.06.013
- [189] S. Ordas, E. Oubel, R. Sebastian, and A. F. Frangi, "Computational Anatomy Atlas of the Heart," *2007 5th International Symposium on Image and Signal Processing and Analysis*, pp. 338–342, 2007. doi:10.1109/ISPA.2007.4383715
- [190] M. Unberath, A. Maier, D. Fleischmann, J. Hornegger, and R. Fahrig, "Open-source 4D statistical shape model of the heart for x-ray projection imaging," *2015 IEEE 12th International Symposium on Biomedical Imaging (ISBI)*, pp. 739–742, 2015. doi:10.1109/ISBI.2015.7163978
- [191] X. Zhuang, K. S. Rhode, R. S. Razavi, D. J. Hawkes, and S. Ourselin, "A registration-based propagation framework for automatic whole heart segmentation of cardiac MRI." *IEEE Trans Med Imaging*, vol. 29, pp. 1612–25, 2010. doi:10.1109/TMI.2010.2047112
- [192] A. Masci, L. Barone, L. Dedè, et al., "The Impact of Left Atrium Appendage Morphology on Stroke Risk Assessment in Atrial Fibrillation: A Computational Fluid Dynamics Study," *Frontiers in Physiology*, vol. 9, 2019. doi:10.3389/fphys.2018.01938
- [193] A. M. Aguado, A. L. Olivares, C. Yagüe, et al., "In silico Optimization of Left Atrial Appendage Occluder Implantation Using Interactive and Modeling Tools," *Frontiers in Physiology*, vol. 10, 2019. doi:10.3389/fphys.2019.00237

- [194] M. Nishimura, F. Lupercio Lopez, and J. C. Hsu, "Left Atrial Appendage Electrical Isolation as a Target in Atrial Fibrillation." *JACC Clin Electrophysiol*, vol. 5, pp. 407–416, 2019. doi:10.1016/j.jacep.2019.02.009
- [195] L. Azzolin, "Atrial Digital Twins to Assess Arrhythmia Vulnerability and Guide Ablation Therapy: Leverage Patient-Specific Atrial Models to Understand Atrial Fibrillation Mechanisms and Provide Personalized Treatments," PhD thesis, Karlsruhe Institut für Technologie (KIT), 2022. doi:10.5445/IR/1000142101
- [196] A. Mincholé, E. Zacur, R. Ariga, V. Grau, and B. Rodriguez, "MRI-Based Computational Torso/Biventricular Multiscale Models to Investigate the Impact of Anatomical Variability on the ECG QRS Complex." *Front Physiol*, vol. 10, p. 1103, 2019. doi:10.3389/fphys.2019.01103
- [197] E. Zacur, A. Mincholé, B. Villard, et al., "MRI-Based Heart and Torso Personalization for Computer Modeling and Simulation of Cardiac Electrophysiology," *Imaging for Patient-Customized Simulations and Systems for Point-of-Care Ultrasound*, vol. 10549, pp. 61–70, 2017. doi:10.1007/978-3-319-67552-7\_8
- [198] C. Sánchez, A. Bueno Orovio, E. Wettwer, et al., "Inter-subject variability in human atrial action potential in sinus rhythm versus chronic atrial fibrillation." *PLoS One*, vol. 9, p. e105897, 2014. doi:10.1371/journal.pone.0105897
- [199] A. Banerjee, J. Camps, E. Zacur, et al., "A completely automated pipeline for 3D reconstruction of human heart from 2D cine magnetic resonance slices," *Philosophical Transactions of the Royal Society A: Mathematical, Physical and Engineering Sciences*, vol. 379, 2021. doi:10.1098/rsta.2020.0257
- [200] C. Nagel, S. Schuler, O. Dössel, and A. Loewe, "A Bi-atrial Statistical Shape Model and 100 Volumetric Anatomical Models of the Atria," *zenodo*, 2020. doi:10.5281/zenodo.4309958
- [201] R. Karim, R. J. Housden, M. Balasubramaniam, et al., "Evaluation of current algorithms for segmentation of scar tissue from late gadolinium enhancement cardiovascular magnetic resonance of the left atrium: an open-access grand challenge." *J Cardiovasc Magn Reson*, vol. 15, p. 105, 2013. doi:10.1186/1532-429X-15-105
- [202] R. Karim, L.-E. Blake, J. Inoue, et al., "Algorithms for left atrial wall segmentation and thickness - Evaluation on an open-source CT and MRI image database." *Med Image Anal*, vol. 50, pp. 36–53, 2018. doi:10.1016/j.media.2018.08.004
- [203] C. Tobon Gomez, A. J. Geers, J. Peters, et al., "Benchmark for Algorithms Segmenting the Left Atrium From 3D CT and MRI Datasets." *IEEE Trans Med Imaging*, vol. 34, pp. 1460–1473, 2015. doi:10.1109/TMI.2015.2398818
- [204] E. M. Marom, J. E. Herndon, Y. H. Kim, and H. P. McAdams, "Variations in pulmonary venous drainage to the left atrium: implications for radiofrequency ablation," *Radiology*, vol. 230, pp. 824–829, 2004. doi:10.1148/radiol.2303030315
- [205] O. Razeghi, J. A. Solís Lemus, A. W. Lee, et al., "CemrgApp: An interactive medical imaging application with image processing, computer vision, and machine learning toolkits for cardiovascular research," *SoftwareX*, vol. 12, p. 100570, 2020. doi:10.1016/j.softx.2020.100570
- [206] R. Bhalodia, S. Y. Elhabian, L. Kavan, and R. T. Whitaker, "DeepSSM: A Deep Learning Framework for Statistical Shape Modeling from Raw Images." *Shape Med Imaging (2018)*, vol. 11167, pp. 244–257, 2018. doi:10.1007/978-3-030-04747-4\_23
- [207] G. Bouabene, T. Gerig, M. Luethi, et al., *ScalismoLab: scalable image analysis and shape modelling*, 2020, accessed December 2, 2020. <https://github.com/unibas-gravis/scalismo/wiki/scalismoLab>

- [208] D. C. Liu and J. Nocedal, "On the limited memory BFGS method for large scale optimization," *Mathematical Programming*, vol. 45, pp. 503–528, 1989. doi:10.1007/bf01589116
- [209] J. Nocedal and S. J. Wright, *Numerical Optimization*. New York, NY :: Springer New York,, 2006. doi:10.1007/978-0-387-40065-5
- [210] J. Whitaker, R. Rajani, H. Chubb, et al., "The role of myocardial wall thickness in atrial arrhythmogenesis," *Europace*, vol. 18, pp. 1758–1772, 2016. doi:10.1093/europace/euw014
- [211] A. P. Tran, S. Yan, and Q. Fang, "Improving model-based functional near-infrared spectroscopy analysis using mesh-based anatomical and light-transport models." *Neurophotonics*, vol. 7, p. 015008, 2020. doi:10.1117/1.NPh.7.1.015008
- [212] C. Geuzaine and J.-F. Remacle, "Gmsh: A three-dimensional finite element mesh generator with built-in pre- and post-processing facilities," *International Journal for Numerical Methods in Engineering*, vol. 79, pp. 1309–1331, 2009. doi:10.1002/nme.2579
- [213] A. Wachter, A. Loewe, M. W. Krueger, O. Dössel, and G. Seemann, "Mesh structure-independent modeling of patient-specific atrial fiber orientation," *CDBME*, vol. 1, pp. 409–412, 2015. doi:10.1515/cdbme-2015-0099
- [214] C. H. Roney, A. Pashaei, M. Meo, et al., "Universal atrial coordinates applied to visualisation, registration and construction of patient specific meshes." *Med Image Anal*, vol. 55, pp. 65–75, 2019. doi:10.1016/j.media.2019.04.004
- [215] J. B. Nielsen, J. T. Kuhl, A. Pietersen, et al., "P-wave duration and the risk of atrial fibrillation: Results from the Copenhagen ECG Study," *Heart Rhythm*, vol. 12, pp. 1887–1895, 2015. doi:10.1016/j.hrthm.2015.04.026
- [216] G. Caixal, F. Alarcón, T. F. Althoff, et al., "Accuracy of left atrial fibrosis detection with cardiac magnetic resonance: correlation of late gadolinium enhancement with endocardial voltage and conduction velocity." *Europace*, 2020. doi:10.1093/europace/euaa313
- [217] S. T. Broughton, W. T. O'Neal, T. Salahuddin, and E. Z. Soliman, "The Influence of Left Atrial Enlargement on the Relationship between Atrial Fibrillation and Stroke." *J Stroke Cerebrovasc Dis*, vol. 25, pp. 1396–402, 2016. doi:10.1016/j.jstrokecerebrovasdis.2016.02.004
- [218] Y. Hamatani, H. Ogawa, K. Takabayashi, et al., "Left atrial enlargement is an independent predictor of stroke and systemic embolism in patients with non-valvular atrial fibrillation." *Sci Rep*, vol. 6, p. 31042, 2016. doi:10.1038/srep31042
- [219] A. M. Pritchett, S. J. Jacobsen, D. W. Mahoney, R. J. Rodeheffer, K. R. Bailey, and M. M. Redfield, "Left atrial volume as an index of left atrial size: a population-based study," *Journal of the American College of Cardiology*, vol. 41, pp. 1036–1043, 2003. doi:10.1016/S0735-1097(02)02981-9
- [220] M. A. Al Mohaisen, M. H. Kazmi, K. L. Chan, and B. J. W. Chow, "Validation of two-dimensional methods for left atrial volume measurement: a comparison of echocardiography with cardiac computed tomography." *Echocardiography*, vol. 30, pp. 1135–42, 2013. doi:10.1111/echo.12253
- [221] M. Salerno, B. Sharif, H. Arheden, et al., "Recent Advances in Cardiovascular Magnetic Resonance: Techniques and Applications." *Circ Cardiovasc Imaging*, vol. 10, 2017. doi:10.1161/CIRCIMAGING.116.003951
- [222] Y. Wang, L. Di Biase, R. P. Horton, T. Nguyen, P. Morhanty, and A. Natale, "Left atrial appendage studied by computed tomography to help planning for appendage closure device placement." *J Cardiovasc Electrophysiol*, vol. 21, pp. 973–82, 2010. doi:10.1111/j.1540-8167.2010.01814.x

- [223] L. Azzolin, G. Luongo, S. Rocher, J. Saiz, O. Doessel, and A. Loewe, "Influence of Gradient and Smoothness of Atrial Wall Thickness on Initiation and Maintenance of Atrial Fibrillation," in *Computing in Cardiology Conference (CinC)*, 2020. doi:10.22489/CinC.2020.261
- [224] A. Loewe, M. Wilhelms, O. Dössel, and G. Seemann, "Influence of chronic atrial fibrillation induced remodeling in a computational electrophysiological model," in *Biomedizinische Technik / Biomedical Engineering*, vol. 59, no. S1. Berlin, Boston: Walter de Gruyter, 2014, pp. S929–S932. doi:10.1515/bmt-2014-5012
- [225] M. Potse, A. Gharaviri, S. Pezzuto, et al., "Anatomically-Induced Fibrillation in a 3D Model of the Human Atria," *2018 Computing in Cardiology Conference (CinC)*, vol. 45, 2018. doi:10.22489/CinC.2018.366
- [226] M. Saha, G. Conte, M. L. Caputo, et al., "Changes in P-wave morphology after pulmonary vein isolation: insights from computer simulations." *Europace*, vol. 18, pp. iv23–iv34, 2016. doi:10.1093/europace/euw348
- [227] S. Pezzuto, A. Gharaviri, U. Schotten, et al., "Beat-to-beat P-wave morphological variability in patients with paroxysmal atrial fibrillation: an in silico study." *Europace*, vol. 20, pp. iii26–iii35, 2018. doi:10.1093/europace/euy227
- [228] G. Luongo, S. Schuler, M. W. Rivolta, O. Dössel, R. Sassi, and A. Loewe, "Automatic ECG-based Discrimination of 20 Atrial Flutter Mechanisms: Influence of Atrial and Torso Geometries," in *2020 Computing in Cardiology Conference (CinC)*, 2020.
- [229] G. Luongo, S. Schuler, A. Luik, et al., "Non-Invasive Characterization of Atrial Flutter Mechanisms Using Recurrence Quantification Analysis on the ECG: A Computational Study," *IEEE Trans Biomed Eng*, vol. 68, pp. 914–925, 2021. doi:10.1109/TBME.2020.2990655
- [230] J. Sánchez, M. Nothstein, A. Neic, et al., "openCARP: An Open Sustainable Framework for In-Silico Cardiac Electrophysiology Research," in *Computing in Cardiology, Computing in Cardiology*, vol. 47, 2020. doi:10.22489/CinC.2020.111
- [231] H. Jasak, "OpenFOAM: Open source CFD in research and industry," *International Journal of Naval Architecture and Ocean Engineering*, vol. 1, pp. 89–94, 2009. doi:10.2478/ijnaoe-2013-0011
- [232] M. A. Rodriguez, C. M. Augustin, and S. C. Shadden, "FEniCS mechanics: A package for continuum mechanics simulations," *SoftwareX*, vol. 9, pp. 107–111, 2019. doi:10.1016/j.softx.2018.10.005
- [233] P. C. Africa, M. Salvador, P. Gervasio, L. Dede', and A. Quarteroni, "A matrix-free high-order solver for the numerical solution of cardiac electrophysiology," *eprint*, 2022. arXiv: 2205.05136v2
- [234] J. Tomek, A. Bueno Orovio, E. Passini, et al., "Development, calibration, and validation of a novel human ventricular myocyte model in health, disease, and drug block," *eLife*, vol. 8, pp. 1813–1828, 2019. doi:10.7554/eLife.48890
- [235] F. Margara, Z. J. Wang, F. Levrero Florencio, et al., "In-silico human electro-mechanical ventricular modelling and simulation for drug-induced pro-arrhythmia and inotropic risk assessment," *Progress in Biophysics and Molecular Biology*, 2020. doi:10.1016/j.pbiomolbio.2020.06.007
- [236] R. H. Clayton, Y. Aboelkassem, C. D. Cantwell, et al., "An audit of uncertainty in multi-scale cardiac electrophysiology models," *Philosophical Transactions of the Royal Society A: Mathematical, Physical and Engineering Sciences*, vol. 378, p. 20190335, 2020. doi: 10.1098/rsta.2019.0335

- [237] A. Muszkiewicz, X. Liu, A. Bueno Orovio, et al., “From ionic to cellular variability in human atrial myocytes: an integrative computational and experimental study,” *American Journal of Physiology-Heart and Circulatory Physiology*, vol. 314, pp. H895–H916, 2018. doi:10.1152/ajpheart.00477.2017
- [238] F. Levrero Florencio, F. Margara, E. Zacur, et al., “Sensitivity analysis of a strongly-coupled human-based electromechanical cardiac model: Effect of mechanical parameters on physiologically relevant biomarkers,” *Computer Methods in Applied Mechanics and Engineering*, vol. 361, p. 112762, 2020. doi:10.1016/j.cma.2019.112762
- [239] G. Volpato, M. Casella, P. Compagnucci, et al., “Conduction velocity mapping in Bachmann Bundle using Omnipolar Technology,” *EP Europace*, vol. 24, 2022. doi:10.1093/europace/euac053.250
- [240] B. Maesen, S. Zeemering, C. Afonso, et al., “Rearrangement of Atrial Bundle Architecture and Consequent Changes in Anisotropy of Conduction Constitute the 3-Dimensional Substrate for Atrial Fibrillation,” *Circulation: Arrhythmia and Electrophysiology*, vol. 6, pp. 967–975, 2013. doi:10.1161/circep.113.000050
- [241] K. Fukumoto, M. Habibi, E. G. Ipek, et al., “Association of Left Atrial Local Conduction Velocity With Late Gadolinium Enhancement on Cardiac Magnetic Resonance in Patients With Atrial Fibrillation,” *Circulation: Arrhythmia and Electrophysiology*, vol. 9, 2016. doi:10.1161/circep.115.002897
- [242] Y. Hori, S. Nakahara, N. Anjo, et al., “Investigation of the atrial conduction time measured by tissue Doppler imaging at the left atrial appendage and the actual electrical conduction time: consideration of left atrial remodeling in atrial fibrillation patients,” *Journal of Interventional Cardiac Electrophysiology*, vol. 48, pp. 89–97, 2017. doi:10.1007/s10840-016-0185-7
- [243] A. Hassankhani, B. Yao, and G. K. Feld, “Conduction velocity around the tricuspid valve annulus during type 1 atrial flutter: defining the location of areas of slow conduction by three-dimensional electroanatomical mapping,” *J Interv Card Electrophysiol*, vol. 8, pp. 121–7, 2003. doi:10.1023/a:1023656800438
- [244] A. Hansson, “Right atrial free wall conduction velocity and degree of anisotropy in patients with stable sinus rhythm studied during open heart surgery,” *European Heart Journal*, vol. 19, pp. 293–300, 1998. doi:10.1053/euhj.1997.0742
- [245] A. Loewe, M. W. Krueger, P. G. Platonov, F. Holmqvist, O. Dössel, and G. Seemann, “Left and Right Atrial Contribution to the P-wave in Realistic Computational Models,” in *Lecture Notes in Computer Science, Functional Imaging and Modeling of the Heart*, H. van Assen, P. Boven-deerd, and T. Delhaas, Eds., vol. 9126, 2015, p. 439–447. doi:10.1007/978-3-319-20309-6
- [246] J. E. Saffitz, H. L. Kanter, K. G. Green, T. K. Tolley, and E. C. Beyer, “Tissue-specific determinants of anisotropic conduction velocity in canine atrial and ventricular myocardium.” *Circulation Research*, vol. 74, pp. 1065–1070, 1994. doi:10.1161/01.res.74.6.1065
- [247] T.-Y. Liu, C.-T. Tai, B.-H. Huang, et al., “Functional characterization of the crista terminalis in patients with atrial flutter: implications for radiofrequency ablation,” *Journal of the American College of Cardiology*, vol. 43, pp. 1639–1645, 2004. doi:10.1016/j.jacc.2003.11.057
- [248] S. E. Petersen, N. Aung, M. M. Sanghvi, et al., “Reference ranges for cardiac structure and function using cardiovascular magnetic resonance (CMR) in Caucasians from the UK Biobank population cohort.” *J Cardiovasc Magn Reson*, vol. 19, p. 18, 2017. doi:10.1186/s12968-017-0327-9
- [249] R. Lemery, D. Birnie, A. S. L. Tang, et al., “Normal atrial activation and voltage during sinus rhythm in the human heart: an endocardial and epicardial mapping study in patients

- with a history of atrial fibrillation,” *J Cardiovasc Electrophysiol*, vol. 18, pp. 402–408, 2007. doi:10.1111/j.1540-8167.2007.00762.x
- [250] N. Pilia, C. Nagel, G. Lenis, S. Becker, O. Dössel, and A. Loewe, “ECGdeli - An open source ECG delineation toolbox for MATLAB,” *SoftwareX*, vol. 13, p. 100639, 2021. doi: 10.1016/j.softx.2020.100639
- [251] H. Welle, C. Nagel, A. Loewe, R. Mikut, and O. Dössel, “Classification of Bundle Branch Blocks with QRS Templates Extracted from 12-lead ECGs,” in *Current Directions in Biomedical Engineering*, vol. 7, no. 2, 2021, pp. 582–585. doi:10.1515/cdbme-2021-2148
- [252] J. Axelsson and J. Sörensen, “The 2D Hotelling filter - a quantitative noise-reducing principal-component filter for dynamic PET data, with applications in patient dose reduction,” *BMC Medical Physics*, vol. 13, 2013. doi:10.1186/1756-6649-13-1
- [253] E. Z. Soliman, A. Alonso, J. R. Misialek, et al., “Reference ranges of PR duration and P-wave indices in individuals free of cardiovascular disease: The Multi-Ethnic Study of Atherosclerosis (MESA),” *Journal of Electrocardiology*, vol. 46, pp. 702–706, 2013. doi: 10.1016/j.jelectrocard.2013.05.006
- [254] A. Loewe, E. Poremba, T. Oesterlein, et al., “Patient-Specific Identification of Atrial Flutter Vulnerability—A Computational Approach to Reveal Latent Reentry Pathways,” *Frontiers in Physiology*, vol. 9, 2019. doi:10.3389/fphys.2018.01910
- [255] O. J. Britton, A. Bueno Orovio, L. Virág, A. Varró, and B. Rodriguez, “The Electrogenic Na<sup>+</sup>/K<sup>+</sup> Pump Is a Key Determinant of Repolarization Abnormality Susceptibility in Human Ventricular Cardiomyocytes: A Population-Based Simulation Study,” *Frontiers in Physiology*, vol. 8, 2017. doi:10.3389/fphys.2017.00278
- [256] M. R. Vagos, H. Arevalo, B. L. de Oliveira, J. Sundnes, and M. M. Maleckar, “A computational framework for testing arrhythmia marker sensitivities to model parameters in functionally calibrated populations of atrial cells,” *Chaos: An Interdisciplinary Journal of Nonlinear Science*, vol. 27, p. 093941, 2017. doi:10.1063/1.4999476
- [257] B. A. J. Lawson, C. C. Drovandi, N. Cusimano, P. Burrage, B. Rodriguez, and K. Burrage, “Unlocking data sets by calibrating populations of models to data density: A study in atrial electrophysiology,” *Sci Adv*, vol. 4, p. e1701676, 2018. doi:10.1126/sciadv.1701676
- [258] C. Corrado, S. Williams, C. Roney, G. Plank, M. O’Neill, and S. Niederer, “Using machine learning to identify local cellular properties that support re-entrant activation in patient-specific models of atrial fibrillation,” *Europace*, 2021. doi:10.1093/europace/euaa386
- [259] C. H. Roney, I. Sim, J. Yu, et al., “Predicting Atrial Fibrillation Recurrence by Combining Population Data and Virtual Cohorts of Patient-Specific Left Atrial Models,” *Circulation: Arrhythmia and Electrophysiology*, 2022. doi:10.1161/CIRCEP.121.010253
- [260] J. Bender, “Classification of Interatrial Conduction Block Based on P waves of the 12-lead ECG,” Bachelor’s thesis, Institute for Applied and Numerical Mathematics; Institute of Biomedical Engineering, Karlsruhe Institute of Technology (KIT), 2022.
- [261] K. Gillette, M. A. F. Gsell, J. Bouyssier, et al., “Automated Framework for the Inclusion of a His–Purkinje System in Cardiac Digital Twins of Ventricular Electrophysiology,” *Annals of Biomedical Engineering*, 2021. doi:10.1007/s10439-021-02825-9
- [262] E. A. Perez Alday, A. Gu, A. J. Shah, et al., “Classification of 12-lead ECGs: the PhysioNet/Computing in Cardiology Challenge 2020,” *Physiological Measurement*, vol. 41, p. 124003, 2020. doi:10.1088/1361-6579/abc960

- [263] C. Nagel, N. Pilia, A. Loewe, and O. Dössel, “Quantification of Interpatient 12-lead ECG Variabilities within a Healthy Cohort,” *Current Directions in Biomedical Engineering*, vol. 6, pp. 493–496, 2020. doi:10.1515/cdbme-2020-3127
- [264] J. W. Kantelhardt, S. Havlin, and P. C. Ivanov, “Modeling transient correlations in heartbeat dynamics during sleep,” *Europhysics Letters (EPL)*, vol. 62, pp. 147–153, 2003. doi:10.1209/epl/i2003-00332-7
- [265] A. Petrenas, V. Marozas, A. Sološenko, et al., “Electrocardiogram modeling during paroxysmal atrial fibrillation: application to the detection of brief episodes,” *Physiol Meas*, vol. 38, pp. 2058–2080, 2017. doi:10.1088/1361-6579/aa9153
- [266] C. Mitchell and D. G. Schaeffer, “A two-current model for the dynamics of cardiac membrane,” *Bulletin of Mathematical Biology*, vol. 65, pp. 767–793, 2003. doi:10.1016/S0092-8240(03)00041-7
- [267] F. Anzlinger, “Assessment of Inpatient ECG Feature Distributions for a Synthesis of Realistic ECG Signals,” Bachelor’s thesis, Institute of Biomedical Engineering, Karlsruhe Institute of Technology (KIT), 2020.
- [268] C. Nagel, O. Dössel, and A. Loewe, “Sensitivity and Generalization of a Neural Network for Estimating Left Atrial Fibrotic Volume Fractions from the 12-lead ECG,” in *Current Directions in Biomedical Engineering*, vol. 7, no. 2, 2021, pp. 307–310. doi:10.1515/cdbme-2021-2078
- [269] C. Nagel, J. Osypka, L. A. Unger, et al., “Improving Clinical ECG-based Atrial Fibrosis Quantification With Neural Networks Through in silico P waves From an Extensive Virtual Patient Cohort,” in *Computing in Cardiology Conference (CinC)*, vol. 49, 2022.
- [270] U. Schotten, D. Dobrev, P. G. Platonov, H. Kottkamp, and G. Hindricks, “Current controversies in determining the main mechanisms of atrial fibrillation,” *J Intern Med*, vol. 279, pp. 428–38, 2016. doi:10.1111/joim.12492
- [271] J. Heijman, D. Linz, and U. Schotten, “Dynamics of Atrial Fibrillation Mechanisms and Comorbidities,” *Annual Review of Physiology*, vol. 83, 2021. doi:10.1146/annurev-physiol-031720085307
- [272] T. Yoshizawa, S. Niwano, H. Niwano, et al., “Prediction of new onset atrial fibrillation through P wave analysis in 12 lead ECG,” *Int Heart J*, vol. 55, pp. 422–7, 2014. doi:10.1536/ihj.14-052
- [273] A. Jadidi, B. Müller Edenborn, J. Chen, et al., “The Duration of the Amplified Sinus-P-Wave Identifies Presence of Left Atrial Low Voltage Substrate and Predicts Outcome After Pulmonary Vein Isolation in Patients With Persistent Atrial Fibrillation,” *JACC Clin Electrophysiol*, vol. 4, pp. 531–543, 2018. doi:10.1016/j.jacep.2017.12.001
- [274] T. Yamaguchi and N. F. Marrouche, “Recurrence Post-Atrial Fibrillation Ablation: Think Outside the Pulmonary Veins,” *Circ Arrhythm Electrophysiol*, vol. 11, p. e006379, 2018. doi:10.1161/CIRCEP.118.006379
- [275] P. M. Boyle, A. R. Ochs, R. L. Ali, N. Paliwal, and N. A. Trayanova, “Characterizing the arrhythmogenic substrate in personalized models of atrial fibrillation: sensitivity to mesh resolution and pacing protocol in AF models,” *EP Europace*, vol. 23, pp. i3–i11, 2021. doi:10.1093/europace/euaa385
- [276] P. M. Boyle, S. Zahid, and N. A. Trayanova, “Using personalized computer models to custom-tailor ablation procedures for atrial fibrillation patients: are we there yet?” *Expert Rev Cardiovasc Ther*, vol. 15, pp. 339–341, 2017. doi:10.1080/14779072.2017.1317593
- [277] P. M. Boyle, S. Zahid, and N. A. Trayanova, “Towards personalized computational modelling of the fibrotic substrate for atrial arrhythmia,” *Europace*, vol. 18, pp. iv136–iv145, 2016. doi:10.1093/europace/euw358

- [278] N. M. S. de Groot, D. Shah, P. M. Boyle, et al., “Critical appraisal of technologies to assess electrical activity during atrial fibrillation: a position paper from the European Heart Rhythm Association and European Society of Cardiology Working Group on eCardiology in collaboration with the Heart Rhythm Society, Asia Pacific Heart Rhythm Society, Latin American Heart Rhythm Society and Computing in Cardiology,” *EP Europace*, 2021. doi:10.1093/europace/euab254
- [279] N. Akoum, M. Daccarett, C. McGann, et al., “Atrial fibrosis helps select the appropriate patient and strategy in catheter ablation of atrial fibrillation: a DE-MRI guided approach,” *J Cardiovasc Electrophysiol*, vol. 22, pp. 16–22, 2011. doi:10.1111/j.1540-8167.2010.01876.x
- [280] A. Blandino, F. Bianchi, S. Grossi, et al., “Left Atrial Substrate Modification Targeting Low-Voltage Areas for Catheter Ablation of Atrial Fibrillation: A Systematic Review and Meta-Analysis.” *Pacing Clin Electrophysiol*, vol. 40, pp. 199–212, 2017. doi:10.1111/pace.13015
- [281] S. Rolf, S. Kircher, A. Arya, et al., “Tailored atrial substrate modification based on low-voltage areas in catheter ablation of atrial fibrillation.” *Circ Arrhythm Electrophysiol*, vol. 7, pp. 825–33, 2014. doi:10.1161/CIRCEP.113.001251
- [282] D. Nairn, H. Lehrmann, B. Müller Edenborn, et al., “Comparison of Unipolar and Bipolar Voltage Mapping for Localization of Left Atrial Arrhythmogenic Substrate in Patients With Atrial Fibrillation,” *Frontiers in Physiology*, vol. 11, 2020. doi:10.3389/fphys.2020.575846
- [283] D. Nairn, D. Hunyar, J. Sánchez, O. Dössel, and A. Loewe, “Inverse Relationship Between Electrode Size and Voltage During Intracardiac Mapping,” 2020, DGBMT.
- [284] J. Ma, Q. Chen, and S. Ma, “Left atrial fibrosis in atrial fibrillation: Mechanisms, clinical evaluation and management,” *Journal of Cellular and Molecular Medicine*, vol. 25, pp. 2764–2775, 2021. doi:10.1111/jcmm.16350
- [285] B. Müller Edenborn, J. Chen, J. Allgeier, et al., “Amplified sinus-P-wave reveals localization and extent of left atrial low-voltage substrate: implications for arrhythmia freedom following pulmonary vein isolation.” *Europace*, 2019. doi:10.1093/europace/euz297
- [286] A. Jadidi, B. Müller Edenborn, J. Chen, et al., “Amplified Sinus P-Wave Duration in Persistent Atrial Fibrillation,” *JACC: Clinical Electrophysiology*, 2018. doi:10.1016/j.jacep.2017.12.001
- [287] J. Caldwell, S. Koppikar, W. Barake, et al., “Prolonged P-wave duration is associated with atrial fibrillation recurrence after successful pulmonary vein isolation for paroxysmal atrial fibrillation,” *J Interv Card Electrophysiol*, 2013. doi:10.1007/s10840-013-9851-1
- [288] Y. Nakatani, T. Sakamoto, Y. Yamaguchi, Y. Tsujino, N. Kataoka, and K. Kinugawa, “P-wave vector magnitude predicts the left atrial low-voltage area in patients with paroxysmal atrial fibrillation.” *J Electrocardiol*, vol. 59, pp. 35–40, 2020. doi:10.1016/j.jelectrocard.2019.12.015
- [289] T. Lankveld, S. Zeemering, D. Scherr, et al., “Atrial Fibrillation Complexity Parameters Derived From Surface ECGs Predict Procedural Outcome and Long-Term Follow-Up of Stepwise Catheter Ablation for Atrial Fibrillation.” *Circ Arrhythm Electrophysiol*, vol. 9, p. e003354, 2016. doi:10.1161/CIRCEP.115.003354
- [290] G. Tse, I. Lakhani, J. Zhou, et al., “P-Wave Area Predicts New Onset Atrial Fibrillation in Mitral Stenosis: A Machine Learning Approach.” *Front Bioeng Biotechnol*, vol. 8, p. 479, 2020. doi:10.3389/fbioe.2020.00479
- [291] J. Kornej, J. W. Magnani, S. R. Preis, et al., “P-wave signal-averaged electrocardiography: Reference values, clinical correlates, and heritability in the Framingham Heart Study,” *Heart Rhythm*, vol. 18, pp. 1500–1507, 2021. doi:10.1016/j.hrthm.2021.05.009
- [292] A. Vranka, V. Bertomeu González, F. Hornero, A. Quesada, R. Alcaraz, and J. J. Rieta, “Splitting the P-Wave: Improved Evaluation of Left Atrial Substrate Modification after Pulmonary Vein

- Isolation of Paroxysmal Atrial Fibrillation,” *Sensors*, vol. 22, p. 290, 2021. doi:10.3390/s22010290
- [293] L. Ciuffo, V. Bruña, M. Martínez-Sellés, et al., “Association between interatrial block, left atrial fibrosis, and mechanical dyssynchrony: Electrocardiography-magnetic resonance imaging correlation,” *Journal of Cardiovascular Electrophysiology*, vol. 31, pp. 1719–1725, 2020. doi:10.1111/jce.14608
- [294] M. U. Rasmussen, A. Fabricius Bjerre, P. Kumarathurai, et al., “Common source of miscalculation and misclassification of P-wave negativity and P-wave terminal force in lead V1.” *J Electrocardiol*, vol. 53, pp. 85–88, 2019. doi:10.1016/j.jelectrocard.2019.01.088
- [295] F. Odille, S. Liu, P. van Dam, and J. Felblinger, “Statistical Variations of Heart Orientation in Healthy Adults,” in *2017 Computing in Cardiology Conference (CinC)*, vol. 44, 2017. doi:10.22489/CinC.2017.225-058
- [296] N. Akoum, C. McGann, G. Vergara, et al., “Atrial fibrosis quantified using late gadolinium enhancement MRI is associated with sinus node dysfunction requiring pacemaker implant,” *J Cardiovasc Electrophysiol*, vol. 23, pp. 44–50, 2012. doi:10.1111/j.1540-8167.2011.02140.x
- [297] T. Nezlobinsky, O. Solovyova, and A. V. Panfilov, “Anisotropic conduction in the myocardium due to fibrosis: the effect of texture on wave propagation.” *Sci Rep*, vol. 10, p. 764, 2020. doi:10.1038/s41598-020-57449-1
- [298] K. S. McDowell, F. Vadakkumpadan, R. Blake, et al., “Methodology for patient-specific modeling of atrial fibrosis as a substrate for atrial fibrillation,” *J Electrocardiol*, vol. 45, pp. 640—645, 2012. doi:10.1016/j.jelectrocard.2012.08.005
- [299] W. Kahlmann, “Development of a Fast Method to Tailor Purkinje Activation Based on QRS Information,” Master’s thesis, Institute of Biomedical Engineering, Karlsruhe Institute of Technology (KIT), Karlsruhe, 2017.
- [300] J. Malmivuo and R. Plonsey, *Bioelectromagnetism: principles and applications of bioelectric and biomagnetic fields*. Oxford University Press, 1995. <http://openlibrary.org/book/OL1431499M>
- [301] P. Kligfield, L. S. Gettes, J. J. Bailey, et al., “Recommendations for the standardization and interpretation of the electrocardiogram: part I: The electrocardiogram and its technology: a scientific statement from the American Heart Association Electrocardiography and Arrhythmias Committee, Council on Clinical Cardiology; the American College of Cardiology Foundation; and the Heart Rhythm Society: endorsed by the International Society for Computerized Electrocardiology.” *Circulation*, vol. 115, pp. 1306–24, 2007. doi:10.1161/CIRCULATIONAHA.106.180200
- [302] G. Conte, A. Luca, S. Yazdani, et al., “Usefulness of P-Wave Duration and Morphologic Variability to Identify Patients Prone to Paroxysmal Atrial Fibrillation.” *Am J Cardiol*, vol. 119, pp. 275–279, 2017. doi:10.1016/j.amjcard.2016.09.043
- [303] C. Nagel, C. B. Espinosa, K. Gillette, et al., “Comparison of Propagation Models and Forward Calculation Methods on Cellular, Tissue and Organ Scale Atrial Electrophysiology,” *IEEE Transactions on Biomedical Engineering*, pp. 1–12, 2022. doi:10.1109/TBME.2022.3196144
- [304] D. Nairn, M. Eichenlaub, B. Müller Edenborn, et al., “LGE-MRI for diagnosis of left atrial cardiomyopathy as identified in high-definition endocardial voltage and conduction velocity mapping,” *medRxiv*, 2022. doi:10.1101/2022.02.02.22269817
- [305] G. Lenis, N. Pilia, A. Loewe, W. H. W. Schulze, and O. Dössel, “Comparison of Baseline Wander Removal Techniques considering the Preservation of ST Changes in the Ischemic ECG: A Simulation Study,” *Computational and Mathematical Methods in Medicine*, vol. 2017, p. 9295029, 2017. doi:10.1155/2017/9295029

- [306] G. Su, H. Cao, S. Xu, et al., “Left Atrial Enlargement in the Early Stage of Hypertensive Heart Disease: A Common But Ignored Condition,” *The Journal of Clinical Hypertension*, vol. 16, pp. 192–197, 2014. doi:10.1111/jch.12282
- [307] M. S. Hazen, T. H. Marwick, and D. A. Underwood, “Diagnostic accuracy of the resting electrocardiogram in detection and estimation of left atrial enlargement: An echocardiographic correlation in 551 patients,” *American Heart Journal*, vol. 122, pp. 823–828, 1991. doi:10.1016/0002-8703(91)90531-L
- [308] A. D. Waggoner, A. V. Adyanthaya, M. A. Quinones, and J. K. Alexander, “Left atrial enlargement. Echocardiographic assessment of electrocardiographic criteria.” *Circulation*, vol. 54, pp. 553–557, 1976. doi:10.1161/01.cir.54.4.553
- [309] M. K. Batra, A. Khan, F. Farooq, T. Masood, and M. Karim, “Assessment of electrocardiographic criteria of left atrial enlargement,” *Asian Cardiovascular and Thoracic Annals*, vol. 26, pp. 273–276, 2018. doi:10.1177/0218492318768131
- [310] C. Ng, A. Ahmad, D. R. Budhram, M. He, N. Balakrishnan, and T. Mondal, “Accuracy of Electrocardiography and Agreement with Echocardiography in the Diagnosis of Pediatric Left Atrial Enlargement,” *Scientific Reports*, vol. 10, 2020. doi:10.1038/s41598-020-66987-7
- [311] J. Jiang, H. Deng, Y. Xue, H. Liao, and S. Wu, “Detection of Left Atrial Enlargement Using a Convolutional Neural Network-Enabled Electrocardiogram,” *Frontiers in Cardiovascular Medicine*, vol. 7, 2020. doi:10.3389/fcvm.2020.609976
- [312] Y.-S. Lou, C.-S. Lin, W.-H. Fang, et al., “Artificial Intelligence-Enabled Electrocardiogram Estimates Left Atrium Enlargement as a Predictor of Future Cardiovascular Disease,” *Journal of Personalized Medicine*, vol. 12, p. 315, 2022. doi:10.3390/jpm12020315
- [313] P. D. Farjo and P. P. Sengupta, “ECG for Screening Cardiac Abnormalities: The Premise and Promise of Machine Learning,” *Circulation: Cardiovascular Imaging*, vol. 14, 2021. doi:10.1161/circimaging.121.012837
- [314] S. Ketu and P. K. Mishra, “Empirical Analysis of Machine Learning Algorithms on Imbalance Electrocardiogram Based Arrhythmia Dataset for Heart Disease Detection,” *Arabian Journal for Science and Engineering*, vol. 47, pp. 1447–1469, 2022. doi:10.1007/s13369-021-05972-2
- [315] M. M. Ahsan and Z. Siddique, “Machine learning-based heart disease diagnosis: A systematic literature review,” *Artificial Intelligence in Medicine*, vol. 128, p. 102289, 2022. doi:10.1016/j.artmed.2022.102289
- [316] O. Rodevan, R. Bjornerheim, M. Ljosland, J. Maehle, H. J. Smith, and H. Ihlen, “Left atrial volumes assessed by three- and two-dimensional echocardiography compared to MRI estimates.” *Int J Card Imaging*, vol. 15, pp. 397–410, 1999. doi:10.1023/a:1006276513186
- [317] R. Andlauer, A. Loewe, O. Dössel, and G. Seemann, “Effect of left atrial hypertrophy on P-wave morphology in a computational model,” in *Current Directions in Biomedical Engineering*, vol. 2, no. 1. De Gruyter, 2016, pp. 603–606.
- [318] G. Arora, P. N. Gona, C. J. Salton, et al., “Impact of sex and advancing age on left atrial volume and shape: the Framingham heart study,” *Journal of Cardiovascular Magnetic Resonance*, vol. 18, 2016. doi:10.1186/1532-429X-18-S1-P130
- [319] N. Akoum, C. Mahnkopf, E. G. Kholmovski, J. Brachmann, and N. F. Marrouche, “Age and sex differences in atrial fibrosis among patients with atrial fibrillation,” *EP Europace*, vol. 20, pp. 1086–1092, 2018. doi:10.1093/europace/eux260
- [320] C. Magnussen, T. J. Niiranen, F. M. Ojeda, et al., “Sex Differences and Similarities in Atrial Fibrillation Epidemiology, Risk Factors, and Mortality in Community Cohorts: Results From

- the BiomarCaRE Consortium (Biomarker for Cardiovascular Risk Assessment in Europe),” *Circulation*, 2017. doi:10.1161/CIRCULATIONAHA.117.028981
- [321] A. Fogli Iseppe, H. Ni, S. Zhu, et al., “Sex-Specific Classification of Drug-Induced Torsade de Pointes Susceptibility Using Cardiac Simulations and Machine Learning,” *Clinical Pharmacology & Therapeutics*, vol. 110, pp. 380–391, 2021. doi:10.1002/cpt.2240
- [322] F. Wiedmann, C. Beyersdorf, X. Zhou, et al., “Pharmacologic TWIK-Related Acid-Sensitive K<sup>+</sup> Channel (TASK-1) Potassium Channel Inhibitor A293 Facilitates Acute Cardioversion of Paroxysmal Atrial Fibrillation in a Porcine Large Animal Model,” *Journal of the American Heart Association*, vol. 9, 2020. doi:10.1161/JAHA.119.015751
- [323] M. Thind, D. S. McKindley, J. A. Reiffel, G. V. Naccarelli, J. Stewart, and P. R. Kowey, “Predictors of dronedarone plasma drug concentrations and effect on atrial fibrillation/atrial flutter recurrence: Analyses from the EURIDIS and ADONIS studies,” *Clinical Cardiology*, 2022. doi:10.1002/clc.23768
- [324] H. Zou, P. Banerjee, S. S. Y. Leung, and X. Yan, “Application of Pharmacokinetic-Pharmacodynamic Modeling in Drug Delivery: Development and Challenges,” *Frontiers in Pharmacology*, vol. 11, 2020. doi:10.3389/fphar.2020.00997



# List of Publications and Supervised Theses

## Journal Articles

- **Claudia Nagel**, Giorgio Luongo, Luca Azzolin, Steffen Schuler, Olaf Dössel, Axel Loewe, *Non-Invasive and Quantitative Estimation of Left Atrial Fibrosis Based on P Waves of the 12-Lead ECG-A Large-Scale Computational Study Covering Anatomical Variability*, Journal of Clinical Medicine 2021;10:8
- **Claudia Nagel**, Steffen Schuler, Olaf Dössel, Axel Loewe, *A bi-atrial statistical shape model for large-scale in silico studies of human atria: Model development and application to ECG simulations*, Medical Image Analysis 2021;74:102210,
- **Claudia Nagel**, Cristian Barrios, Karli Gillette, Matthias A.F. Gsell, Jorge Sánchez, Gernot Plank, Olaf Dössel, Axel Loewe, *Comparison of source models and forward calculation methods on cellular, tissue and organ scale atrial electrophysiology*, IEEE Transactions on Biomedical Engineering 2022
- Nicolas Pilia, **Claudia Nagel**, Gustavo Lenis, Silvia Becker, Olaf Dössel, Axel Loewe, *ECGdeli - An open source ECG delineation toolbox for MATLAB*, SoftwareX2021; 13:100639
- Olaf Dössel, Giorgio Luongo, **Claudia Nagel**, Axel Loewe, *Computer Modeling of the Heart for ECG Interpretation—A Review*, Hearts 2021;2:350–368
- Giorgio Luongo, Gaetano Vacanti, Vincent Nitzke, Deborah Nairn, **Claudia Nagel**, Diba Kabiri, Tiago P Almeida, Diogo C Soriano, Massimo W Rivolta, Ghulam André Ng, Olaf Dössel, Armin Luik, Roberto Sassi, Claus Schmitt, Axel Loewe, *Hybrid machine learning to localize atrial flutter substrates using the surface 12-lead electrocardiogram*, EP Europace 2022.
- Luca Azzolin, Martin Eichenlaub, **Claudia Nagel**, Deborah Nairn, Jorge Sánchez, Laura Unger, Olaf Dössel, Amir Jadidi, Axel Loewe, *Personalized ablation vs. conventional ablation strategies to terminate atrial fibrillation and prevent recurrence*, EP Europace 2022

## Refereed Preprints

- Luca Azzolin, Martin Eichenlaub, **Claudia Nagel**, Deborah Nairn, Jorge Sánchez, Laura Unger, Amir Jadidi, Olaf Dössel, Axel Loewe, *AugmentA: Patient-specific Augmented Atrial model Generation Tool*, medRxiv 2022
- Deborah Nairn, Martin Eichenlaub, Heiko Lehrmann, Björn Müller-Edenborn, Juan Chen, Taiyuan Huang, **Claudia Nagel**, Jorge Sánchez, Giorgio Luongo, Thomas Arentz, Olaf Dössel, Amir Jadidi, Axel Loewe, *Spatial Correlation of Left Atrial Low Voltage Substrate in Sinus Rhythm versus Atrial Fibrillation: Identifying the Pathological Substrate Irrespective of the Rhythm*, medRxiv 2022
- Deborah Nairn, Martin Eichenlaub, Björn Müller-Edenborn, Heiko Lehrmann, **Claudia Nagel**, Luca Azzolin, Giorgio Luongo, Rosa M. Figueras Ventura, Barbara Rubio Forcada, Anna Vallès Colomer, Thomas Arentz, Olaf Dössel, Axel Loewe, Amir Jadidi, *LGE-MRI for diagnosis of left atrial cardiomyopathy as identified in high-definition endocardial voltage and conduction velocity mapping*, medRxiv 2022

## Refereed Conference Articles

- **Claudia Nagel**, Nicolas Pilia, Laura Unger, Olaf Dössel, *Performance of Different Atrial Conduction Velocity Estimation Algorithms Improves with Knowledge about the Depolarization Pattern*, Current Directions in Biomedical Engineering, vol. 5, no. 1, 2019, pp. 101-104.
- **Claudia Nagel**, Nicolas Pilia, Axel Loewe, Olaf Dössel, *Quantification of Interpatient 12-lead ECG Variabilities within a Healthy Cohort*, Current Directions in Biomedical Engineering, vol. 6, no. 3, 2020, pp. 493-496.
- **Claudia Nagel**, Olaf Dössel, Axel Loewe, *Sensitivity and Generalization of a Neural Network for Estimating Left Atrial Fibrotic Volume Fractions from the 12-lead ECG*, Current Directions in Biomedical Engineering, vol. 7, no. 2, 2021, pp. 307-310.
- **Claudia Nagel**, Matthias Schaufelberger, Olaf Dössel, Axel Loewe, *A Bi-atrial Statistical Shape Model as a Basis to Classify Left Atrial Enlargement from Simulated and Clinical 12-Lead ECGs*, Statistical Atlases and Computational Models of the Heart. Multi-Disease, Multi-View, and Multi-Center Right Ventricular Segmentation in Cardiac MRI Challenge, 2021, pp.38-47
- **Claudia Nagel**, Johannes Osypka, Laura Anna Unger, Deborah Nairn, Armin Luik, Reza Wakili, Olaf Dössel, Axel Loewe, *Improving Clinical ECG-based Atrial Fibrosis Quantification With Neural Networks Through in silico P waves From an Extensive Virtual Patient Cohort*, Computing in Cardiology, 2022

- Hannes Welle, **Claudia Nagel**, Axel Loewe, Ralf Mikut, and Olaf Dössel, *Classification of Bundle Branch Blocks with QRS Templates Extracted from 12-lead ECGs* Current Directions in Biomedical Engineering, vol. 7, no. 2, 2021, pp. 582-585.
- Deborah Nairn, **Claudia Nagel**, Björn Müller-Edenborn, Heiko Lehrmann, Thomas Arntz, Olaf Dössel, Amir Jadidi, Axel Loewe, *Optimal Regional Voltage Thresholds for Identifying Ablation Targets in Patients with Atrial Fibrillation*, Computing in Cardiology, 2021
- Luca Azzolin, **Claudia Nagel**, Deborah Nairn, Jorge Sánchez, Tianbao Zheng, Martin Eichenlaub, Amir Jadidi, Olaf Dössel, Axel Loewe, *Automated Framework for the Augmentation of Missing Anatomical Structures and Generation of Personalized Atrial Models from Clinical Data*, Computing in Cardiology, 2021
- Albert Dasí, **Claudia Nagel**, Axel Loewe, Alfonso Bueno-Orovio, Blanca Rodriguez, *Electrogram analysis reveals ionic current dysregulation relevant for atrial fibrillation*, Computing in Cardiology, 2022
- Jule Bender, **Claudia Nagel**, Jonathan Froehlich, Christian Wieners, Olaf Doessel, Axel Loewe, *A Large-scale Virtual Patient Cohort to Study ECG Features of Interatrial Conduction Block*, Current Directions in Biomedical Engineering, 2022

## Refereed Conference Abstracts

- **Claudia Nagel**, Cristian Alberto Barrios Espinosa, Karli Gillette, Matthias Gsell, Gernot Plank, Olaf Dössel, Axel Loewe, *Comparison of source models and forward calculation methods for atrial electrophysiology regarding activation times and electrocardiograms*, iHeart - Modeling the Cardiac Function, Milan, Italy (online), 2021
- **Claudia Nagel**, Olaf Dössel, Axel Loewe, *Assessing fidelity of simulated 12-lead ECGs in reduced clinical ECG eigenspaces*, Virtual Metrology Meeting, Berlin, Germany (online), 2021
- **Claudia Nagel**, Olaf Dössel, Axel Loewe, *Non-invasive identification of fibrotic atrial cardiomyopathy with neural networks based on 642,400 12-lead ECGs from an extensive cohort simulation study*, American Heart Association Scientific Sessions, Boston, USA (online), 2021
- **Claudia Nagel**, Hannes Welle, Steffen Schuler, Olaf Dössel, Axel Loewe, *Quantifying the influence of ventricular shape variability on the QRS morphology in simulated 12-lead electrocardiograms*, Cardiac Physiome Workshop, Boston, USA (online), 2021
- Deborah Nairn, **Claudia Nagel**, Björn Müller-Edenborn, Heiko Lehrmann, Amir Jadidi, Axel Loewe, *Spatial and quantitative assessment of the correlation between sinus rhythm and atrial fibrillation voltage mapping to identify low voltage substrate in persistent atrial fibrillation*, EHRA, online, 2021
- Patricia Martínez Díaz, Jorge Sánchez, **Claudia Nagel**, Deborah Nairn, Ismael Hernández-Romero, Maria de la Salud Guillem Sánchez, Olaf Doessel, Axel Loewe, *Personalized*

*Modeling of Atrial Activation and P-waves: a Multimodality Approach*, Computing in Cardiology, Tampere, Finland, 2022

- Jenny Venton, Karli Gillette, Matthias Gsell, Axel Loewe, **Claudia Nagel**, Benjamin Winkler, Louise Wright, *Sensitivity Analysis of ECG Features to Computational Model Input Parameters*, Computing in Cardiology, Tampere, Finland, 2022
- Philip Aston, Temesgen Mehari, Alen Bosnjakovic, Peter Harris, Ashish Sundar, Steven Williams, Axel Loewe, **Claudia Nagel**, Nils Strodthoff, Olaf Doessel, *Multi-Class ECG Feature Importance Rankings: Cardiologists vs. Algorithms*, Computing in Cardiology, Tampere, Finland, 2022

## Conference Presentations

- **Claudia Nagel**, Nicolas Pilia, Laura Unger, Olaf Dössel, *Performance of Different Atrial Conduction Velocity Estimation Algorithms Improves with Knowledge about the Depolarization Pattern*, 53rd DGBMT Annual Conference, Frankfurt, Germany, 2019
- **Claudia Nagel**, Nicolas Pilia, Axel Loewe, Olaf Dössel, *Quantification of Interpatient 12-lead ECG Variabilities within a Healthy Cohort*, 54th DGBMT Annual Conference, Leipzig, Germany (online), 2020
- **Claudia Nagel**, Olaf Dössel, Axel Loewe, *Sensitivity and Generalization of a Neural Network for Estimating Left Atrial Fibrotic Volume Fractions from the 12-lead ECG*, 55th DGBMT Annual Conference, Hannover, Germany, 2021
- **Claudia Nagel**, Cristian Alberto Barrios Espinosa, Karli Gillette, Matthias Gsell, Gernot Plank, Olaf Dössel, Axel Loewe, *Comparison of source models and forward calculation methods for atrial electrophysiology regarding activation times and electrocardiograms*, iHeart - Modeling the Cardiac Function, Milan, Italy (online), 2021
- **Claudia Nagel**, Matthias Schaufelberger, Olaf Dössel, Axel Loewe, *A Bi-atrial Statistical Shape Model as a Basis to Classify Left Atrial Enlargement from Simulated and Clinical 12-Lead ECGs*, Statistical Atlases and Computational Models of the Heart, Strasbourg, France (online), 2021
- **Claudia Nagel**, Olaf Dössel, Axel Loewe, *Assessing fidelity of simulated 12-lead ECGs in reduced clinical ECG eigenspaces*, Virtual Metrology Meeting, Berlin, Germany (online), 2021
- **Claudia Nagel**, Johannes Osypka, Laura Anna Unger, Deborah Nairn, Armin Luik, Reza Wakili, Olaf Dössel, Axel Loewe, *Improving Clinical ECG-based Atrial Fibrosis Quantification With Neural Networks Through in silico P waves From an Extensive Virtual Patient Cohort*, Computing in Cardiology, Tampere, Finland, 2022

## Invited Talks

- 4th OpenCarp User Meeting, September 21st, 2021, Karlsruhe, Germany: Statistical shape models as modeling resources: Evaluating shape statistics of your own cohort or using available data repositories
- Atrial Signals 2021, September 25th, 2021, Karlsruhe, Germany: Generating big synthetic data for arrhythmia research: Simulation of 100,000 P waves

## Reports, Theses, Book Chapters, Grant Proposals

- *Robust conduction velocity estimation in a clinical setting*, Master's Thesis, Institute of Biomedical Engineering, Karlsruhe Institute of Technology (KIT), 2019
- Axel Loewe, Patricia Martínez Díaz, **Claudia Nagel**, Jorge Sánchez *Cardiac Digital Twins*, chapter in textbook *Innovative Treatment Strategies for Clinical Electrophysiology*, 2022
- Axel Loewe, **Claudia Nagel** *Cohort modeling of the human atria for in silico trials*, German research foundation grant proposal, 2022

## Data and Code Repositories

- **Claudia Nagel**, Jorge Sánchez, Luca Azzolin, Tianbao Zheng, Steffen Schuler, Olaf Dössel, Axel Loewe *A Bi-atrial Statistical Shape Model and 100 Volumetric Anatomical Models of the Atria*, <https://zenodo.org/record/5571925#.YtZ1pi-22Zw>
- Nicolas Pilia, **Claudia Nagel**, Axel Loewe, *ECGdeli - ECG delineation algorithms*, <https://github.com/KIT-IBT/ECGdeli>

## Supervised Student Theses

- Fabian Anzlinger, *Assessment of Inpatient ECG Feature Distributions for a Simulation of Realistic 12-Lead ECG Signals*, Bachelor's Thesis, Institute of Biomedical Engineering, Karlsruhe Institute of Technology (KIT), 2020
- B.Sc. Salma Touil, *Parameterization of an Electrophysiological Simulation for a Biventricular Shape Model based on a Predefined QRST Morphology*, Master's Thesis, Institute of Biomedical Engineering, Karlsruhe Institute of Technology (KIT), 2021
- B.Sc. Maximilian Sachs, *Investigating the Use of Machine Learning for Classifying Atrial Diseases Based on P-wave Simulations on a Biatrial Shape Model*, Master's Thesis, Institute of Biomedical Engineering, Karlsruhe Institute of Technology (KIT), 2021

- B.Sc. Hannes Welle, *Quantifying the influence of simulation and geometry parameters on the QRS morphology for large-scale simulations of healthy and bundle branch block ECGs*, Master's Thesis, Institute of Biomedical Engineering, Karlsruhe Institute of Technology (KIT), 2021
- B.Sc. Johannes Osypka, *Application of Deep Neural Networks for Clinical ECG-based Identification of Atrial Fibrosis*, Master's Thesis, Institute of Biomedical Engineering, Karlsruhe Institute of Technology (KIT), 2021
- Jule Bender, *Classification of interatrial conduction blocks from simulated P waves of the 12-lead ECG*, Bachelor's Thesis, Institute of Biomedical Engineering, Karlsruhe Institute of Technology (KIT), 2022
- B.Sc. Nadine Eichhorn, *Implementation of an HRV and AV node delay model for synthesizing simulated P waves and QRST segments*, Student research project, Institute of Biomedical Engineering, Karlsruhe Institute of Technology (KIT), 2022

## Awards & Grants

- 1st price in student competition, 53rd DGBMT Annual Conference, Frankfurt, Germany, 2019, **Claudia Nagel**, Nicolas Pilia, Laura Unger, Olaf Dössel, *Performance of Different Atrial Conduction Velocity Estimation Algorithms Improves with Knowledge about the Pattern of Depolarization*
- Best oral presentation award, Statistical Atlases and Computational Modeling of the Heart, Strasbourg, France (online), 2021, **Claudia Nagel**, Matthias Schaufelberger, Olaf Dössel, Axel Loewe, *A bi-atrial statistical shape model as a basis to classify left atrial enlargement from simulated and clinical 12-lead ECGs*
- Clinical Needs Translational Award, Computing in Cardiology, Brno, Czech Republic, 2021, Deborah Nairn, **Claudia Nagel**, Björn Müller-Edenborn, Heiko Lehrmann, Thomas Arentz, Olaf Dössel, Amir Jadidi, Axel Loewe, *Optimal Regional Voltage Thresholds for Identifying Ablation Targets in Patients with Atrial Fibrillation*
- 2nd price in student competition, 55th DGBMT Annual Conference, Hannover, Germany, 2021, Hannes Welle, **Claudia Nagel**, Axel Loewe, Ralf Mikut, Olaf Dössel, *Classification of Bundle Branch Blocks with QRS Templates Extracted from 12-lead ECGs*
- Travel research grant 2022, Karlsruhe House of Young Scientists (KHYS), full coverage of travel and living expenses for a three month research stay at University of Oxford, Oxford, UK
- Travel grant, Simula Summer School in Computational Physiology 2019 at Simula Research Laboratory, Oslo, Norway, and University of California San Diego, San Diego, USA